Real-time study of model biological samples on dedicated microfluidic platform coupled with multiplexed biosensor : one step towards Lab-on-Chip for CTC-clusters

Syed Harris Hussain

To cite this version:

Syed Harris Hussain. Real-time study of model biological samples on dedicated microfluidic platform coupled with multiplexed biosensor : one step towards Lab-on-Chip for CTC-clusters. Other. Ecole Centrale de Lyon; RMIT University (Melbourne), 2023. English. NNT : 2023ECDL0023 . tel-04186824

HAL Id: tel-04186824
https://theses.hal.science/tel-04186824v1

N° d’ordre NNT : 2023ECDL0023

THESE de DOCTORAT DE L’ECOLE CENTRALE DE LYON

membre de l’Université de Lyon

En cotutelle internationale avec Royal Melbourne Institute of Technology (RMIT)

Ecole Doctorale N° 160
Electronique, Electrotechnique et Automatique

Spécialité de doctorat : Ingénierie pour le vivant

Soutenue publiquement le 15/06/2023, par :

Syed Harris Hussain

Real-time study of model biological samples on dedicated microfluidic platform coupled with multiplexed biosensor: one step towards Lab-on-Chip for CTC-clusters

---

Devant le jury composé de :

Dr. ROUPIOZ	Yoann	Directeur de Recherche CNRS	SyMMES, Grenoble	Rapporteur
Pr. LEBLOIS	Thérèse	Professeure des Universités	Université de Franche-Comté	Rapporteure
Pr. VELLUTINI	Luc	Professeur des Universités	Université de Bordeaux	Examinateur
Dr. LAURENCEAU	Emmanuelle	Maîtresse de conférences, HDR	École Centrale de Lyon	Directrice de thèse
Dr. HUERTAS	Cesar S.	Post-Doctoral researcher	Royal Melbourne Institute of Technology	Directeur de thèse
Pr. MITCHELL	Arnan	Professeur	Royal Melbourne Institute of Technology	Co-directeur de thèse
Dr. DEMAN	Anne-Laure	Maîtresse de conférences, HDR	Université Lyon 1	Co-directrice de thèse (Invitée)
Dr. SZYDZIK	Crispin	Post-Doctoral researcher	Royal Melbourne Institute of Technology	Invité

Acknowledgements

Firstly, I would like to thank the jury members, Yoann, Thérèse, and Luc for being part of my thesis examination and for all their comments and interesting remarks regarding my work. I am grateful for your participation. I would deeply like to thank my supervisors Emmanuelle Laurenceau and Anne-Laure Deman at INL and Cesar S. Huertas, Crispin Szydzik and Arnan Mitchell at InPAC. I am grateful that they have given me the opportunity to work on this multi-disciplinary project covering applied chemical approaches and development of integrated microfluidic and optical system focusing on its application for pathological conditions specifically cancer. Working on understanding cancer is close to my heart and for that I am indebted. Thank you very much for your warm welcome and especially your time, valuable (repeated) feedbacks, and continuous support, which I believe have molded me the person that I am today.

I would like to acknowledge the ECLAUSion, CoFUND directed by Christian Grillet and Arnan Mitchell and ALPhFA project that financially supported my PhD project both in France and Australia and gave me the opportunity to present my work in different international conferences, research events and to sponsor my stay in Melbourne. I would also like to thank all the administrative and technical staff at both ECL and RMIT for helping me my maneuver around all the infamous French and Australian administration.

To all the team members of DSE at INL: Yann, Thomas, Isabel, Christelle, Virginie, Magalie, Jean-Pierre and Charles, DSE at La Doua: Magalie, Pascal, and Caterina, and ECL: Bertrand, Cecile, and Catherine, thank you very much for your continuous help and guidance. And to all the team members at Center of Nanoscale Photonics: Blanca, RMMF, MNRF at RMIT: Billy, Zeyad, Rachel, Brian, Ruth, Chenglong and Dashen for all your help and support while I was getting lost in the labs at RMIT.

At INL, I would personally like to appreciate Isabel (especially for replacing all the glassware that I used to broke), Thomas and Yann for teaching me the basics around the lab (and for their never-ending patience) and Magalie for her help in conducting cell experiments. At RMIT, I would like to thank Billy, Zeyad and Chenglong for their help on surface characterization experiments, April for cell experiments and Blanca for optical setup experiments along with Rachael for general help and to integrate me within InPAC.

And to all the friends that I have met over the past 4 years and hopefully will continue to be a part of in the future, I would like to thank all the ECLAUSion students specifically:

Panteha, Ana-Maria, Greta, Marko, Mohab and Kokou (Firmin), who I have shared this beautiful 'sejour' at INL and InPAC, these are the ones that have the privilege to have been bothered by me. In addition, I cannot forget all my friends that I have shared this research life within France: Oleh, Antonin, Jesus, Paule, Gaukhar, Clement, Abel, Rachael, Solene, and Lucie. Thank you very much for bearing me, introducing me to different people and for all the coffee breaks, lunches, dinners, trips. These are some of the many cherished memories I have of you all. And to the friends I met in Australia, thank you very much to Jorge, Siew, Karen, Paul, Wade (Wei-Che), Sonya and Madhuri for all your help and time spent with me either for experiments and/or just lounging off. In my personal life I would like to thank all the people that have helped in Lyon and Melbourne, and especially my roommates that I have shared my life with throughout this PhD Ebrahim and Aniel.

I would like to take some time and mention all my previous teachers and supervisors from kindergarten to primary through middle and high school to intermediate college, university for both bachelors and masters specifically Reiner, Kashif, Nasr and Bilal for your guidance and support towards me. And I must acknowledge all the beautiful people who I have met during my time and hold dear even to this day, Husam, Ahmed, Hammad, Ahmed, Ali bhai, Asad, Ismayil, Israr bhai, Kafeel bhai, Adnan bhai, Atif bhai, Farhan, Fahad, Umair, Hammad, Fazal, and Maaz that have supported me personally not only on this journey but from before when we were naïve, though I still am.

Finally, I would like to thank my family, uncles and aunts, my cousins especially Julie bhai, that have supported me since I have embarked on this journey and since I was born and have continue to do so. I am and will be eternally grateful and indebted. Lastly, my family, my parents (Mama: Irrum Muarraf nee Pasha and Baba: Dr. Syed Muarraf Hussain), my brother Moiz, Chachu (Dr. Mukarram), Minda: (Misbah), Munim, Daisy (Maham), and Munif, words will not be enough, to describe my feelings that I have for you. Without all of you, your support and motivation, not only this project but me as person who I am would not have been possible.

I wish everyone of you all the best in your professional and especially personal endeavors, I will be rooting for you (live long and prosper). And thank you very much for keeping me on my toes, I will try my best so that you all will always be proud of me. Peace.

Table of Contents

List of Figures

List of Tables

Glossary

Ab	Antibody
Ab-N_3	Azide activated antibody
Ab-SH	Fragmented antibody
ADIBO/DIBO	Aza-dibenzocyclooctyne
ADT	Androgen Depletion Therapy
AFM	Atomic Force Microscopy
AR-V7	Androgen receptor Splice Variant 7
ARXPS	Angle Resolved X-ray Photoelectron Spectroscopy
Au-NHA	Gold-nanohole arrays
AuNPs	Gold nanoparticles
BARAC	Biarylazacyclooctynone
BiMW	Bi-modal waveguide
BSA	Bovine Serum Albumin
C/NHS	Carbodiimide/N-hydroxysuccinimidyl ester chemistry
CA	Cancer antigen
CA 15-3	Cancer antigen 15-3
CA125	Cancer antigen 125
CD	Cluster of differentiation
CEA	Carcinoembryonic antigen
cfDNA	Cell-free DNA
CK	Cytokeratins
CL/CLIA	Chemo-luminescence/chemiluminescence immunoassays
COOH/OH Alkyls	1/1 Carboxylated/Hydroxylated Alkylated monolayers
COP	Cyclic olefin polymers
CRET	Chemo-luminescence resonance energy
CTC Cluster V1/V2/V3	CTC Cluster microfluidic device version 1/2/3
CTCs	Circulating tumour cells
ctDNA	Circulating tumour DNA
CuAAC	Copper based Azide Alkyne Cycloaddition
CYFRA21-1	Fragments of cytokeratin 19
DBCO	Dibenzocyclooctyne
DBCO PEGs/OH Alkyls	1/1 DBCO terminated PEGs/Hydroxylated Alkyl monolayers

DBCO/OH Alkyls	1/1 DBCO terminated/Hydroxylated Alkyl monolayers
DBCO/OH PEGs	1/1 DBCO/Hydroxylated PEGs 2k PEGs monolayers
DBCO-NHS	Dibenzocyclooctyne - N-hydroxysuccinimidyl ester
DFF	Dean Flow Fractionation
DIBAC	Dibenzocyclooctyne
DIC	N,N′ -diisopropyl-carbodiimide
DIFO	Difluorinated cyclooctyne
DMEM	Dulbecco Modified Eagle medium
DMSO	Dimethyl sulfoxide
DNA	Deoxyribose nucleic acid
E-cad	E-cadherin
ECL	Ecole Centrale de Lyon
EDC/NHS	N’-ethylcarbodiimide/- N-hydroxysuccinimidyl ester chemistry
ELISA	Enzyme linked immunosorbent assay
EMT	Epithelial to Mesenchymal transition
EpCAM	Epithelial Cell Adhesion Molecule
Fab	Antigen binding fragment
Fc	Constant fragment
FGF2	Fetal growth factor 2
FIB	Focused ion beam
FOV	Field of view
FRET	Fluorescence resonance energy transfer
FWHM	Full-wdith half max
HER2	Human Epidermal Growth Factor Receptor 2
Ig	Immunoglobulin
IgG	Immunoglobulin G
IHC	Immunohistochemistry
IL-2/6/8	Interleukin-2/6/8
INL	Institut des Nanotechnologies des Lyon
InPAC	Integrated Photonics and Applications Centre
ISET	Isolation of epithelial tumour cells
Ki-67	Antigen identified by monoclonal antibody Ki-67
KLK3	Gamma-semino protein or kallikrein-3
LCa	Lung cancer

LOC	Lab-on-a-chip
LOD	Limit of detection
LOQ	Limit of quantification
LSP	Localized surface polaritons/plasmons
LSPR	Localized surface plasmon resonance
Lys	Lysine
mCR-PCa	Metastatic castration resistant prostate cancer
MET	Mesenchymal to Epithelial transition
mM/µM/nM/pM	Milli/micro/nano/pico molar
mL/µL/nL/pL	Milli/micro/nano/pico litre
MOFO	Monofluorinated cyclooctyne
MRR	Multiring resonantors
MW	Molecular weight
MZI	Mach-Zehnder Interferometer
N-cad	N-cadherin
NHA	Nanohole arrays
NHS/OH Alkyls	N-hydroxysuccinimidyl/Hydroxylated Alkyl monolayers
NSC-LCa	Non-small cell lung cancer
NSE	Neuron Specific Enolase
OS	Overall survival
PBS	Phosphate Buffer Saline
PbZrTi	Lead zirconium titanium
PCa	Prostate cancer
PCR	Polymerase chain reaction
PD-L1	Programmed death ligand 1
PDMS	Polydimethylsiloxane
PEG	Polyethylene glycol
PM-IRRAS	Polarized modulation infrared adsorption spectrscopy
PMMA	Polymethylmethacrylate
POC	Point-of-care
PSA	Prostate specific antigen
PSMA	Prostate specific membrane antigen
PSPPs	Propagating surface plasmon polaritons
QCM	Quartz crystal microbalances

QD	Quantum dots
R/R1/R2	Fluidic resistance/Pathway 1/2 fluidic resistance
RI/RIUs	Refractive index units
RMIT	Royal Melbourne Institute of Technology University
RNA	Ribose nucleic acid
S/N	Signal-to-Noise ratio
SCC	Squamous cell carcinoma /antigen
SC-LCa	Small cell lung cancer
SEM	Scanning electron microscope
SERS	Surface enhanced Raman spectroscopy
SPAAC	Strain promoted azide alkyne cycloaddition
SPANC	Strain promoted alkyne nitrone cycloaddition
SPR	Surface plasmon resonance
TEM	Transmission electron microscope
TGF-β	Tumour growth factor-beta
THF	Tetrahydrofuran
TNF/TNFR2	Tumour necrosis factor-2 receptor
Tof-SIMs	Time of flight
WBCs	White blood cells
WD	Working distance
XPS	X-Ray Photoelectron Spectroscopy

Chapter 1

Introduction

Cancer is defined as purposeless proliferation of persistent and non-functional cells within any part of the body. Some of these cells shed and separate from the primary tumour mass, join the blood circulation, and attach themselves to another part of the body resulting in tumour spread and metastasis. Such cells are termed as circulating tumour cells (CTCs), and recent research has shown link between CTCs and aggressive metastatic growth and cancer spread [1]. Aggressive disease progression and shorter overall survival (OS) have been observed in patients with elevated CTC numbers (more than 10 CTCs per mL of blood)[1].

Liquid biopsies are the blood or biological fluid that contains CTC or other disease biomarkers like circulating tumour DNA (ctDNA) and exosomes which can be used for early cancer diagnosis and prognosis. Compared with conventional tissue biopsies, which are gold diagnostic standard for cancers, these liquid biopsies are inherently less invasive and can be used for screening, diagnosis and monitoring of cancer [2].

The key scientific hurdle for analysing CTCs from liquid biopsies is their rarity among the other cells and thus their efficient isolation and specific detection of various associated biomarkers in real-time. More so, CTCs express different biomarkers depending on stage of cancer progression, thus, their analysis can give a broader picture of the disease state and progression, shedding light on new ways for cancer diagnosis and treatment. Commercial setups like CELLSEARCH® which is the only FDA approved or kits like isolation of epithelial tumour cells (ISET) are used for initial CTC sorting. However such devices do not isolate all CTC sub-populations, targeting epithelial cells only [3,4] and they are not capable of analysing biomarker secretion from different sub-populations. For CTC-biomarker analysis, conventional immunological assays including immunohistochemistry (IHC) and enzyme-linked immunosorbent assay (ELISA), and genetic testing are mostly used to detect intracellular and cell membrane biomarkers and to analyse proliferative activity of cancer cells from tissue samples or fixed cells [5]. . All these methods need to be employed sequentially to get a picture for one patient, making this extremely time consuming with further requiring large and repeated sample volumes resulting in overall high operational costs.

To overcome such hurdles, biosensing technology have come to the forefront. Biosensor is an analytical device comprised of a bio-recognition element, transducer, and signal output. For detection of cancer cells and associated biomarkers, different transducing elements like mass based/piezoelectric, electrochemical, and optical modalities have been researched upon extensively. However, for fabrication of any biosensor, attachment of bio-recognition element onto solid substrates like metal surface such as gold (Au) and/or glass is a vital step and surface chemistry plays a pivotal role to producing highly accurate and selective biosensors. Optimization of surface modification through chemical functionalization and biological immobilization needs to be addressed. Carbodiimide/NHS is a conventional covalent approach. However, this coupling requires specific pH and temperature conditions, making it prone to poor product yields during reactions specifically for immunoglobulins and enzymes due to activity loss [6]. To overcome these problems, copper-free click chemistry can be exploited, which is a recent approach and refers to a group of chemical reactions used for specific conjugation of biomolecules. Such reactions are fast, versatile, simple to perform, easy to purify, stereospecific and they produce only harmless by-products making them suitable for biomolecule manipulation.

In addition, biosensors have the capacity to provide analysis in a multiplexed (analysing more than one parameter) and real-time fashion and can further be fully integrated with a microfluidic platform. In biology, microfluidics has widespread applications ranging from microarrays for PCR and LOC to high-speed DNA systems and microchips for drug screening and investigation of cultured cells. This field has progressed rapidly and for CTCs, efficient trapping while keeping their biological integrity intact has been imperative. Microfluidic devices are portable and can better be adapted for CTC trapping requiring small sample volumes further minimizing costs. More so, such devices can be automated that decrease overall operational manpower.

Various groups developed and patented microfluidic technology, where different modalities have been employed for fabrication of complex micro-structures for CTC isolation and trapping [7,8]. Descamps et al., along with Jackson and group presented a comprehensive comparative analysis of the different microfluidic approaches for CTC isolation and trapping [9,10]. Isolation efficiency rates for conventional CELLSEARCH® setup hovers between 75 to more than 85% depending on the cancer type while different microfluidic based chips used for CTC isolation through biological and/or physical parameters show rates of 90 to more than 95% showcasing increased performance [9]. Further microfluidic devices have showcased analysis of single-CTC or CTCs clumped together to form Cluster-CTCs from patients for further genetic analysis [7].

For my PhD project, I have focused on fabricating a lab-on-a-chip (LOC) system, by integrating a microfluidic platform capable of performing CTC trapping with a biosensing modality for analysis of CTC-biomarker expression. Such a microsystem will make it possible to analyse CTCs from patients and carry out chemosensitivity studies on CTCs, which will subsequently contribute to the development of more efficient tools for CTC classification and personalized cancer therapies. This project is part of an international cotutelle between Ecole Centrale de Lyon (ECL) and Royal Melbourne Institute of Technology (RMIT) under the umbrella of European Union and Marie Curie framework. My work was divided between two laboratories: (i) Devices for health and environment (DSE), Institute of Nanotechnologies of Lyon (INL) at ECL and Claude Bernard Lyon-1 University; (ii) the Integrated Photonics and Applications Centre (InPAC) at RMIT University.

This thesis is further divided into 5 parts. In **Chapter 2**, State of the Art highlights general cancer diagnostics specifically focusing on CTCs, characteristics and conventional methods used for analysis. In addition, this chapter showcases general physiology and common biomarkers for CTCs along with CTC-biomarkers associated with lung cancer and prostate cancer. Afterwards, biosensing modalities like mass-based/piezoelectric, electrochemical, and optical approaches specific for these biomarkers is presented along with an in-depth comparative analysis is performed for such transducing elements.

Chapter 3 focuses on surface modification for efficient site-specific, directed, and oriented antibody immobilization for biosensor fabrication. Comparative analysis between two different click reactions i.e., strain promoted azide-alkyne cycloaddition (SPAAC) and thiol-yne reaction, and conventional carbodiimide/NHS coupling were performed for antibody immobilization on alkylated and PEGylated functionalized surface. More so, biosensing efficiency of the different antibody immobilization modalities for the detection of cancer-associated biomarkers was evaluated through SPRi measurements.

Chapter 4 showcases fabrication of a complex microfluidic device for optimal trapping of CTCs. Such a microfluidic platform with pneumatic valves and trap units was actuated through moulding protocol. Literature review on pneumatic valve actuation for microfluidic devices have been further highlighted along with the in-depth details on the moulding protocol. Initial characterization of the pneumatic valves was performed through different device iterations. In addition, characterization through flow rate manipulation, bead trapping and subsequent cell trapping was showcased. More so, calculations on different biomarkers secretions were performed for cancer cells.

Chapter 5 highlights development of a biosensing setup integrated with a microfluidic platform capable of performing real-time biomarker detection for specific interleukin-6 (IL-6) and non-specific tumour necrosis factor receptor II (TNFR2) signal interactions. Label-free optical biosensing through plasmonic nanohole arrays (NHA) were fabricated through E-beam deposition and characterized through dual scanning electron microscope (SEM)/ focused ion beam (FIB) setup. In addition, evaluation of such NHA through an opto-spectroscopic setup was performed by analysing bulk refractive index changes because of different glycerol concentrations for initial characterization of setup sensitivity. And lastly, conclusions from my PhD work and future perspectives are presented in the last part of this thesis.

References:

1. Alix-Panabières, C. & Pantel, K. Clinical prospects of liquid biopsies. *Nat. Biomed. Eng.* **1**, (2017).
2. Young, R. Circulating Tumor Cells in Lung Cancer. 655–660 (2012) doi:10.1159/000345182.
3. Nagrath, S. *et al.* Isolation of rare circulating tumour cells in cancer patients by microchip technology. *Nature* **450**, 1235–1239 (2007).
4. Khoo, B. L. *et al.* Expansion of patient-derived circulating tumor cells from liquid biopsies using a CTC microfluidic culture device. *Nat. Protoc.* **13**, 34–58 (2018).
5. Axelrod, H. D., Pienta, K. J. & Valkenburg, K. C. Optimization of Immunofluorescent Detection of Bone Marrow Disseminated Tumor Cells. *Biol. Proced. Online* **20**, 1–13 (2018).
6. Wickramathilaka, M. P. & Tao, B. Y. Characterization of covalent crosslinking strategies for synthesizing DNA-based bioconjugates. *J. Biol. Eng.* **13**, 8–17 (2019).
7. Khoo, B. L. *et al.* Expansion of patient-derived circulating tumor cells from liquid biopsies using a CTC microfluidic culture device. *Nat. Protoc.* **13**, 34–58 (2018).
8. Kulasinghe, A., Zhou, J., Kenny, L., Papautsky, I. & Punyadeera, C. Capture of circulating tumour cell clusters using straight microfluidic chips. *Cancers (Basel).* **11**, 1–11 (2019).
9. Jackson, J. M., Witek, M. A., Kamande, J. W. & Soper, S. A. Materials and microfluidics: Enabling the efficient isolation and analysis of circulating tumour cells. *Chem. Soc. Rev.* **46**, 4245–4280 (2017).
10. Descamps, L., Roy, D. Le & Deman, A. Microfluidic-Based Technologies for CTC Isolation : A Review of 10 Years of Intense Efforts towards Liquid Biopsy. (2022).

Chapter 2

State of the Art

2.1. General overview of Cancer:

Cancer is defined as the persistent proliferation of purposeless, non-functional cells, capable of propagating in any part of the body, whereas metastasis is the spread of such tumour cells from one part of the body to another, making the condition more aggressive and malignant. Due to its persistence, cancer and metastasis are one of the leading causes of death worldwide where 1 in 6 deaths is cancer-related and this number is expected to increase based on statistical data highlighted by the World Health Organization (WHO) [1]. According to 2020 World Cancer Report published by International Agency for Research on Cancer (IARC) and WHO, lung cancer (LCa) is the most common type of cancer for incidence and mortality among males with around 1.4 million new cases and 1.2 million deaths were recorded in 2020. Following LCa, prostate cancer (PCa) is the second most common cancer among males, with an estimated 1.4 million new cases diagnosed and about 375,000 reported deaths worldwide [1]. For females, breast cancer is the leading form of cancer with 2.2 million case incidences and 0.6 million reported deaths closely followed by LCa with similar mortality rates [1], as highlighted in the Fig. 2.1.1.

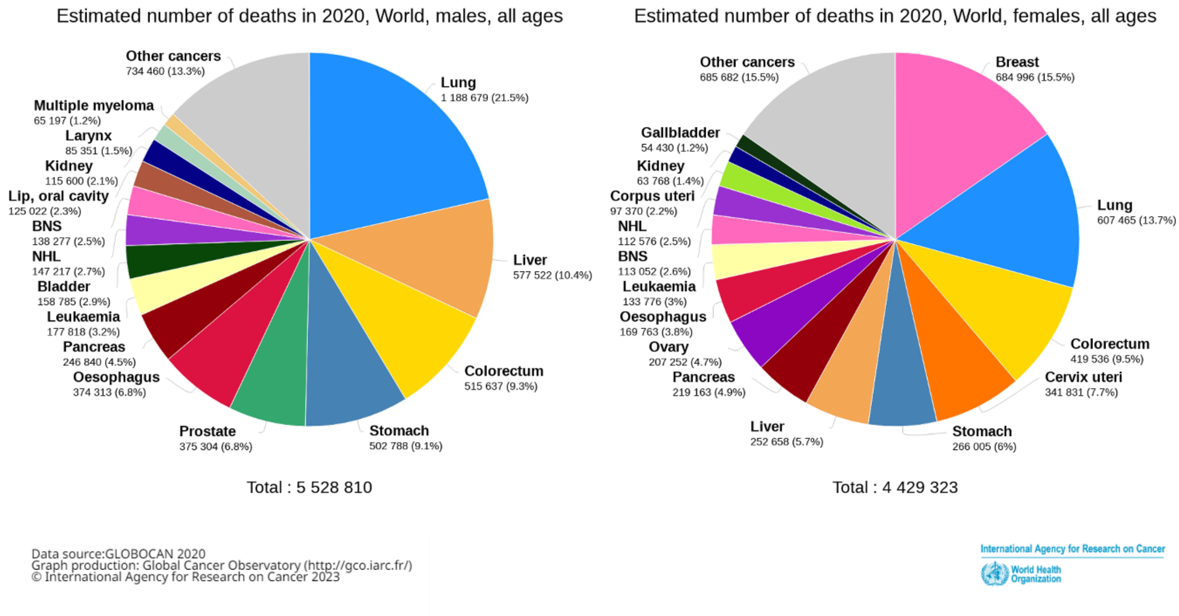

Figure 2.1.1.: Cancer mortality rates for male and female in 2020, all ages. Data sourced from GLOBOCAN2020 published on International Agency on Cancer 2023

For cancer diagnosis, conventional methods are tissue biopsies followed by histopathological characterization, imaging modalities and cancer biomarker analysis. Standard laboratory methods for cancer biomarker analysis focus on immunofluorescence and immunohistochemistry (IHC), enzyme-linked immunosorbent assay (ELISA), and gene sequencing. IHC is a qualitative approach, primarily used for detection of intracellular and cell membrane biomarkers and for further analysis of proliferative cancer cell activity from tissue samples or fixed cells [2]. ELISA on the other hand allows quantitative detection of soluble or free biomarkers in liquid samples such as blood, serum, urine, or saliva and with varying detection ranges between 0.1 pg/mL to 500 ng/mL [3]. It should be noted however, the range and limit of detection (LOD) depends on the biomarker of interest and the kit/protocol used. For effective screening, tracking, and monitoring of the disease, all these standard techniques need to be performed at regular intervals which can take a toll on patients. The diagnostic gold standard for tumour confirmation are tissue biopsies, where going under the needle for the patients can be extremely invasive and a traumatic experience, specifically in cases for LCa where the probe must be introduced orally as seen in Fig. 2.1.2. (A) and for PCa where it must be introduced via rectum as showcased in Fig. 2.1.2 (B). In addition, both LCa and PCa have the tendency to propagate rapidly and metastasize if unchecked, thus regular check-ups are required. Tissue biopsies are therefore incompatible with real-time monitoring for cancer progression which is a stumbling block for the development of personalized treatment further being a detriment on patient upkeep.

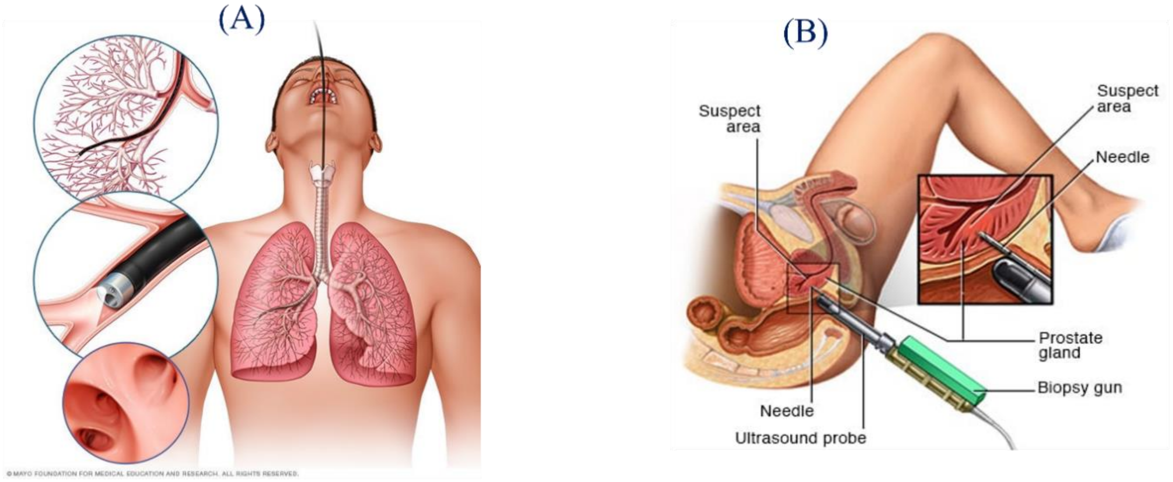

https://www.mayoclinic.org/diseases-conditions/lung-cancer/diagnosis-treatment/drc-20374627 https://www.mayoclinic.org/tests-procedures/prostate-biopsy/about/pac-20384734

Figure 2.1.2.: Conventional tissue biopsies for **(A)** Lung cancer and **(B)** Prostate cancer

A growing interest in cancer diagnostics has been shifted towards ‘liquid biopsies’, focusing on the analysis of circulating biomarkers in blood sample but also sometimes urine, saliva, or semen as shown in Fig. 2.1.3. Analysis of liquid biopsies focuses specifically on circulating tumour DNA (ctDNA), cell-free DNA (cfDNA) and miRNAs, exosomes, circulating tumour cells (CTCs), and cancer-related soluble proteins. This makes liquid biopsies vs the conventional tissue biopsies more readily accessible and capable of performing repeated multiple times with minimal invasiveness, thus making it a strong candidate for efficient cancer monitoring. Among biomarkers, circulating tumour cells (CTCs) are strong diagnostic candidate for early metastatic indicator. CTCs are specific tumour cells dislodged from the primary tumour found circulating within the blood circulation. Their count and biomarker analysis can provide invaluable insights on the patient’s tumour detection and profile and metastatic potential.

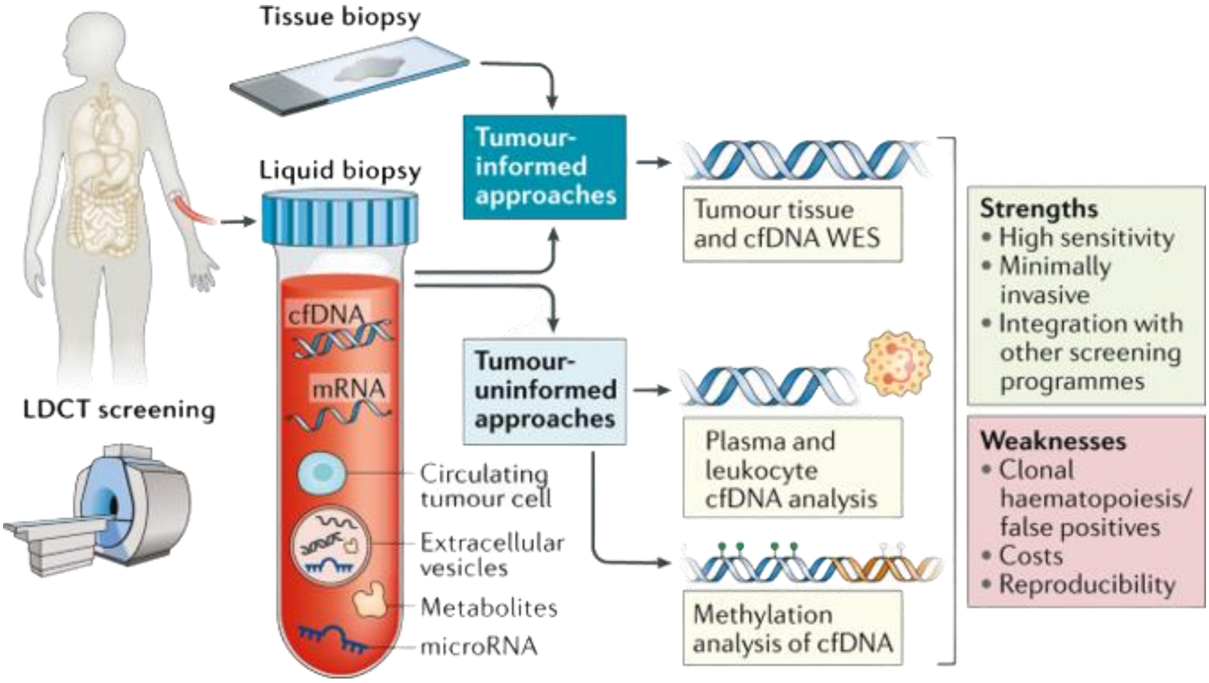

Figure 2.1.3.: Liquid biopsy for early lung cancer detection including biomarker sources such as cell- free DNA (cfDNA), extracellular vesicles, microRNAs, circulating tumour cells and tumour-derived metabolites. WES: Whole exome sequencing; LDCT: low- dose CT [4].

2.2. Circulating Tumour Cells (CTCs) in Cancer Diagnosis:

2.2.1. CTC characteristics:

CTCs and their associated biomarkers as liquid biopsies can provide valuable information regarding cancer progression and metastatic potential on patient-to-patient basis. The key scientific hurdles for CTC analysis are their rarity, heterogeneity of sub-populations in blood and their complex biological viability. CTCs are extremely rare, approximately 1 to 100 CTCs per 10^8 white blood cells (WBCs) in 1 mL of blood [5], making them a difficult target to isolate effectively. CTCs are also present in healthy patients albeit in low number [6,7], compared with cancer patients where their numbers significantly increase depending on disease progression. CTCs compared with functional cells exhibit specific biological characteristics such as higher diameter, a higher nuclear to cytoplasmic ratio, irregular nuclei, anisonucleosis (ratio from one nucleus to another > 0.5) and lack of specific cell surface markers defined as cluster of differentiation (CD) i.e., CD45 and CD15 receptors [8,9]. Physiologies of CTCs are like their primary tumour sites however, in the bloodstream, these can be identified as either single cells or as CTC-clusters where group of CTCs are clumped together. In addition, it has been presented between single and cluster-CTCs, worst overall survival has been showcased for cluster-CTCs [10–12]. However, it is technically challenging to isolate and enumerate such cells while further preserving their biological integrity for future functional analysis [13,14].

CTCs can either be epithelial (differentiated) or mesenchymal (undifferentiated) in nature depending on their tumour environment and biological conditions, where such cells can further undergo phenotypic changes i.e., switching between epithelial and mesenchymal characteristics. Indeed, when dislodging from the primary tumour site and entry into the blood circulation, CTCs undergo Epithelial to Mesenchymal Transition (EMT) where specific loss of cell adhesion and epithelial phenotype shedding is observed which plays an important role in metastatic spread [15]. And when CTCs attach themselves on the epithelial lining of another secondary tumour site for proliferation under favourable conditions, they undergo Mesenchymal to Epithelial Transition (MET) as highlighted in Fig. 2.1.4. It has been showcased that single CTCs exhibiting EMT phenotype express only EMT-associated markers but for CTC-clusters, they have the ability to retain their epithelial nature required for cell-cell interaction and adhesion while also possessing mesenchymal profile needed for cellular mobility and migration [16,17], making clusters over single CTCs aggressive and prone to propagation and metastasis.

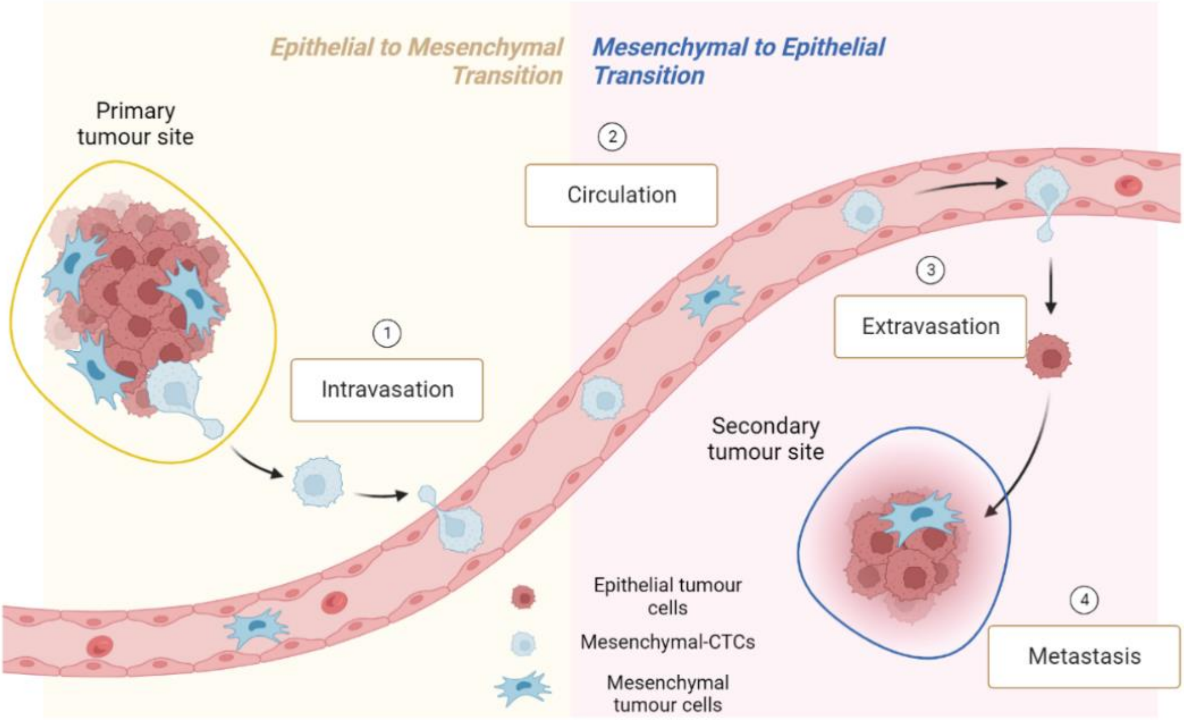

Figure 2.1.4.: Metastatic propagation via Epithelial to Mesenchymal Transition (EMT) and Mesenchymal to Epithelial Transition (MET): (1) Intravasation of epithelial-CTCs into the blood circulation, (2) Circulation, (3) Extravasation of mesenchymal-CTCs and (4) Colonization and metastasis to distant and secondary sites. CTCs undergo EMT and MET spreading cancer by BioRender.com.

2.2.2. CTC purification and sorting techniques:

Before CTCs and biomarker analysis, efficient and specific CTCs isolation needs to be focused on. As discussed above, CTCs are rare and have different sub-populations making their isolation and recovery challenging, where such CTCs must be kept alive for real-time biomarker expression analysis and treatment responses against different therapeutic agents. This could be touted as a promising avenue for early cancer diagnosis and could provide an avenue for the development of personalized diagnostics. Currently, CELLSEARCH® as highlighted in Fig. 2.1.5. is the only FDA-approved device which focuses on CTC selection through EpCAM expression for cell enumeration.

Unfortunately, this system does not allow the recovery of CTCs expressing other markers such as EpCAM.

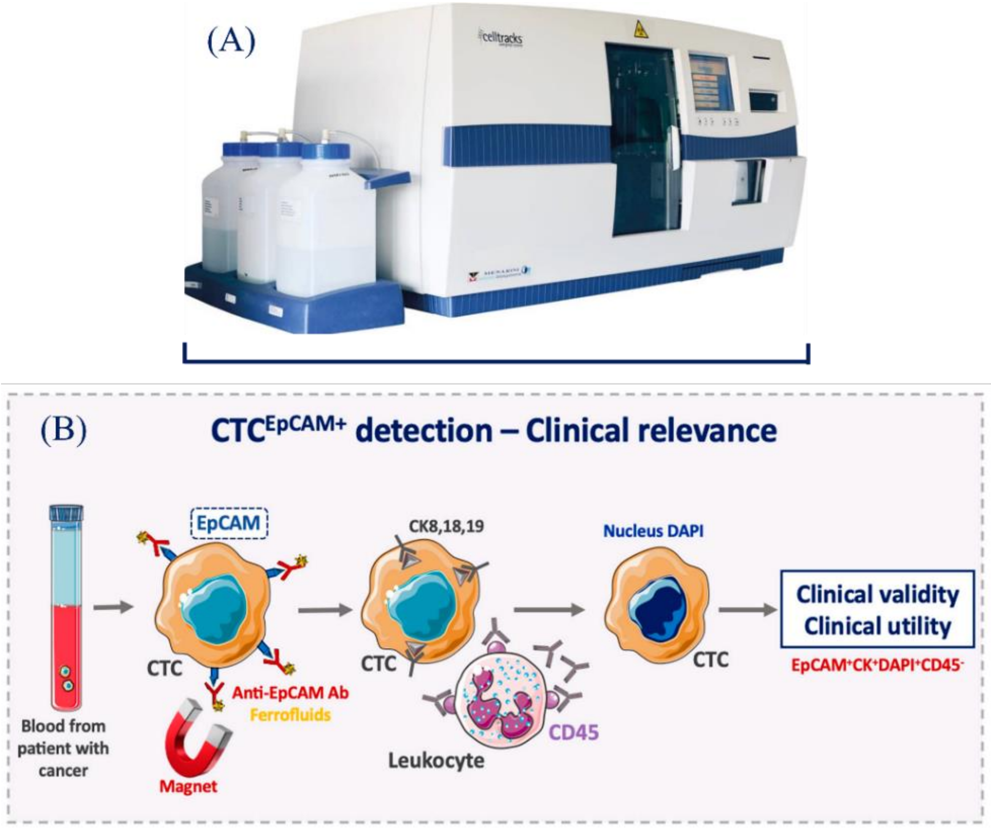

Figure 2.1.5.: **(A)** CELLSEARCH® and **(B)** Isolation principle for CELLSEARCH® focusing on CTC EpCAM+ detection where magnetically labelled antibodies against EpCAM are used for positive selection of CTCs. In addition, labelling antibodies against various cytokeratin (CK9, 18, 19) and DAPI nucleus are used for optimal selection [18].

Whereas RosetteSep™ as showcased in Fig. 2.1.6. is another technique for CTC isolation based on immuno-density characteristic. Red blood cells and most white blood cells are immune-linked and could be separated from the tumour cell population based on different density gradients. However, on one hand different kits are required depending on the type of tumour, on the other hand, isolation of these tumour cells based on density gradient interface to be an arduous task that may further compromise CTC biological integrity. CTCs can additionally be isolated based on their size via ISET (Isolation by Size of Epithelial Tumour cells) kits but like CELLSEARCH®, such kits focus only on epithelial cells. For such isolation techniques, non-epithelial/mesenchymal CTCs sub-populations are not selected.

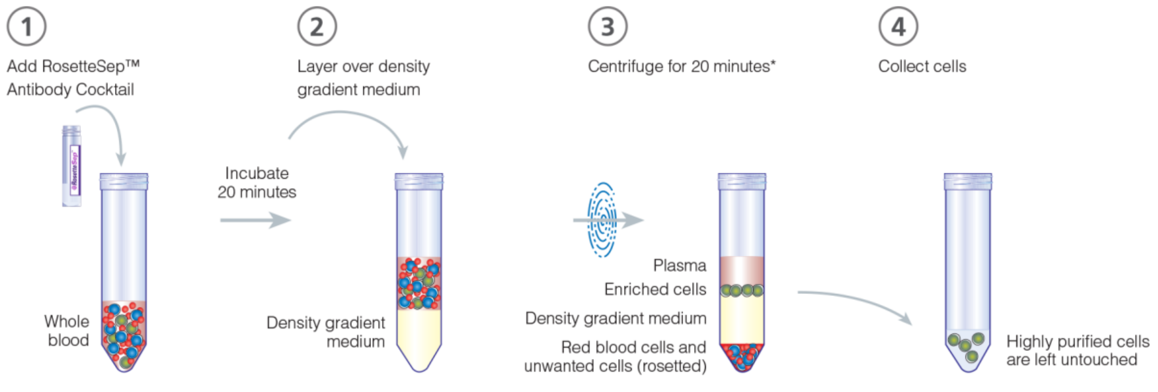

*Use SepMate™ to reduce centrifugation time to 10 minutes with brake on.

Figure 2.1.6.: Principle for RosetteSep™ technology for specific cell isolation focusing on **(1)** Addition of antibody cocktail, **(2)** Layer over density gradient medium, **(3)** Centrifugation and **(4)** Collection of specific cells (https://www.stemcell.com/products/brands/rosettesep-immunodensity-cell-separation.html)

To overcome such setbacks, in recent decades, microfluidic technology has come to the forefront focusing on CTC sorting, enumeration, isolation, and trapping. Microfluidic format performs manipulations on the cellular scale and allows for the implementation of various functions on a single chip, further providing avenues for cell isolation based on either their biological and/or physical properties. In addition, it has been showcased by different groups recently, microfluidics based isolation is comparatively inexpensive and could be easily mass-produced [19,20]. Various microfluidic based devices are being developed and patented for specific CTC isolation [10,19–22]. CTCs can be isolated based on their physical properties such as size, density and/or deformability or biomarker expression. One example is the commercially available ClearCell® FX1, a fully automated modality focusing on single-use microfluidic biochip. Separation of general CTCsis performed through Dean Flow Fractionation (DFF) keeping isolated CTCs biologically viable and intact for downstream analysis applications as showcased in Fig. 2.1.7. (A).

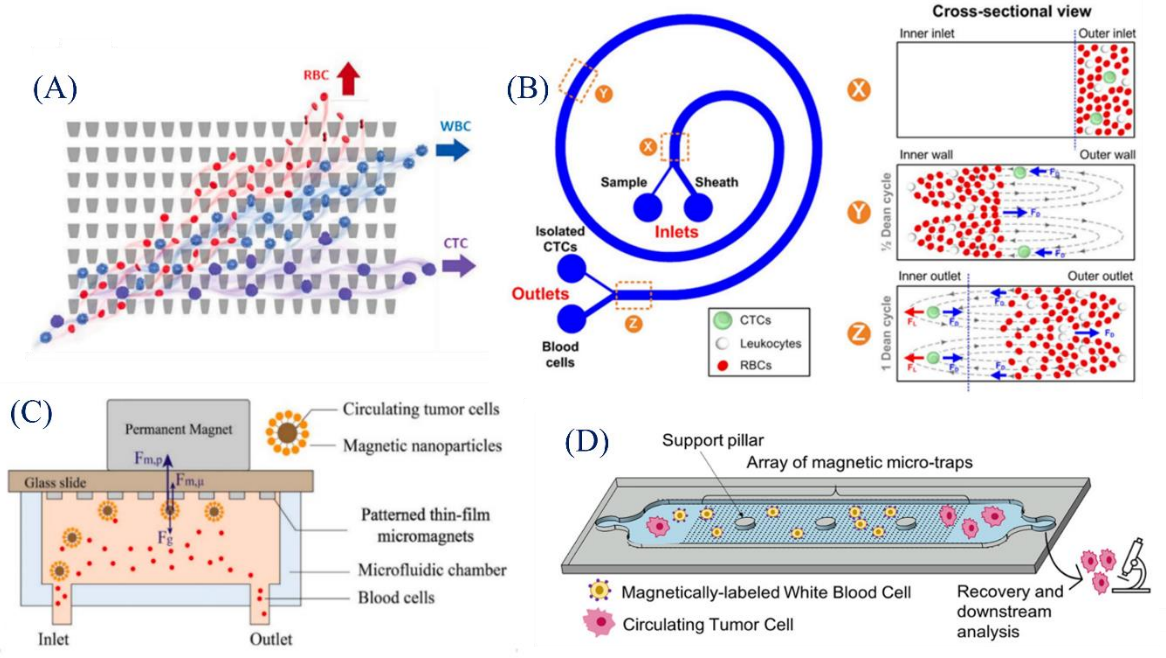

Figure 2.1.7.: **(A)** Continuous deformability-based cell separation using oscillatory diagonal flow through a matrix of funnel constrictions. The cell sample is infused into the bottom-left corner of the constriction and propelled by a biased oscillatory flow from the oscillation inlets and a constant rightward flow from the buffer inlet. The infused cells proceed in a zigzag diagonal pattern across the funnel matrix. Highly deformable RBCs pass through the top of the funnel matrix. CTCs and leukocytes proceed diagonally until reaching a blocking funnel row where they proceed horizontally toward separate outlets [23]. **(B)** Schematic illustration for separation principle of high-throughput CTCs isolation using Dean Flow Fractionation (DFF). Blood sample and sheath fluid are pumped through the outer and inner inlets of the spiral device respectively. Under the influence of Dean drag forces (FD (blue arrows)), the smaller hematologic cells (RBCs and leukocytes) migrate along the Dean vortices towards the inner wall, then back to outer wall again (Dean cycle 1), while the larger CTCs experience additional strong inertial lift forces (FL (red arrows)) and focus along the microchannel inner wall, thus achieving separation [24]. **(C)** Toward the combination of X-shaped velocity valleys as low-flow velocity regions with circular nickel microstructures as capture spots. This configuration achieved a >90% capture efficiency for cancer cell lines with various EpCAM expression levels and enabled them to be magnetically ranked, thanks to the gradual increase in nickel microstructure size. The capture of low-expression cells requires the action of larger nickel structures; therefore, it occurs in the later zones of the chip [25]. **(D)** Schematic of the device for the negative selection of CTCs. Magnetically labelled WBCs are captured on magnetic micro-traps while CTCs are collected for downstream analysis [26]**.**

More so, based on differences in physical properties, Park et al., developed deformability-based device to enrich viable CTCs directly from whole blood by integrating funnel- shaped constrictions as presented in Fig 2.1.7. (A) [23]. Lim et al, on the meantime, implemented Dean Flow Fractionation (DFF) separation that causes large cells (CTCs) to move toward the inner wall, due of the balance between inertial lift force and Dean drag force, while small cells (RBCs and WBCs) move toward the outer wall (Fig 2.1.7. (B)). Approaches based on the differences in biological properties, mainly use magnetic particles that are labeled with antibodies specific for either CTCs or white blood cells. Different approaches were developed to integrate magnetic micro-traps [25], such as nickel (Ni) microstructures (Fig C), or composite permanent micromagnets as demonstrated in Fig 2.1.7. (D) [27].

Several microfluidic technologies, awaiting FDA clearance, have been commercialized for physical-based CTC isolation, such as Parsortix® (ANGLE plc, UK), ClearCell® FX1 (Biolidics, Singapore), and VTX-1 (Vortex Biosciences, USA) [27]. Despite considerable advances in CTC isolation devices, physicians and biologists do not routinely use them, as there are still challenges specific to CTCs: population of remaining white blood cells, recovery of live CTCs for subsequent analysis, separation time compatible with clinical follow-up, ease of use of separation systems.

2.2.3. Common CTC biomarkers:

Different CTC sub-population can be identified depending on their nature and various biomarker expression. These CTC associated biomarkers can be defined as internal biomarkers expressed within the cells or external biomarkers being expressed on the cells as cell receptors or secreted in the tumour microenvironment. Summarized picture of common CTCs biomarkers has been highlighted in Table 2.1.1., further highlighting the role of these markers for EMT and MET.

Table 2.1.1.: Comparative analysis of common EMT and MET biomarkers and their functional descriptions for epithelial and mesenchymal CTCs

CTC sub-populations	EMT/MET	Biomarkers	Biomarker type	Function	Ref.
Mesenchymal CTCs	**EMT Biomarker**	Vimentin	Internal	Predominantly expressed in mesenchymal cells, marker associated with increased tumour growth and invasive potential, activity directly dependent with N-cadherin	[15,28,29]
		TWIST	Internal	Involved in cell differentiation, upregulation of N-cadherin and downregulation of E-cadherin	[15,28,29]
		SNAIL	Internal	Regulates EMT during embryonic development and tumour progression	[9]
		c-MET	Cell Surface	Involved in Tyrosine kinase activity, activation of various oncogenic signalling pathways and upregulate angiogenesis promoting tumour growth	[30]
		Integrins	Cell Surface	Involved in cell-extracellular matrix (ECM) adhesion, activation of various cell signalling pathways and cell cycle regulation	[29]
		N-Cadherin	Cell Surface	Hallmark of mesenchymal cells or tissues, mediating cell-cell adhesion, activity dependent on the expression of E-cadherin	[15,28]

		Fibronectin	Secreted	Involved in binding with integrins, and other extracellular matrix components, major role in cell adhesion, growth, migration, and differentiation	29
		TGF-β	Secreted	Multifunctional cytokine from the TGF-β superfamily, involved in metastatic progression and promotes tumourigenesis	9
Epithelial CTCs	**MET Biomarker**	Cytokeratins (CK8, CK18, CK19)	Internal	Provide mechanical support to the cell, used as a marker for differentiating between various epithelial cells. Luminal and Basal cytokeratins are used for CTC detection	8,15
		Epithelial Cell Adhesion Molecule (EpCAM)	Cell Surface	Hallmark of epithelial nature downregulated during cell differentiation, Involved in Cell-Cell adhesion, and upregulated in various carcinomas	15,31
		E-Cadherin	Cell Surface	Tumour suppressor biomarker, involved in intercellular junctions by hemophilic interactions and joining actin microfilaments	15,29,32

Numerous biomarkers such as Epithelial Cell Adhesion Molecule (EpCAM), E-Cadherin (E-Cad) and various cytokeratin (CK) like CK8, CK18 and CK19 are CTC associated biomarkers presenting epithelial phenotype. During EMT, such epithelial markers are repressed, and this downregulation initiates the expression of various mesenchymal markers such as Vimentin, TWIST and N-Cadherin (N-Cad), which further increase cell motility allowing these CTCs to circulate within the bloodstream [8,15]. And once these mesenchymal CTCs attach to a secondary tumour site to form micro-metastases, mesenchymal biomarkers are repressed while expression of epithelial biomarkers are in turn upregulated.

Different oncogenic signalling pathways during EMT are upregulated specifically through c-MET activity, which involved in RAS, PI3K, STAT3 and β-catenin activation along with upregulating metastatic progression through production of metalloproteases [33,34]. In addition, E-cad activity is repressed due to the activation of certain transcription factors such as TGF-β and SNAIL. For CTC-clusters, increased expression of SNAIL, TWIST and TGF-β transcription factors are observed, which could be responsible for bad overall survival and aggressive metastatic spread [9,35]. As cells are transitioning from an epithelial to a mesenchymal phenotype, sequential activation of fibronectin and the linked integrins network may cause cytoskeletal changes within the extracellular matrix (ECM) resulting in the loss of tight and adherent junctions [36–38]. A graphical representation of CTC and their various epithelial/mesenchymal biomarker expression are shown Fig. 2.1.8.

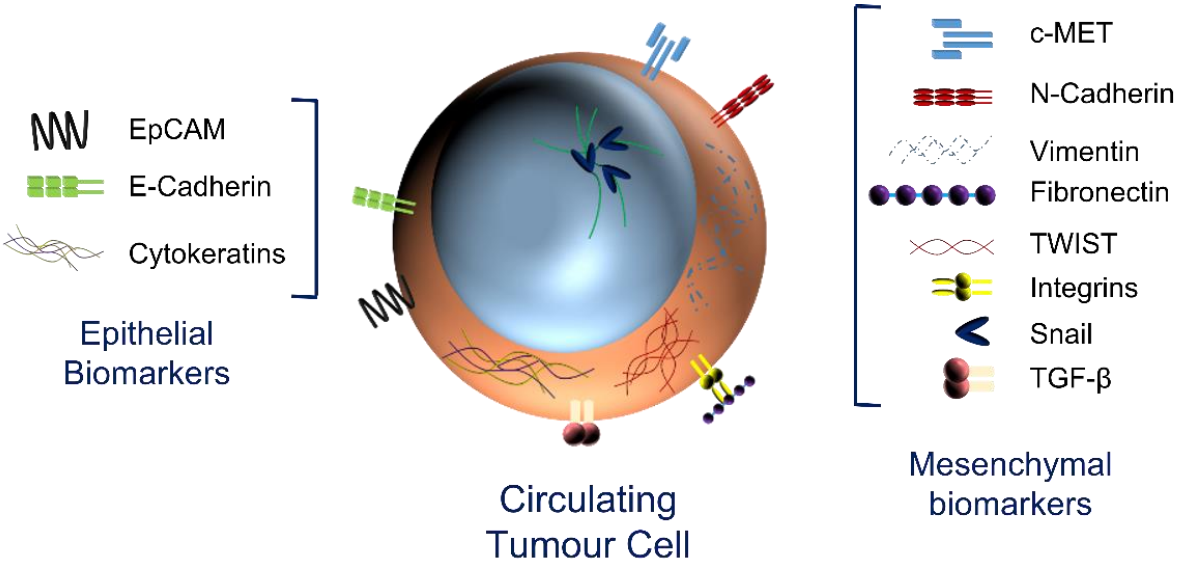

Figure 2.1.8.: Analytes for specific detection and analysis of CTCs and associated epithelial and mesenchymal biomarkers.

Due to the global incidence and mortality rates of LCa for males and females and their metastatic potential, the following sub-section will focus on CTC-biomarkers in LCa. In addition, PCa will be further highlighted for the state of the art due to high incidences. For following more information regarding breast cancer (BCa), comprehensive research has been showcased in various review articles for the role of CTCs in metastatic spread [39].

2.2.4. CTC-biomarkers in Lung cancer:

Among LCa, Non-Small Cell Lung Cancer (NSC-LCa) accounts for about 80-85% of cases while Small Cell Lung Cancer (SC-LCa) accounts for the remaining 15-20% [1]. SC-LCa is comparatively aggressive, malignant, prone to metastasis, and treatment focuses on strong radiotherapeutic and chemotherapeutic regimens. For different cancer types, specific biomarkers can vary between different sub-classifications and can further depend on the disease stage. For LCa diagnosis, serum levels of tumour markers such as carcinoembryonic antigen (CEA), fragments of cytokeratin 19 (CYFRA21-1) and neuron specific enolase (NSE) are commonly analysed along with Cancer Antigen 125 (CA125), Squamous Cell Carcinoma Antigen (SCC), Cytokeratin 8 (CK8) and

Programmed death ligand 1 (PD-L1) depending on LCa sub-classification. These biomarkers are showcased to be linked with CTCs specifically for different LCa types that have been compared and presented comprehensively in Table 2.1.2.

Table 2.1.2.: LCa biomarkers specific for CTCs regardless of their sub-populations. The markers mentioned here have been researched specifically in the context of CTC for SC-LCa and NSC-LCa. * 32.5% of NSC-LCa patients expressed PD-L1 but in different studies higher expression ranging from 50% to 72.7% has been observed.

Biomarker		**Biomarker type**	**Concentration levels**	**Cancer type**	**Ref.**
Lung cancer (LCa)					
Tumour marker antigen					
CEA	Carcinoembryonic antigen	Surface	Normal level: <2.5 ng/mL (Smoker: <5.0 ng/mL) Upper limit: 5 ng/mL	NSC-LCa,	12,40
CA125	Carbohydrate antigen 125 (Cancer antigen 125)	Surface	Elevated levels: ≥ 35 U/mL	NSC-LCa, SC-LCa	12,41
CYFRA21-1	Cytokeratin-19 Fragments	Internal	< 3.5 ng/mL cut off value set by Japan CYFRA team	NSC-LCa	12,42
SCC	Squamous cell carcinoma antigen	Secreted	Median level: 1.0 ng/mL	NSC-LCa	12,41
NSE	Neuron Specific Enolase	Secreted	Elevated levels: ≥ 12.5 ng/mL	SC-LCa	12,41
CTC associated					
PD-L1	Programmed death ligand 1	Surface	Expression depends on the clinico-pathological parameters*	NSC-LCa, SC-LCa	43,44
CK8	Cytokeratin 8	Internal	86.29 ± 12.1 ng/mL in NSC-LCa 16.89/5.2 ng/mL in SC-LCa > 50 ng/mL better OS	NSC-LCa, SC-LCa	45

CEA is considered a common tumour biomarker upregulated in several cancers, specifically for LCa, it has been reported as a prognostic marker providing critical information on metastatic dissemination. However, studies showed that CEA is a more useful tumour marker for NSC-LCa comparatively than for SC-LCa [46]. Like CEA, CYFRA21-1 seems to predict tumour prognosis and relapse specifically for NSC-LCa. However, high preoperative CYFRA21-1 values in heavy smokers and benign lung disorders i.e., pulmonary fibrosis and pneumonia patients outline the need to clarify its role [47].

Tumour markers such as CK8 and PD-L1 have been studied extensively due to their relation to CTCs and LCa progression. Compared with SC-LCa, high CK8 levels were observed for NSC-LCa and such elevated levels are further linked with increased tumour invasiveness. In addition, PD-L1 has been studied as a potential biomarker. A favourable treatment response has been observed in NSC-LCa patients where PD-L1 was inhibited using anti-PD-L1 antibodies. However, PD-L1 measurements over time could be unreliable due to false negatives [48]. Thus, other techniques need to be developed for real-time measurements and better critical tracking [43,48]. Moreover, elevated CTCs number for LCa are directly associated with larger tumour size and tendency for bone metastasis [49,50]. In addition, the role of CTCs has been highlighted in LCa before angiogenesis, making them and their associated biomarkers ideal for early cancer detection for symptomatic and asymptomatic patients [49].

2.2.5. CTC-biomarkers in Prostate cancer:

Prostate is an endocrine organ which is located at pelvic floor in males and abnormal growth due to the presence of elevated levels of androgens such testosterone is defined as prostate cancer (PCa). Conventional treatments to address such cancers focus on androgen depletion therapy (ADT) either through surgical removal of testicles or targeted drugs that stop/block androgen production. However, around 10-20% of PCa cases are castration-resistant where cancer continues to grow even after ADT. In addition, compared with other form of cancers, prostate cancer is predisposed to metastasis and about 80% of such cancer cells spread to different parts of the body specifically to bones i.e., hip, spine, and pelvic bones [51,52]. This highlights further complication of when the cancer started to spread and migrated to various parts making treatment and overall patient survival compromised.

For detection, disease progression and treatment response, the most common biomarker for earlier PCa stages is serum prostate-specific antigen (PSA). PSA also known as gamma-semino protein or kallikrein-3 (KLK3) is a glycoprotein enzyme, member of the kallikrein-related peptidase family and secreted by the epithelial cells of prostate glands. It is present in blood at very low levels for healthy individuals (<4 ng/mL) and an increase is PSA levels is an indicative marker for PCa, however false negatives are often observed [52]. More so, PSA was shown to be unreliable under metastatic setting specifically for metastatic castration-resistant prostate cancer (mCR-PCa), and its relationship with CTC numbers in PCa patients [53] is still a “grey area” [53,54].

Various CTCs biomarkers have been studied for their prognostic, survival, and metastatic detection value in PCa. The activity of androgen receptors (AR) has been investigated in CTCs detected from PCa patients. PSA and Prostate Specific Membrane Antigen (PSMA) levels were analysed to estimate the relative activity of AR signalling [54]. PSA+/PSMA- was defined as androgen induced (AR-on), PSA-/PSMA+ was defined as androgen suppressed (AR-off) while cells displaying both PSA+/PSMA+ were defined as AR-mixed transitioning between both states. AR state has been analysed in CTCs from PCa patients using polymerase chain reaction (PCR), fluorescent *in situ* hybridization (FISH), and other genomic technologies. Amplification of AR gene was observed in CTCs from 38% of mCR-PCa patients. PCa-CTCs have been showcased to be associated with different biomarkers such as AR-V7 [55], Ki-67 [54], Basic Fibroblast Growth Factor (FGF2) in combination with PSA or in combination with CK5, CK7 and CK8 [22]. In Table 2.2.3., a summarized picture of specific PCa biomarkers and their clinical significance in different PCa sub-types is shown.

Table 2.1.3.: PCa biomarkers specific for CTCs regardless of their sub-populations. The markers mentioned here have been researched specifically in the context of CTC and mCR-PCa. *Integrated Intensity units = IU = 100 ug/Lane for Western blotting ** BPH=Benign Prostatic Hyperplasia *** Serum-FGF2 **** Plasma-FGF2

Biomarker	**Biomarker type**	**Concentration levels**	**Cancer type**	**Ref.**	
Prostate Cancer (PCa)					
Tumour marker antigen					
Ki-67	Antigen identified by monoclonal antibody Ki-67	Internal	> 5% staining prostate tissue staining	PCa, mCR-PCa	[22,54,56]
PSA	Prostate Specific Antigen	Secreted	< 4.0 ng/mL (Average for all ages)	PCa, mCR-PCa	[52,54,57]
PSMA	Prostate Specific Membrane Antigen	Secreted	0 - 9.56 - 16.8 IU* (For male < 50 years - > 50 years)	PCa, mCR-PCa	[54,58]
CTC associated					
CK5	Cytokeratin 5	Internal	93.3% in BPH** 20% in PCa	PCa, mCR-PCa	[22,59]
CK7	Cytokeratin 7	Internal	80% in BPH 13.3% in PCa	PCa, mCR-PCa	
CK8	Cytokeratin 8	Internal	100% in BPH 93.3% in PCa	PCa, mCR-PCa	
FGF2	Basic Fibroblast Growth Factor	Secreted	S-FGF2***: < 4.0 ng/L P-FGF2****: < 6.4 ng/L	PCa, mCR-PCa	[52,60]
AR-V7	Androgen receptor Splice Variant 7	mRNA	Average 18.3% (range 17.8% –28.8%	PCa, mCR-PCa	[55,61]

For PCa, conventional methods such as tissue biopsy is highly invasive and less invasive methods such as biomarker profiling are not conclusive enough in many cases. As discussed above, PSA/PSMA levels are monitored for treatment efficacy, however, their levels may not directly indicate disease progression as PSA levels can rise due to different non-cancer reasons such as prostate inflammation. Similarly, decrease in PSA levels may not necessarily indicate tumour eradication [49,50].

Varying levels of CTCs can also give an insight on disease status and cancer progression where, slower disease progression has been observed in patients with low levels of CTCs [44]. Because of the molecular variation in different metastatic states, CTCs can provide a broader picture of the disease state, disease progression and metastatic potential. The cut-off number of 5 CTC in 7.5 mL of blood for PCa has been linked with poor treatment outcome for the disease specifically metastasis [49,50]. Thus, CTCs cannot only provide beneficial prognostic information but can also provide information for patients who do not exhibit any CTC sub-populations.

2.3. Perspectives on biomarkers selection:

Based on this literature review, there are different secreted CTC-biomarkers that can be selected not only for lung or prostate cancer but for several different kinds of tumours. Certain cytokines, secreted proteins involved in cell signalling are significantly upregulated in various tumours playing a vital role in evading the immune response. Such cytokines are secreted when the tumour growth is either in epithelial or mesenchymal state. Interleukins, a specific class of cytokine are secreted by immune cells involved in cell regulatory activity and function [62].

Various classes of interleukins have been discovered focusing on different functionalities and in humans up to 36 interleukin classes have been identified. Among these classes, certain interleukins such as interleukin-6 (IL-6) and interleukin-8 (IL-8) have been shown to play a vital role in cancer cell progression and induce metastasis [63,64] specifically for both lung and prostate cancer along with breast and ovarian tumours. In addition, such interleukin classes have been identified to upregulate metastasis via CTCs propagation [65,66]. As discussed above, in addition to IL-6 and IL-8, TGF-β and fibronectin have been highlighted as common CTC secreted biomarkers playing vital roles in EMT and MET. So, my PhD project focuses on specifically analysing IL-6 and IL-8 along with TGF-β and fibronectin, highlighting their secretions in real-time and multiplexed format.

CTC biomarker analysis is realized through IHC/Immunofluorescence, ELISA, and gene sequencing. However, to get a comprehensive picture of CTC landscape, one must consider that all such conventional techniques must be performed sequentially making CTCs characterization time-consuming, costly, and requiring added technical support. In addition, little is known on a cellular and genetic level about the processes involved in CTC survival and dissemination and how they are linked with metastatic progression. Different techniques ranging from DNA (DNA-seq) and RNA sequencing (RNA-seq) to chromatin immunoprecipitation sequencing (ChIP-seq) and RNA in situ hybridization (RNA-ISH) have been focused for molecular CTC analysis [67]. DNA-seq is used to analyse mutations or copy number variations within the genome of the cancer cells [67] whereas RNA-seq allows monitoring of RNA expression and transcriptome variations associated with tumour classification and progression [68]. Protein interactions with DNA are observed through ChIP-seq while profiling of the whole transcriptome is done through RNA-ISH.

And although, such standard protocols are sensitive and selective, they have their shortcomings ranging from extremely time-consuming to slow response time and often requiring expensive equipment and experienced operators. In addition, specifically for early cancer stages (I and II), some of these conventional techniques are not as sensitive for early detection due to the presence of low biomarker concentration. In contrast, biosensing technology in recent years have been shown to be implemented for quantitative and qualitative analysis of CTCs further providing dynamic real-time and multiplex monitoring. Various biosensing modalities and different transducing elements specific for CTC and biomarker analysis will be presented in the following sub-section.

2.4. Biosensors for CTC analysis:

A biosensor can be defined as an analytical device used for the detection of a biological entity or event [69], comprised further of three basic components: a bio-recognition element, a transducing element and a readout modality. Analyte(s) of interest can be specifically recognized and detected from a biological sample such as plasma, blood, serum, urine, sweat or saliva by bio-recognition elements that can range from nucleic acids, proteins i.e., cell surface receptors, antibodies and antigens to cells and tissues [70]. Bio-recognition elements are further coupled with a transducing element that allow for the conversion of the biological event to a readable and quantifiable signal. As of now, countless biosensors have been developed and patented for analysis of different biological interactions to help, understand and specifically monitor various life threatening diseases, including cancer [71,72].

For all such limitations, the main challenge is their cost-effectiveness and suitability for real-life applications. These challenges need to be overcome for efficient commercialization and overall deployment in clinical settings. From Global Biosensors Market Report 2021-2026, in 2021, the biosensors market is valued at 25.5 billion USD and expected to reach 36.7 billion USD by 2026 growing at a compound annual growth rate (CAGR) of 7.5% during this time. The growth of point-of-care (POC) global market has been adversely affected by cost that could be attributed to insufficient budgets and reimbursement losses. Worldwide, expenditure on medical devices including POC and biosensors is at risk because of the decrease on healthcare products list eligible for reimbursements. This in turn creates pressure on the industry and as a result, manufacturers find it difficult to be more cost-effective and preclude margin erosion having to deal with rising competition. Hence, cost management seems to pose a key challenge for the growth of this market in the years to come. For cancer diagnostics and disease monitoring, biosensors can play a vital role. With efficient testing and research, appropriate progress and commercialization can be achieved by focusing specifically on cost-effectiveness. In addition, multidisciplinary approach must be considered where biosensors coupled with different technologies can be fully employed for this field, in parallel with already established protocols used in clinical setting.

Biosensors can further be classified as label-based or label-free based on their detection modes. Label-based biosensors utilize fluorescent compounds such as luminescent probes for the detection of biological recognition event [73]. In addition, such biosensing modalities are well established, allowing ultra-high throughput analysis of molecular interactions and have been the cornerstone of different biological research. However, drawbacks such as lack of specificity and interference along with cross-reactivity caused by different (not of interest) biomolecules have curtailed their bio-applications in the long-run. For different biomolecules, labelling efficiency varies that can in turn result in noise and background signals. Label-free biosensors on the other hand are an effective solution to overcome such setbacks and have showcased improved efficiency, sensitivity and specificity while meeting the challenges of multiplexing and high throughput [73]. Nanotechnology has further be touted as an avenue for signal enhancement, where different nanoparticles or nanomaterials provide excellent prospects to further improve biosensing capabilities [74].

For the state of the art, most of the research highlighted here would focus on label-free biosensors and specifically for cancer applications. Depending on the transducing elements, such biosensors can be classified as piezoelectric/mass-based, electrochemical, and optical. The following subsections will focus on such modalities along with their application in cancer cell/CTC biomarker analysis and further in-depth comparative analysis will be presented.

2.4.1. Piezoelectric Biosensors:

Piezoelectricity is defined as the generation of electrical signals by the application of mechanical stress on piezoelectric materials such as quartz crystals and synthetic polycrystalline ferroelectric ceramics, of which lead titanate zirconate (PZT) is most commonly used [75]. Piezoelectric biosensors employ such materials as transducers variations in mass attached on the surface is measured. By applying an electric field to such piezoelectric materials, a mechanical movement is generated and if such mechanical movement matches the acoustic frequency of the crystal (like tuning fork), then the material will oscillate and ‘ring’. This frequency depends on the mass adhered to the surface. Thus, bio-recognition elements are immobilized on the material surface for target detection. The sensitivity of piezoelectric transducers depends on their physical properties such as area, thickness, and oscillating frequency. The choice of an optimal piezoelectric material relies on technical possibilities for cost, miniaturization, surface characterization and fabrication capabilities along with flexibility in higher resonant frequencies.

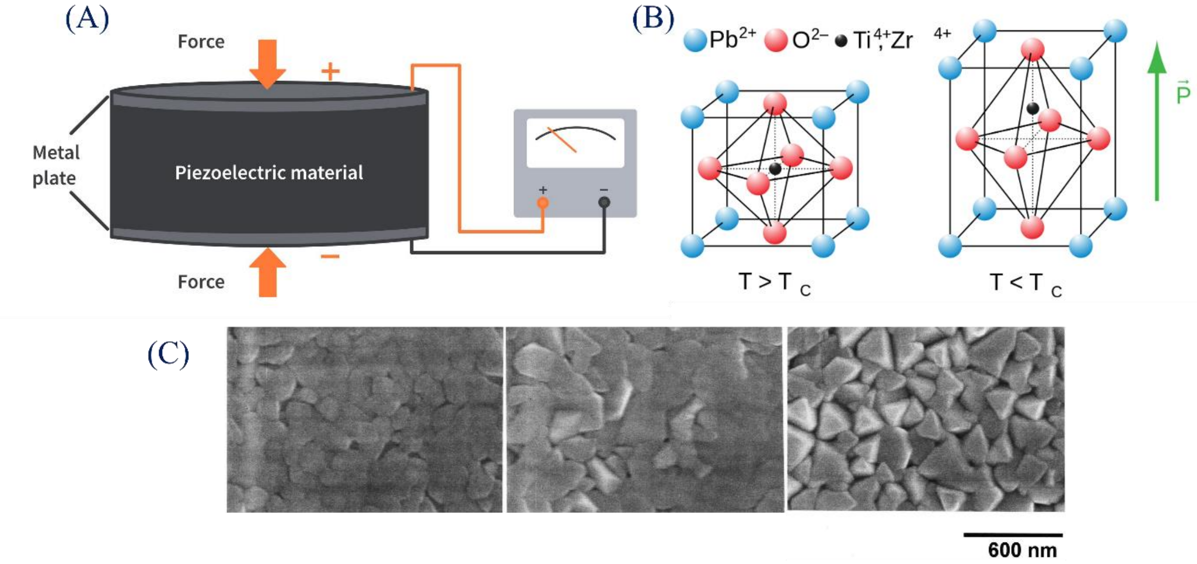

Figure 2.2.1.: **(A)** Schematic for principle of a piezoelectric biosensor, where variation of physical properties on the piezoelectric material i.e., PbZrTi can generates a readable and quantifiable electrical signal. **(B)** Crystal lattice of PbZrTi, conventional piezoelectric material. **(C)** SEM images of PbZrTi [76].

The most commonly used piezoelectric materials for biosensing are quartz crystals due to their high sensitivities [77,78]. They are normally termed as quartz crystal microbalances (QCM) [75,78] and various QCM biosensors have been developed for the detection and analysis of cancer cells, cancer-related proteins, and nucleic acids. Shan and group fabricated an aptamer based QCM biosensor for selective detection of leukemia cells like CCRF-CEM cells, a T-lymphoblastoid cell line. For signal enhancement, the group prepared amino-phenyl boronic acid modified gold nanoparticles (APBA-AuNPs) that were used for specific cell labelling while silver enhancement was utilized for signal amplification as highlighted in Fig. 2.2.2. (A). AuNPs were used as nucleation sites and in the presence of a reducing agent, such as hydroquinone, automatic catalysis was observed where, silver ions were reduced to silver metal. This deposition of silver metal was measured via the QCM as it was mass change sensitive on the electrode surface as showcased in Fig. 2.2.2. (B). This biosensing architecture was used to detect leukemia cells showing linear relationship between the frequency change and the cell concentration measured in the range of $2x10^3$ - $1x10^5$ cells/mL with a limit of detection (LOD) of 1160 cells/mL [79] as presented in Fig. 2.2.2. (C). The biosensor specificity was demonstrated by testing a different cell line, as well as with QCM sensors modified with a random DNA sequence and further validated via fluorescence microscopy experiments.

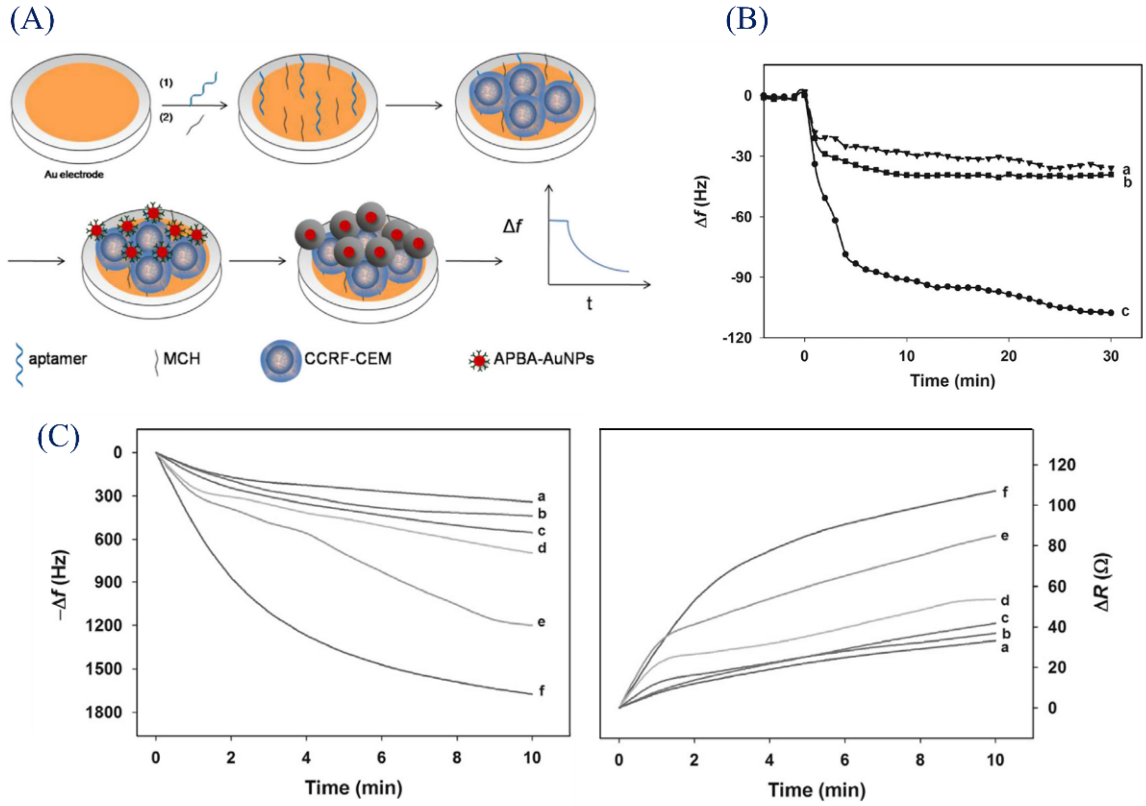

Figure 2.2.2.: **(A)** Schematic setup of the fabrication of the QCM biosensor for analysis of the leukemia cells and **(B)** Resonant frequency responses of different electrodes upon the additions of 10,000 cells: (a) Romas cells added to aptamer-modified surface; (b) CCRF-CEM cells added to random DNA sequence-modified surface; (c) CCRF-CEM cells added to aptamer-modified surface. **(C)** Resonant frequency and resonant resistance responses during the silver enhancement processes of the aptamer-based QCM sensor incubated with different concentrations of cells followed by APBA-AuNPs labeling. Cell concentrations: (a)–(f) $2x10^3$, $6x10^3$, $1x10^4$, $2x10^4$, $6x10^4$, and $1x10^5$ cells/mL [80].

Another way to enhance the signal detection of cancer cells is to increase the sensor surface area and to further increment the number of bio-receptors. This would subsequently promote more interactions of the analyte with the biosensor and therefore result in overall increment of mass change. Bakhshpour et al. functionalized QCM-chip with Poly 2-hydroxyethyl methacrylate nanoparticles (PHEMA-NPs) to increase the sensor surface area as presented in Fig. 2.2.3. (A) for the detection of highly metastatic breast cancer cell line MDA MB 231 cells. In this cell line, the Notch-4 receptor pathway is overexpressed, which is involved in cancer progression, apoptosis inhibition and cancer cell survival promotion. PHEMA-NPs thus allow immobilization of greater number of Notch-4 receptor antibodies resulting in increasing number of interactions being detected with the Notch-4 receptors on MDA MB 231 cells. For such biosensing platform, the LOD was improved to 12 cells/mL for detection numbers between 50-300 cells/mL as shown in Fig. 2.2.3. (B) [81].

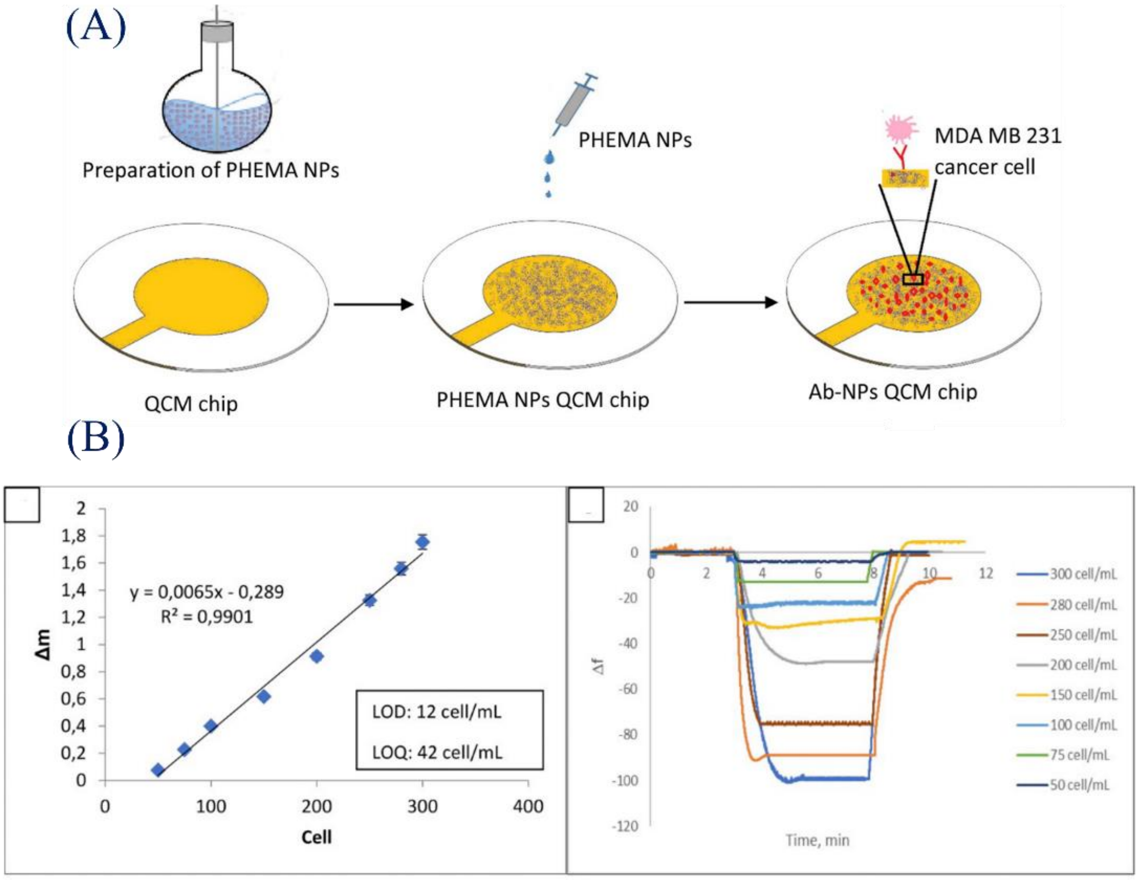

Figure 2.2.3.: **(A)** Schematic setup of the fabrication of the QCM biosensor for analysis of the MDA MB 231 cells and **(B)** Kinetics of QCM biosensor [82].

Different materials such as PbZrTi ceramic resonators have also been explored to increase the sensitivity of piezoelectric biosensors while reducing operational cost and improving portability. Su et al. used such PbZrTi resonators for label free detection of PSA, biomarker associated with PCa [83]. A dual sensing system as presented in Fig. 2.2.4. (A) was used, where two 40 MHz ceramic resonators one as a sensing platform and one as a control unit were connected to an impedance analyser in parallel to further reduce environmental influences like temperature fluctuation caused by the increased sensitivity.

The ceramic wafers had gold plated electrodes on both sides, which were chemically functionalized with either Protein A or Nafion linker solution for coupling with anti-PSA antibody. Spiked human PSA-serums samples at different concentrations from 2.5 to 10 to 50 ng/mL were used for detection. Recovery rates for PSA at 2.5, 10 and 50 ng/mL were around 95.2%, 97.5% and 108.7% respectively. A detection ranges from 0.025 to 2.5x10^{2} ng/mL and LOD of 0.25 ng/mL for PSA was achieved as shown in Fig. 2.2.4. (B) [83]. This PbZrTi sensor is label-free, low cost and capable of performing direct cancer biomarker detection. More so, high sensitivity and fast detection (within 30 min) for PSA from a sample compatible with clinical measurements (1 mL) was showcased. Furthermore, it allows combination of different chemical functionalization which could miniaturize overall system making such platforms suitable for sensor array fabrication for multiplex detection.

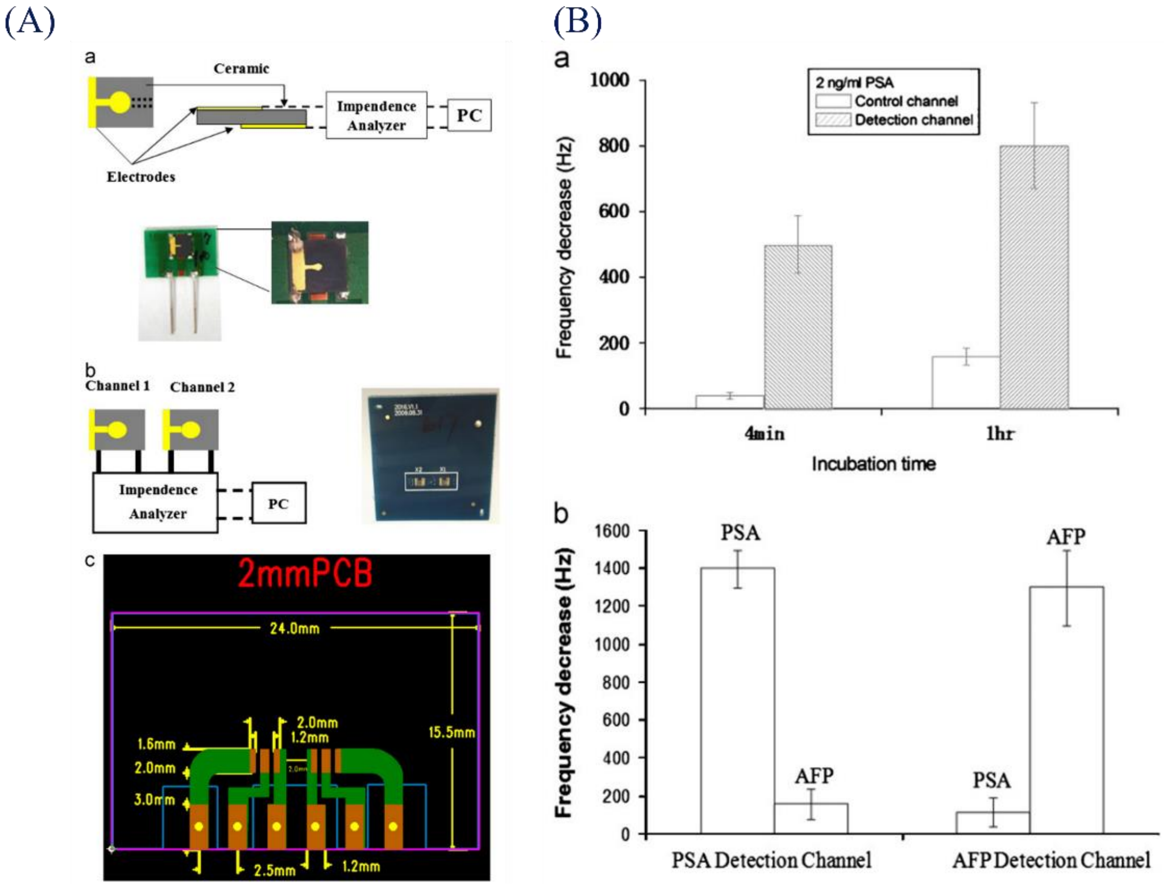

Figure 2.2.4.: (**A**): (a) Schematic layout of ceramic resonator and the measurement system (up) and photo of a ceramic resonator (below); (b) Schematic layout of dual ceramic resonators and the measurement system (left) and photo of a ceramic resonator (right); (c) Dimensions of the electrode leads and connections on the printed circuit board for dual ceramic resonators. (**B**): (a) The frequency changes of the binding of PSA (2 ng/ml) to PSA antibody- immobilized resonator (detection channel) or control channel (without PSA antibody) at 4 min and 1 hr were compared. (b) Specific antigen binding evaluation on PSA and AFP detection channels, where the PSA and AFP solutions are 10 ng/ml and 1 mg/ml respectively [83].

To summarize, piezoelectric biosensing modalities have been demonstrated for detection of cancer cells and their related biomarkers. Most examples highlighted here focus on the use of cancer cell lines rather than clinical samples, moreover, use of various probes for detection and validation makes multiplex and real-time analysis more challenging. Furthermore, additional amplification steps may/can be required for further improving overall sensitivity of the platform making the whole protocol intricate. For fabrication of optimal piezoelectric sensors, thinner and smaller piezoelectric materials need to be developed with high characteristic resonant frequencies. This would further require complex processes and high-end equipment for fabrication that will greatly affect the overall cost. Hence, further research is needed to make such biosensing modalities suitable for application in real clinical conditions. A comprehensive comparative analysis has been performed for piezoelectric transducers for cancer cell and cancer biomarker detection which has been compiled in Table 2.2.1., focusing on sensing platform design and sensor characteristics such as LOD and range.

Table 2.2.1.: Comparative analysis of different piezoelectric systems for detection of cancer cells and analysing cancer biomarkers

Biosensor	Sensing platform	Analyte/Bio-recognition element	Sensor characteristics	Ref.
Piezoelectric biosensors for detecting cancer cells				
Aptamer-QCM	APBA-AuNPs + Ag enhancement with Hydroquinone as reducing agent	CCRF-CEM T-lymphoblastoid cell line	Range: 2x10^3 – 1x10^5 cells/mL LOD: 1160 cells/mL	79
QCM	PHEMA-NPs + Anti-Notch-4 antibodies	MDA MB 231 cells	Range: 50 – 300 cells/mL LOD: 12 cells/mL	81
Piezoelectric biosensors for analysing cancer biomarkers				
PbZrTi	Protein A/Nafion + Anti-PSA antibodies	Human serum samples spiked with known PSA concentrations (2.5, 10 and 50 ng/mL)	Range: 0.025 – 2.5x10^2 ng/mL LOD: 0.25 ng/mL	83
QCM	Duplex Specific Nuclease (DSN) + Magnetic beads	LMCF-7 for microRNA-203 spiked in cell lysates	LOD: 1 pM	84

2.4.2. Electrochemical Biosensors:

Electrochemical biosensors rely on analysing variations in an electric field generated after biological interactions. Normally, the bio-recognition elements are coupled on the electrode surface much like piezoelectric modalities, where specific targets when presented onto such modified electrodes, binding event follows generating electric flux. Electrochemical biosensors consist of an electrical source and a domain, while the variations in the sensor response are measured as exhibited in Fig. 2.2.5. Such variations can be in the form of electrical potential, current, impedance and/or conductance giving rise to potentiometric, amperometric, impedimetric and/or conductimetric biosensing modalities [77,85].

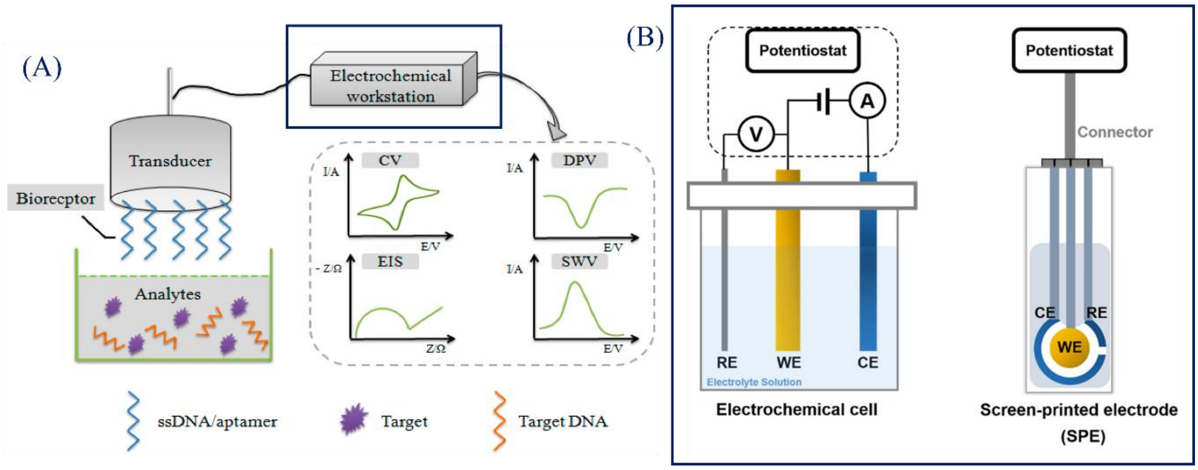

Figure 2.2.5.: **(A)** Schematic for principle of electrochemical biosensor, where variation of electrical properties is analysed as a quantifiable signal for signal detection for which different readouts i.e., cyclic voltammetry (CV), differential pulse voltammetry (DPV), electrochemical impedance spectrometry (EIS), and Square Wave Voltammetry (SWV) can be employed among others [86]. **(B)** An example of electrochemical workstation showcasing electrochemical cells and/or screen-printed electrodes (SPE) employed for signal interaction [87].

For analysis of cancer biomarkers, electrochemical immuno-sensors are of high interest taking advantage of their specificity and sensitivity regarding antigen-antibody interaction. Jayanthi et al., in their review, compiled different examples of electrochemical biosensors using electrochemical impedance spectroscopy (EIS) and differential pulse voltammetry (DPV) methodologies coupled with nanotechnology for the detection of cancer biomarkers [72]. Here, for this subsection, I focused on electrochemical biosensors for CTC detection and their biomarker analysis.

For specific CTCs detection through an electrochemical setup, Chen and group fabricated a two-dimensional MoS2/Folic acid (FA) modified gold electrode (2D-MoS2/FA/AuE) as seen in Fig. 2.2.6. (A). Initially, the modified electrode was evaluated for the detection of HeLa cells spiked with healthy cells and then linear range of 50 - 10^5 cell/mL and LOD of 52.24 cells/mL were achieved [88]. The group further performed impedance measurements on clinical samples (4 liver cancers, 4 cervical cancers and 8 healthy controls) for biosensing feasibility. Conventional flow cytometry and this novel EIS strategy was employed for CTCs analysis where all liver and cervical cancer patients, between 5-100 CTCs/mL were detected (47.2 ± 1.8 liver CTCs/mL; 37.3 ± 2.4 cervical CTCs/mL) but almost no CTCs (mean=1 ± 0.2 CTCs/mL) were observed in hyperplastic prostate donors and healthy controls as highlighted in Fig. 2.2.6. (B) [88]. This biosensing approach was able to differentiate tumour samples from normal controls, but for now, the group focused on detecting CTCs and hypothesized that the number of CTCs was a marker of metastatic potential. However, they have not focused on the specific analysis of biomarkers associated with CTC progression and dissemination.

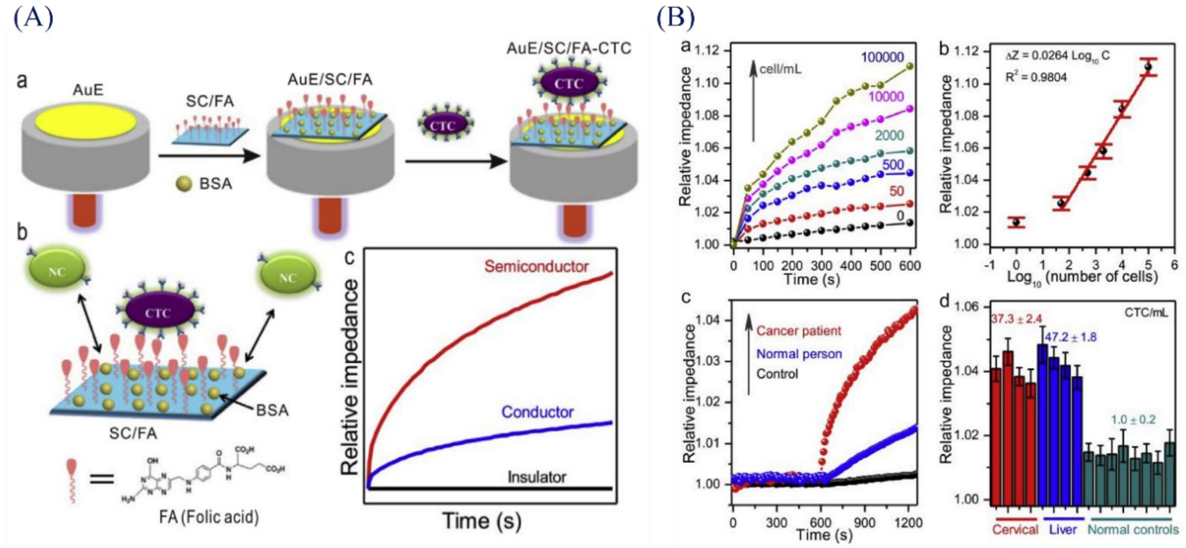

Figure 2.2.6.: **(A)** Schematic diagram of the electrochemical impedance cyto-sensor with SC/FA probe for detection of CTC. (a) The fabrication of 2D-MoS2/FA/AuE for CTC capture. (b) Schematic model of HeLa cell binding with folic acid (FA) and repelling normal cell (NC) on a negatively charged 2D-MoS2/FA/AuE electrode surface and (c) the corresponding impedance curves. SC: Semiconductor; AuE: gold electrode; BSA: al- bumin from bovine serum; CTC: circulating tumor cells; FA: folic acid; NC: normal cells with low folic receptor expression. **(B)** Application of CTC detection. (a) Relative impedance with time for 2D-MoS2/FA/AuE electrodes scanned while immersed in healthy blood serum samples containing HeLa cells with different con- centrations. (b) Calibration plot of relative impedance at 10 min for determining HeLa cells at 2D-MoS2/FA/AuE electrodes while changing the con- centration of HeLa cell. (c) Relative impedance with time for 2D-MoS2/FA/AuE electrodes scanned while immersed in PBS for 10 min followed by adding whole blood of cervical cancer patient, healthy people, and PBS as control. (d) Relative impedance measured from 16 clinical samples. Cervical and liver represent clinical samples of cervical and liver caners, respectively. Normal controls indicate the samples of healthy people [88].

There are some examples of electrochemical biosensors used for the analysis of CTC-associated biomarkers. One way is to use gold nano-electrode ensemble (3D-GNEE) as shown in Fig. 2.2.7. (A), imprinted with thin films of template epithelial ovarian cancer antigen-125 (CA125) protein, associated with CTC-LCa. Cyclic voltammetry (CV), differential pulse voltammetry (DPV) and electrochemical impedance spectroscopy (EIS) measurements were performed to analyse the binding event and CA125 concentrations. Spiked human blood serum and real patient samples were used for validation of electrochemical biosensor and results highlighted sensitivity values of 0.5-400 U/mL and LOD of around 0.5 U/mL [89]. Compared with conventional ELISA, this biosensor was able to achieve similar sensitivity ranges for CA125 (between 0.5-400 U/mL) as highlighted in Fig. 2.2.7. (B), which could further provide information on real-time kinetics and multiple analysis.

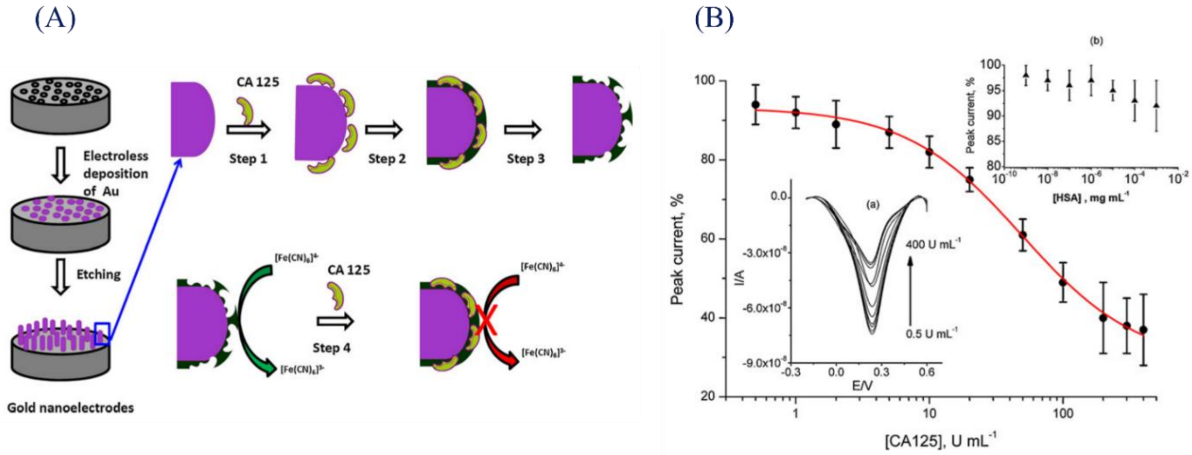

Figure 2.2.7.: **(A)** Schematic representation of molecular imprinted protein nanosensor fabrication and template protein detection. Step1 – adsorption of CA 125 on to the nanoelectrodes surface; Step 2 – electrochemical polymerization of phenol; Step 3 – template protein removal; Step 4 – CA 125 binding and signal generation. **(B)** CA 125 concentration-dependent peak current response represented as the percentage of peak current (%) versus concentration (U mL – 1) on semi log plot. Inset (a), DPV current responses to CA 125. Inset (b), DPV current responses to different HSA concentrations [89].

Another detection method comprised on electric flux variation via enzymatic ion generation due to selective biomarker interaction. For example, the quantification of Human Epidermal Growth Factor Receptor 2 (HER2) extracellular domain (ECD) in serum was performed using monoclonal anti-HER2 antibodies. These antibodies were immobilized on modified gold nanoparticle screen printed onto the carbon electrode as a transducing element highlighted in Fig. 2.2.8. (A). HER2 ECD detection in samples were performed through the interaction with biotinylated monoclonal anti-human HER2 antibodies and streptavidin-alkaline phosphatase conjugate. Silver ions were used with enzymatic substrate (3-indoxyl phosphate, 3-IP) for the specific detection of antibody-antigen interaction. These ions underwent reduction to metallic silver, which can be detected by anodic stripping using linear sweep voltammetry. In this study, human serum samples with a known concentration range of 15 to 150 ng/mL HER2 ECD were analysed and the lowest LOD of 4.4 ng/mL was achieved as showcased in Fig. 2.2.8. (B) [90]. However, additional studies need to be performed on blood samples of healthy controls and cancer patients to evaluate and validate sensor's performance in clinical environment.

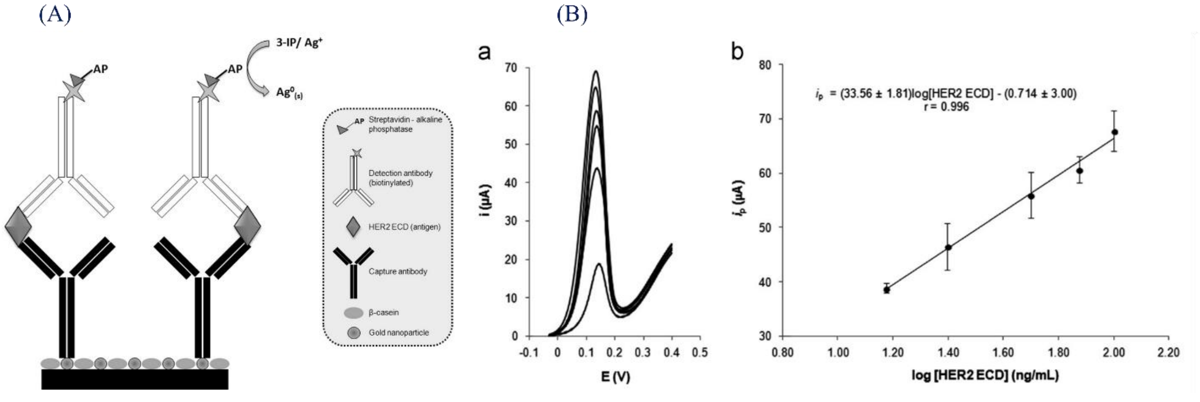

Figure 2.2.8.: **(A)** Schematic representation of the immunoassay **(B)** (a) Linear sweep voltammograms (-0.03 V to +0.4 V, scan rate: 50 mV/s) and (b) Calibration curve (i_p vs. log [HER2 ECD]) for the analysis of HER2 ECD in human serum using the developed immunosensor. ([HER2 ECD] (ng/mL): 0, 15, 25, 50, 75 and 100, Ab-capture: 50 μg/mL, casein: 2%, Ab-detection: 1 μg/mL, S-AP: $2x10^{-10}$ M, 3-IP: 1.0 mM and Ag^{+}: 0.40 mM) [90].

Different electrochemical biosensors have been employed for the cancer cell detection and analysis of their associated biomarkers. Such biosensors can achieve lower LOD, and sensitivity values compared with ELISA. However, they require electroactive intermediaries such as buffers and detection molecules, making their characterization complex. In addition, cells and proteins behaviours might be affected by changes in an electric field as cells and tissues functions on specific electric potential for optimal upkeep. A comprehensive comparative analysis has been performed for electrochemical transducers for cancer cell and cancer biomarker detection that have been compiled in Table 2.2.2., highlighting sensing platform, design, and sensor characteristics like LOD and range.

Table 2.2.2.: Comparative analysis of different electrochemical systems for detection of cancer cells and analysing cancer biomarkers

Biosensor	Sensing platform	Analyte/Bio-recognition element	Sensor characteristics	Ref.
Electrochemical biosensors for detecting cancer cells				
Gold nanostructured electrode (AuE)	2D MoS2/FA functionalized AuE	HeLa cells	Range: 50 - 105 cell/mL LOD: 52.24 cells/mL	88
		Cervical cancer CTCs	Range: 5 - 100 CTCs/mL LOD: 37.3 ± 2.4 CTCs/mL	
		Liver cancer CTCs	Range: 5 - 100 CTCs/mL LOD: 47.2 ± 1.8 CTCs/mL	
Electrochemical biosensors for analysing cancer biomarkers				
Gold nanoelectrode ensemble	CA125 imprinted polymer	Spiked CA125 and unknown human serum blood samples	Range: 0.5 - 400 U/mL LOD: 0.5 U/mL	89
Gold nanoparticle-modified	Monoclonal Anti-HER2 antibodies	Spiked HER2 human serum samples	Range: 15 - 150 ng/mL LOD: 4.4 ng/mL	90

screen-printed carbon electrode	Streptavidin Alkaline phosphatase for labelling			

2.4.3. Label-free Optical Biosensors:

2.4.3.1. Principle of optical biosensing:

Optical biosensors focus on the analysis of variations in optical/light properties such as refractive index, wavelength, resonance, or intensity, to detect biomolecules and biological interactions [91]. Like previous approaches, optical biosensors can either be label-based or label-free depending on the type of detection modalities. Label-based optical biosensors detect variations in colour and/or the activity of optical labels like different fluorescent probes, dyes or intercalators at a characteristic wavelength [71,72,74]. Various optical modalities ranging from fluorescence spectroscopy, fluorescence resonance energy transfer (FRET), chemo-luminescence (CL) and chemo-luminescence resonance energy transfer (CRET) have been used for the development of label-based optical biosensors. Specifications such as label availability coupled with different functional groups covering large spectral range, reduction in operational complexity and ability to achieve single molecule detection has made fluorescence the standard in optical biosensing [71,72,74]. However, such biosensors are prone to bleaching, non-specific labelling and false results which in turn, reduces their overall efficiency and further application in clinical setting down the line [69,91].

To overcome such disadvantages, optical technologies are evolving towards label-free approaches. Different optical properties such as light scattering or generation of evanescent wave have been employed for label-free biosensor development for the detection and analysis of specific biological interactions. For the fabrication of such label-free optical biosensors, interferometers like Mach-Zehnder interferometers (MZI). Young interferometer, bimodal waveguide interferometers (BiMW) resonators i.e., micro-ring resonators (MRR), surface plasmon resonance (SPR), localized SPR, spectroscopy of guided modes of optical waveguides such as resonant mirror and grating coupler and surface enhanced Ramen spectroscopy (SERS) have all been used and researched upon extensively [71,72,74].

Label-free optical modalities allow direct measurement and are often comparatively simpler, faster and can analyse real-time activity. More so, such biosensors provide further information on the kinetic and thermodynamic parameters of the bio-recognition event [92]. The capability of detecting such biological interactions in real-time without employing any labels or fluorescent probes makes this optical approach more favourable for cancer biomarkers detection and analysis [74]. Photonic transducers for label-free approach can be further classified as plasmonic based and silicon photonics based [69]. Plasmonic biosensors are by far the most widely employed further pioneered by the principle of surface plasmon resonance (SPR). SPR based biosensors can detect the interaction of cells and biomolecules due to the light-induced excitation of surface plasmon waves on the interface of a metal usually gold and the dielectric medium as shown in Fig. 2.2.9. (B). Such excitation can be achieved by different approaches using prism, waveguides, diffraction gratings or optical fibres [70]. These surface plasmon waves produce an evanescent field over the sensor surface, which is sensitive to refractive index changes of the external medium conferring such biosensing modality with label-free capabilities LOD in picomolar to nanomolar (pM - nM) range as highlighted in Fig. 2.2.9. (C).

Success of such SPR biosensors relies on the advent of nanotechnology that has inspired researchers to follow suit, generating more compact, multiplexed, and easier to integrate biosensors using gold nanostructures like arrays of nano disks, nanoholes, nano slits, etc as shown in Fig. 2.2.9. (D). These gold nanostructures facilitate the generation of multiplexed surfaces using simpler light coupling approaches. Such nanostructures can further be harnessed to fabricate SERS based biosensors, that instead of relying on the evanescent field effect, employ these structuration for enhancement of Raman scattering phenomena [93].

On the other hand, there has been a parallel development of label-free optical biosensors based on optical waveguides using silicon photonics technology. Among silicon photonic-based biosensors interferometers like MZI, BiMW and MRR [94] have been employed as presented in Fig. 2.2.9. (E), (F), and (G). These silicon structures can also generate an evanescent field by light propagation in optical waveguides that transduce biological interactions into the interference signals or vary resonant peaks respectively.

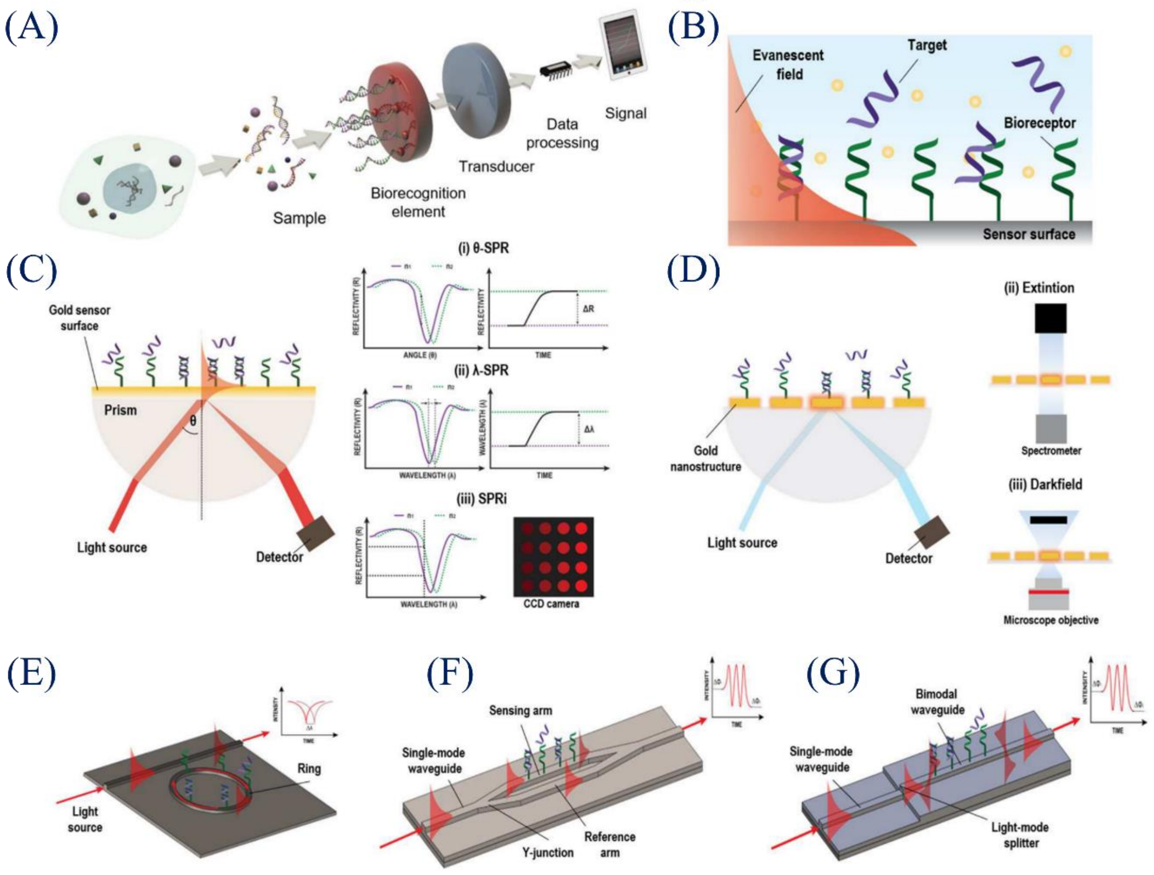

Figure 2.2.9.: **(A)** Scheme of a biosensor **(B)** Evanescent field principle. **(C)** SPR biosensor based on Krestchman configuration and different detection modes: (i) fixed angle, (ii) fixed wavelength, and (iii) fixed angle and wavelength (SPRi). **(D)** LSPR light coupling methods: (i) prism, (ii) extinction, and (iii) dark field. **(E)** Micro-ring resonator, **(F)** MZI biosensor, and **(G)** BiMW biosensor designs and working principles [69].

2.4.3.2. Label-free optical biosensors for CTCs and CTC-biomarkers detection:

The study of optics has expanded the capabilities of such biosensors fairly enhancing their robustness and sensitivities through innovative signal processing approaches [95]. Such approaches can be able to fabricate highly sensitive biosensors capable of performing multiplexed analysis on the same chip [96]. To further highlight this, I have compiled some examples of label-free optical biosensors for cancer cell detection and biomarker analysis relevant for CTCs.

For example, Mousavi's group used an SPR-based biosensor for CTC counting. The biosensor consisted of a gold nano-slit substrate that, when illuminated with light allowed extraordinary optical transmission as shown in Fig. 2.2.10. (A). This biosensor was integrated with a microfluidic device using functionalized magnetic nanoparticles (MNPs) coupled with antibodies for specific isolation and capture of CTCs as presented in Fig. 2.2.10. (B). They used whole blood samples spiked with the lung cancer cell line CL1-5 to demonstrate their methodologies by achieving LOD of 13 cells/mL after enriching their samples by pre-concentration and separation of CTCs through magnetic nanoparticles [97]. This study demonstrated the advantages of combining microfluidic format with an optical modality for sensitive detection and specific capturing of CTCs and in addition, further highlighted real-time monitoring the capturing processes.

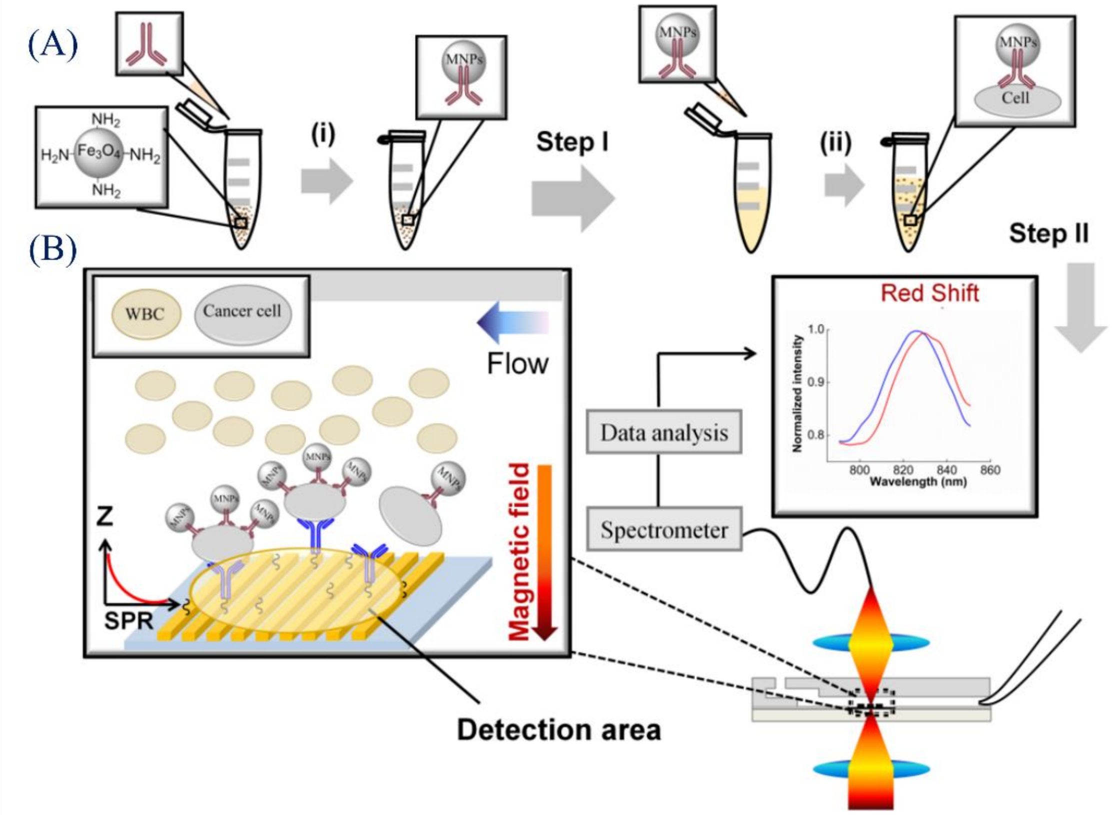

Figure 2.2.10.: **(A)** A schematic of biosensing setup. (a) The first step includes: (i) Functionalizing the MNPs with antibody I; (ii) Mixing the functionalized MNPs (carrying antibody I) with the sample to capture the target cells. **(B)** The second step includes introducing the mixture of blood sample and MNPs to the microfluidic chip and capturing the MNPs-cells to binds to the antibody II on the gold nanoslits. The cell binding on the gold nanoslits was monitored by the wavelength shift of the SPR spectrum generated by the gold nanoslits. The detection area of the nanoslits is defined by the focal spot of the probe light [97].

Such biosensing approaches can further be employed for biomarker analysis directly secreted by cells. Li et al. developed a label-free opto-fluidic nano-plasmonic biosensor which was used for real-time analysis of a single cell. Modified gold surfaces with nanohole arrays (NHA) were used for their device and were further functionalized with PEGylated thiol self-assembled monolayers (SAMs) having –COOH terminal groups. The functional groups were activated to covalently bind a mixture of poly-L-lysine and streptavidin where, poly-L-lysine was used for the specific capture of cells on the sensor surface and streptavidin was used to analyse the cytokines through firm attachment of biotinylated antibodies as shown in Fig. 2.2.11. (A). A multifunctional microfluidic system was incorporated within the biosensor design facilitating reliable monitoring of cytokine secretion from individual cells while preserving sample evaporation by including a regulation channel. This integrated setup was employed to analyse interleukin-2 (IL-2) secretions and different concentrations ranging from 50 pg/mL to 1 ng/mL were observed along with 39 pg/mL LOD as highlighted in Fig. 2.2.11. (B) and (C) [98]. The group showcased a novel optofluidic nano-plasmonic biosensor for single-cell cytokine secretion analysis. Ultrasensitive gold nanohole arrays were integrated with a sophisticated, easy to fabricate microfluidic system for real-time monitoring of protein secretion. This approach further provides detection data over several hours without interruption.

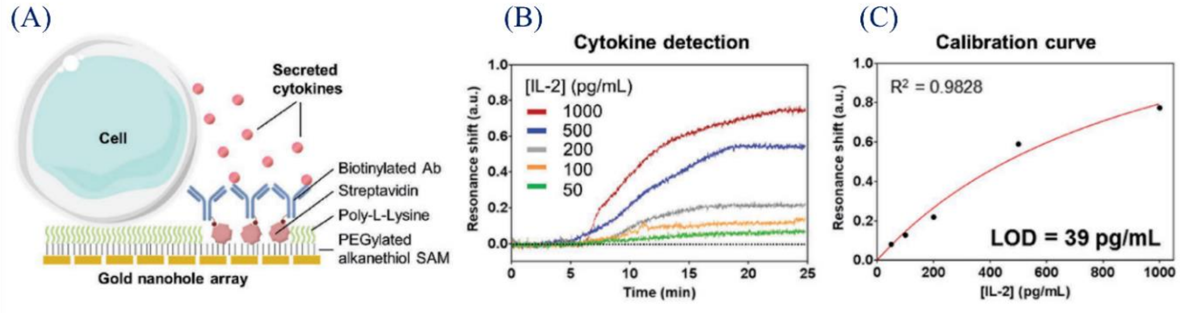

Figure 2.2.11.: Surface chemistry and characterization of the NHA biosensor for IL-2 detection. **(A)** Surface functionalization strategy for cell attachment and in situ detection of secreted cytokines. **(B)** Real-time sensorgrams of dif- ferent concentration of cytokines (IL-2) ranging from 50 pg mL − 1 to 1 ng mL − 1. **(C)** Standard calibration curve for direct and label-free detection of IL-2 molecules [98].

The real-time analysis of cancer biomarkers was also explored through a photonic crystal surface mode (PC-SM) system by recording total internal reflection angles and excitation angles from the PC surface wave as presented in Fig. 2.2.12. (A). This approach was used for simultaneous detection of an ovarian and lung cancer biomarker CA125 and two breast cancer biomarkers HER2 and cancer antigen 15-3 (CA15-3). Rather than using serum samples, spiked samples with known concentrations of biomarkers were tested. LOD of around 620 fg/mL for HER2 as showcased in Fig. 2.2.12. (B) and minimal detectable values for CA125 and CA15-3 of 0.55 U/mL and 1.84 U/mL respectively were achieved [99]. This label-free PC-SM system was able to detect these three CA125, CA15-3 and HER2 biomarkers in a single analytical setup. Compared to conventional HER2 detection methods, high sensitivities with low LOD were obtained yielding promising results, but further analysis needs to be performed on patient samples in terms of clinical applications.

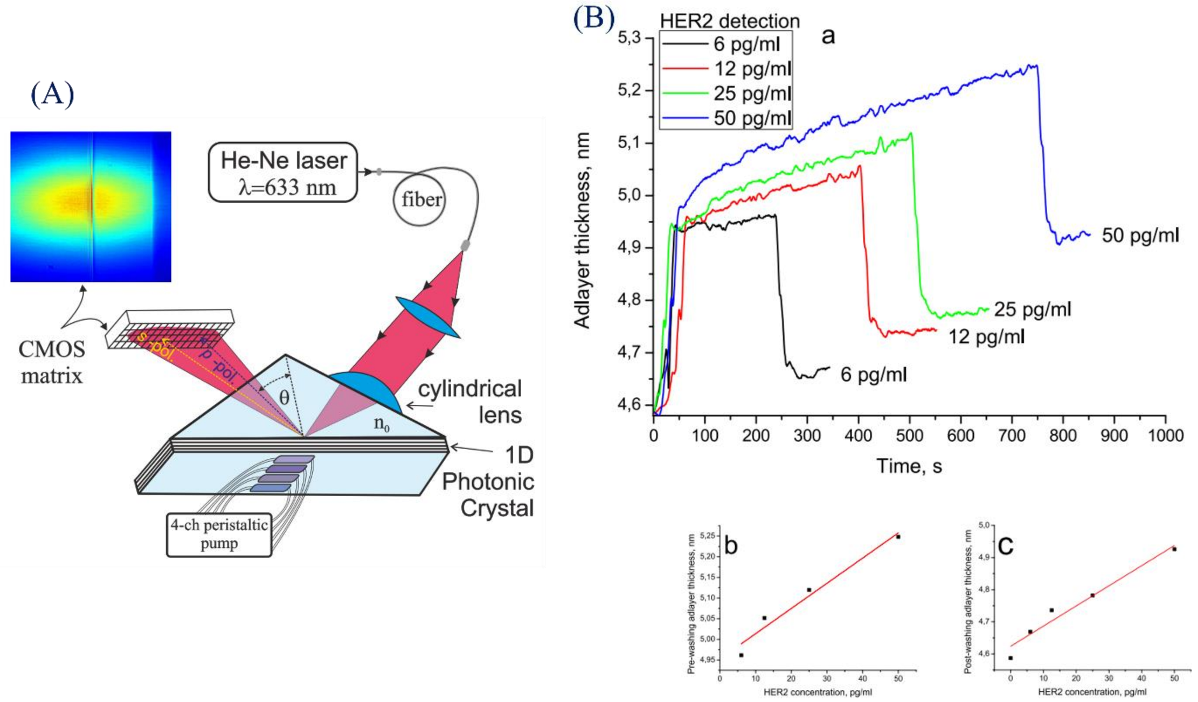

Figure 2.2.12.: **(A)** A sketch of the EVA biosensor based on angle interrogation of a photonic crystal surface mode (PC SM). A circular-polarized laser beam from a stabilized He–Ne laser is sent to the sensor surface through a polarization-maintaining fibre cable. The beam is focused by a cylindrical lens in such a way that the excitation angle of one s-polarized PC surface mode (existing in this 1D PC) and TIR angle (in p-polarization) are contained in the convergence angle of the beam. The reflected angular profile (see the colour inset) is recorded by the CMOS matrix. The one-dimensional spatial selectivity of this setup allows simultaneous recording of biochemical reactions in four fluid channels. **(B)** Quantitative detection of HER2 antigen using photonic crystal surface mode detection. (a) The dependence of the adlayer thickness increase and decrease on the HER2 concentration; after the start of the HER2 flow, the signal was allowed to reach a plateau (pre-washing adlayer thickness); then, the solution was switched to PBS to begin the washing stage; the washing stage was marked with a rapid decrease in the signal intensity until it reached a new plateau (post-washing adlayer thickness). (b) The linear dependence of the pre- washing adlayer thickness on the HER2 concentration. (c) The linear dependence of the post-washing adlayer thickness on the HER2 concentration (the value before HER2 binding taken to be the zero point) [99].

While these results, for such optical biosensing modalities [98,99] were performed using PBS and in some cases diluted cultured medium, moving on for analysis in blood and diluted blood mediums is a challenging step to overcome as there are numerous cells and biomarkers have to be taken into consideration in addition to parameters of interest. For optical biosensing modalities, there are still some challenges that need to be overcome such as complex design and bulky instrumentation affecting the overall cost which further limits their application. More so, long-term stability, and performance in terms of reproducibility and stability needs to be addressed if such biosensors are ultimately to be used in the clinical setting. Following on this, a comprehensive comparative analysis has been performed for label-free optical transducers for cancer cell and biomarker detection compiled in Table 2.2.3., focusing on sensor design and characteristics.

Table 2.2.3.: Comparative analysis of different label-free optical systems for detection of cancer cells and analysing cancer biomarkers

Biosensor	Sensing platform	Analyte/Bio-recognition element	Sensor characteristics	Ref.
Optical biosensors for detecting cancer cells				
Gold nano slit	Magnetic NPs coupled with a microfluidic system	CL1-5 lung cancer cell lines	LOD: 13 cells/mL	97
Optical biosensors for analysing cancer biomarkers				
NHA gold surface	PEGylated alkane thiol SAMs Poly-L-lysine and Streptavidin	Single EL4 cell for IL-2 secretion	Range: 50 pg/mL - 1 ng/mL LOD: 39 pg/mL	98
Photonic crystal surface mode (PC-SM)	Independent recording of the total internal reflection angle and the excitation angle of the PC surface wave	Human serum samples spiked wth CA125, HER2 and CA 15-3	LOD: CA125: 0.55 U/mL HER2: 620 fg/mL CA 15-3: 1.84 U/mL	99

As mentioned previously, conventional techniques for biomarker analysis are time consuming, expensive, required qualified manpower and in addition, have limitations on real-time and efficient multiplexed analysis. Biosensors can provide an avenue to overcome such drawbacks and provide high analytical performance i.e., specificity, sensitivity, stability, reproducibility, low cost, real-time and multiplexing.

Different transducing technologies like piezoelectric, electrochemical, and optical approaches have been discussed above that could be employed for biomarker analysis. For development of piezoelectric biosensors, research need to be focused on novel piezoelectric materials and limiting operational costs as such materials and their optimal integration for analysing biological interactions is difficult. On the other hand, electrochemical transducers face the same shortcomings. Different technologies like nanoparticles, carbon materials and quantum dots have all been utilized for signal amplification. However, keeping biological integrity of analytes using such transducers is tedious and thus, further research on understanding electrochemical nature of biomolecules and cells needs to be performed. For optical biosensors, operational costs and bulky instrumentation are some of the hurdles that need to be overcome. However, recent advancements in plasmonics, nano-structuration have further focused on efficient detection of circulating biomarkers for different diseases by exploiting their opto-electronic properties.

The biosensing field is vast and their applications can range from disease diagnostics and tracking via either LOC and wearable/patch sensors to pharmaceuticals and environments. Moreover, with the possibility of biosensors being compatible with the microfluidic format, this can open promising prospects for integrated lab-on-a-chip (LOC) systems for efficient tracking and monitoring which we will try to explore for my PhD project.

2.5. Current challenges for CTC-biomarkers analysis:

Cancer is a pathological condition where non-functional cells proliferate uncontrollably. Such cells can divide in any part of the body and have the potential to further spread from one part to another causing metastasis. As a result, metastatic spread is more aggressive and results in shorter overall survival and weaker treatment responses. Thus, it is vital to identify numerous biological parameters involved in such tumour spread for early diagnostic and treatment applications.

The conventional protocol for cancer diagnosis is to perform multiple imaging protocols and then confirm the type and staging of cancer through tissue biopsies, which is the gold standard. This is time consuming and extremely invasive. To overcome such drawbacks, focus has been turned towards liquid biopsies that mostly consist of blood sampling and could further provide tons of valuable information. Liquid biopsy contains numerous biomarkers such as CTCs, ctDNAs, extracellular vesicles (EVs) and circulating proteins allowing the easier follow-up of cancer progression. Moreover, multiple liquid biopsies can be sampled easily at regular intervals for the real-time mapping of cancer and metastatic progression. Focusing on a more combinatorial approach where more than one parameter like CTCs and EVs could be analysed would be more beneficial for rapid tracking and diagnostics as EVs have much higher concentration than CTCs.

CTCs express various kind of biomarkers that can be analysed, including intracellular biomarkers, cell surface biomarkers and extracellularly secreted biomarkers. For efficient analysis of intracellular and cell surface biomarkers, CTCs are mostly immuno-labelled leading to their permanent modification and death. In contrast, analysis of secreted biomarkers while maintaining CTCs alive, could allow to follow their expression and progression as a function of time and treatment.

My PhD project focuses on analysing secreted cancer biomarkers, where real-time tracking should be managed through a label-free optical biosensing modality. Based on project requirements, our end goals and team expertise, I would focus on creating an integrated Lab-on-a-Chip (LOC) system to analyse biomarkers secreted directly by cells. This LOC would be comprised of two components: microfluidic manipulation for efficient cell trapping and label-free optical biosensing specifically nano-plasmonics for detection of these cell secretions in real-time and in multiplexed format. We can envisage a future where such systems can be used for cancer patient samples enabling processing for specific separation and concentrations of CTCs and their culture growth while detecting associated biomarkers all in a single micro-system. Personalized healthcare systems based on integrated biosensors and different technologies seem to be an achievable possibility soon. For cancer diagnostics, LOC systems offer an avenue steadily gaining momentum for point-of-care (POC) systems. Such integrated systems can track and monitor cancer in real-time providing information that could alleviate therapeutic success rates. In addition, these devices can provide comprehensive picture for staging, detailed molecular profiling and monitoring disease remission and possible recurrence.

References:

1. IARC. *World Cancer report 2020*. *Cancer Control* vol. 199 (2020).
2. Axelrod, H. D., Pienta, K. J. & Valkenburg, K. C. Optimization of Immunofluorescent Detection of Bone Marrow Disseminated Tumor Cells. *Biol. Proced. Online* **20**, 1–13 (2018).
3. Zhang, S., Garcia-D'Angeli, A., Brennan, J. P. & Huo, Q. Predicting detection limits of enzyme-linked immunosorbent assay (ELISA) and bioanalytical techniques in general. *Analyst* **139**, 439–445 (2013).
4. Rolfo, C. & Russo, A. Liquid biopsy for early stage lung cancer moves ever closer. *Nat. Rev. Clin. Oncol.* **17**, 523–524 (2020).
5. Krebs, M. G. *et al.* Molecular analysis of circulating tumour cells - Biology and biomarkers. *Nat. Rev. Clin. Oncol.* **11**, 129–144 (2014).
6. Attard, G. & de Bono, J. S. Utilizing circulating tumor cells: Challenges and pitfalls. *Curr. Opin. Genet. Dev.* **21**, 50–58 (2011).
7. Che, J., Yu, V., Garon, E. B., Goldman, J. W. & Di Carlo, D. Biophysical isolation and identification of circulating tumor cells. *Lab Chip* **17**, 1452–1461 (2017).
8. Pecot, C. V. *et al.* A novel platform for detection of CK + and CK - CTCs. *Cancer Discov.* **1**, 580–586 (2011).
9. Sundling, K. E. & Lowe, A. C. Circulating Tumor Cells: Overview and Opportunities in Cytology. *Adv. Anat. Pathol.* **26**, 56–63 (2019).
10. Kulasinghe, A., Zhou, J., Kenny, L., Papautsky, I. & Punyadeera, C. Capture of circulating tumour cell clusters using straight microfluidic chips. *Cancers (Basel).* **11**, 1–11 (2019).
11. Khoo, B. L. *et al.* Expansion of patient-derived circulating tumor cells from liquid biopsies using a CTC microfluidic culture device. *Nat. Protoc.* **13**, 34–58 (2018).
12. Li, Y. *et al.* Clinical significance of circulating tumor cells and tumor markers in the diagnosis of lung cancer. *Cancer Med.* **8**, 3782–3792 (2019).
13. Shao, H., Chung, J. & Issadore, D. Diagnostic technologies for circulating tumour cells and exosomes. *Biosci. Rep.* **36**, 1–9 (2016).
14. J. Zhang, K. Chen, and Z. H. F. Circulating Tumor Cell Isolation and Analysis. *Adv. Clin. Chem.* Volume **75**, 1–31 (2016).
15. Wu, S. *et al.* Classification of circulating tumor cells by epithelial-mesenchymal transition markers. *PLoS One* **10**, 1–14 (2015).
16. Chen, L., Bode, A. M. & Dong, Z. Circulating tumor cells: Moving biological insights into detection. *Theranostics* **7**, 2606–2619 (2017).
17. Joosse, S. A., Gorges, T. M. & Pantel, K. Biology, detection, and clinical implications of circulating tumor cells. *EMBO Mol. Med.* **7**, 1–11 (2015).
18. Eslami-S, Z., Cortés-Hernández, L. E. & Alix-Panabières, C. Epithelial Cell Adhesion Molecule: An Anchor to Isolate Clinically Relevant Circulating Tumor Cells. *Cells* **9**, (2020).
19. Jackson, J. M., Witek, M. A., Kamande, J. W. & Soper, S. A. Materials and microfluidics: Enabling the efficient isolation and analysis of circulating tumour cells. *Chem. Soc. Rev.* **46**, 4245–4280 (2017).
20. Cho, H. *et al.* Microfluidic technologies for circulating tumor cell isolation. *Analyst* **143**, 2936–

2970 (2018).

21. Khoo, B. L. *et al.* Expansion of patient-derived circulating tumor cells from liquid biopsies using a CTC microfluidic culture device. *Nat. Protoc.* **13**, 34–58 (2018).
22. Chen, C. L. *et al.* Single-cell analysis of circulating tumor cells identifies cumulative expression patterns of EMT-related genes in metastatic prostate cancer. *Prostate* **73**, 813–826 (2013).
23. Park, E. S. *et al.* Continuous Flow Deformability-Based Separation of Circulating Tumor Cells Using Microfluidic Ratchets. *Small* **12**, 1909–1919 (2016).
24. Hou, H. W. *et al.* Isolation and retrieval of circulating tumor cells using centrifugal forces. *Sci. Rep.* **3**, (2013).
25. Huang, Y. Y. *et al.* Screening and Molecular Analysis of Single Circulating Tumor Cells Using Micromagnet Array. *Sci. Rep.* **5**, 1–11 (2015).
26. Descamps, L. *et al.* MagPure chip: an immunomagnetic-based microfluidic device for high purification of circulating tumor cells from liquid biopsies. 4151–4166 (2022) doi:10.1039/d2lc00443g.
27. Descamps, L., Roy, D. Le & Deman, A. Microfluidic-Based Technologies for CTC Isolation : A Review of 10 Years of Intense Efforts towards Liquid Biopsy. (2022).
28. Alix-Panabières, C., Schwarzenbach, H. & Pantel, K. Circulating Tumor Cells and Circulating Tumor DNA. *Annu. Rev. Med.* **63**, 199–215 (2012).
29. Mani, S. A. *et al.* The Epithelial-Mesenchymal Transition Generates Cells with Properties of Stem Cells. *Cell* **133**, 704–715 (2008).
30. Alix-Panabier`es, C. & Pantel, K. Circulating tumor cells: Liquid biopsy of cancer. *Clin. Chem.* **59**, 110–118 (2013).
31. Went, P. T. *et al.* Frequent EpCam Protein Expression in Human Carcinomas. *Hum. Pathol.* **35**, 122–128 (2004).
32. Thiery, J. P. Epithelial–mesenchymal transitions in tumour progression. *Nat. Rev. Cancer* **2**, 442–454 (2002).
33. Pennacchietti, S. *et al.* Hypoxia promotes invasive growth by transcriptional activation of the met protooncogene. *Cancer Cell* **3**, 347–361 (2003).
34. Bottaro, D. P. *et al.* Identification of the hepatocyte growth factor receptor as the c-met proto-oncogene product. *Science (80-.).* **251**, 802–804 (1991).
35. Olmeda, D. *et al.* SNAI1 Is Required for Tumor Growth and Lymph Node Metastasis of Human Breast Carcinoma MDA-MB-231 Cells. (2007) doi:10.1158/0008-5472.CAN-07-2318.
36. Han, G. On the structure of a class of graded modules related to symmetric pairs. *Algebr. Colloq.* **13**, 315–328 (2006).
37. Jerhammar, F. *et al.* Fibronectin 1 is a potential biomarker for radioresistance in head and neck squamous cell carcinoma. *Cancer Biol. Ther.* **10**, 1244–1251 (2010).
38. Pankov, R. & Yamada, K. M. Fibronectin at a glance. *J. Cell Sci.* **115**, 3861–3863 (2002).
39. Mittal, S., Kaur, H., Gautam, N. & Mantha, A. K. Biosensors for breast cancer diagnosis: A review of bioreceptors, biotransducers and signal amplification strategies. *Biosens.*

Bioelectron. **88**, 217–231 (2017).

40. Akcam, T. I. *et al.* The prognostic value of carcinoembryonic antigen levels in blood and intraoperative pleural lavage fluid in non-small-cell lung cancer. *Kardiochirurgia i Torakochirurgia Pol.* **14**, 104–109 (2017).
41. Yu, D., Du, K., Liu, T. & Chen, G. Prognostic value of tumor markers, NSE, CA125 and SCC, in operable NSCLC patients. *Int. J. Mol. Sci.* **14**, 11145–11156 (2013).
42. Takada, M. *et al.* Measurement of cytokeratin 19 fragments by. (1995).
43. Janning, M. *et al.* Determination of PD-L1 expression in circulating tumor cells of NSCLC patients and correlation with response to PD-1/PD-L1 inhibitors. *Cancers (Basel).* **11**, 1–16 (2019).
44. Pawelczyk, K. *et al.* Role of PD-L1 expression in non-small cell lung cancer and their prognostic significance according to clinicopathological factors and diagnostic markers. *Int. J. Mol. Sci.* **20**, 1–15 (2019).
45. Fukunaga, Y. *et al.* Expression of cytokeratin 8 in lung cancer cell lines and measurement of serum cytokeratin 8 in lung cancer patients. *Lung Cancer* **38**, 31–38 (2002).
46. Grunnet, M. & Sorensen, J. B. Carcinoembryonic antigen (CEA) as tumor marker in lung cancer. *Lung Cancer* **76**, 138–143 (2012).
47. Matsuoka, K., Sumitomo, S., Nakashima, N., Nakajima, D. & Misaki, N. Prognostic value of carcinoembryonic antigen and CYFRA21-1 in patients with pathological stage I non-small cell lung cancer. *Eur. J. Cardio-thoracic Surg.* **32**, 435–439 (2007).
48. Niemeijer, A. *et al.* MA 05.07 Whole Body PD-1 and PD-L1 PET in Pts with NSCLC. *J. Thorac. Oncol.* **12**, S1817 (2017).
49. Potdar, P. & Lotey, N. Role of circulating tumor cells in future diagnosis and therapy of cancer. *J. Cancer Metastasis Treat.* **1**, 44 (2015).
50. Lianidou, E. S. Gene expression profiling and DNA methylation analyses of CTCs. *Mol. Oncol.* **10**, 431–442 (2016).
51. Tombal, B. & Lecouvet, F. Modern detection of prostate cancer's bone metastasis: Is the bone scan era over? *Adv. Urol.* **2012**, (2012).
52. Budna-Tukan, J. *et al.* Analysis of circulating tumor cells in patients with non-metastatic high-risk prostate cancer before and after radiotherapy using three different enumeration assays. *Cancers (Basel).* **11**, (2019).
53. Grisanti, S. *et al.* Analysis of circulating tumor cells in prostate cancer patients at psa recurrence and review of the literature. *Anticancer Res.* **36**, 2975–2981 (2016).
54. Miyamoto, D. T., Sequist, L. V. & Lee, R. J. Circulating tumour cells - Monitoring treatment response in prostate cancer. *Nat. Rev. Clin. Oncol.* **11**, 401–412 (2014).
55. Scher, H. I. *et al.* Association of AR-V7 on circulating tumor cells as a treatment-specific biomarker with outcomes and survival in castration-resistant prostate cancer. *JAMA Oncol.* **2**, 1441–1449 (2016).
56. Tretiakova, M. S. *et al.* Prognostic value of Ki67 in localized prostate carcinoma: A multi-institutional study of >1000 prostatectomies. *Prostate Cancer Prostatic Dis.* **19**, 264–270 (2016).

57. Doyen, J. *et al.* Circulating tumor cells in prostate cancer: A potential surrogate marker of survival. *Critical Reviews in Oncology/Hematology* vol. 81 241–256 (2012).

58. Beckett, M. Lou, Cazares, L. H., Vlahou, A., Schellhammer, P. F. & Wright, G. L. Prostate-specific membrane antigen levels in sera from healthy men and patients with benign prostate hyperplasia or prostate cancer. *Clin. Cancer Res.* **5**, 4034–4040 (1999).

59. Adisa, J. O., Egbujo, E. C., Ibrahim, B., Musa, B. & Madukwe, J. Expression of some selected cytokeratins and Ki67 protein in prostatic tumor: Can these be used as tumor markers. *Pan Afr. Med. J.* **20**, 1–8 (2015).

60. Larsson, A., Sköldenberg, E. & Ericson, H. Serum and plasma levels of FGF-2 and VEGF in healthy blood donors. *Angiogenesis* **5**, 107–110 (2002).

61. Sciarra, A. *et al.* Androgen receptor variant 7 (AR-V7) in sequencing therapeutic agents for castratrion resistant prostate cancer: A critical review. *Medicine (Baltimore).* **98**, e15608 (2019).

62. Izuhara, K., Nunomura, S., Ohta, S., Ogawa, M. & Nanri, Y. Cytokine network. *Evol. Atopic Dermat. 21st Century* **7**, 97–112 (2017).

63. Ueda, T., Shimada, E. & Urakawa, T. Serum levels of cytokines in patients with colorectal cancer: Possible involvement of interleukin-6 and interleukin-8 in hematogenous metastasis. *J. Gastroenterol.* **29**, 423–429 (1994).

64. Tawara, K., Oxford, J. T. & Jorcyk, C. L. Clinical significance of interleukin (IL)-6 in cancer metastasis to bone:Potential of anti-IL-6 therapies. *Cancer Manag. Res.* **3**, 177–189 (2011).

65. Liu, T. *et al.* Self-seeding circulating tumor cells promote the proliferation and metastasis of human osteosarcoma by upregulating interleukin-8. *Cell Death Dis.* **10**, (2019).

66. Wang, C. Q. *et al.* Interleukin-6 enhances cancer stemness and promotes metastasis of hepatocellular carcinoma via up-regulating osteopontin expression. *Am. J. Cancer Res.* **6**, 1873–1889 (2016).

67. Ortiz, V. & Yu, M. Analyzing Circulating Tumor Cells One at a Time. *Trends Cell Biol.* **28**, 764–775 (2018).

68. Lv, D., Hu, Z., Lu, L., Lu, H. & Xu, X. Three-dimensional cell culture: A powerful tool in tumor research and drug discovery. *Oncol. Lett.* **14**, 6999–7010 (2017).

69. Huertas, C. S., Calvo-Lozano, O., Mitchell, A. & Lechuga, L. M. Advanced Evanescent-Wave Optical Biosensors for the Detection of Nucleic Acids: An Analytic Perspective. *Front. Chem.* **7**, 1–25 (2019).

70. Soler, M., Huertas, C. S. & Lechuga, L. M. Label-free plasmonic biosensors for point-of-care diagnostics: a review. *Expert Rev. Mol. Diagn.* **19**, 71–81 (2019).

71. Roointan, A. *et al.* Early detection of lung cancer biomarkers through biosensor technology: A review. *J. Pharm. Biomed. Anal.* **164**, 93–103 (2019).

72. Jayanthi, V. S. P. K. S. A., Das, A. B. & Saxena, U. Recent advances in biosensor development for the detection of cancer biomarkers. *Biosens. Bioelectron.* **91**, 15–23 (2017).

73. Syahir, A., Usui, K., Tomizaki, K., Kajikawa, K. & Mihara, H. Label and Label-Free Detection Techniques for Protein Microarrays. *Microarrays* **4**, 228–244 (2015).

74. Soper, S. A. *et al.* Point-of-care biosensor systems for cancer diagnostics/prognostics.

Biosens. Bioelectron. **21**, 1932–1942 (2006).

75. Zeng, L. & Xiao, Z. Biosensors and Biodetection. *Methods Mol. Biol.* **1572**, 421–430 (2017).
76. Kim, D.-H., Na, J. S. & Rhee, S.-W. Metallorganic Chemical Vapor Deposition of Pb(Zr, Ti)O[sub 3] Films Using a Single Mixture of Metallorganic Precursors. *J. Electrochem. Soc.* **148**, C668 (2001).
77. Vigneshvar, S., Sudhakumari, C. C., Senthilkumaran, B. & Prakash, H. Recent advances in biosensor technology for potential applications - an overview. *Front. Bioeng. Biotechnol.* **4**, 1–9 (2016).
78. Pohanka, M. Overview of piezoelectric biosensors, immunosensors and DNA sensors and their applications. *Materials (Basel).* **11**, (2018).
79. Shan, W. *et al.* An aptamer-based quartz crystal microbalance biosensor for sensitive and selective detection of leukemia cells using silver-enhanced gold nanoparticle label. *Talanta* **126**, 130–135 (2014).
80. Shan, W. *et al.* An aptamer-based quartz crystal microbalance biosensor for sensitive and selective detection of leukemia cells using silver-enhanced gold nanoparticle label. *Talanta* **126**, 130–135 (2014).
81. Bakhshpour, M., Piskin, A. K., Yavuz, H. & Denizli, A. Quartz crystal microbalance biosensor for label-free MDA MB 231 cancer cell detection via notch-4 receptor. *Talanta* **204**, 840–845 (2019).
82. Bakhshpour, M., Piskin, A. K., Yavuz, H. & Denizli, A. Quartz crystal microbalance biosensor for label-free MDA MB 231 cancer cell detection via notch-4 receptor. *Talanta* **204**, 840–845 (2019).
83. Su, L. *et al.* Detection of cancer biomarkers by piezoelectric biosensor using PZT ceramic resonator as the transducer. *Biosens. Bioelectron.* **46**, 155–161 (2013).
84. Guo, Y., Wang, Y., Yang, G., Xu, J. J. & Chen, H. Y. MicroRNA-mediated signal amplification coupled with GNP/dendrimers on a mass-sensitive biosensor and its applications in intracellular microRNA quantification. *Biosens. Bioelectron.* (2016) doi:10.1016/j.bios.2016.06.013.
85. Khanmohammadi, A. *et al.* Electrochemical biosensors for the detection of lung cancer biomarkers: A review. *Talanta* **206**, 120251 (2020).
86. Wu, Q., Zhang, Y., Yang, Q., Yuan, N. & Zhang, W. Review of electrochemical DNA biosensors for detecting food borne pathogens. *Sensors (Switzerland)* **19**, (2019).
87. Damiati, S. & Schuster, B. Electrochemical biosensors based on S-layer proteins. *Sensors (Switzerland)* **20**, 1–22 (2020).
88. Chen, Y. *et al.* Ultrasensitive label-free detection of circulating tumor cells using conductivity matching of two-dimensional semiconductor with cancer cell. *Biosens. Bioelectron.* **142**, 111520 (2019).
89. Viswanathan, S., Rani, C., Ribeiro, S. & Delerue-Matos, C. Molecular imprinted nanoelectrodes for ultra sensitive detection of ovarian cancer marker. *Biosens. Bioelectron.* **33**, 179–183 (2012).
90. Marques, R. C. B., Viswanathan, S., Nouws, H. P. A., Delerue-Matos, C. & González-García,

M. B. Electrochemical immunosensor for the analysis of the breast cancer biomarker HER2 ECD. *Talanta* **129**, 594–599 (2014).

91. Soler, M., Huertas, C. S. & Lechuga, L. M. Label-free plasmonic biosensors for point-of-care diagnostics: a review. *Expert Rev. Mol. Diagn.* **19**, 71–81 (2019).
92. Peltomaa, R., Glahn-Martínez, B., Benito-Peña, E. & Moreno-Bondi, M. C. Optical Biosensors for Label-Free Detection of Small Molecules. *Sensors (Basel).* **18**, (2018).
93. Li, P. *et al.* Fundamentals and applications of surface-enhanced Raman spectroscopy–based biosensors. *Current Opinion in Biomedical Engineering* (2020) doi:10.1016/j.cobme.2019.08.008.
94. Graybill, R. M., Cardenosa-Rubio, M. C., Yang, H., Johnson, M. D. & Bailey, R. C. Multiplexed microRNA expression profiling by combined asymmetric PCR and label-free detection using silicon photonic sensor arrays. *Anal. Methods* **10**, 1618–1623 (2018).
95. Knoerzer, M. *et al.* Optical frequency comb based system for photonic refractive index sensor interrogation. *Opt. Express* **27**, 21532 (2019).
96. Huertas, C. S., Fariña, D. & Lechuga, L. M. Direct and Label-Free Quantification of Micro-RNA-181a at Attomolar Level in Complex Media Using a Nanophotonic Biosensor. *ACS Sensors* **1**, 748–756 (2016).
97. Mousavi, M. Z. *et al.* Label-free detection of rare cell in human blood using gold nano slit surface plasmon resonance. *Biosensors* **5**, 98–117 (2015).
98. Li, X. *et al.* Label-Free Optofluidic Nanobiosensor Enables Real-Time Analysis of Single-Cell Cytokine Secretion. **1800698**, 1–11 (2018).
99. Petrova, I., Konopsky, V., Nabiev, I. & Sukhanova, A. Label-Free Flow Multiplex Biosensing via Photonic Crystal Surface Mode Detection. *Sci. Rep.* **9**, 1–9 (2019).

Chapter 3

Surface functionalization of the plasmonic immunosensor: Click chemistry versus carbodiimide/NHS chemistry

3.1. Introduction:

Plasmonic immunosensor are fabricated generally composed of noble metals such as gold either in the form of film or nanoparticles, for which the bio-recognition elements are grafted on the surface to detect analytes based on antibody/antigen sensing mechanisms. Such sensors have come to the forefront to analyse various biological interactions and have the potential to be implemented in clinical settings as well as for environmental monitoring, food control and safety. Such biosensors focus on label-free approach by exploiting the principle of surface plasmon resonance (SPR) [1,2] and further rely on optimal immobilization of antibodies on the surface for biosensing. Upon target recognition by these immobilized antibodies, the surface refractive index changes and further induces electromagnetic modifications on the resonance conditions being propagated as plasmons highlighted in Fig. 3.1.1. Performance of these devices depend on both their sensitivity to refractive index changes and proper surface functionalization to effectively capture antigen of interest specifically while limiting non-specific adsorption [1,2].

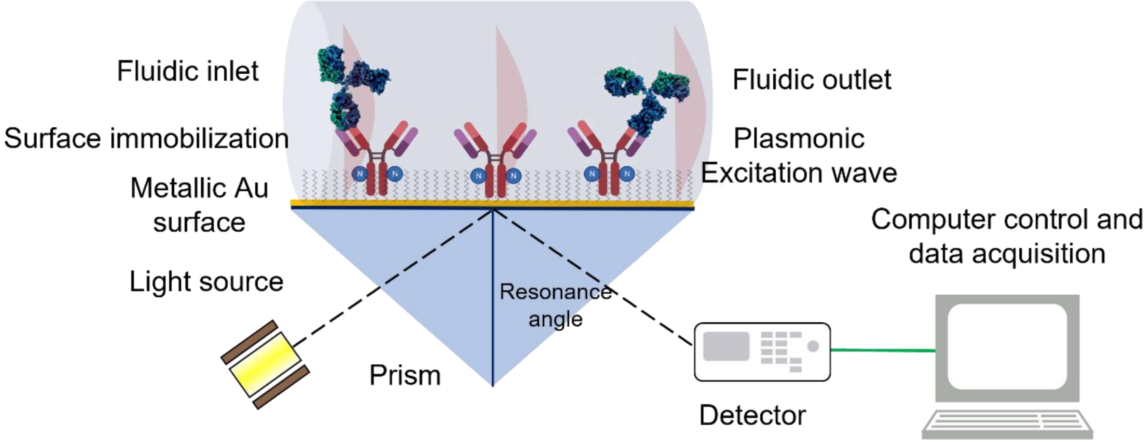

Figure 3.1.1.: Setup schematic and Principle of Surface plasmon resonance imaging setup (SPRi).

For fabrication of efficient plasmonic immunosensors, chemical functionalization of gold surface is a key step. Improper functionalization can lead to desorption of the antibody (Ab) resulting to non-specific adsorption of other biomolecules present in the sample such as non-specific cells, markers, and proteins. This can subsequently lead to low reproducibility and false positive signals. Chemical functionalization relies on the arrangement of chemical moieties such as self-assembled monolayers (SAMs) of organic molecules in an oriented manner. These organic molecules usually consist of hydrocarbon chains, carrying a thiol group (-SH) at one end that links onto the gold through Au–S bonds via the oxidation–reduction reaction, while a functional group on the other end can establish bonds with the antibodies [3,4].

For bio-recognition of different protein targets, different immunoglobulin (Ig) classes of antibodies (Ab) can be selected such as IgA, IgD, IgE, IgG and IgM of which, IgG is the most conventional immunoglobulin. IgG antibodies contain around 30 cysteine molecule that are potential reaction/immobilization sites [5]. The structure of such antibodies comprised of a Y-shape with heavy chain backbone connected via the hinge region containing disulphide bonds (-S-S-). In addition, each IgG have light chain fragments on top of these heavy chain connected in similar -S-S- fashion.

More so, such antibodies have a constant region which is common for all IgG termed as Fc. Fab fragments defined as antigen binding fragment specific for bio-conjugation are variable for different antibodies [6] as showcased in Fig. 3.1.2. (A).

The C- /COOH- terminus of the antibody structure is at one end of the Fc fragment on the heavy chain, while on the other end, N-/NH_2- terminus is presented, specifically for both heavy and light chains on the Fab fragment. A single antibody is composed of multiple amino acids that bear different functional groups like -NH2, -COOH, and -OH among others on their lateral chain. Specifically, terminus groups are exploited for bio-immobilization of these IgG antibodies via covalent coupling. Glycosylation sites showcased in Fig. 3.1.2. (B) and (C) are a core structure of an IgG antibodies and are common for all human and rodent species.

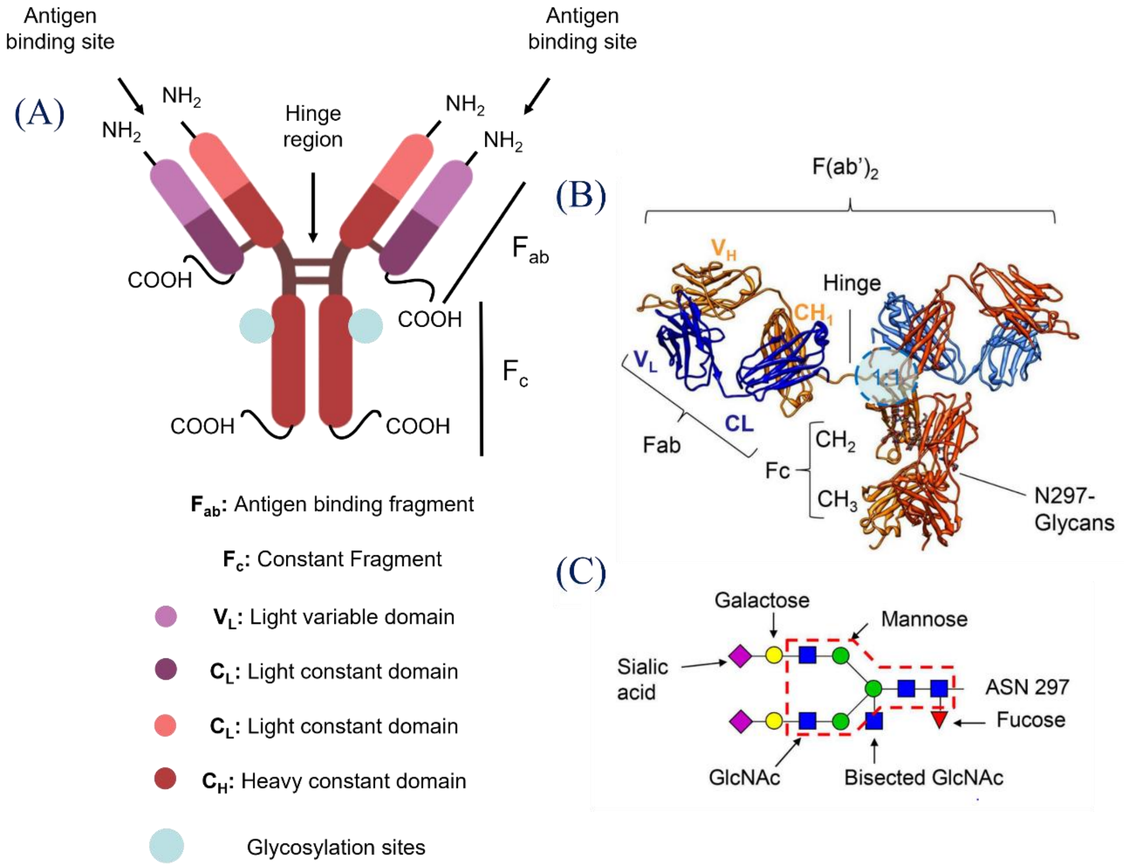

Figure 3.1.2.: **(A)** Chemical and **(B)** Crystal structure of IgG Antibody showcasing the Fc and Fab fragments along with antigen binding and glycosylation sites with the disulphide hinge region. The binding location for FcγR, binding IgG asymmetrically in a 1:1 configuration. **(C)** The N-linked glycan found at position 297 can be found as a core structure, common to all IgG found in human beings and rodents (core structure indicated with a red dashed line) [7].

Various approaches ranging from affinity based coupling such as avidin/biotin and protein A/G [8,9] to covalent binding can be employed for surface biofunctionalization. Affinity based modalities have shown high stability and specificity, however, they have their limitations due to non-orientation or low rate of Ab immobilization [10,11]. Some of these drawbacks can be overcome by covalent strategies using specific chemical groups coupled with the functionalized monolayers on the gold surface, of which carbodiimide/NHS (C/NHS) chemistry via amine coupling is the most well-known approach

[8,12,13]. In recent years, for further improving surface immobilization for efficient fabrication of plasmonic immunosensors, click chemistry, specifically copper-free click chemistry has come to the forefront.

In my PhD project, I focused on antibody immobilization through two covalent strategies: (i) novel site-specific click chemistry via enzymatic activation and (ii) conventional C/NHS chemistry via amine coupling for comparative analysis. In the following section, I will present state of the art regarding gold surface chemistry, conventional C/NHS chemistry and copper-free click chemistry and their biosensing applications.

3.1.1. Overview:

Different covalent based functionalized approaches like carbodiimide/NHS (C/NHS) and copper free click chemistries i.e., dibenzocyclooctyne (DBCO) have been employed to highlight site-specific and directed antibody immobilization on gold surfaces [14,15]. For all functionalized surfaces, 1/1 molar concentration mixing were prepared for functional chemical moieties (NHS-/COOH- for C/NHS, NH_2/DBCO-terminal heads for DBCO surfaces) and diluents (OH-terminal head for both C/NHS and DBCO chemistry). For further activation, DIC and NHS were used for C/NHS chemistry while DBCO-NHS was employed for DBCO/OH Alkyls.

As highlighted in Fig. 3.1.3. (A), comparative analysis was performed between conventional C/NHS chemistry and DBCO chemistry where different antibody immobilizations were focused on. For C/NHS chemistry, mixed COOH/OH Alkyls with both -COOH and -OH terminal moieties were functionalized on Au surface and were subsequently activated to mixed NHS/OH Alkyls with NHS/OH terminal moieties via DIC/NHS. For DBCO surfaces, two different strategies were presented i.e., activated DBCO/OH Alkyls and mixed DBCO PEGs. For mixed DBCO/OH Alkyls, like mixed NHS/OH Alkyls, NH_2/OH Alkyls surfaces with NH_2/OH terminal heads were activated to DBCO/OH Alkyls through DBCO-NHS. While for DBCO PEGs/OH Alkyls, terminal DBCO moiety with PEGs chain and SH tail group was functionalized directly on the surface as a single step compared with the above-mentioned approaches which require further activation.

The functional groups for Ab immobilization for IgG1 antibodies have been presented in Fig. 3.1.3. (B) NHS group on the NHS/OH Alkyls and DBCO group on DBCO/OH Alkyls and DBCO PEGs/OH Alkyls are specific for covalent antibody coupling. Specifically for NHS group, COOH/NH2 groups surrounding non-modified Ab allow covalent immobilization whereas for DBCO group, -SH group on fragmented Ab-SH and $-N_3$ on azide activated Ab-N_3 are specific for covalent attachment. Following sub-sections will focus on Materials and Methods and Results for the different approaches discussed above with comprehensive comparative analysis performed for these surfaces and immobilized antibodies approaches.

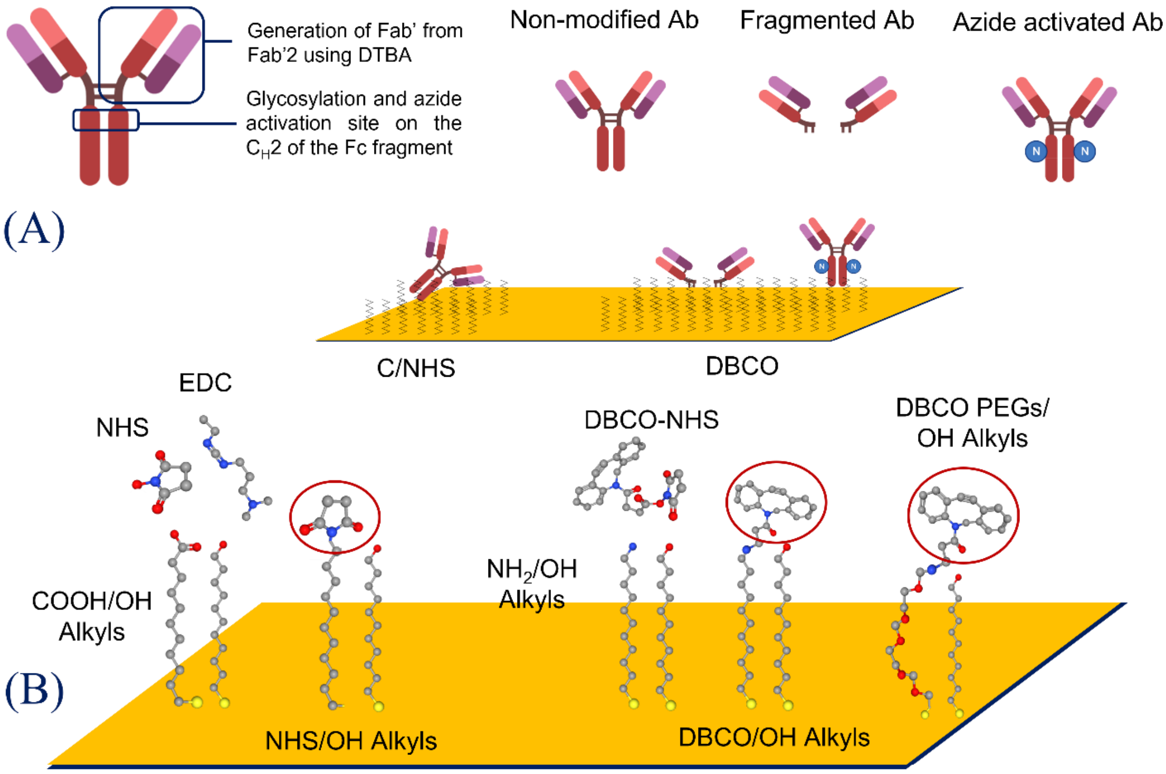

Figure 3.1.3.: Surface functionalization strategies: **(A)** Functional groups for antibody (Ab) immobilization are highlighted for all surfaces. Non-modified Ab is immobilized onto carbodiimide/NHS (C/NHS) functionalized surface. Fragmented antibody (Ab-SH) and azide activated antibody (Ab-N_3) are immobilized onto DBCO functionalized surfaces. **(B)** Chemical structure of functionalized gold surfaces. NHS/OH Alkyls surface is obtained after EDC/NHS activation of mixed COOH/OH Alkyls monolayers; DBCO/OH Alkyls surface is obtained after DBCO-NHS grafting onto mixed NH_2/OH Alkyls monolayers; DBCO PEGs/OH Alkyls surface is obtained directly by mixed DBCO PEGs/OH Alkyls monolayer functionalization.

3.2. State of the art:

3.2.1. Chemical functionalization of gold surfaces:

One of the valuable platforms for antibody coupling via chemical functionalization are metal surfaces. Different species can be immobilized strongly via covalent bonds due to strong interactions between sulfanyl group (-SH) and metal surfaces [16]. Specifically, gold surfaces have been frequently employed for development of bioanalytical devices because of its inert oxidative resistance, conductivity, and simpler fabrication of thin films. In addition, gold surfaces can be used for surface plasmon resonance (SPR) angle shift, that has been found useful for analysing and monitoring molecular binding events on the sensor surfaces [16].

Optical variations are extremely sensitive to the reflectivity of such thin gold films under the proper conditions, however bare gold surfaces do not have specific sites for biomolecular interaction where proteins and biocomponents could adhere spontaneously and non-selectivity. However, terminal functionalization techniques have developed for gold surfaces playing a critical role in analytical applications including SPR/plasmonic sensors, electrochemical analysis, quartz crystal microbalance measurements and so on [16,17].

For specific modification of gold surfaces, monolayers of alkanethiols as shown in Fig. 3.1.4. have been employed as convention with various functional groups such as carboxyl (-COOH), amino (-NH2), and hydroxyl (-OH) among others have been bound to gold substrates via terminally functionalized alkanethiols [16,18]. Monolayers offer well-defined chemical interface between gold surfaces and biological species of interest where typical monolayer synthesis focuses on mixed approach where functional monolayers along with diluent are functionalized on the surface. The surface modification is specific due to the formation of oxido-reductive thiol-gold (Au-S) reaction. Although, such modification is robust for constructing functionalized gold surfaces, however it is vital to achieve balance between terminal functionalization and preparation of anti-fouling surface [16–18].

$$Au + R - alkyl - SH + R - PEG - SH \rightarrow Au - S - alkyl/PEG - R$$

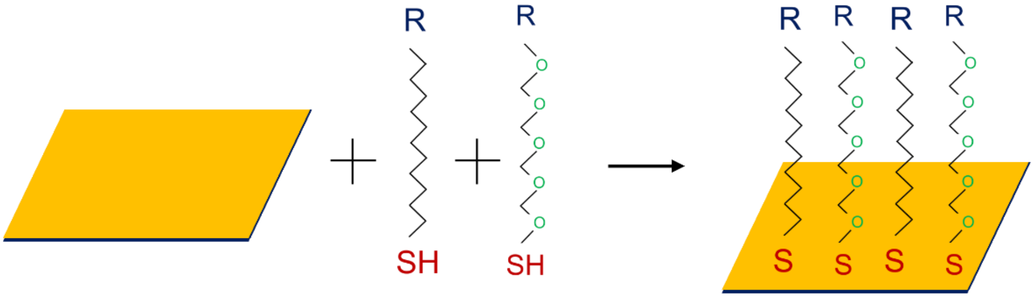

Figure 3.1.4.: Chemical **(A)** reaction and **(B)** schematic for functionalization on gold surface via Au-S reaction where R could be functional groups like -COOH, -NH2 and OH and so on and alkylated and PEGylated chains are presented as mixed monolayers.

Compared with alkylated (-C-C-) chains, PEGylated (-C-O-C-) moieties have been highlighted to improve characteristics regarding background noise and S/N signals [19–22]. Polyethylene glycol (PEG) and PEG tethered chains have been showcased for constructing anti-fouling surfaces with biological media, drastically decreasing non-specific protein adsorption on surfaces for numerous biomedically relevant systems [18]. PEG chains highlighted high hydrophilicity, appreciable flexibility, non-ionic nature for controlled repulsion of proteins from the surface by steric exclusion [18,20]. Such properties were showcased through SPR sensing where in addition, mixed PEGylated chains with different molecular weights and lengths were compared [20]. Between mono vs mixed monolayers, mixed monolayers presented high non-fouling characteristics due to PEG chain packing and have further showcased to improve reactivity of different immobilization species. Furthermore, for such mixed functionalization approaches no blocking treatment is required [20,22].

For further improving the stability of such surface functionalization approaches, chain type and length of these monolayers is an important parameter to be considered. These surface modifications can further reduce background signal and improve signal-to-noise (S/N) ratio allowing the consequent reduction of non-specific adsorption. Chain length as a factor that have been presented to reduce steric hindrances between charged terminal molecules.

However, charged head groups like -NHS, -COOH and DBCO seem to influence surface coverage tilt angle regardless of chain length [23]. Such packing is governed by parallel orientation of the first

C – C bonds, where nematic order parameter values govern this phenomenon near the surface. Both short and long alkyl chain presented well defined hexagonal packing at high surface coverage however, short chains present a large tilt angle distribution while long chains do not which can reduce further non-specific adsorption [23].

One of the factors contributing to resistance of non-specific protein adsorption is steric hindrances between chain polymers. These hinderances arise when proteins or biomolecules encounters functionalized monolayers, where such polymers are 'squeeze' together at high entropy discouraging adsorption to the surface. PEG chains have been exhibited to improve anti-fouling properties of surface at room temperature [22]. Such orientation further increases grafting density and brush height indicating steric hindrance to be critical for antifouling PEG properties as exhibited in Fig. 3.1.5. In addition, such molecular adsorption is influenced by charge density and overall surface hydrophilicity along with interfacial pH and surface roughness [22,24].

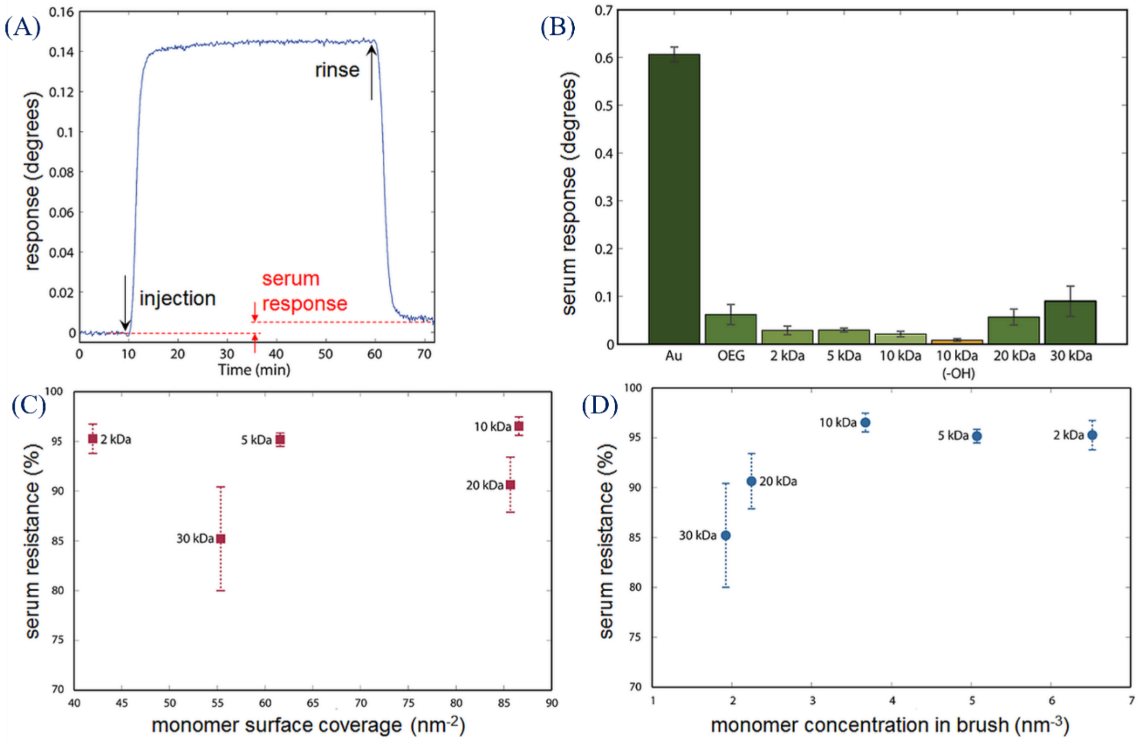

Figure 3.1.5.: Serum protein adsorption on poly (ethylene glycol) brushes on gold measured with surface plasmon resonance. Results from oligo (ethylene glycol) monolayers are included for comparison. **(A)** shows a typical serum injection and illustrates the total response, defined as the shift after 50 min exposure. (Most of the immediate signal is due to the high refractive index of the serum solution.) **(B)** shows the final signals, **(C)** the serum resistance (fraction reduced response compared to pure gold) vs monomer surface coverage, and **(D)** serum resistance vs average monomer concentration inside the brush [24].

The following section will focus on exploiting chemical functionalization via covalent coupling specifically conventional carbodiimide/NHS interaction for antibody immobilization.

3.2.2. Covalent immobilization of antibodies for immunosensors:

For carbodiimide/NHS coupling on gold surfaces, COOH-terminated monolayers are functionalized, which are further employed for biosensor fabrication to attach various amine-containing biomolecules. For efficient coupling of biomolecules with the functionalized monolayers via covalent amide bond, the carboxylic (COOH) groups are activated to NHS terminated monolayers via carbodiimide and N-hydroxysuccinimidyl ester (NHS-ester) groups specific for amine abundant biomolecules. Various research groups have focused on understanding this covalent based approach [25], however the conditions for optimal C/NHS activation relies on different parameters and experimental conditions such as monolayer concentration, temperature, pH conditions, concentration of activation compounds among others [25].

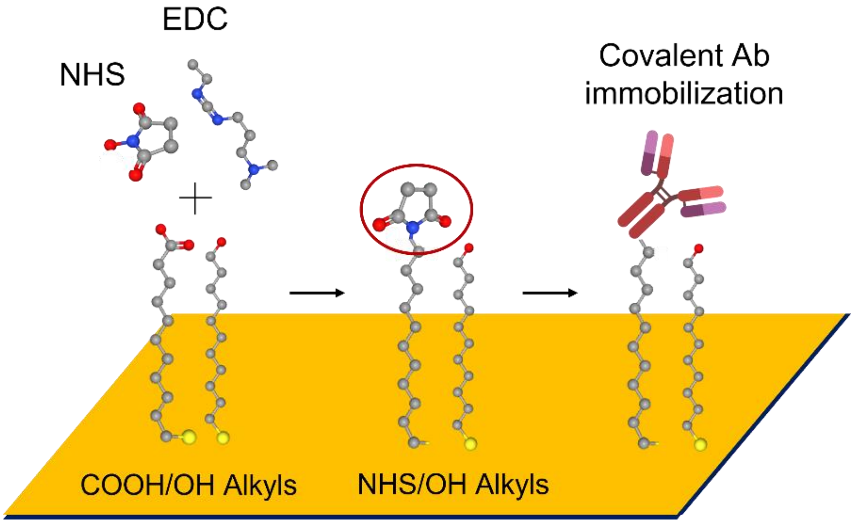

Figure 3.1.6.: Chemical schematic for C/NHS chemistry of our approach where COOH/OH Alkyls are initially functionalized and further activated to NHS/OH Alkyls via DIC/NHS. Afterwards, non-modified antibodies are immobilized on the surface amide bond formation with the functional groups on the antibodies.

However, C/NHS activation has been showcased to be complex due to different by-products formation highlighted in Fig. 3.1.6., where solvent nature and reactant concentrations play a crucial role in activation kinetics and efficiency. Furthermore, activation of carboxylic group to NHS-ester is complex and prone to by-product formation as presented in reactions (1), (2) and (3) in Fig. 3.1.7. Such species make the activation more intricate where carboxylic groups can be regenerated via hydrolysis of O-acylurea or NHS-ester [25] and could produce further urea derivatives.

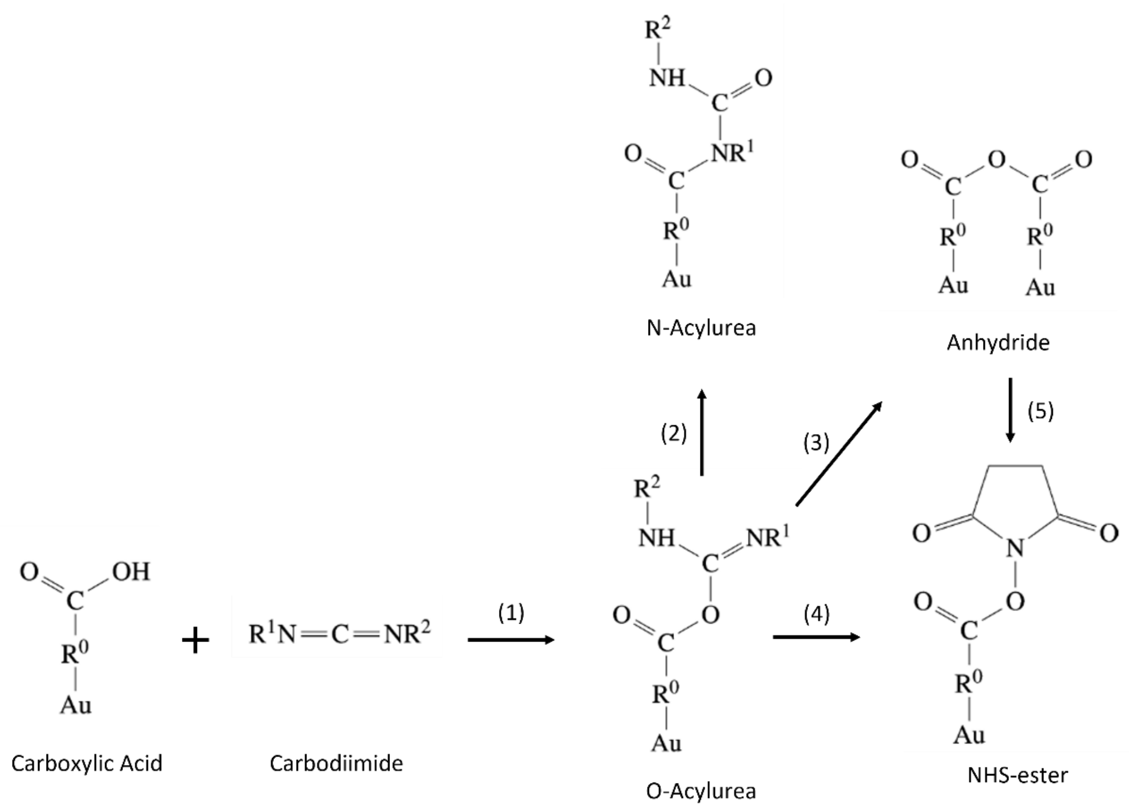

Figure 3.1.7.: Chemical reaction scheme for carbodiimide/NHS chemistry focusing on the generation of different by-products like (1) O-Acylurea, (2) N-acylurea and (3) Anhydride for activation of carboxylic groups (COOH) to NHS ester.

More so, activation times along with carbodiimide and NHS concentration for activation vary greatly for optimal NHS activation and subsequent antibody immobilization. Palazon and group showcased optimization of activation times ranging from 30 min to 24 hrs for C/NHS chemistry showcased in Fig. 3.1.8. where activation was performed in either non-organic solvent like (A) water and organic solvent like (B) Tetrahydrofuran (THF). In this article, further comparison was performed with different carbodiimide chemicals which will be covered later on [25].

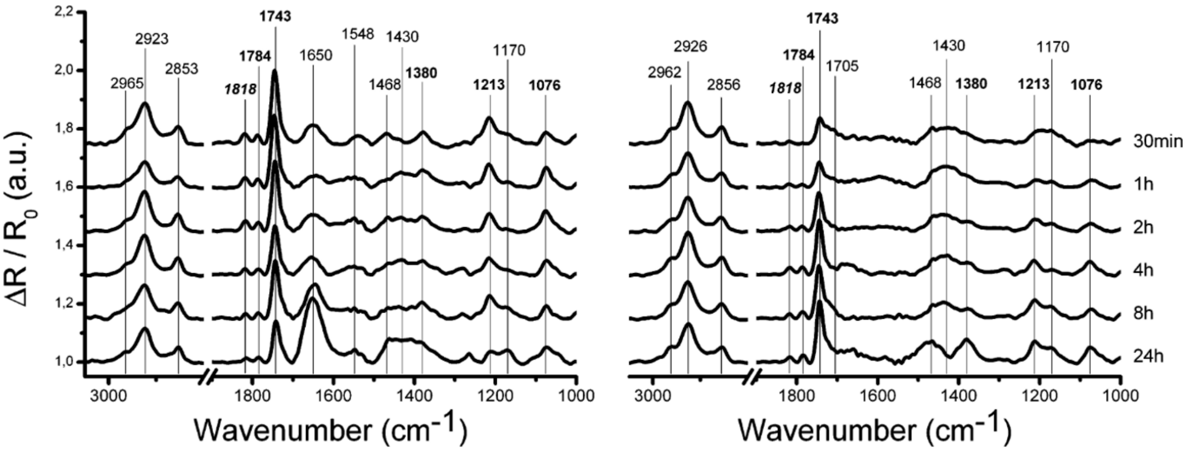

(A) Water (B) THF

Figure 3.1.8.: Samples activated in (A) water and (B) THF with 100 mM concentrations of the corresponding carbodiimide and NHS. Characteristic NHS absorption wavenumbers are written in bold, and the 1818 cm^{-1} peak, characteristic of NHS-ester, is written in bold and italic from 30 min to 1 h to 2 h to 4 h to 8 h and 24 h [25].

Different solvents ranging from water to organic chemicals such as dimethyl sulfoxide (DMSO) or tetrahydrofuran (THF) have been highlighted for N-(3- (dimethylamino)propyl)-N′ -ethylcarbodiimide (EDC), N,N′ -dicyclohexylcarbodiimide (DCC) and N,N′ -diisopropyl-carbodiimide (DIC) driven activation characterized through polarization modulation infrared adsorption spectroscopy (PM-IRRAS) and time-of-flight secondary ion mass spectrometry (Tof-SIMs) [25].

However, due to such varying condition requirements, it is difficult to prove biomolecules like proteins and antibodies to couple optimally in a covalent manner as such compounds have the tendency to easily physiosorbed and bind to the non-activated COOH rather than NHS-ester as highlighted due to formation of multiple by-products [25]. Furthermore, for the immobilization of antibodies, orientation remains an hindering issue where antigen binding sites for bio-detection could attach on the functionalized monolayer due to random coupling [10,12,26,27].

Among antibodies, IgG1 are commonly used for immobilization on functionalized gold surfaces via covalent C/NHS chemistry due to abundant lysine residues (~85), however, this binding could happen in an undirected and non-site specific manner leading to partial loss of efficiency in target capture and reproducibility [27,28]. To overcome such drawbacks, various covalent strategies can be harnessed specifically click chemistry and copper free click chemistry have been researched extensively by the turn of the decade, which will be focused on in the following section.

3.2.3. Copper Free Click chemistry for biomolecule conjugation:

Click chemistry initially described by Sharpless and group in 2001, presented a desire to follow nature's lead and endeavour on joining small units together with heteroatom links (C-X-C) to harness power molecular assembly [29,30]. The logic behind click chemistry is to develop and exploit reactions that are selective, stereospecific (but not necessarily enantio- selective), modular, result very high yields and generate only non-toxic by-products which can be removed via non-chromatographic methods [30]. Characteristics of such process include simple reaction conditions insensitive to oxygen and water, readily available reagents and materials, application of non-toxic solvents that could be easily removed and simple product isolation [30]. In addition, complex purification methods should not be required, and the resulted product must be stable under physiological conditions.

Bertozzi, Meldal and Sharpless have been awarded the Nobel prize in Chemistry for developing click chemistry and bio-orthogonal chemistry, where Sharpless and Meldal laid the fundamental foundation for functional click chemistry where molecular building blocks snap together quickly and efficiently and Bertozzi presented a new dimension where this chemistry was employed in living organisms. Click reactions achieve required properties by having comparatively higher thermodynamic driving force i.e., greater than 20 kcal/mol. Such processes are rapid and tend to be highly selective for single product as being 'spring-loaded' for single trajectory [30]. Different reactions have been classified for chemical 'click' transformations highlighted from Fig. 3.1.9. to Fig. 3.1.12.:

a. [3+2] Cycloadditions like Huisgen 1,3-dipolar cycloaddition, specifically Cu(I)-catalysed refer simply as copper catalysed Azide-Alkyne Cycloaddition (CuAAC) [30,31]

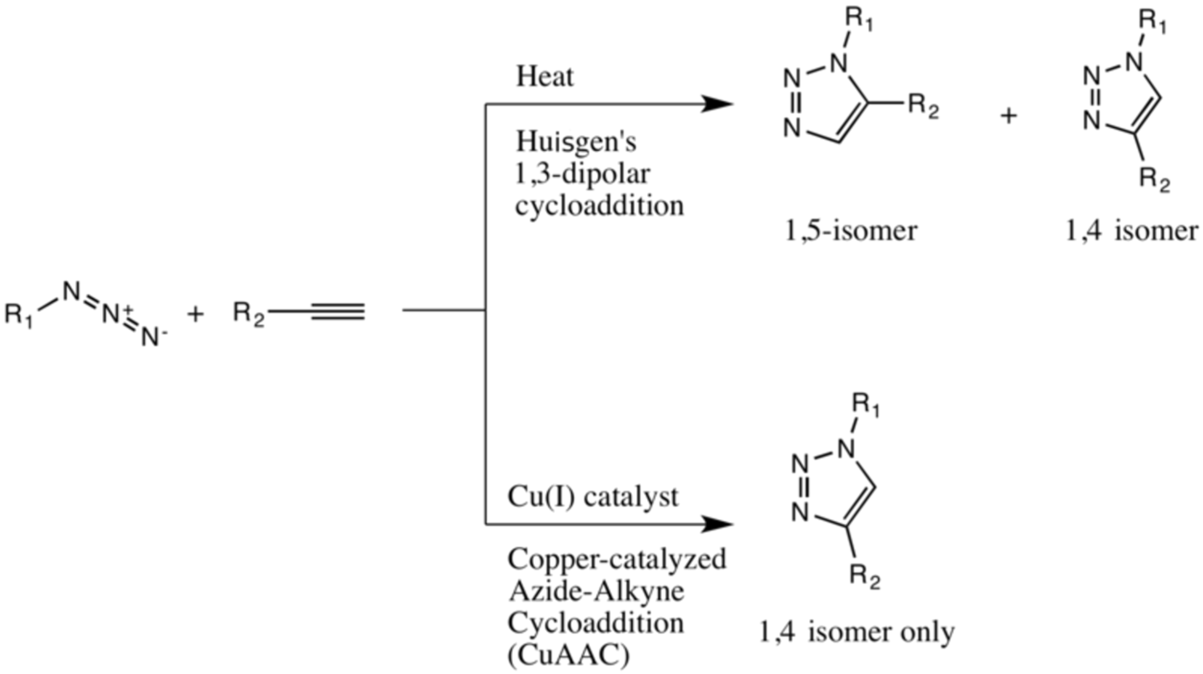

Figure 3.1.9.: Reactions schematic for Huisgen's 1,3-dipolar cycloaddition and copper-catalysed Azide Alkyne Cycloaddition (CuAAC)

b. Strain promoted Azide-Alkyne Cycloaddition (SPAAC) [32] and Strain-promoted alkyne-nitrone cycloaddition (SPANC) [33]

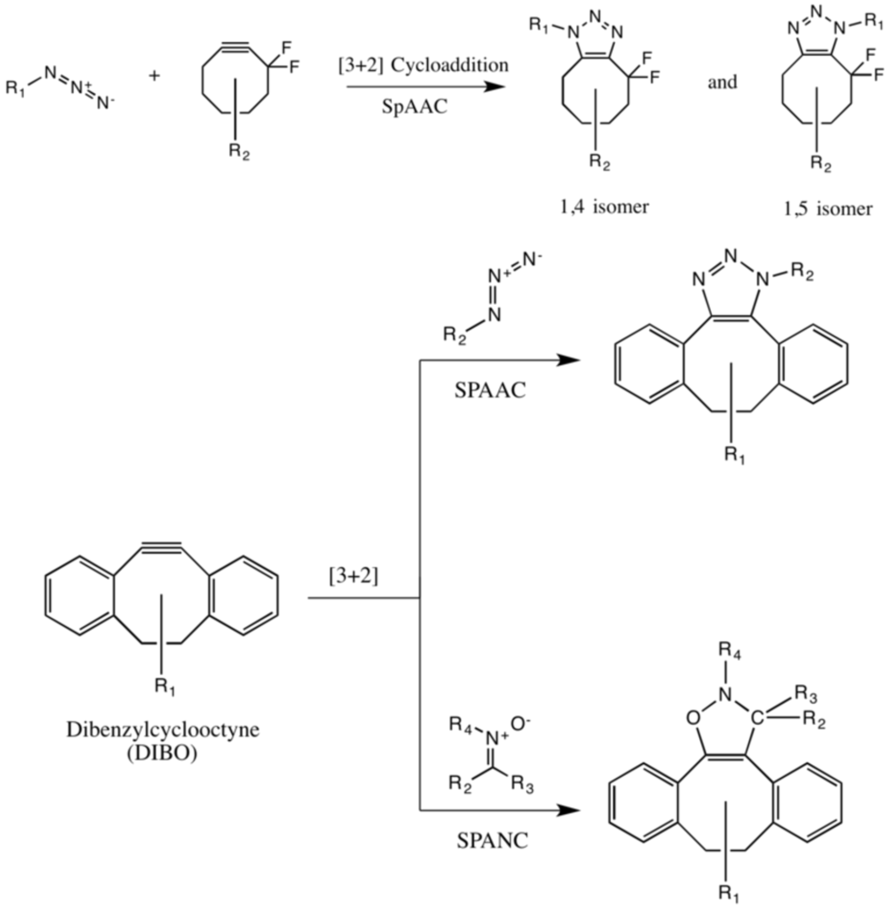

Figure 3.1.10.: Reactions schematic for Strain promoted Azide-Alkyne cycloaddition (SPAAC) and difference between [3+2] SPAAC and strain promoted alkyne-nitrone cycloaddition (SPANC)

c. Cycloadditions of unsaturated species, especially 1,3-dipolar cycloaddition reactions, like Diels-Alder family of transformations [34,35]
d. [4+1] cycloadditions between isonitriles (isocyanides) and tetrazines [36]

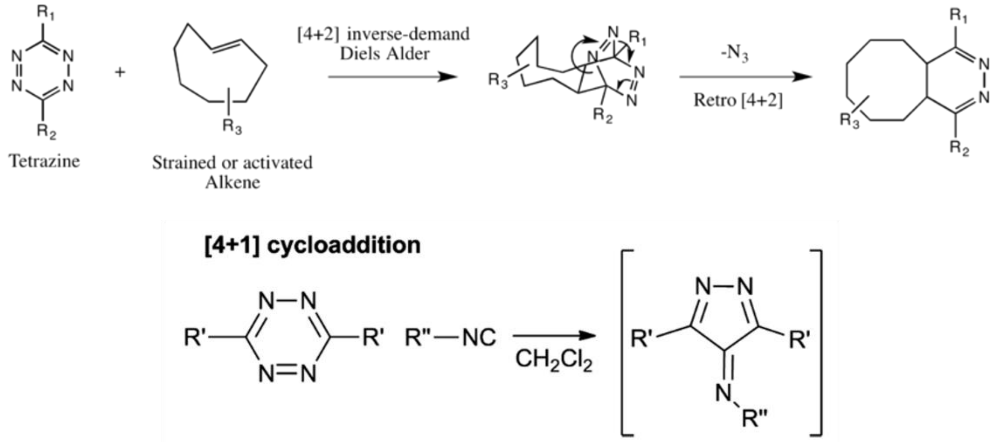

Figure 3.1.11.: Reactions schematic for [4+2] inverse demand Diels Alder, an example of such transformation along with [4+1] isonitrile cycloaddition.

e. Nucleophilic substitutions especially strained rings i.e., epoxy and aziridines [37]

f. Addition reactions to carbon-carbon double bonds such as dihydroxylation or the alkynes in the thiol-yne reaction [38,39]
g. Thiol-ene reaction [40]

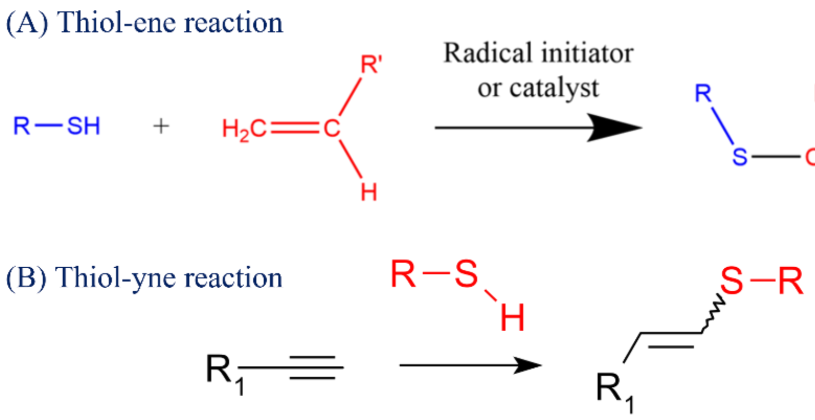

Figure 3.1.12.: Schematic for thiol-ene and thiol-yne reactions.

Click products are not only used for antibody conjugation but also for nucleic acids and exosomes, as well as for nanoparticle manipulation [41,42]. In recent years focusing on biological applications, CuAAC and SPAAC/SPANC chemistry along with thiol-ene/yne approach have been focused on [39,43,44]. As CuAAC reactions are generally catalysed via copper, raising concerns about their biocompatibility, for my project, I focused on SPAAC and thiol-yne reactions. As showcased in Fig. 3.1.13., different cycloalkyne products such as biarylazacyclooctynone (BARAC), aza-dibenzocyclooctyne (ADIBO or DIBO) or dibenzocyclooctyne (DIBAC commonly known as DBCO) and mono- and difluorinated cyclooctyne (MOFO or DIFO) have been research extensively that can be employed for various applications.

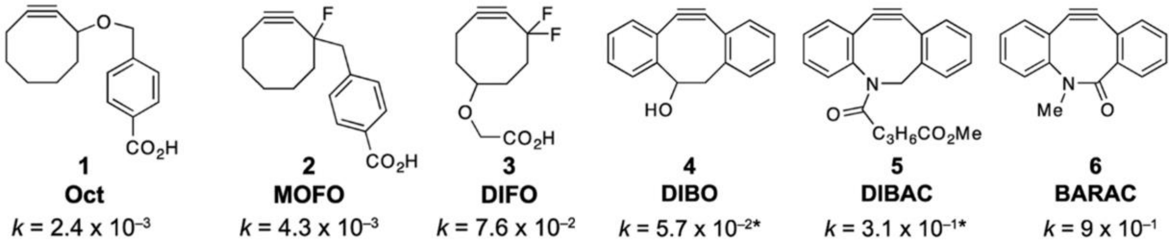

Figure 3.1.13.: Cyclo-alkynes with their second order rate constant used for click-based bio-conjugation. Oct: Cyclooctynes; MOFO: monofluorinated cyclooctyne; DIFO: difluorinated cyclooctyne; DIBO: aza-dibenzocyclooctyne ; DIBAC: dibenzoazacyclooctyne, precursor for DBCO: Dibenzocycloocytne; BARAC: biarylazacyclooctynone [45].

Based on their reaction rates: MOFO < DIBO <DIFO < DBCO/ADIBO < BARAC [45]. For cyclooctynes selection of our application, DBCO was opted due to stable product formation after reaction and conjugation and favourable reaction rates [39,43]. In addition, studies have focused on showcasing such cyclic compounds for bio-labelling, cell adhesion, spatial and temporal tissue monitoring, surface modification and so on [44,46–50].

Based on SPAAC and thiol-yne chemistry, DBCO has been identified by various research groups for different applications ranging from monolayer modifications for photoactivable surfaces [51] to site-selective acetylation for immunoglobulin modifications [52] to directed nanoparticle conjugation [53]. In addition, discrete libraries for polyethylene glycol (PEG) chains with SPAAC based functional groups have been exhibited to minimize non-specific interactions showcasing synthesis, assembly, and bioactivity [54]. Furthermore, nanomaterials for biological applications and self-assembled vesicle surfaces were showed using SPAAC based click chemistry [55,56].

Different groups have showcased the applications of SPAAC for biosensing applications. Gobbo and group presented modifying SPAAC chemistry for fabrication of versatile water- and organic solvent-soluble gold nanoparticles (AuNPs). X-ray photoelectron spectroscopy, nuclear magnetic resonance (NMR) and transmission electron microscopy (TEM) was performed for characterization as highlighted in Fig. 3.1.14. Reactivity towards interfacial SPAAC reaction was demonstrated by azide polymersomes as bioorthogonal reaction partners [53]. In addition, they further functionalized such nanoparticles with oligopeptides for a variety of applications in targeted cancer diagnosis and therapies [57].

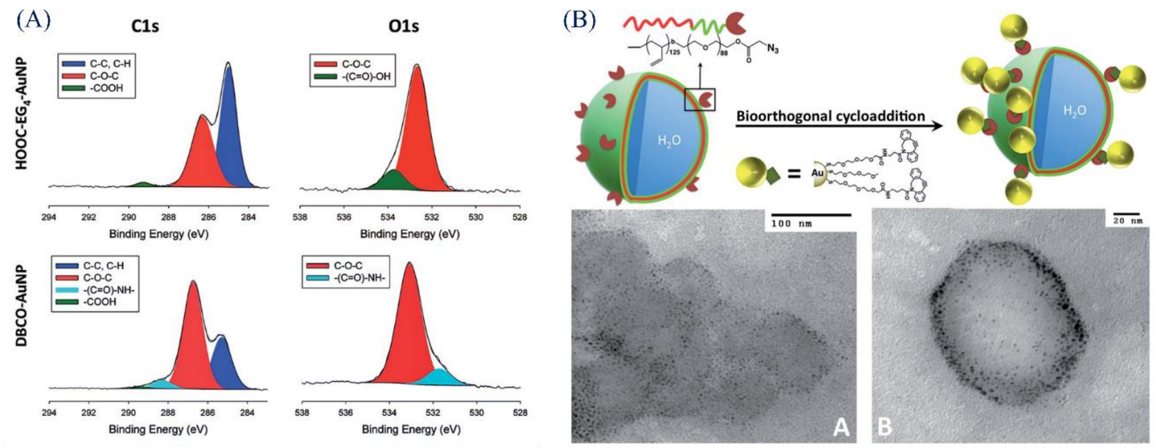

Figure 3.1.14.: **(A)** High-resolution C 1s and O 1s XPS spectra for HOOC–EG4– AuNPs and DBCO–AuNPs. **(B)** Top: a cartoon representing the I-SPAAC reaction between DBCO–AuNPs and azide-functionalized polymersomes. (A) TEM mage of the control experiments methyl-PEG-AuNP (Me–EG3–AuNP) + azide-functionalized polymersomes. (B) TEM image of vesicles covered with AuNPs through the I-SPAAC reaction [53].

Fan and group showcased the application of SPAAC chemistry for development of an electrochemical DNA (E-DNA)/aptamer biosensor for detection of DNAs and proteins using surface-anchored oligonucleotides on screen-printed oligonucleotides [58]. The conjugation was based on SPAAC chemistry, where (DBCO)-modified oligonucleotides were covalently conjugated to azide-terminated gold- plated screen-printed carbon electrodes as showcased in Fig. 3.1.15.

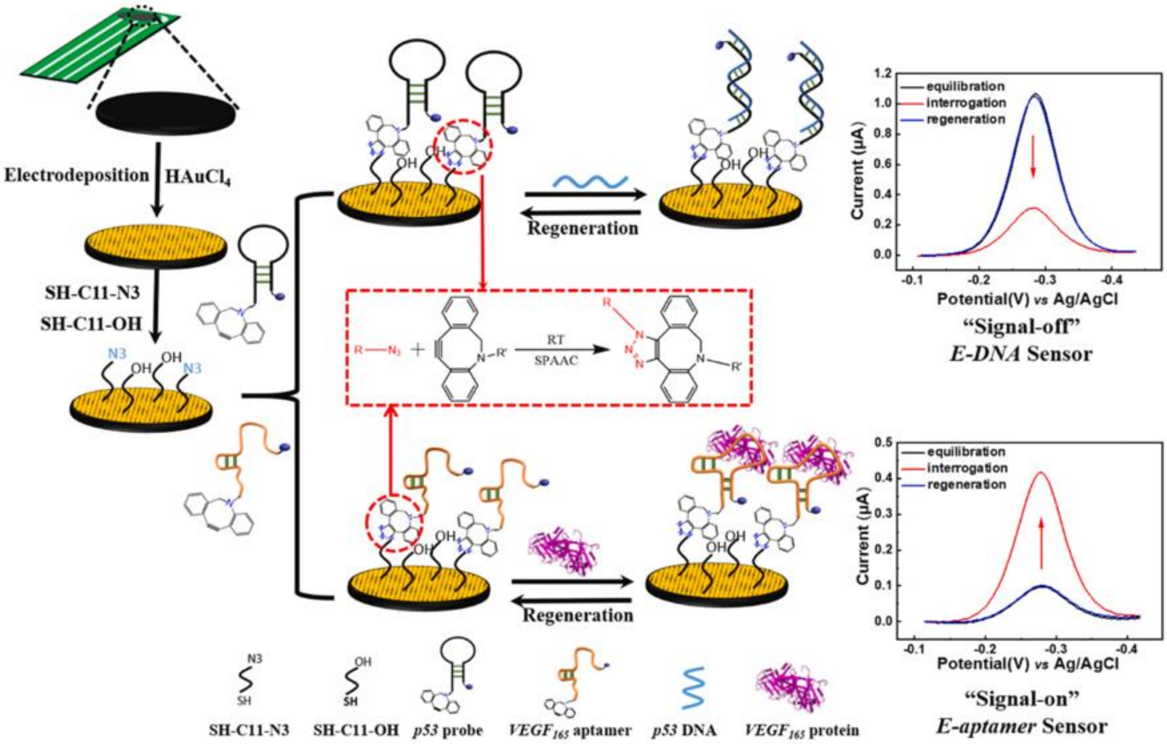

Figure 3.1.15.: Schematic illustration of E-DNA/aptamer sensors fabricated based on copper-free strain-promoted azide-alkyne cycloaddition (SPAAC) on the screen- printed carbon electrode (SPCE) [58].

In addition, different groups have showcased thiol-yne reaction using DBCO moieties for specific conjugation. Zhang and group presented a site-selective cysteine–cyclooctyne conjugation reaction between a seven-residue peptide tag (DBCO-tag, Leu-Cys-Tyr-Pro-Trp-Val-Tyr) at the N or C terminus of a peptide or protein and various aza-dibenzocyclooctyne (DBCO) reagents showcased in Fig. 3.1.16. Compared with a cysteine peptide control, DBCO tag increased rate of thiol–yne reaction 220-fold, enabling selective DBCO-tag conjugation to DBCO-linked fluorescent probes, affinity tags, and cytotoxic drug molecules. Fusion of DBCO-tag with the protein of interest enables regioselective cysteine modification on proteins that contain multiple endogenous cysteines like the antibody trastuzumab highlighted in Fig 3.1.20 [59].

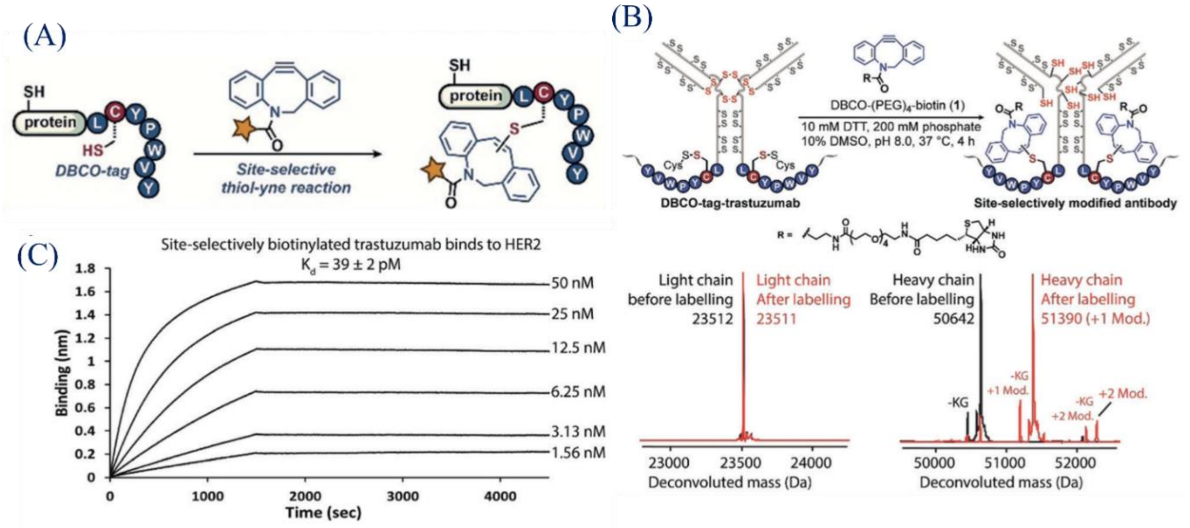

Figure 3.1.16.: **(A)** DBCO-tag enables site-selective thiol–yne reaction to modify the DBCO-tag cysteine in the presence of other competing cysteine residues on the same protein. DBCO-tag-enabled site-selective antibody labelling without impairing the protein-binding function. **(B)** Site-selective antibody modification using DBCO-tag. DBCO-tag was placed at the C terminus of antibody heavy chain. A small amount of C-terminal truncation (minus Lys-Gly) was present in the starting material and was labelled as "-KG". Reaction conditions: 100 µM DBCO-tag-trastuzumab, 2 mM 1, 0.2 M phosphate,10 mM DTT, pH 8.0, 10% DMSO, 37 ° C, 4hours. **(C)** Site-selectively biotinylated trastuzumab retains its binding affinity to recombinant HER2 in Octet BioLayer Interferometry assay. 20 µm site-selectively biotinylated DBCO-tag-trastuzumab was immobilized on the streptavidin biosensors and sampled with serially diluted concentrations of recombinant HER2 (concentrations shown next to each sensorgram) [59].

More so, another group focused on site-specific dual functionalization focusing on thiol-yne and SPAAC dual functionalization of cysteine residue in peptides and proteins with 2-Azidoacrylates specifically DBCO moieties as showcased in Fig. 3.1.17. [60]. Ariyasu and group showcased 2-azidoacrylates to perform site-specific dual functionalization of the cysteine residue of peptides and bovine serum albumin (BSA), a native protein containing one free cysteine residue. The sulfhydryl group of the cysteine residue was conjugated with 2-azidoacrylates bearing various functionalities, such as fluorescent dyes under physiological aqueous buffer conditions exhibited in Fig. 3.1.21, to afford peptide and protein conjugates anchoring an azide moiety. Successive azide– alkyne cycloaddition enables installation of the second functionality, thus affording dual-functionalized peptide- and protein- based materials [60].

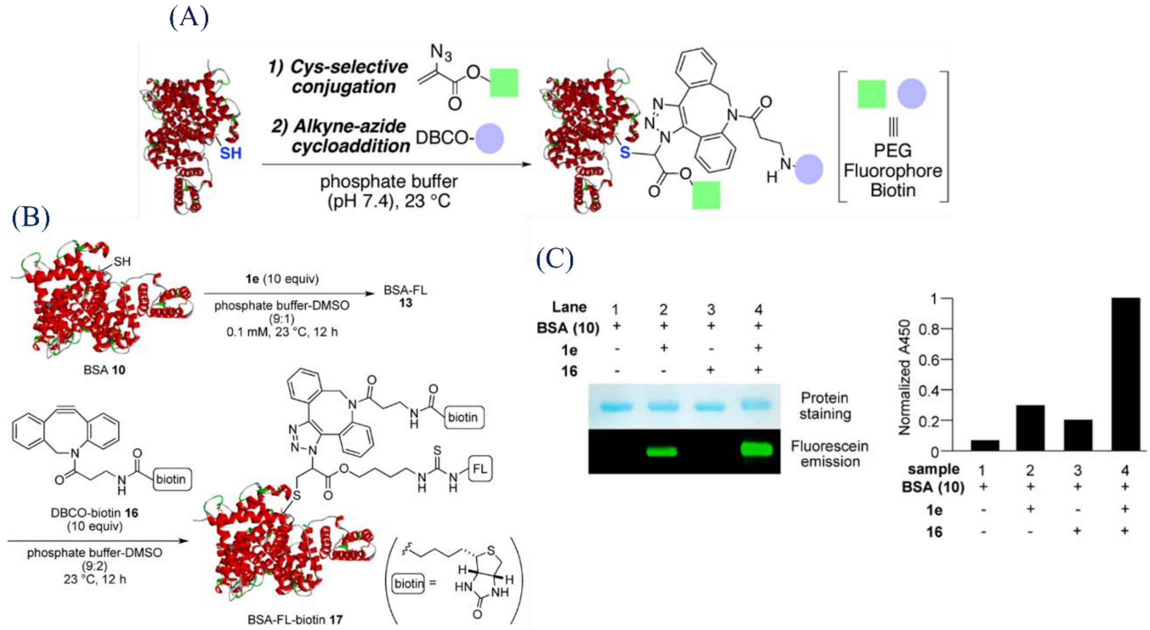

Figure 3.1.17.: **(A)** General schematic for the dual functionalization approach. **(B)** BSA-flurophore (BSA-FL 13) was applied for biotinylation using DBCO-biotin to prepare dual-functionalized BSA – FL – biotin 17. **(C)** In SDS-PAGE analysis, BSA – FL – biotin 17 exhibited green fluorescence originated from fluorescein. To confirm the successful incorporation of biotin, enzyme-linked immunosorbent assay (ELISA) of BSA – FL – biotin 17, and its control samples were conducted by using streptavidin-coated beads, anti-BSA-antibody, and horseradish peroxidase (HRP)-conjugated secondary antibody. **(C)** Only sample 4, containing BSA – FL – biotin, 17 exhibited significant HRP activity, suggesting that biotin moiety is incorporated into BSA through the dual functionalization. Because biotin itself does not bear fluorescence property, concise incorporation of another reporter moiety such as fluorescent dyes into biotinylated proteins would enable tracing target proteins [60].

As showcased from our literature review, site-specific, directed, and oriented conjugation can be performed for DBCO moieties via triazole formation with an azide moiety (-N_3/SPAAC) and thiol (-SH) group as presented in Fig. 3.1.18. For immobilization of antibodies on the DBCO functionalized surface, functional groups on the antibodies can be modified to present either -N_3 or -SH group for specific conjugation. Specifically such reactive groups (-SH and -N_3) can be presented by various modifications such as antibody fragmentation and glycosylated coupling on the antibody [39,40,56].

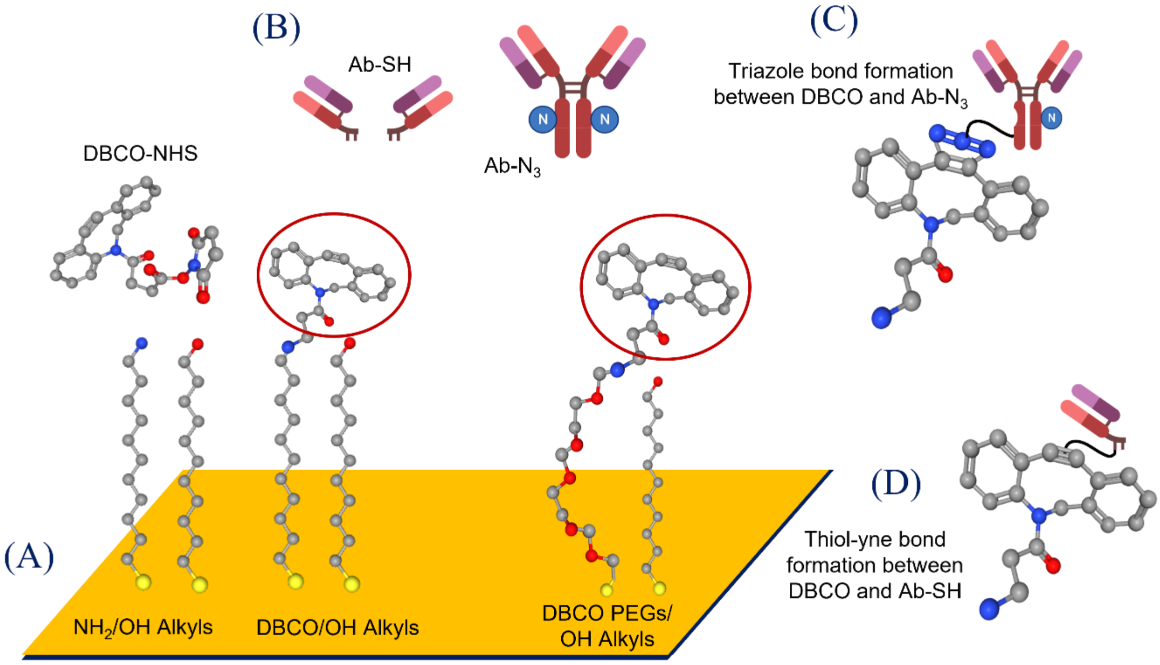

Figure 3.1.18.: **(A)** Monolayer formation with mixed NH2/OH Alkyls further activated to DBCO/OH Alkyls and direct functionalization of DBCO PEGs/OH Alkyls. **(B)** Ab-N$_3$ for DBCO-SPAAC conjugation and Ab-SH for DBCO-thiol-yne conjugation **(C)** Triazole formation for DBCO-Ab-N$_3$ conjugation **(D)** Thiol-yne bond formation between DBCO-Ab-SH.

For thiolated Ab-SH, fragmentation could be performed on the hinge of the disulphide bonds showcased in Fig. 3.1.19. by reducing the -S-S- bond to -SH bond. Hence, oriented antibody immobilization on DBCO via thiol-yne reaction can be initiated by fragmentation albeit it could be slow resulting in low yield [61].

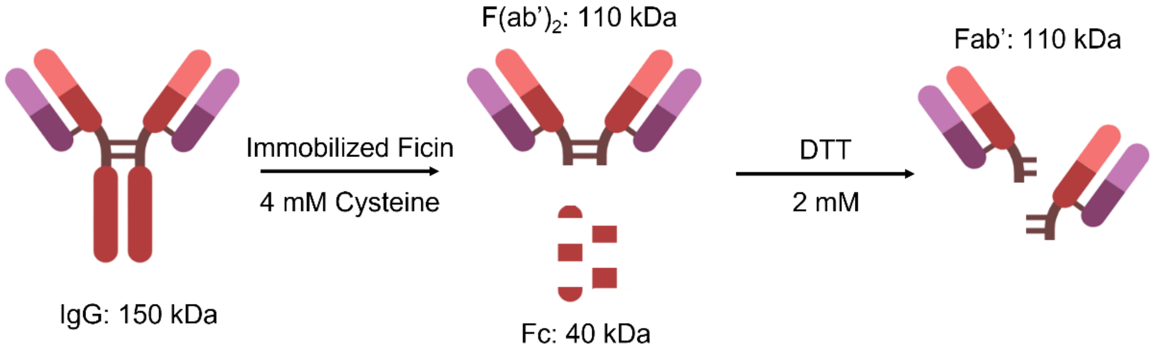

Figure 3.1.19.: Schematic for the fragmentation of IgG antibodies to F(ab')2 via immobilized ficin activity to Fab' fragments through dithiothreitol (DTT) activity at 2 mM concentration.

For triazole formation through azide (-N$_3$) activation for antibody immobilization in an oriented and site-specific manner. The introduction of -N$_3$ group on the antibody could be performed chemically or enzymatically. however enzymatic activation seems more prudent for keeping the biological activity of modified antibodies intact where glycosylation sites showcased in Fig. 3.1.2. can be exploited for site-specific conjugation. The use of several enzymes for enzymatic N$_3$ activation has been reported such as transaminase, MTGase or glycosyltransferase. Subsequently, a combination of galactosidase and galactosyltransferase is used to introduce modified GalNAz (N-azidoacetylgalactosamine) on the glycosylation sites of the antibodies, specifically keeping antigen binding site free for interaction highlighted in Fig. 3.1.20 [56].

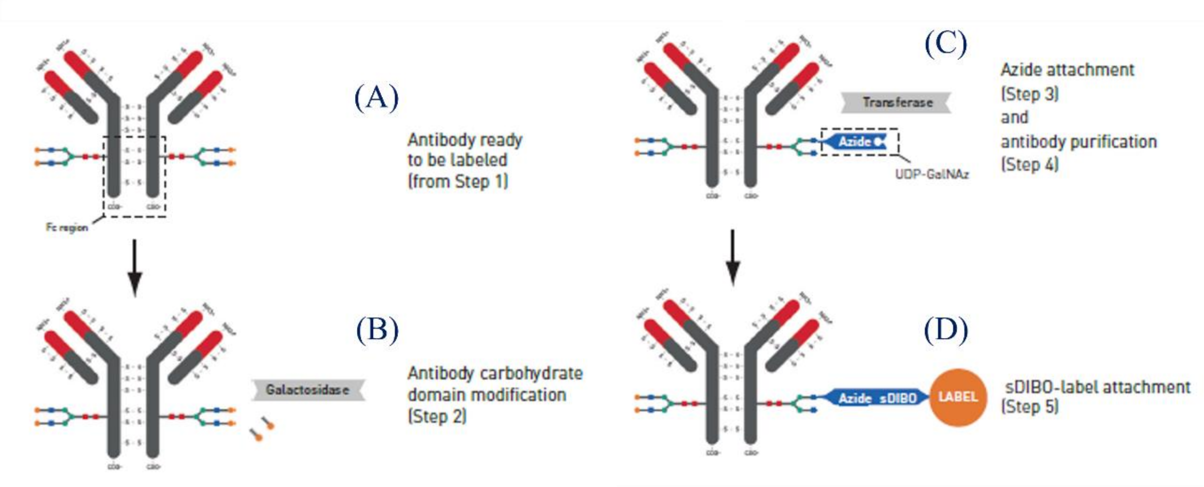

Figure 3.1.20.: Schematic for azide modification for IgG antibodies. **(A)** Non-modified IgG antibody highlighted with glycosylation sites **(B)** Enzymatic activity of galactosidase cleaving the galactosidase group with salicylic acid **(C)** Transferase activity which attaches azide group **(D)** Example of site-specific conjugation on antibodies with azide and DIBO moiety.

In addition, many efforts have been devoted for the unique antibody modification with azide group for drug coupling [27]. The following section will focus on the materials and methods highlighting the chemical and biological products used along with different physico-chemical techniques used for characterization and analysis.

3.3. Materials and Methods:

3.3.1. Chemicals:

1-Mercapto-11-undecanoic acid 95% (COOH-Alkyls-SH) 99%, 11 Amino 1- undecanethiol 99% (NH_2-Alkyls-SH), 11-Mercapto-1-undecanol 97% (OH-Alkyls-SH), N-hydroxysuccinimide 97% (NHS), N,N′ -diisopropyl-carbodiimide 98% (DIC), Ethanol 99.8%, tetrahydrofurane 99% (THF), dimethylsulfoxide 99.9% (DMSO), (S)-2-Aminobutane-1,4-dithiol hydrochloride 99% (DTBA), Acetone 99.5%, Dichloromethane 99.8% and Methanol 99.9% were purchased from Sigma-Aldrich. Dibenzocyclooctyne-N-hydroxysuccinimidyl ester >95% (DBCO-NHS) was purchased from Conju Probe LLC and Dibenzocycolctyne PEG thiol (DBCO-PEGs-SH), DBCO 2000PEG thiol (DBCO-PEGs 2k-SH) and OH PEG thiol (OH-PEGs 2k-SH) was purchased from Nanocs. The chemical structures of the monolayers and activation molecules have been presented in Fig. 3.2.1.

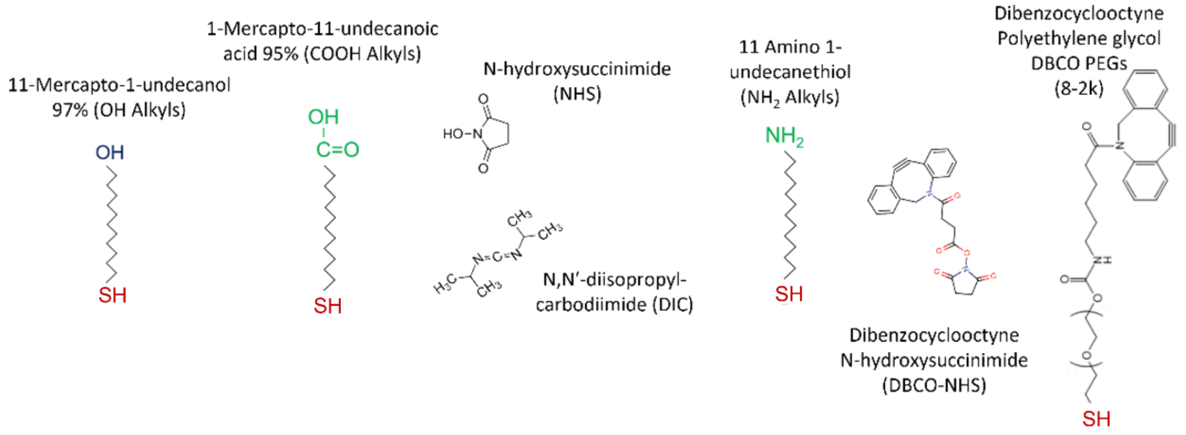

Figure 3.2.1.: Chemical structures of used for gold surface functionalization.

3.3.2. Biological Products:

EpCAM mouse Monoclonal Antibody (323/A3), ErbB2 mouse Monoclonal Antibody (N12), Urokinase mouse Monoclonal Antibody (U-16) and IgG1 Cross-Adsorbed Goat anti-Mouse were all purchased from Thermo Fisher. Phosphate Buffer Saline pH 7.4 (PBS) and Bovine Serum Albumin 98% (BSA) were purchased from Sigma-Aldrich while Tween® 20 was acquired from Carl Roth. Both Pierce™ F(ab')2 Preparation Kit (Fab') and SiteClick™ Antibody Azido Modification Kit (N_3) were purchased from Thermo Fisher. Interleukin-6 (IL-6), Mouse Anti-IL-6 antibody, Interleukin-8 (IL-8), Mouse Anti-IL-8 antibody, Tumour growth factor – beta (TGF-β) and Mouse Anti-TGF-β antibody were procured from Peprotech (a subsidiary of Thermo Fisher). Dulbercco's Modified Eagle Medium (DMEM) culture medium was procured from Gibco and was further modified by adding 1% Penicillin-Streptomycin to limit bacterial growth and 10% Fetal Bovine Serum (FBS).

3.3.3. Gold substrate preparation:

Leybold S.A. Electron Beam Physical Vapor Deposition (e-beam evaporation) Germany was used to prepare 200 nm Au substrates on glass slides with an adhesion layer of 5 nm chromium at Nanolyon platform. The deposition rate for the gold layer was around 1-2 Å/s. After solvent cleaning, Harrick plasma-O_2 USA was used at high radio frequency (RF) signal for 10 min for further cleaning the substrates. For SPRi analysis, bare SPRi-slides were acquired from Horiba Scientific France.

Before functionalization, gold substrates were washed with dichloromethane, acetone, and methanol for 10 min each under ultrasonic conditions. Ethanol and deionized water were used for further cleaning and then the surfaces were dried under nitrogen flow. Lastly, the substrates were cleaned with plasma-O_2.

3.3.4. Chemical functionalization of gold surfaces:

Mixed COOH/OH Alkyls monolayers were obtained by immersing clean gold substrate in 10 mM COOH-Alkyls-SH solution and 10 mM OH-Alkyls-SH solution (1:1 molar ratio) in degassed ethanol/water solution (95/5, v/v) as previously described by Palazon et al. [25]. The substrates were incubated over night at room temperature under dark conditions. Functionalized samples were then washed with ethanol/deionized water solution (95/5, v/v) for 2 × 5 min under sonication and then soaked in deionized water for 5 min before drying with nitrogen flow.

Mixed COOH/OH Alkyls surface was further activated with DIC/NHS prior to antibody immobilization to obtain the so-called “NHS/OH Alkyls” surface. Thus, mixed COOH/OH Alkyls samples were incubated with 100 mM DIC and 100 mM NHS in THF, overnight under dark condition at room temperature. They were washed in THF and Dichloromethane for 5 min each under sonication. Afterwards, soaking in deionized water for 5 min before drying with nitrogen flow.

Mixed NH_2/OH Alkyls monolayers were obtained by immersing clean gold substrate in 1 mM NH_2–Alkyls-SH solution and 1 mM OH-Alkyls-SH solution (1:1 molar ratio) in degassed ethanol solution. Incubation was done overnight under dark condition at room temperature. Functionalized samples were than washed with ethanol for 2 x 10 min under sonication and then soaked in deionized water for 5 min before drying with nitrogen flow.

Mixed NH_2/OH Alkyls functionalized gold surface was further incubated with 0.5 mM DBCO-NHS in DMSO, overnight under dark condition at room temperature to obtain the so-called “DBCO/OH Alkyls” surface. Afterwards, samples were washed with DMSO for 2 x 5 min and with methanol for 15 min under ultrasonic conditions before being dried with nitrogen flow.

Mixed DBCO PEGs/OH Alkyls monolayers were obtained by immersing clean gold substrate in 1 mM DBCO-PEGs-SH solution and 1mM OH-Alkyls-SH solution (- 1:1 molar ratio) in degassed ethanol solution. Incubation was done overnight under dark condition at room temperature. Functionalized samples were than washed with ethanol for 2 x 10 min under sonication and then soaked in deionized water for 5 min before drying with nitrogen flow.

Mixed DBCO/OH PEGs 2K monolayers were obtained by immersing clean gold substrate in DBCO-PEGs 2k-SH solution and OH-PEGs 2k-SH solution prepared in degassed ethanol. Various molar ratios were prepared as 1/0, 1/1 and 1/4 presented in Table 3.1.2. Incubation was done overnight under dark condition at room temperature. Functionalized samples were than washed with ethanol for 2 x 10 min under sonication and then soaked in deionized water for 5 min before drying with nitrogen flow.

Table 3.2.1.: Different surfaces for both C/NHS and DBCO surface chemistry highlighted with their respective functional monolayers and diluent monolayers along with the concentration used.

Surfaces	Functional monolayers (Conc.)	Diluent monolayers (Conc.)
C/NHS chemistry at INL/ECL		
Mixed COOH/OH Alkyls	COOH Alkyls: 10 mM	OH Alkyls: 10 mM
Mixed NHS/OH Alkyls	DIC: 100 mM	NHS: 100 mM
DBCO surfaces at INL/ECL		
Mixed NH_2/OH Alkyls	NH_2 Alkyls: 1 mM	OH Alkyls: 1 mM
Mixed DBCO/OH Alkyls	DBCO-NHS: 0.5 mM	
Mixed DBCO PEGs/ OH Alkyls	DBCO PEGs: 1 mM	OH Alkyls: 1 mM
DBCO PEGs surface chemistry at RMIT		
1/0 DBCO/OH PEGs 2k	DBCO PEGs 2k: 0.2 mM	OH PEGs 2k: 0 mM

1/1 DBCO/OH PEGs 2k	DBCO PEGs 2k: 0.1 mM	OH PEGs 2k: 0.1 mM
1/4 DBCO/OH PEGs 2k	DBCO PEGs 2k: 0.04 mM	OH PEGs 2k: 0.16 mM

3.3.5. Surface characterization of functionalized gold surfaces:

3.3.5.1. Contact angle (CA) goniometry:

Contact angle measurements were performed with GBX-Digidrop MCAT goniometer (France) at room temperature. Contact angles θ were measured from sessile deionized water drops of 1 µL using the Visiodrop software. The sessile drop method is used for the solid-liquid surface energy characterization and analyses the wettability of a solid substrate with a liquid droplet. The solid-gas γ_{sv}, liquid-solid γ_{sl} and gas-liquid γ_{lv} interfaces are calculated for contact angle θ measurements as highlighted in Fig. 3.2.2. At least five measurements were performed for each sample and the averages was calculated.

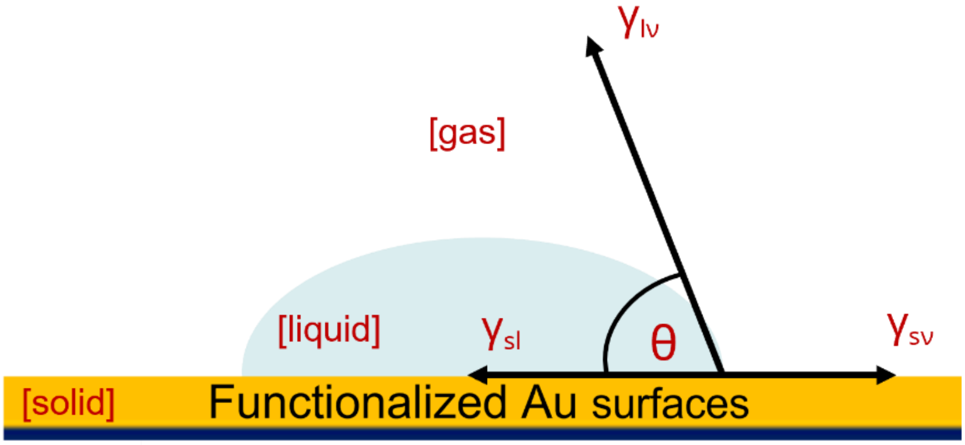

Figure 3.2.2.: Contact angle measurements highlighting θ for different surfaces where solid-gas γ_{sv}, liquid-solid γ_{sl} and gas-liquid γ_{lv} interfaces are presented.

3.3.5.2. Atomic force microscopy (AFM):

The surface thickness and topography images were collected using a Bruker Dimension Icon AFM using “Scanasyst-air” AFM tips. NanoScope® 1.8 and Gwyddion®-2.61 software was used for image processing and analysis. SCM PIT V2 (resonance frequency 75 kHz, spring constant 3 N/m, radius ~25 nm) coated conductive AFM tip was used to obtain topographical scans for mixed DBCO PEGs 2k functionalized surfaces. AFM scan size of 500 nm x 500 nm and 2 µm x 2 µm were measured in contact mode by applying AC signal (driving excitation) to the conductive AFM tip with a frequency of 15 kHz, chosen to be far away from the cantilever resonance frequency (330 kHz). For measurement of resulting vertical deflection of the cantilever, a lock-in amplifier was used, which was reflected in the final output as amplitude and phase change during AFM imaging. Hardware gain of x16 was used to enhance amplitude response signal during scanning and to assure accuracy and reliability of our measurements, the same AFM instrument and techniques were used as standard reference [62].

3.3.5.3. Polarization Modulation Infrared Adsorption Spectroscopy (PM-IRRAS):

Polarization-modulation infrared reflection-adsorption spectroscopy (PM-IRRAS) was performed using Nicolet 6700 FTIR spectrometer from Thermo Scientific the wavenumber of optimum detection was set at 2000 cm^{-1}. All the spectra were acquired at resolution of 4 cm^{-1} and for optimum sensitivity for Au samples, the angle of incidence was set at 85° . Further spectral analysis was performed with the TQ Analyst software and Origin 9.6.5. For all the substrates (clean Au surfaces, monolayer functionalized Au substrates), the baseline correction was done for the whole scan (4000-800 cm^{-1}). This was corrected every time by a spline line fitted on the regions, where no peak should be expected dividing it with the experimental spectrum. Spectra were plotted as normalized differential reflectivity according to the cubic spline fitting.

3.3.5.4. X-ray Photoelectron Spectroscopy (XPS):

Four samples clean Au surface, mixed NH_2/OH Alkyls, mixed DBCO/OH Alkyls and mixed DBCO PEGs/OH Alkyls were characterized at INL NanoLyon platform. X-ray photoelectron spectroscopy analyses were conducted in a vacuumized chamber equipped with a PREVAC EA15 Poland hemispherical deflection analyser-VSW spectrometer having a focused mono-chromatized X-ray source (Al Kα 1486.6 eV). The chamber pressure was kept at 10^{-8} Torr and the angle between the detector and the incident beam was at the magic angle. The takeoff angle was first 90° relative to the substrate surface and then 60° to have resolved peaks. The angular resolution was kept at 3° and the energetic resolution was 0.2 eV. The surface sensitivity for characterization through XPS is < 4 nm. Analysis of the spectra was performed initially with PREVAC software 'Spectrum' and then with CasaXPS software and Origin 9.6.5. C-C, C-H binding energy was set at 285 eV. Five different species were focused: Au4f, S2p, C1s, O1s and N1s. A Shirley background was subtracted from all the species of interest when coming from the bulk elements. The peaks were fitted by a Gauss-Lorentz curve.

Mixed DBCO PEGs 2k monolayers (molar ratios 1:0, 1:1 and 1:4) were characterized at RMIT facilities through angle resolved XPS (ARXPS). Kratos Axis Supra equipped with a monochromated dual Al Kα & Ag Lα X-ray source was employed. X-ray source power was 90 W for both sources (15 KV, 6 mA). Electron-only charge neutralisation was used with a bias of 1.3 V and current of 0.37 A. The pass energy was set to 80 eV & energy step size was 0.1 eV. 15 sweeps of 100 ms dwell time per energy step were used for spectra collected with the Al Kα source. This was increased to 100 sweeps for spectra collected with the Ag Lα source. The FWHM of an Ag $3d_{5/2}$ peak from an ion sputter-cleaned Ag standard was 1.2 eV when measured using either X-ray source at a pass energy of 80 eV.

ARXPS is a technique for non-destructive depth-dependent chemical analysis within the first few nanometres of a sample [63]. The principle focuses on electron emission from an atom on a comparatively flat sample at z-depth that should be transported through z/cos(θ) distance of material. Angle between the detector (referred as take-off angle) and normal to the sample surface is considered as θ. Photoelectron attenuation is increased based on path length to the vacuum at higher emission angle at larger depths, characterizing depth resolution.

The peak intensity from a given element & orbital can be described by,

$$I = \int_0^\infty I_0 \, c(z) \, e^{\frac{z}{\lambda \cos \theta}} \, dz \tag{1}$$

Concentration as a function of z is $c(z)$, attenuation length is λ and unattenuated intensity of photoelectrons is I_0. Based off this equation, angle-resolved peak intensity can be calculated if $c(z)$ is known.

3.3.5.5. Data Analysis for ARXPS:

Regularized ARXPS algorithms are performed by minimization of a quantity, Q, where:

$$Q = \chi^2 + \alpha R \tag{2}$$

X^2 is the difference between measured concentration and the calculated concentration at each angle calculated by equation (1) using an initial 'assumed' $c(z)$.

$$\chi^2 = \sum_{j=A}^{N} \sum_{k=1}^{N} \frac{(c_{meas} - c_{calc})^2}{\sigma^2} \tag{3}$$

X^2 is summed over j elements & k angles. σ^2 is the variance in each of the measured data points, representing the error in the experimental measurements. The goal of the algorithm is to alter $c(z)$, such that χ^2 approaches zero, indicating that $c(z)$ represents a concentration depth profile consistent with the experimental ARXPS measurements. In the MS Excel files (used with permission from Dr. Billy Murdoch, original proprietor of the software at RMIT Microscopy and Microanalysis Facility at RMIT, Melbourne), the total z range is separated into 'slabs' of thickness i, which serves as the step size of $c(z)$.

R is the regularization term and is used to penalize overfitting of the ARXPS data to ensure that non-physical features, such as spikes or noise, are not observed in the optimized $c(z)$. Tikhonov regularization uses a linear term such as the *squared concentration* $\int_0^\infty c(z)^2\,dz$ or squared concentration gradient $\int_0^\infty \left(\frac{dc(z)}{dz}\right)^2 dz$.

α is a Lagrange multiplier, used to control the degree to which the overfitting of X^2 is suppressed by the regularization term. If α is too small, then overfitting is likely to occur. However, if α is too large then $c(z)$ will not agree with the experimental data. The optimization of α is discussed below. Ideally, optimization of α should have unbiased criterion. One of the previously used methods is the S-curve method [64]. It is an approach where χ^2 value is minimised by varying α. The minimum χ^2 value is observed where log(α) is between -14 and -10 ($\alpha = 1 \times 10^{-4} - 1 \times 10^{-6}$). Overfitting can happen when X^2 increases slightly below this α range, as model complexity increases. For our simulations, *RMMF ARXPS DP Modelling* was used for assessment of α value appropriateness.

Squared concentration gradient was chosen for regularization as general regularization penalizes $c(z)$ spikes to a lesser degree compared to Tikhonov methods. Total concentration of each element is penalized because of the Tikhonov regularization terms, $\int_0^\infty c(z)^2\,dz$ which forces $c(z)$ towards zero as z approaches the bulk. This can lead to anomalies in $c(z)$ when substrates are included in the analysis. Therefore, following is the most stable algorithm based on what has been discussed above:

$$Q = \chi^2 + \alpha \int \left(\frac{dc(z)}{dz}\right)^2 dz \tag{4}$$

Compared to the squared concentration gradient, squared concentration has been found to be a superior regularization term for analysis of discrete layers [65]. However, if a single optimization term is to be used for all elements in all layers, the squared concentration gradient will be the best choice.

3.3.6. Antibody immobilization for functionalized gold surfaces:

Mouse IgG1 monoclonal antibodies (323/A3, N12 and U-16) were pooled and the concentration was set at 0.7 mg/mL. Mouse IgG1 Fab fragment (Ab-SH) was generated using Pierce™ F(ab')$_2$ Preparation Kit (SH) followed by reduction through 2 mM DTBA solution for Ab-SH. F(ab')$_2$ fragments were incubated between 2-3 hours with DTBA solution. Afterwards, the solution was filtered through 3K Nanosep ultracentrifugation tubes and the filtrate was stored and kept at 4° C before immobilization. Azide-modified mouse IgG1 antibody (Ab-N_3) was obtained using SiteClick™ Antibody Azido Modification Kit and was stored and kept at 4° C before immobilization.

For CTC-associated IL-6, IL-8 and TGF-β biomarker sensing, anti-IL-6, anti-IL-8 and anti-TGF-β antibodies were activated through SiteClick™ Antibody Azido Modification Kit and was stored and kept at 4° C until immobilization. The final concentration after activation was as follows: Anti-IL-6: 1.01 mg/mL, Anti-IL-8: 0.08 mg/mL and Anti-TGF-β: 0.75 mg/mL.

Non-modified mouse IgG1 antibodies (Ab), mouse IgG1 Fab fragments (Ab-SH) and azide-modified mouse IgG1 antibodies (Ab-N_3) were spotted onto the different functionalized gold surfaces using Scienion sciFLEXARRAYER S3 (Germany). The spotting map consisted of four arrays 2x2 spots composed of PBS1X spot (negative control), Ab, Ab-SH and Ab-N_3. The spot volume was around 10 nL for each species and the immobilization was carried out by incubation for 2h at RT in humidified atmosphere (around 75-80% humidity). The spotted surfaces were washed with 1X PBS for 2 x 5 min and with 0.1% Tween – 1X PBS for 5 min. Surface passivation was performed with 4% (w/v) bovine serum albumin (BSA) in 1X PBS for 30 min and afterwards, rinsing with 0.1 % Tween – 1X PBS for 2 x 5 min and with 1X PBS for 5 min.

For biomarker sensing, like above, 2x2 spotting array was composed of PBS1x spot (negative control), Anti-IL-6, Anti-IL-8 and Anti-TGF-β. Similar spot volume of 10 nL was incubated for 2h at RT in humidified atmosphere (around 75-80% humidity). Similar washing protocol was followed.

3.3.6.1. Surface plasmon resonance imaging (SPRi):

SPRi analysis was performed on the Horiba Scientific OpenPlex system using accompanied fluidic kit with degasser and peristaltic pump at 12.5 µL/min. The running buffer for the system was PBS1X. For data acquisition, the system acquires on average 20 images/min (1 image/3 sec) and the SPR signal was converted to normalized percentage change in reflectivity by using 10X PBS solution. Polyclonal goat anti-mouse IgG was selected as target to analyse immobilization efficiency of spotted antibodies. Following target interaction, 10-20 mM HCl solution in PBS 1X was used to regenerate the surface and to restore the signal back to the baseline of the running buffer. As a control for non-specific target interaction response, glucose oxidase solution at 16 µg/mL was used to create a noise baseline and standard deviation (SD) to showcase the specificity of the. Signal regeneration was performed by injecting 20 mM HCl solution in the running PBS1X buffer.

For associated biomarker sensing of CTC (IL-6, IL-8 and TGF-β) modified DMEM cancer cell culture medium was used as running buffer. For initial characterization of immobilized antibodies, polyclonal goat anti-mouse IgG was injected and for surface regeneration, 50 mM HCl solution in running buffer was used. Afterwards for characterization, highest concentration of IL-6 and TGF-β at 5.7 µg/mL and IL-8 at 2.9 µg/mL was injected. Polyclonal antibodies injection was used as confirmation of antibody immobilization and viability on the surface after regeneration. For SPRi signal analysis, ImageJ-Fiji software and Origin 9.6.5 was used.

3.4. Results and Discussions:

For generation of functional DBCO monolayers on gold surfaces, two different approaches were employed. On one hand, a two-step approach using NH_2 terminated alkyl molecules mixed with OH Alkyls diluent (NH_2/OH Alkyls) were functionalized and subsequently activated to DBCO/OH Alkyls via DBCO-NHS as highlighted in Fig. 3.1.22. On the other hand, direct functionalization of DBCO terminated PEGs chains showcased in Fig. 3.1.22. were focused on for minimizing undesired interactions and creating brush coating on the surface showcasing anti-fouling properties [16,19,21]. Comparative analysis was performed between these two DBCO approaches vs bare gold surface and conventional carbodiimide/NHS chemistry, for which COOH terminated Alkyls mixed with OH Alkyls diluent (COOH/OH Alkyls) were functionalized and activated to NHS/OH Alkyls via DIC/NHS exhibited in Fig. 3.1.7.

In addition, for an optimal functionalization approach, comparative analysis between different spacing ratios was performed i.e., 1/0, 1/1 and 1/4 for the optimal surface functionalization. More so, to confirm biosensing efficiency of immobilized antibodies, non-modified Ab, fragmented Ab-SH, and azide activated Ab-N_3 were attached on the functionalized surfaces presented in Fig. 3.1.3., where their binding kinetics were analysed. Comparative immobilization analysis between DBCO and C/NHS surfaces was further highlighted focusing on S/N between specific and non-specific interactions, protein surface coverage and reaction kinetics. Following selection of the optimal functionalization and immobilization approach, characterization was showcased for sensing cancer biomarkers via conventional SPRi setup.

3.4.1. Physico-chemical characterization of gold functionalized surfaces:

3.4.1.1. Contact Angle characterization:

For initial surface characterization, contact angle (CA) measurements were performed as shown in Table 3.3.1. for both DBCO and C/NHS surfaces. CA measurements provided an avenue for rapid confirmation of surface functionalization. Analysis of surface wettability with functional groups such as -COOH, -NHS, -NH_2, and -DBCO for different surfaces could be confirmed by contact angle variations corresponding to hydrophilic and/or hydrophobic characteristic. More so, increase or decrease in CA measurements after surface activation could indicate changes in surface modification on the top layer.

Table 3.3.1.: CA measurements for C/NHS (mixed COOH/OH Alkyls and NHS/OH Alkyls) and SPAAC (mixed NH_2/OH Alkyls, activated DBCO/OH Alkyls and mixed DBCO PEGs/OH Alkyls) surface chemistry with bare Au substrate as a reference for rapid qualitative marker. Standard deviation measurements were performed by doing quintuplicates on each surface.

Surfaces	**CA° ± S.D.**
Clean Au substrates	1.8° ± 0.4
C/NHS at INL/ECL	
Mixed COOH/OH Alkyls	38.9° ± 5.2
Mixed NHS/OH Alkyls	43.4° ± 2.6
DBCO at INL/ECL	
Mixed NH_2/OH Alkyls	41.2° ± 0.9
Mixed DBCO/OH Alkyls	49° ± 0.9
Mixed DBCO PEGs/OH Alkyls	58.6° ± 1.1
Spacing ratios: DBCO/OH PEGs at RMIT	
Clean Au substrates	66.3° ± 5.8
1/0	39.6° ± 2.6
1/1	38.2° ± 3.4
1/4	38.6° ± 2.8

For clean Au samples, CA measurements were between 0° and 5° for surfaces developed at INL/ECL, indicating high hydrophilic nature of fresh clean gold surface. For C/NHS surfaces, compared with clean bare Au, increase of around 40° was observed after COOH/OH Alkyls functionalization showcasing decreasing hydrophilic nature due to presence of organic components such as alkylated chain on the interface. After activation to mixed NHS/OH Alkyls, similar contact angles were analysed with no significant difference observable between different functional groups as highlighted by previously published data from our group [25].

For DBCO surfaces characterized at INL/ECL showcased in Table 3.3.1., mixed DBCO/OH Alkyls were generated via activation of NH_2/OH Alkyls through DBCO-NHS. Compared with clean bare Au, increase of around 40° in contact angle was observed for NH_2/OH Alkyls indicating modification on the surface interface. And after activation to DBCO/OH Alkyls, CA increased significantly to around 50° which could be attributed to DBCO presence. For DBCO PEGs/OH Alkyls, increase of around 60° was measured, which could be due to the presence of both alkylated and PEGylated chains as well as DBCO/OH functional groups on the interface. Similar contact angle measurements for PEGylated chains were observed for previously published data [66–68].

Contact angle measurements performed at RMIT were focused on different spacing ratios between DBCO/OH PEGs 2k highlighted in Table 3.3.1. For clean Au surfaces, CA of around 66.3° was observed unlike gold surfaces being fabricated at INL/ECL. For both gold surfaces, E-beam deposition were used however this difference could be attributed due to different machines, protocols, thickness, and recipes being used. Similar CA for bare Au surface was observed for Al-

Ani and group and their published data [66]. This could be due to surface roughness which could be characterized using atomic force microscopy explained in detail in the following section.

Different spacing ratios of 1/0, 1/1 and ¼ between DBCO PEGs 2k as functional monolayer and OH PEGs 2k as diluent were characterized having PEG chain length between 30-40 C-O-C moieties. CA measurements become more hydrophilic when functionalized with DBCO/OH PEGs 2k as 1/0, 1/1 and ¼ spacing ratio compared with clean Au surface (~66°). However, no significant difference was observed between such spacing ratios where the CA was between 38° to 39° .

In conclusion, for CA measurements performed at INL/ECL, significant difference in CA were observed between clean bare Au surfaces and C/NHS surfaces as well as DBCO based surfaces. Similar observations were concluded from CA measurements performed at RMIT. Difference between CA of clean bare Au at INL/ECL and RMIT could be due to the different parameters employed for fabrication of thin gold films. However, significant difference after functionalization for all the surfaces signal surface modification that could indicate the presence of monolayers that have to be quantitatively characterized using infrared and x-ray photoelectron spectroscopy.

3.4.1.2. AFM analysis of DBCO/OH PEGs surfaces:

AFM characterization provides topographical information on surface roughness, density, and depth profile for different DBCO/OH PEGs 2k spacing ratio highlighted in Fig. 3.3.1. This was performed to understand significant difference between CA measurements of clean Au films fabricated at INL/ECL and RMIT and to further characterize the spacing ratios.

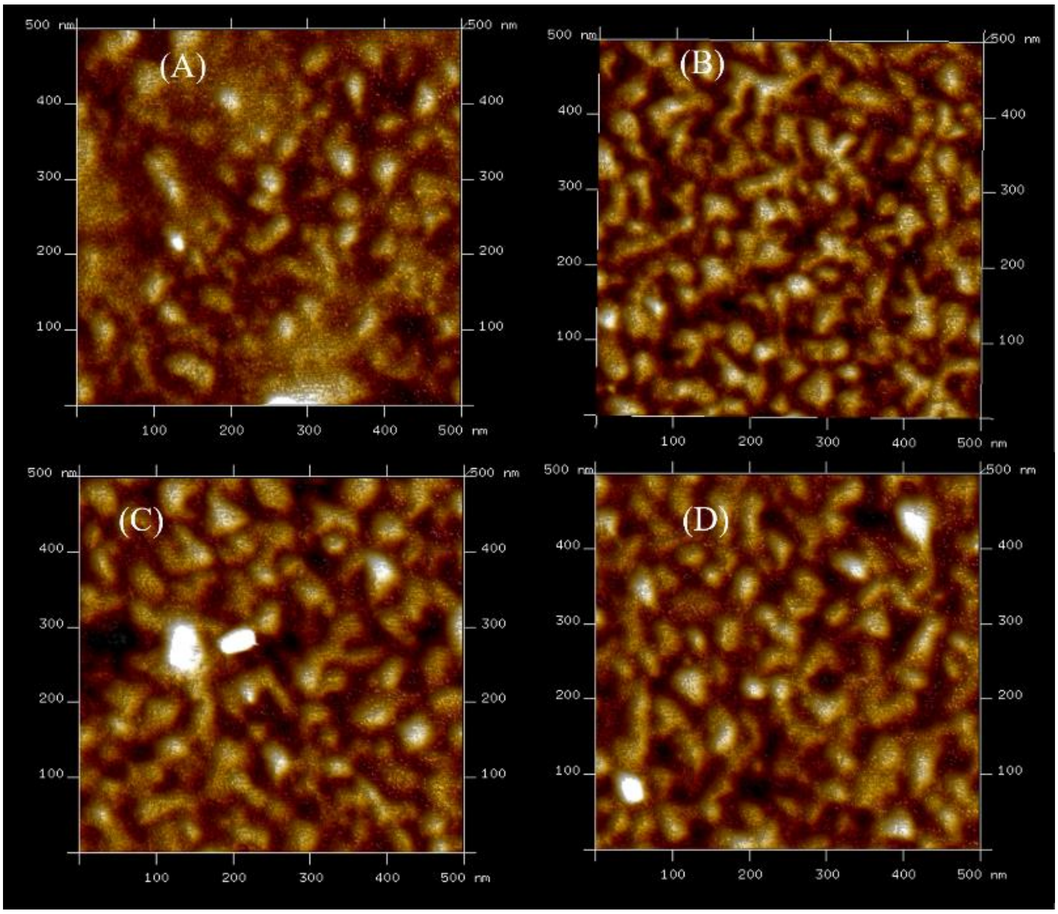

Figure 3.3.1.: Atomic force microscopy of **(A)** clean Au surface and different spacer ratios **(B)** 1/0, **(C)** 1/1 and **(D)** ¼ for DBCO/OH PEGs after monolayer functionalization.

In addition to surface roughness, depth profile was analysed focusing on max roughness R_{max} and image surface area difference. Results for R_{max} and surface area difference are compiled in Table 3.3.2.

Table 3.3.2.: Atomic force microscopy (AFM) of different spacer ratios 1/0, 1/1 and 1/4 for DBCO/OH PEGs. Surface roughness parameters i.e., roughness R_{max}, and image surface area difference were considered.

Surface	Surface area difference	Roughness R_{max}
Clean Au	2.18%	9.11 nm
1/0 DBCO/OH PEGs 2k	0.96%	6.53 nm
1/1 DBCO/OH PEGs 2k	0.58%	5.79 nm
1/4 DBCO/OH PEGs 2k	0.51%	5.56 nm

Compared with clean Au surface, significant decrease in roughness parameters can be observed for DBCO/OH PEGs 2k after functionalization, which can be further confirmed from Fig. 3.3.1. Between spacing ratios, slight decrease in Rmax and area difference is highlighted which could be due to the presence of diluents for 1/1 and 1/4 DBCO/OH PEGs 2k. This is further showcased in Fig. 3.3.2. for comparative depth profile between spacing ratios.

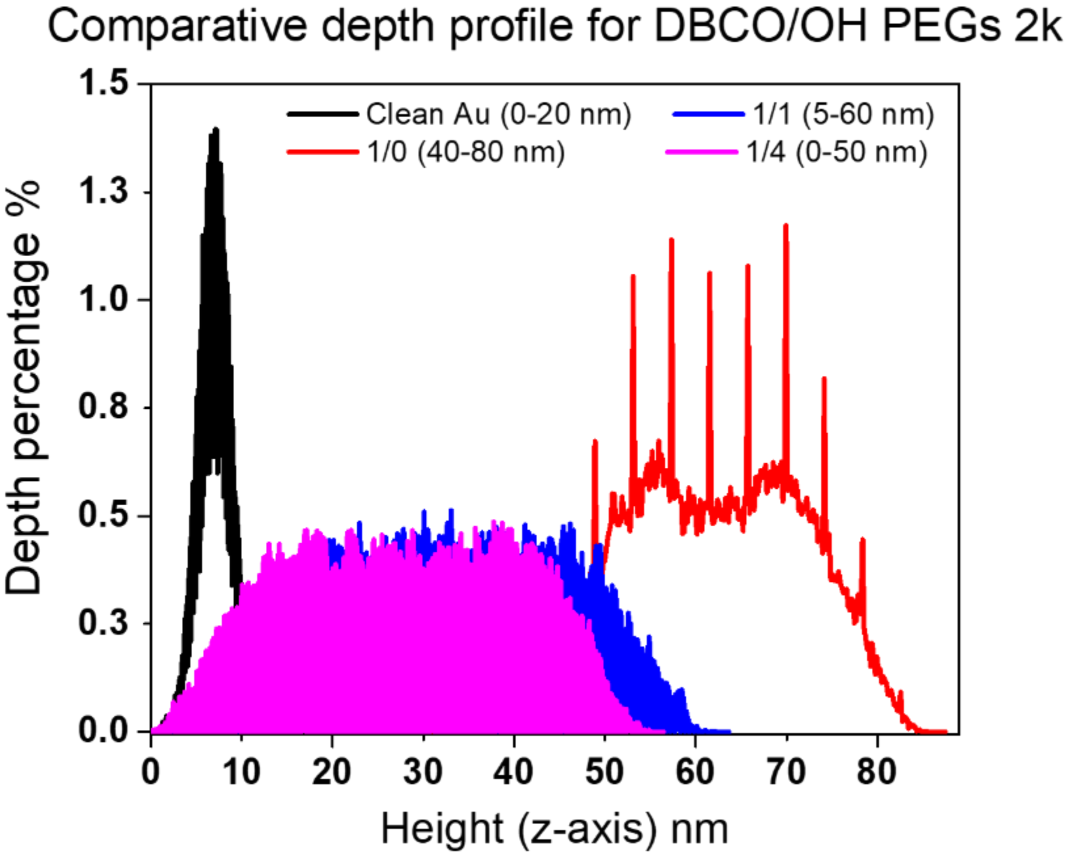

Figure 3.3.2.: Atomic force microscopy histogram of measurements of brush heights for clean Au and DBCO/OH PEGs 2k spacing ratios. The tip is pushed through the brush until it contacts the hard surface.

The effect for the presence of diluents can be exhibited from comparative depth profilometry performed for bare clean Au and DBCO/OH PEGs 2k spacing ratios. As highlighted in Fig. 3.3.2., the histograms of depth percentage significantly varied before and after monolayer functionalization and significant difference could be observed with the presence of diluents as highlighted for 1/1 and 1/4 spacing ratios. This further qualitatively confirmed the presence of monolayer formation and further difference between spacing ratios (1/0: where no diluent was mixed, 1/1: equal part functional and diluent were functionalized, 1/4: where one-part functional moiety and 4-part diluents were functionalized). In addition, between 1/1 and 1/4, no significant difference in histogram distribution was evident.

In conclusion, AFM characterization provided information regarding surface roughness and qualitative depth profilometry. Increased surface roughness for clean Au surface could indicate the increase CA measurement between Au surfaces fabricated at INL/ECL and RMIT. In addition, comparative analysis between clean Au surface and DBCO/OH PEGs 2k spacing ratio indicate qualitative confirmation of monolayer formation. More so, significant difference between histogram distribution of depth profile between 1/0 and 1/1 and 1/4 showcased the effect of the presence of diluent on the functionalized monolayers. However, quantitative characterization needs to be performed through spectroscopic methods.

3.4.1.3. Surface chemical characterization through PM-IRRAS analysis:

Polarization-Modulation Infrared Adsorption spectroscopy (PM-IRRAS) is a quantitative method for the characterization of thin films or monolayer functionalization on substrates, with high surface sensitivity. In addition to the conventional IR spectroscopy, analysis through PM-IRRAS, modulated reflectivity is independent of the isotropic adsorption from gas and water in the atmosphere explained above. PM-IRRAS characterization was performed for C/NHS surfaces and compared with the clean Au surfaces, where no significant peaks for specific functional groups were observed as highlighted in Fig. 3.3.3.

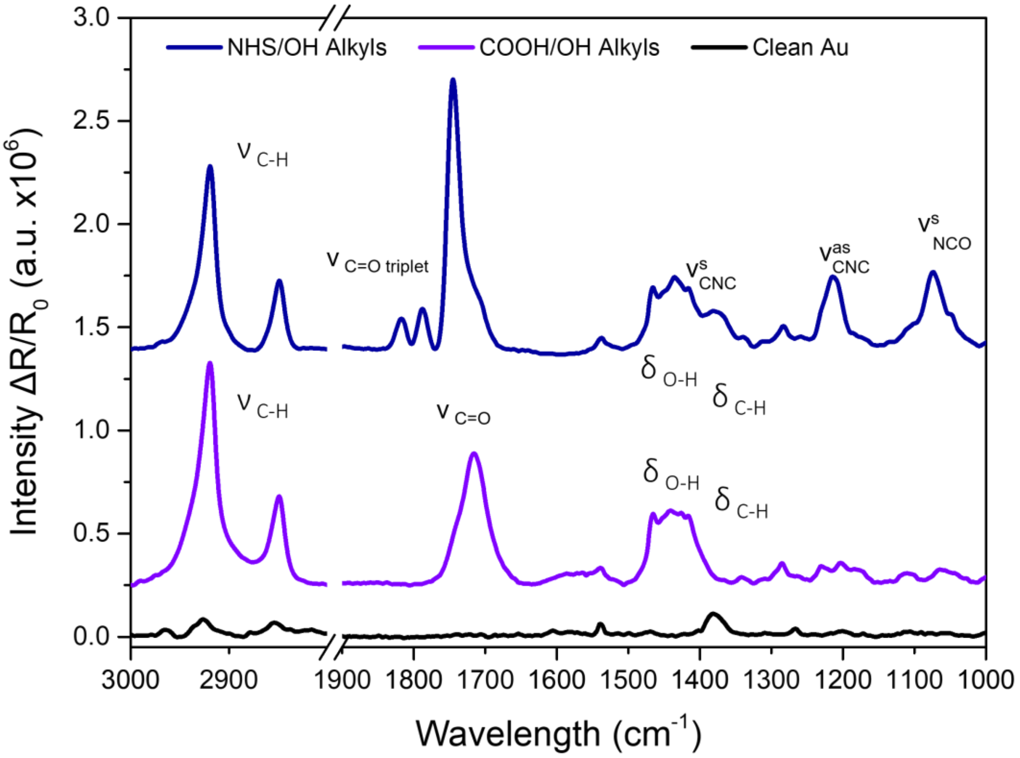

Figure 3.3.3.: PM-IRRAS spectral analysis of C/NHS (mixed COOH/OH and NHS/OH Alkyls). For NHS/OH Alkyls, C=O stretching triplet, CNC symmetric and asymmetric stretching are highlighted along with the symmetric NCO stretching. All the peaks for C/NHS chemistry are compiled in Table 3.3.2.

As expected, characteristic peaks for vibrational modes of alkyl chain were observed between 2919-2849 cm^{-1} and 1465-1416 cm^{-1} corresponding to stretching ν C-H, bending δ O-H and δ C-H. Presence of COOH group on the monolayer was confirmed by the prominent peak at 1715 cm^{-1} for stretching ν C=O and bending δ O-H peak around 1465-1416 cm^{-1} (see table 3.3.3.). For NHS/OH Alkyls activation, presence of amine groups (C-N) and C=O triplets were confirmed with ν C=O triplets between 1820-1743 cm^{-1}, symmetric stretching ν CNC and ν NCO at 1380 cm^{-1} and 1075 cm^{-1} and asymmetric ν CNC at 1213 cm^{-1}. These results are in agreement with already published data [25].

Table 3.3.3.: PM-IRRAS spectral peaks for carbodiimide/NHS (C/NHS) surfaces. For COOH/OH Alkyls, COOH- functional group, alkyl chains are showcased, unfortunately thiol tail group could not have been observed. After activation to NHS/OH Alkyls via DIC/NHS, NHS triplet and alkyl chain regions were observed but like COOH/OH Alkyls, thiol groups could not be observable.

Carbodiimide/NHS chemistry at INL: COOH/OH Alkyls		
Corresponding bonds		**Observed range**
COOH/OH head	ν C=O and δ O-H	**1715 cm^{-1}** **1465-1416 cm^{-1}**
Alkyl chains	ν C-H, and δ C-H	**2919-2849 cm^{-1}**
Thiol tail	S-H	**N.R.**
NHS/OH Alkyls at INL		
NHS/OH head	ν C=O triplet, ν CNC sym, ν CNC assym and ν NCO sym	**1817, 1786 and 1743 cm^{-1}** **1380 cm^{-1} and 1213 cm^{-1}** **1075 cm^{-1}**
Alkyl chains	ν C-H, δ O-H and δ C-H	**2919-2849 cm^{-1}** **1465-1416 cm^{-1}**
Thiol tail	S-H	**N.R.**

For DBCO based surfaces, PM-IRRAS characterization of both activated DBCO/OH Alkyls and DBCO PEGs/OH Alkyls surfaces have been showcased in Fig. 3.3.4. and their binding energies compiled in Table 3.3.4. As expected, for NH_2/OH Alkyls, vibrational modes for alkyl chains were observed between 2919-2849 cm^{-1} and 1465-1416 cm^{-1} corresponding to stretching ν C-H, bending δ O-H and δ C-H. The presence of $-NH_2$ group on mixed NH_2 /OH Alkyls was confirmed by the prominent amine peak at 1550 cm^{-1} for bending δ C-N. After activation to DBCO/OH Alkyls, amide I and II peaks were exhibited at 1660 cm^{-1} and 1539 cm^{-1} respectively.

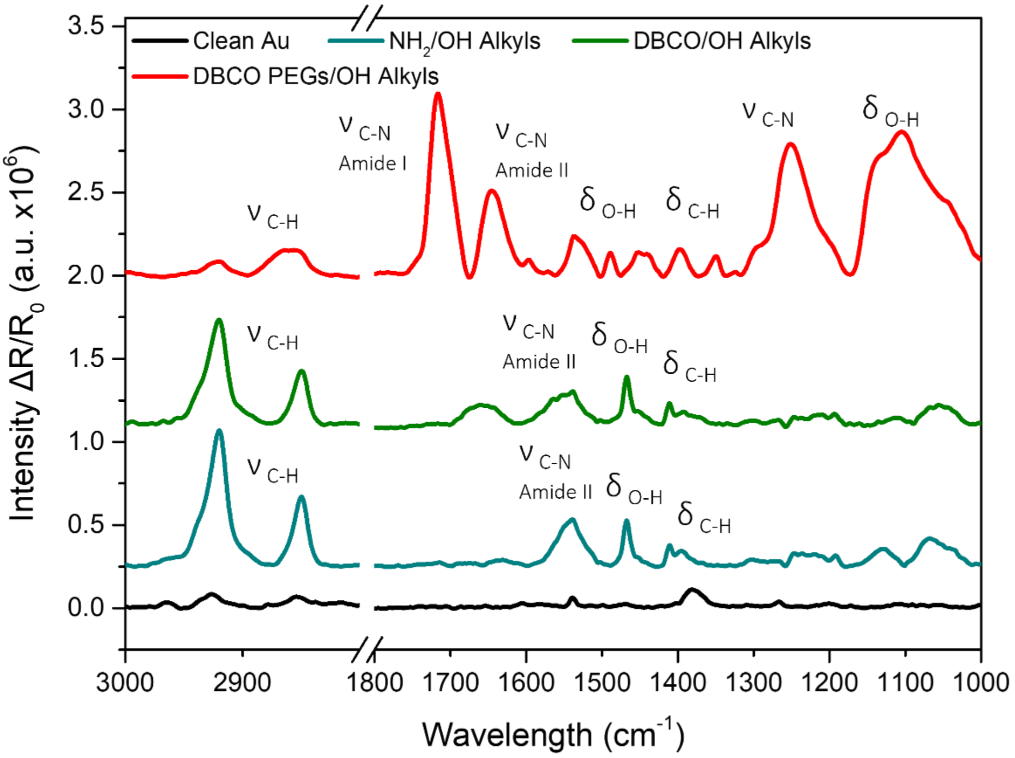

Figure 3.3.4.: PM-IRRAS spectral analysis of SPAAC surfaces (mixed NH$_2$/OH, DBCO/OH Alkyls and DBCO PEGs/OH Alkyls). For activated DBCO/OH Alkyls and DBCO PEGs/OH Alkyls, amide and amide II peaks are showcased along with the C-O-C contribution. All the peaks for DBCO surfaces are compiled in Table 3.3.3.

For DBCO PEGs/OH Alkyls, the presence of amide I peak (at 1645 cm^{-1}) and amide II peak (at 1537 cm^{-1}) in addition to peaks of N-O stretching (at 1540 cm^{-1}) , aromatic C-N amine (between 1301 and 1266 cm^{-1}) , aromatic *ν* C-O ester stretching (at 1250 cm^{-1}) and *ν* C-N amine stretching (at 1106 cm^{-1}) confirm the grafting of DBCO group on the functionalized surface. Furthermore, the presence of C-O-C contribution at 1717 cm^{-1} and C-O ester stretching at 1192 cm^{-1} indicate the grafting of PEG chains versus alkyl chains.

Table 3.3.4.: PM-IRRAS spectral peaks for DBCO surfaces. For NH_2/OH Alkyls, NH_2- functional group, alkyl chains are showcased. After activation to DBCO/OH Alkyls via DBCO-NHS, amide I and amide II peaks were observed along with the alkyl chain. For DBCO PEGs/OH Alkyls, amide I and II, C-O-C peak and C-N peaks were measured but thiol groups could not be observable for all the DBCO surfaces.

DBCO surfaces at INL: Mixed NH_2/OH Alkyls		
Corresponding bonds		**Observed range**
NH_2/OH head	δ C-N, and δ O-H	**1550 cm^{-1}** **1465-1416 cm^{-1}**
Alkyl chains	ν C-H, and δ C-H	**2919-2849 cm^{-1}** **1465-1416 cm^{-1}**
Thiol tail	S-H	**N.R.**
Activated DBCO/OH Alkyls and DBCO PEGs/OH Alkyls at INL		
Corresponding bonds		**Observed range**
DBCO head	Amide I and Amide II, N-O, aromatic C-N amine and aromatic C-O ester	**1659 and 1540 cm^{-1}** **1540 cm^{-}1, 1250 cm^{-1},** **1106 cm^{-1}** **1730 cm^{-1}**
PEG chain	ν C-O-C	**1717 cm^{-1}**
Alkyl chains	ν C-H, δ O-H and δ C-H	**2919-2849 cm^{-1}** **1465-1416 cm^{-1}**
DBCO: Alkyne/Alkene bonds	C≡C, C=C	**N.R.**
Thiol tail	S-H	**N.R.**

However, for both DBCO surfaces, characteristic peaks for C≡C (3500-3300 cm^{-1}) and C=C (1650-1566 cm^{-1}) of the DBCO group along with C-S peaks (750-730 cm^{-}1) for thiol coupling of the monolayers around were not visible on IR spectra. This might be due to setup sensitivity or complexity of monolayer mixing, thus, for further confirmation, XPS analysis were performed.

3.4.1.4. XPS characterization of DBCO surfaces:

C1s, O1s, N1s, S2p and Au4f were analysed on clean Au surface and DBCO surfaces at 0° take off angle. Atomic specie percentages were compiled in Table 3.3.5.

Table 3.3.5.: XPS atomic percentages for N1s, O1s, C1s, S2p and Au4f of mixed NH2/OH Alkyls, DBCO/OH Alkyls and DBCO PEGs/OH Alkyls.

Surfaces	N1s	O1s		C1s			
	N-C	O-C	O=C	C=O	C-O/C-N	C-C/C-H	Au4f
NH_2/OH Alkyls	-	-	1.5	-	0.8	5.7	92.0
DBCO/OH Alkyls	-	-	3.3	-	0.6	4.9	91.2
DBCO PEGs/ OH Alkyls	2.9	17.8	3.0	0.2	7.5	11.4	57.2

Based on atomic percentage analysis, significant difference was observed between alkylated DBCO surfaces (mixed NH_2/OH Alkyls and DBCO/OH Alkyls) and PEGylated DBCO surfaces (mixed DBCO PEGs/OH Alkyls). For alkylated DBCO surfaces, however, no significant difference was analysed where most of the contributions are presented from Au4f species rather than the functional species indicating monolayer functionalization. As exhibited in Fig. 3.3.5., specie contributions from clean bare Au surface indicate oxidative contamination specifically for O=C of O1s contributions.

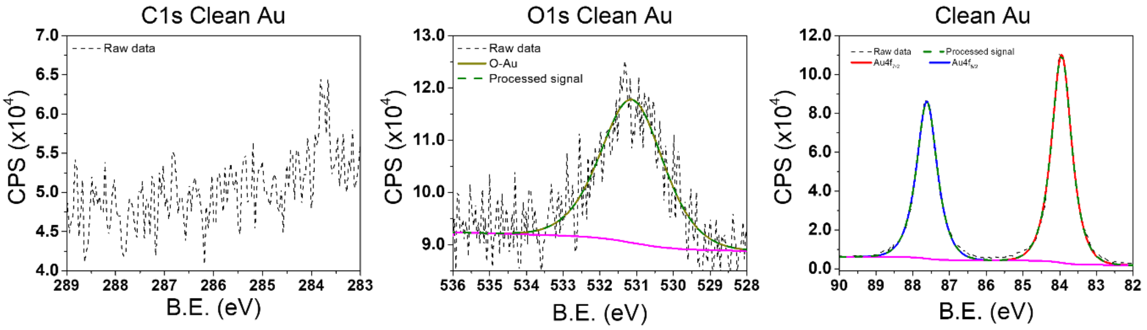

Figure 3.3.5.: XPS spectra for clean bare Au surfaces. C1s, O1s, and Au4f contributions are highlighted where O=C peaks are prevalent due to oxidative contamination.

Presence of C-C/C-H along with C-O/C-N could be indicative of alkylated chains and NH_2/-OH groups and amide bond between DBCO and alkylated chains highlighted in Fig. 3.3.6., however, such contributions are significantly lowered compared with the Au4f contributions. For both mixed NH_2/OH Alkyls and DBCO/OH Alkyls, similar peak contributions were observed that could indicate preferential weak adsorption of OH Alkyls and subsequent improper DBCO activation. In addition, for both these surfaces, presence of O=C over O-C contributions could be due to oxidative contamination highlighted in Fig. 3.3.5., hence these contributions are not complemented for C=O contributions.

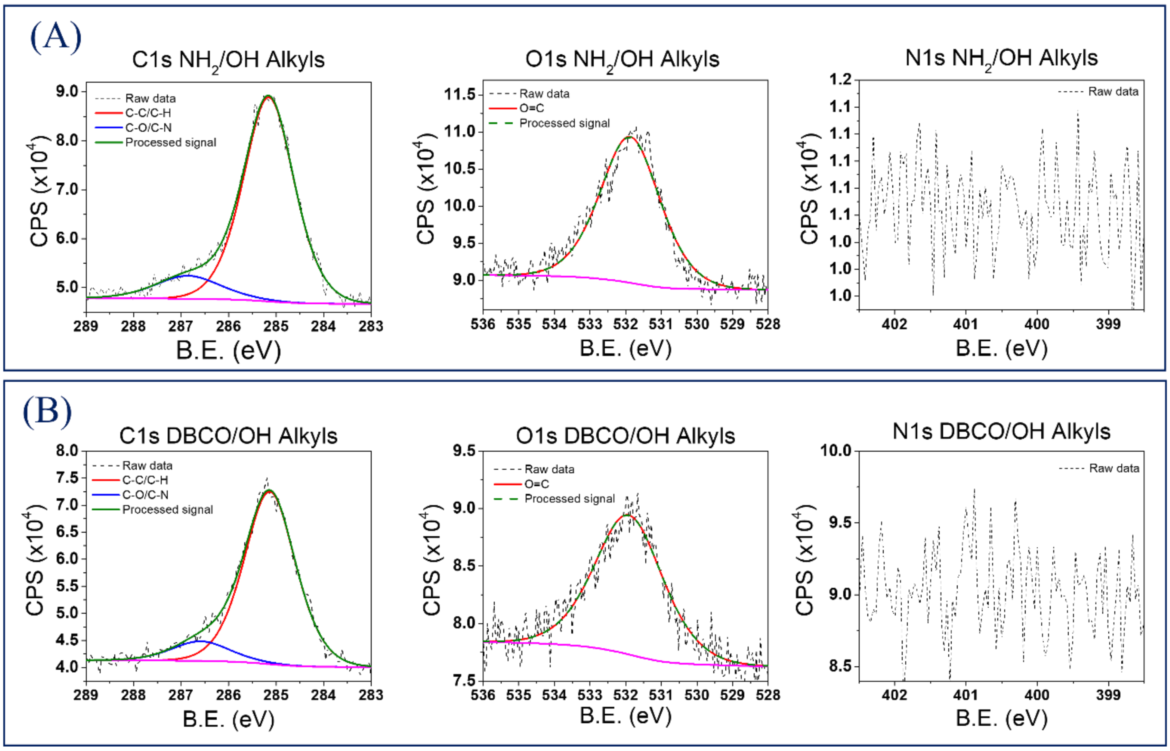

Figure 3.3.6.: Comparative analysis of XPS spectra for **(A)** NH$_2$/OH Alkyls, **(B)** DBCO/OH Alkyls. For NH$_2$/OH and DBCO/OH Alkyl, similar contributions of C-C/C-H and C-O/C-N were observed for C1s while for O1s, only O=C was prevalent due to contamination.

Unlike alkylated DBCO surfaces, mixed DBCO PEGs/OH Alkyls showcased significant decrease of Au4f species, which resulted in marked increase in functional specie percentages specifically N1s, O1s and C1s showcased in Fig. 3.3.7. with specie complementarity among the contributions. However, for this monolayer, as DBCO PEGs and OH Alkyls are mixed in 1/1 ratio, it is difficult to establish which moiety is specific for subsequent specie percentage.

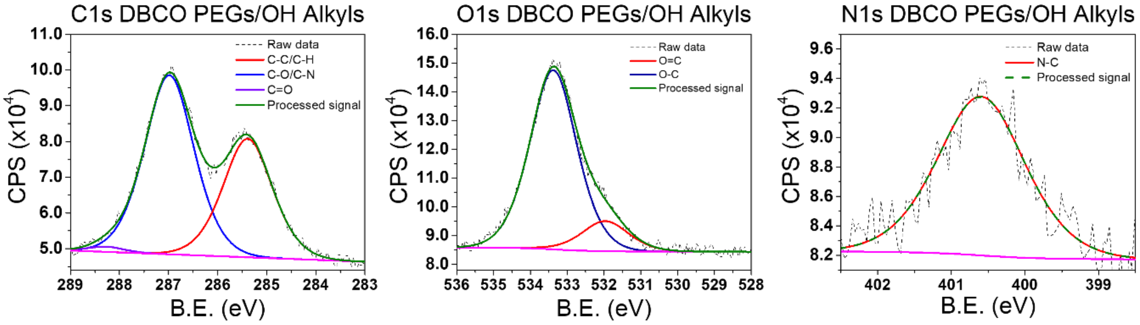

Figure 3.3.7.: Comparative analysis of XPS spectra for DBCO PEGs/OH Alkyls. For DBCO PEGs/OH Alkyls, C-C/C-H, C-O/C-N and C=O was analysed for C1s, O=C and O-C for O1s and N-C for N1s was presented.

Specie contributions for DBCO PEGs/OH Alkyls presented a comprehensive and holistic picture. All functional species were showcased, and complementarity was established between each contribution significant to the clean bare Au surfaces indicating monolayer functionalization. Similarly, for DBCO PEGs/OH Alkyls surfaces, DBCO/OH PEGs 2k were characterized by XPS, where different spacing ratios i.e., 1/0, 1/1 and 1/4 were analysed. Atomic specie percentages for these surfaces were compiled in Table 3.3.6.

Focusing on the percentage complementarity between species for each mixing ratios (1/0, 1/1 and 1/4), some differences were presented specifically for N-C/O-C for N1s and O1s species vs C-O/C-N for C1s. This could be due to monolayer orientation, but further analysis needed to perform on further understanding as this was presented for surface with and without diluent mixing (1/0, 1/1 and 1/4). In contrast, percentages of O=C for O1s and C=O for C1s for all three DBCO/OH PEGs 2k surfaces were similar, where no significant difference was showcased.

Table 3.3.6.: XPS atomic percentages for N1s, O1s, C1s, S2p and Au4f of DBCO/OH PEGs 2k in various diluent ratios (1/0, 1/1 and 1/4).

	N1s	O1s		C1s				
Surfaces	**N-C**	**O-C**	**O=C**	**C=O**	**C-O/C-N**	**C-C/C-H**	**S2p**	**Au4f**
1/0	1.3	14.0	4.4	3.5	37.8	6.5	1.9	29.7
1/1	0.9	16.7	3.2	2.9	39.8	5.4	1.1	29.3
1/4	1.2	15.0	5.0	3.2	40.4	5.7	1.2	27.3

Compared with DBCO PEGs/OH Alkyls where around 57% of Au4f contributions were exhibited, significant difference for DBCO/OH PEGs 2k surfaces was observed where Au4f contributions were around 27%-29%. This decrease in contribution could be due to increased presence of functional monolayers. In addition, S2p contributions were presented for these surfaces unlike DBCO PEGs/OH Alkyls, where such contributions were not evident indicating the presence of tail groups of the thiolated monolayers coupled on the gold surface. These Au4f and S2p contributions are further highlighted in Fig. 3.3.8. for DBCO/OH PEGs 2k surfaces.

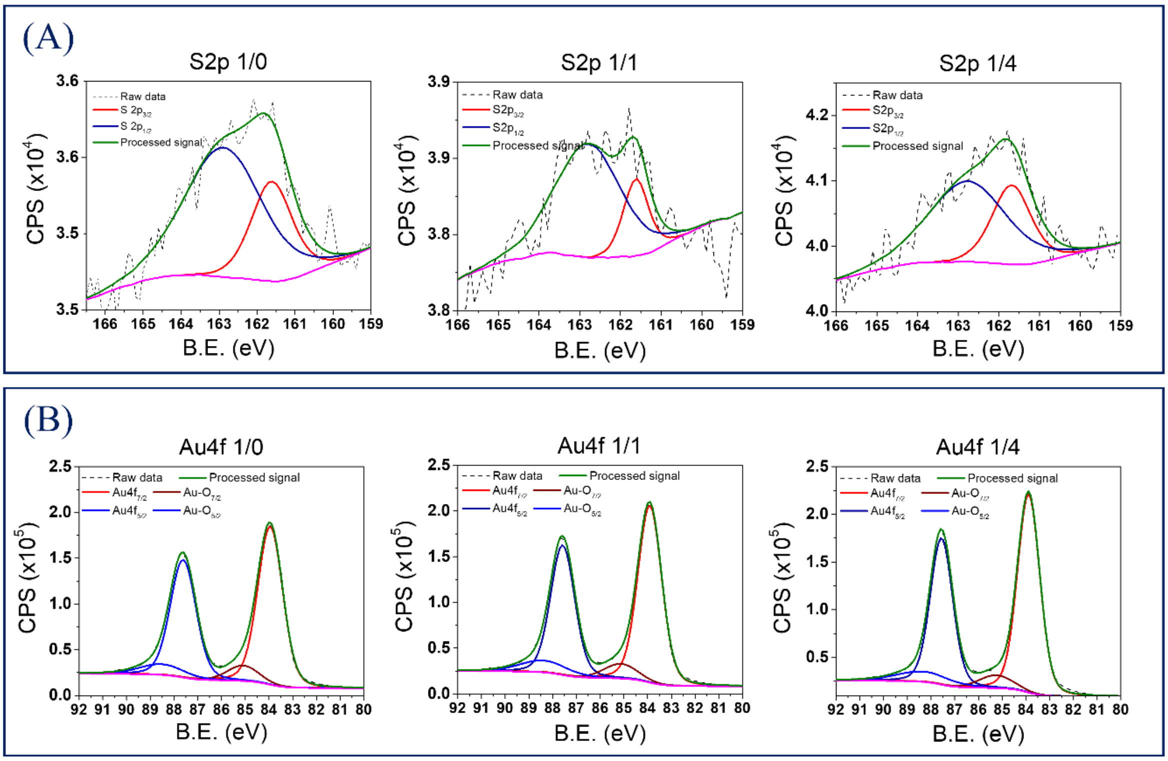

Figure 3.3.8.: XPS spectral peaks of **(A)** S2p and **(B)** Au4f for DBCO/OH PEGs 2k for different spacer ratios from1/0 to 1/1 to 1/4 at 0° . $S2p_{3/2}$ and $S2p_{1/2}$ peaks are presented above for S2p contributions while $Au4f_{7/2}$ and $Au4f_{5/2}$ are showcased for Au4f contributions along with Au-O for both 7/2 and 5/2 metallic spin.

However, for atomic percentages of DBCO/OH PEGs 2k surfaces, no significant difference was observed between the spacing ratios while increasing the presence of diluents from 1/0 to 1/1 to 1/4. Similarly, all functional species of interest i.e., C1s, O1s and N1s were presented for DBCO/OH PEGs 2k in Fig. 3.3.8. and no significant difference between peak species was exhibited.

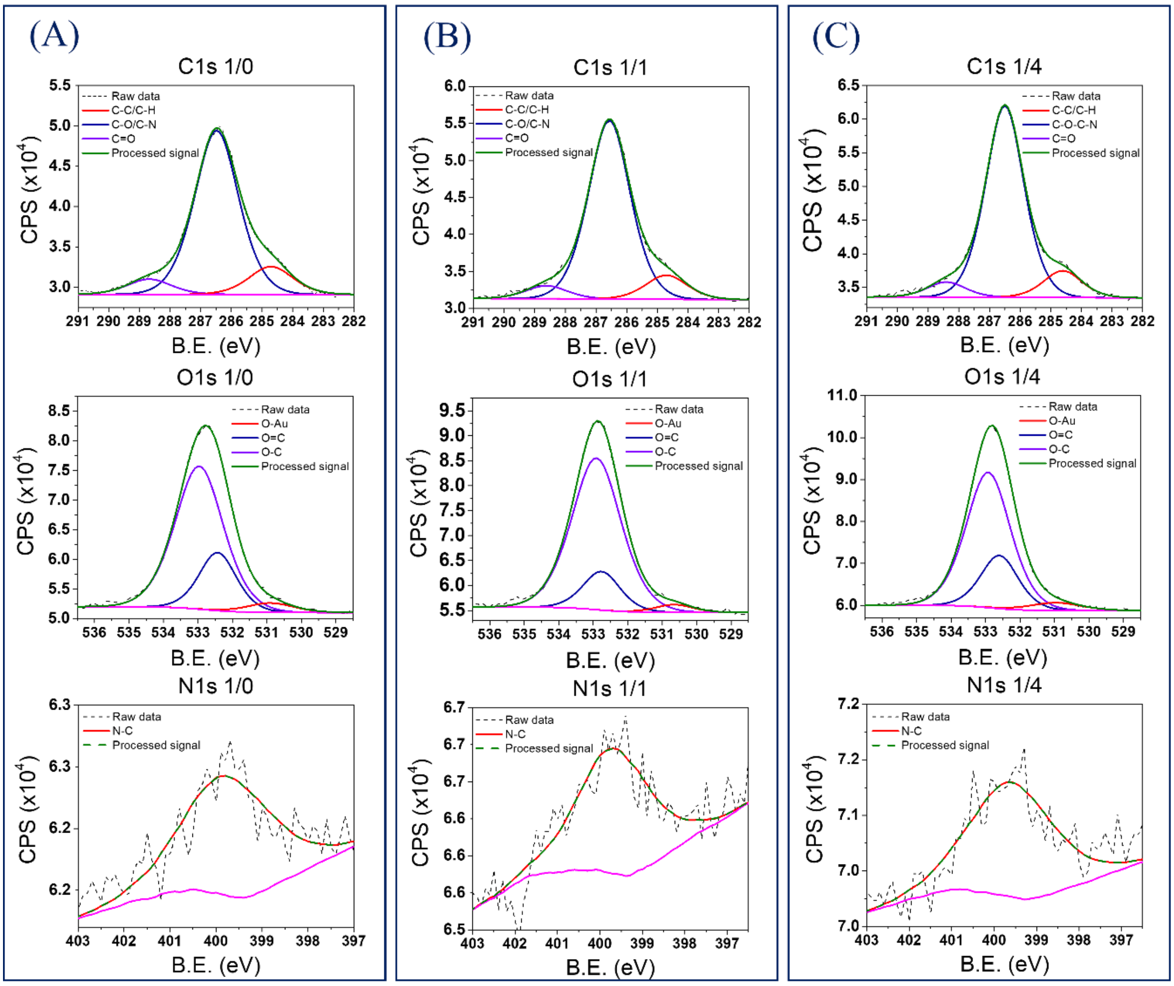

Figure 3.3.9.: Comparative analysis of XPS spectral peaks for DBCO/OH PEGs 2k for different spacer ratios from **(A)** 1/0 to **(B)** 1/1 to **(C)** 1/4 at 0° . C1s, O1s and N1s peak contributions are presented above. For C1s, C-C/C-H, C-O/C-N and C=O should be analysed while for O1s and N1s, O-C, O=C and N-C are focused on.

In conclusion, XPS characterization for DBCO surfaces presented a more comprehensive picture specifically for both alkylated DBCO surfaces and PEGylated DBCO surfaces in addition to the different spacing ratios. XPS highlighted preferential adsorption of OH Alkyls over NH_2 Alkyls resulting in improper DBCO conjugation for DBCO/OH Alkyls, which could further impact antibody immobilization. However, unlike alkylated DBCO surfaces, DBCO PEGs/OH Alkyls as well as DBCO/OH PEGs 2k presented optimal monolayer functionalization. The following sub-section will focus on further understanding monolayer orientation due to the different diluent ratios (1/0, 1/1 and 1/4) by angle resolved XPS (ARXPS) and depth profilometry. ARXPS is a technique for depth-dependent chemical analysis within the first few nanometres of a functionalized sample at different angles [63] which will be discussed in detail.

3.4.1.5. ARXPS and depth profilometry of DBCO/OH PEGs 2k monolayers:

ARXPS was performed for all three 1/0, 1/1 and 1/4 spacing ratios of DBCO/OH PEGs 2k monolayers showcased in Table 3.3.9. at characteristic take-off angles of 0° , 40° , 53° , 66° and 70° , highlighting surface monolayer orientation. A characteristic trend between specie contributions in ascending take off angles could be indicative of defined monolayer orientation either laying on the surface or in an upright fashion.

At different take off angles, peak positions were like 0° , however, specie percentages varied due to excitation of monolayer due to analysis at varying characteristic angles depending on the surface orientation. Tail group species like Au4f and S2p are expected to decrease with increasing take off angles, while for functional specie contributions i.e., C1s, O1s and N1s are expected to increase. This is due to take-off angle being tilted away from the surface, where bulk of the contributions are from DBCO/OH terminal groups and PEGylated chains focusing on top and middle layers.

Table 3.3.7.: ARXPS atomic percentages for N1s, O1s, C1s, S2p and Au4f of DBCO/OH PEGs 2k in various spacer ratios (1/0, 1/1 and 1/4) at 0° , 40° , 55° , 63° and 70° .

1/0 DBCO/OH PEGs 2k					
	O1s	**C1s**	**N1s**	**S2p**	**Au4f**
0°	19.3	47.8	1.3	1.9	29.7
40°	22.2	49.3	0.4	1.3	26.9
55°	22.9	51.5	0.6	4.5	20.5
63°	24.2	55.5	0.7	4.3	15.3
70°	27.9	56.8	0.0	4.1	11.2
1/1 DBCO/OH PEGs 2k					
	O1s	**C1s**	**N1s**	**S2p**	**Au4f**
0°	20.6	48.0	0.9	1.1	29.3
40°	21.7	51.9	0.9	1.3	24.2
55°	24.3	56.2	1.0	0.7	17.8
63°	27.4	58.3	0.7	0.5	13.1
70°	29.2	61.3	0.6	0.8	8.2
1/4 DBCO/OH PEGs 2k					
	O1s	**C1s**	**N1s**	**S2p**	**Au4f**
0°	21.0	49.2	1.2	1.2	27.3
40°	19.3	48.5	1.4	1.7	29.2
55°	21.6	54.0	1.3	1.1	22.1
63°	25.5	57.6	0.5	1.4	15.0

70°	26.7	61.0	0.8	0.6	10.9

Between the different spacing ratios i.e., 1/0, 1/1 and 1/4 no significant difference was observed between contributions. However, for each monolayer functionalization significant trend was exhibited for the specie contributions for top and bottom layers. As expected, tail group Au4f and S2p contributions decreased by increasing the take-off angles from 0° to 70° . Similarly, for functional C1s and O1s contributions, specie percentages increased significantly for all three spacing ratios. Specifically at 70° take off angle for 1/0 1/1 and 1/4 monolayers, bulk of the contributions were from PEGylated chain as 1:2 ratio was observed for O1s:C1s species.

Based on the specie percentage analyses for 1/0, 1/1 and 1/4 DBCO/OH PEGs 2k monolayers, simulations for depth profiles were performed to characterize monolayer orientations presented in Fig. 3.3.10. (A) 1/0, (B) 1/1, and (C) 1/4. The depth profilometry was performed from 0 nm to 7 nm and simulated atomic percentages were charted for top, middle and bottom layers at characteristic 0° , 40° , 55° , 63° and 70° angles respective to ARXPS surface sensitivity using Tikhonov regularization.

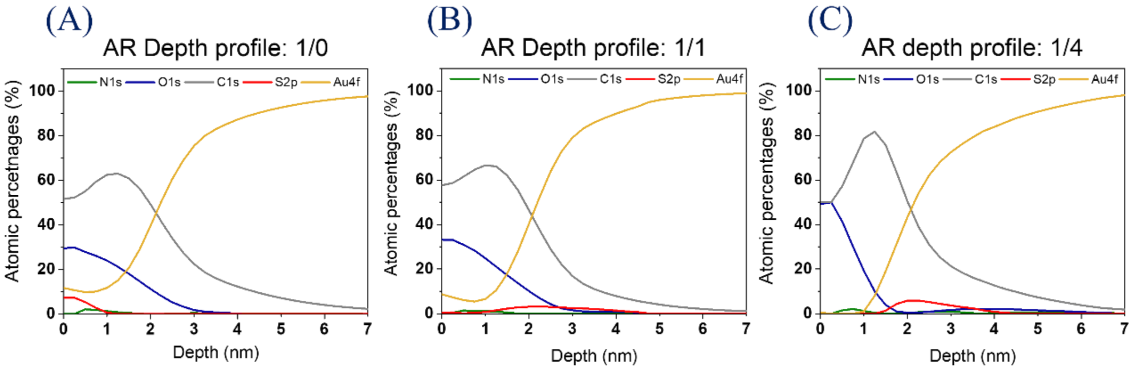

Figure 3.3.10.: ARXPS depth profile for DBCO/OH PEGs 2k **(A)** 1/0, **(B)** 1/1 and **(C)** 1/4. N1s, O1s, C1s, S2p and Au4f are considered as species of interest and their atomic percentages for each surface are compiled above. Depth profiles for top layer ranged from 0 nm to 1 nm, middle layer ranged from 1 nm to 2 nm and bottom layer from 2 nm onwards.

For optimal monolayer orientation based on our assumptions, top layer should have C1s contributions due to DBCO with 2 benzene rings couple with a cyclooctyne group having an alkyne bond. In addition, some N1s and O1s contributions are to be expected due to the amide bond between DBCO and PEGylated chain. Middle layer contributions should be abundant from C1s and O1s species indicative of PEGylated chain, while the bottom layer should exhibit decreasing C1s, O1s and N1s contributions due to amide bond between PEGylated chain and -SH group, while, afterwards, bulk of the contributions should be from S2p and Au4f species. For an upright monolayer orientation, this trend is followed for top, middle, and bottom layer contributions, however if the monolayers are laying on the surface, N1s and S2p contributions along with Au4f species might be presented at top and middle layers. In addition, monolayer coverage can be corroborated from Au4f contributions, where increased contributions on top layer indicate free spaces/gaps between the monolayers.

Based on our simulations, significant difference was observed between the three spacing ratios. For 1/0 DBCO/OH PEGs 2k, increased Au4f contributions around 10% were exhibited indicative of inefficient monolayer surface coverage or ‘gaps’ due to the absence of OH PEGs 2k as diluent. Like 1/0, increased Au4f contributions of around 7% were observed for 1/1 spacing ratio. However, O1s and C1s contributions followed 1:2 trend due to the presence of PEGylated chain. We can hypothesize the addition of OH PEGs as diluent in equal parts enhanced surface coverage due to Au4f contribution and further increased monolayer density due to C1s and O1s contributions. However, 1/4 spacing presented a comprehensive monolayer orientation, where little to no contributions were observed for Au4f on the top layer indicating optimal surface coverage. In addition, 1:2 trend for PEGylated chain were showcased for C1s and O1s contributions along with the presence of amide bonds at the top and bottom layers.

In conclusion, comparative ARXPS analysis was performed for DBCO/OH PEGs 2k, where no significant difference was observed between the three spacing ratios however, trends for specie contributions were evident, where functional species i.e., C1s, O1s and N1s increased with increasing take off angles while tail Au4f and S2p contributions decreased. More so, AR depth profile showcases an overview on such contributions along the z-axis of the surface providing information on monolayer orientation. Optimal surface coverage and monolayer density was exhibited for 1/4 DBCO/OH PEGs 2k functionalization, compared with 1/0 and 1/1 spacing ratios, which could be due to dense packing of OH PEGs between DBCO PEGs.

The following sub-section focuses on the characterization of sensing efficiency of different immobilized antibodies for DBCO functionalized surfaces i.e., DBCO/OH Alkyls and DBCO PEGs/OH Alkyls. In addition, comparative analysis between the optimal DBCO surface and conventional NHS/OH Alkyls was performed through SPRi setup to present an optimal site-specific, oriented, and directed surface immobilization approach.

3.4.2. Sensing characterization of immobilized antibodies on gold functionalized surfaces:

3.4.2.1. Evaluation of antibody immobilization onto DBCO functionalized surfaces:

For developing oriented and site-specific immobilization of antibody through click chemistry, we developed two-steps and one-step DBCO functionalized surfaces. The cyclooctyne of DBCO group is known to favourably react with both - SH and -N3 groups via site-specific click cycloaddition. Thus, immobilization efficiency of fragmented Fab antibodies (Ab-SH) containing a free -SH group, and enzymatically azide activated antibodies (Ab-N_3) were compared along with non-modified antibody (Ab) on (A) DBCO/OH Alkyls and (B) DBCO PEGs/OH Alkyls surfaces. Both the fragmented Ab-SH and azide activated Ab-N3 were generated enzymatically using commercial kits to safeguard their biological activity after modification explained in detail in Section 3.3.6. A 2X2 array was spotted onto each surface as highlighted in Fig. 3.3.11. and polyclonal secondary antibody (Pc Ab) was used as target for specific recognition of immobilized antibodies.

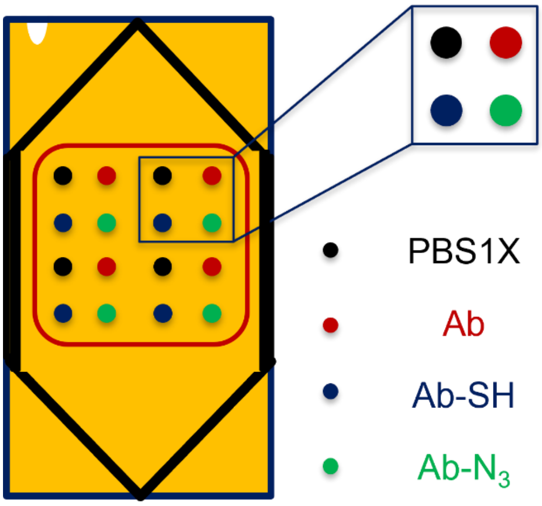

Figure 3.3.11.: 2x2 spot array for characterization of biosensing immobilization where PBS1X is spotted for non-specific interaction and Ab, Ab-SH and Ab-N_3, where polyclonal secondary antibodies are injected at initial 16 µg/mL concentration.

Sensing performances were evaluated through conventional SPRi setup as described in Section 3.6.1. Results are presented in Fig. 3.3.12.

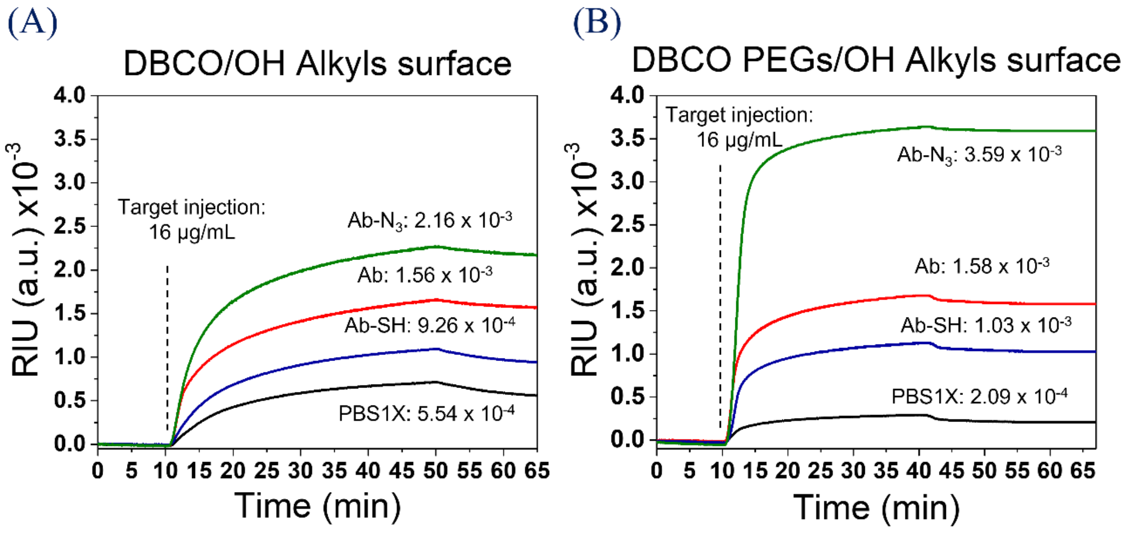

Figure 3.3.12.: SPRi sensorgrams for non-modified Ab (red line), fragmented Ab-SH (blue line), azide activated Ab-N3 (green line) and PBS1X (black line) immobilized on **(A)** DBCO/OH Alkyls and **(B)** DBCO PEGs/OH Alkyls functionalized surfaces. Pc Ab (target) was injected at 16 µg/mL to analyse specific recognition.

For DBCO PEGs/OH Alkyls, non-specific adsorption (PBS1x signal) of Pc Ab target was exhibited to be twice as lowered compared to DBCO/OH Alkyls which could be attributed to the anti-fouling properties of PEGylated chains over alkylated ones. For both surfaces SPRi signal obtained for non-modified Ab corresponds to the specific detection of non-covalently immobilized Ab onto DBCO-functionalized surfaces. Results indicate that the amount of adsorbed Ab on both surfaces is in the same range (1.56-1.58 x 10^{-3} RIU). However, compared to SPRi signal obtained for Ab-N_3 which corresponds to the specific detection of covalently immobilized Ab onto DBCO-functionalized surfaces, it appears that only 1.4 times more of Ab-N_3 is immobilized onto DBCO/OH Alkyls (2.16 x 10^{-3} RIU), whereas more than 2.3 times more Ab-N_3 is immobilized onto DBCO PEGs/OH Alkyls surface (3.59 x 10^{-3} RIU).

This could be further explained by either (i) improper activation of mixed NH_2/OH alkyls via DBCO-NHS as discussed before, (ii) less steric hindrance of DBCO moieties with PEGs chains vs alkyls chains. In addition, reaction velocities, calculated by analysing the ON-rate and OFF-rate reaction kinetics for immobilized Ab-N_3 recognition with Ab Pc, were calculated to be 4.5 times faster on DBCO PEGs/OH Alkyls (2.4E^{-3} s^{-1}) compared to DBCO/OH Alkyls (1.1E^{-2} s^{-1}). From these results we can assume that immobilized Ab-N_3 is better accessible to the target Ab Pc on DBCO PEGs/OH Alkyls functionalized surface than on DBCO/OH Alkyls one probably due to the efficient oriented and site-specific immobilization of Ab-N_3. Concerning the specific detection of immobilized Ab-SH, we expected a lower SPRi signal than with Ab-N_3 as the Fc fragment of the antibody was removed due to fragmentation, but a higher SPRi signal than with non-modified Ab as Ab-SH should be covalently and oriented immobilized onto both DBCO surfaces. However, in both cases, the recognition of immobilized Ab-SH is lower (9.26 x 10^{-4} - 1.03 x 10^{-3} RIU) than the one of non-modified Ab (2.16 - 3.59 x 10^{-3} RIU) suggesting that covalent immobilization onto DBCO moiety was not efficient with –SH group. This could be due to oxidation of fragmented Ab-SH back to Fab'$_2$, which could be reversible in nature. In addition, increased signal response of non-modified Ab coupled on DBCO surface could be explain by the presence of cysteine bonds and the natural reduction of disulphide bond for human IgG1 antibodies. Results showcased by Chumsae and group indicated different levels of free sulfhydryl due to unpaired multiple cysteine residues in the constant and variable domain [5]. These free sulfhydryl levels can couple with DBCO moiety on the monolayer via thiol-yne reaction, like the fragment Ab-SH immobilization. Thus, we can conclude that optimal surface functionalization was achieved with DBCO PEGs/OH Alkyls leading to the efficient oriented and site-specific immobilization of Ab-N_3.

3.4.2.2. Comparative analysis of antibody immobilization efficiency between C/NHS and DBCO-SPAAC surfaces:

As discussed previously, NHS/OH Alkyls for C/NHS chemistry are specific for non-modified Ab, whereas for DBCO PEGs/OH Alkyls, signal interaction for Ab-N_3 is specific. For a site-specific and oriented strategy, we could expect Ab-N3 signal interaction for NHS/OH Alkyls and Ab interaction for DBCO PEGs/OH Alkyls to be minimal. In addition, between NHS/OH Alkyls and DBCO PEGs/OH Alkyls, PEGylated chains are expected to minimize non-specific interaction for PBS1X spots. As showcased in Table 3.3.8., signal interactions for both surfaces are presented for both Ab and Ab-N_3 immobilization. The non-specific signal exhibited for NHS/OH Alkyls is higher compared to DBCO PEGs/OH Alkyls due to anti-fouling properties of the PEGylated chains. More so, for NHS/OH Alkyls, signal interaction for Ab and Ab-N_3 were within standard deviation of each other. However, significant difference was evident for DBCO PEGs/OH Alkyls for both immobilization species, specifically for Ab-N_3, which exhibited higher signal response.

Table 3.3.8.: SPRi signal (in RIU) and standard deviation (S.D.) at 16 µg/mL polyclonal goat anti-mouse IgG1 injection on NHS/OH Alkyls and DBCO PEGs/OH Alkyls for PBS1X (non-specific adsorption) and immobilized Ab and Ab–N_3.

Surface chemistry	**Biological immobilization**		
	PBS ± S.D.	**Ab ± S.D.**	**Ab–N_3 ± S.D.**
NHS/OH Alkyls	5.70×10^{-4} ± 8.74×10^{-6}	3.29×10^{-3} ± 6.09×10^{-4}	3.57×10^{-3} ± 6.24×10^{-4}
DBCO PEGs/OH Alkyls	2.09×10^{-4} ± 8.52×10^{-6}	1.58×10^{-3} ± 7.16×10^{-5}	3.59×10^{-3} ± 4.28×10^{-4}

More so, signal interactions as signal-to-noise ratio (S/N) were measured by dividing specific signal interaction with the non-specific one (PBS1X spots) presented in Fig 3.3.13. (A). On NHS/OH Alkyls, for both immobilized antibodies, no distinct trend was observed (Ab: 5.7; Ab-N_3: 6.1), which might be due to the functional groups around both Ab and Ab-N_3 couple or adsorb non-specifically on the surface resulting in random and non-oriented immobilization.

However, on DBCO PEGs/OH Alkyls, S/N for Ab-N_3 (~17.2) exhibited 2.3 times higher response compared with the Ab signal response (~7.3), which signify site-specific and direct conjugation of -N_3 with the DBCO moiety on the surface. For non-modified Ab, signal response was 1.2 times higher for DBCO PEGs/OH Alkyls vs NHS/OH Alkyls which could be due to anti-fouling effect of the PEGylated chain. Whereas, for Ab-N_3, DBCO PEGs/OH Alkyls showcased the comparatively higher signal response i.e., 2.8 times over NHS/OH Alkyls. This indicates better orientation of the antibodies coupled on the surface in a directed manner for Ab-N_3 on DBCO PEGs/OH Alkyls over Ab or Ab-N_3 on NHS/OH Alkyls.

Furthermore, it has been showcased that activation of COOH to NHS/OH Alkyls via C/NHS is not as stable and is prone to reversion [25]. Thus, DBCO-SPAAC (Ab-N_3 on DBCO PEGs/OH Alkyls) have been presented to provide stable surface functionalization and antibody immobilization for fabrication of efficient plasmonic immunosensors.

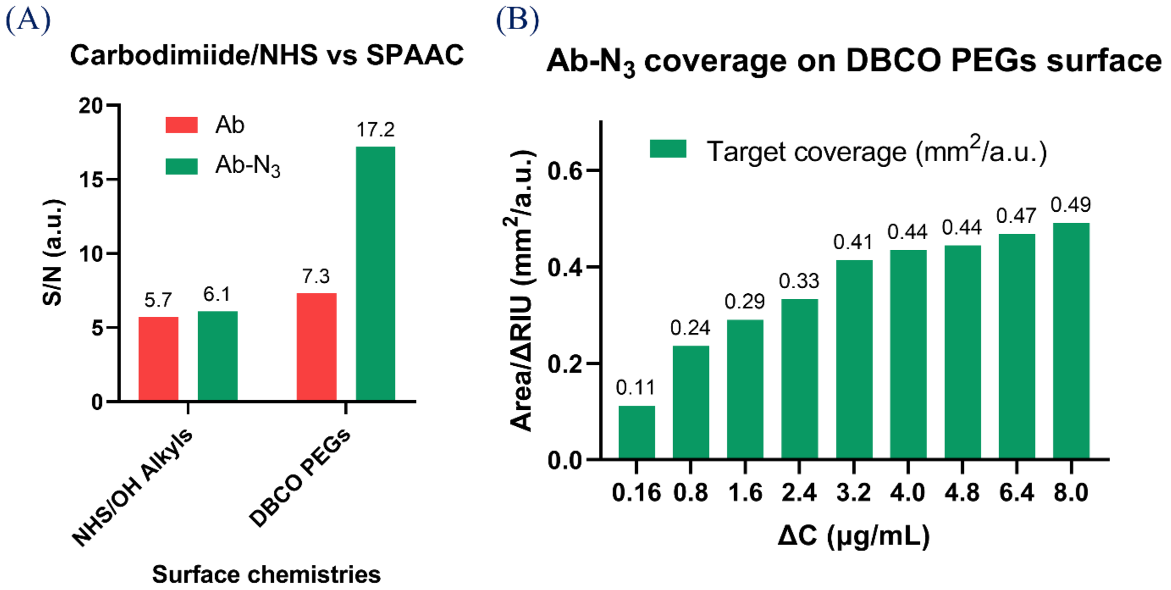

Figure 3.3.13.: **(A)** Comparative analysis for Signal to Noise (S/N) ratio of biosensing performance. polyclonal goat anti-mouse IgG1 was used as target for the detection of non-modified Ab and azide activated Ab-N3 immobilized on the surface of conventional NHS/OH Alkyls for carbodiimide/NHS chemistry and DBCO PEGs/OH Alkyls for SPAAC chemistry. S/N was calculated by dividing the specific detection signal (Ab and Ab-N_3) with the non-specific signal (PBS1X). **(B)** Analysis of target coverage for Ab-N_3 on DBCO PEGs/OH Alkyls monolayers. For measuring minimum target coverage, bulk refractive index change after interaction with the concentration was considered.

Additional characterization of DBCO PEGs/OH Alkyls coupled with Ab-N_3 on monolayer stability for multiple injections was performed. Multiple target injections at varying concentrations from 0.16 μg/mL to 8 μg/mL was showcased in Fig. 3.3.13. (B). For minimum target coverage, spotting area of interest ~0.15 mm^2 was selected and the calculations were performed by measuring the RI change induced by target recognition with the concentration of bound targets. After each target injection, surface was regenerated using 10 mM HCl.

These interactions showcased this directed and oriented coupling to be concentration dependent whereby increasing target concentration, surface coverage increased. In addition, saturation of surface coverage around 0.44 – 0.49 mm^2/a.u. was exhibited after 4 μg/mL target injection onwards. A conventional IgG antibody has surface area of ~123 nm^2 (length: 14.5 nm ; width: 8.5 nm ; height: 4 nm) with antigen binding sites spaced at 13.7 nm interval [69]. Based on these calculations, around 3.2 x 10^9 number of antibodies should be immobilized for an optimal monolayer coverage on the surface. For area coverage at ~0.49 mm^2/a.u. at 8 μg/mL, around 1.6 x 10^9 antibodies were calculated to be captured by Ab-N_3 on DBCO PEGs/OH Alkyls resulting in an optimal monolayer. In addition, we can extrapolate multilayers to form when surface coverage increases 1 mm^2/a.u. from 16 μg/mL onwards.

In conclusion, concentration dependent target recognition and target surface saturation highlight monolayer stability for multiple interactions for Ab-N_3 immobilized on DBCO PEGs/OH Alkyls. The following section will highlight the application of this site-specific DBCO PEGs/OH Alkyls approach for cancer marker biosensing through azide activating different antibodies and analysis their signal interaction.

3.4.2.3. Cancer biomarker analysis for biosensing characterization of DBCO PEGs/OH Alkyls – Ab-N_3 approach:

Based on literature review and state of the art performed for circulating tumour cells (CTCs), interleukin-6 (IL-6), interleukin-8 (IL-8) and tumour growth factor-beta (TGF-β) were selected as characteristic tumour biomarkers to provide a picture for metastatic state of the patient. Gold surfaces were functionalized with DBCO PEGs/OH Alkyls in 1/1 molar mixing and Anti-IL-6, Anti-IL-8 and Anti-TGF-β antibodies were azide activated and immobilized on the functionalized monolayers. Although, anti-TGF-β spot on the surfaces could not have been identified, sensing efficiency of the remaining spot species were measured as showcased in Fig. 3.3.14.

For characterization of biosensing efficiency of cancer biomarker detection, azide activated Anti-IL-6, Anti-IL-8 and Anti-TGF-β were immobilized along with PBS1X on the DBCO PEGs/OH Alkyls functionalized gold surface as a 2X2 spotting array like Fig. 3.3.11. Polyclonal goat anti-mouse Ab (Pc Ab) was injected at 7.5 µg/mL concentration, in between biomarker detection for confirmation of immobilized antibodies on the surface. This analysis was performed in cell culture medium and the surface was regenerated using 50 mM HCl solution in running buffer. Results presented in Fig. 3.3.13., showcase signal interaction for azide activated Anti-IL-6 and Anti-IL-8 along with PBS1X, as we were unable to detect Anti-TGF-β spots. In addition, signal interaction for biomarker detection was performed at maximum target injections (IL-6: 5.7 µg/mL; IL-8: 2.9 µg/mL; TGF-β: 5.7 µg/mL).

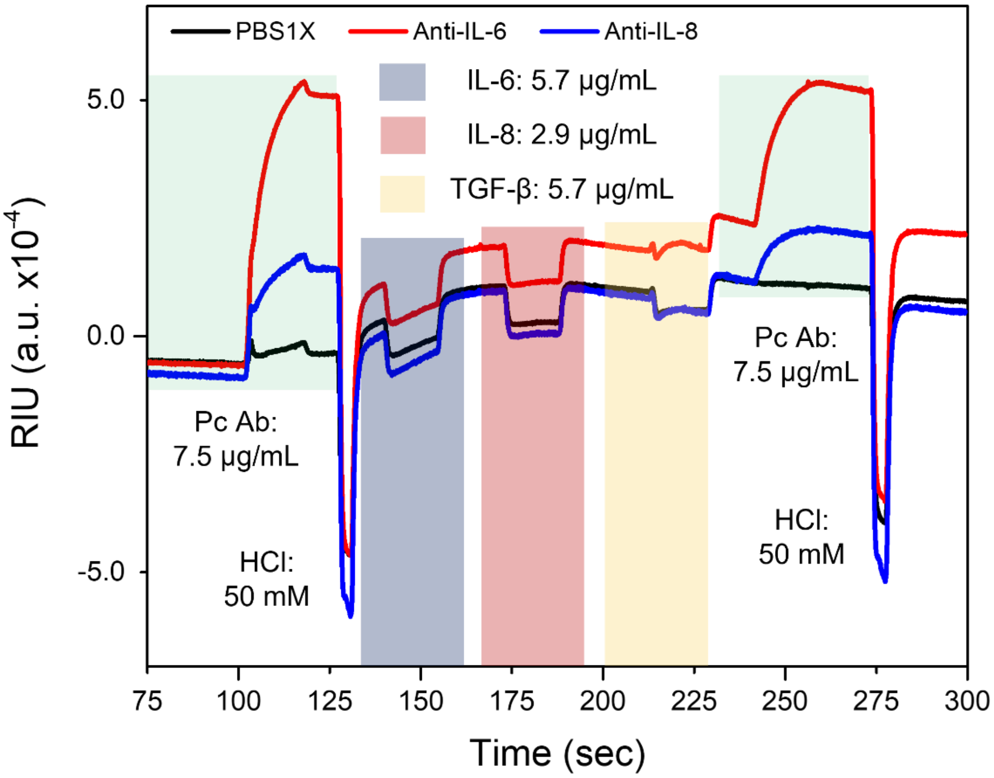

Figure 3.3.14.: Cancer biomarker sensing using Ab-N_3 - DBCO PEGs/OH Alkyls approach. Signal interaction for polyclonal secondary antibodies followed by injection of IL-6, IL-8 and TGF-β has been highlighted.

Immobilized antibodies on DBCO PEGs/OH Alkyls were confirmed by signal interaction of polyclonal secondary antibodies and subsequent regeneration, however for biomarker characterization, no signal interaction was detected for either IL-6, IL-8 and TGF-β at high concentrations. This could either be due to (i) setup sensitivity of the conventional SPRi for small biomarkers; (ii) Sensing efficiency affected by minute molecular weights ranging from 20.9 kDa to 8.9 kDa to 25 kDa for IL-6, IL-8 and TGF-β respectively. (iii) Complexity due to mixing spacing ratios where Alkyls are mixed with PEGylated chains.

Compared with polyclonal secondary antibodies having an average molecular weight of 150 kDa, the tumour markers of interest were between 6 times smaller for IL-6 and TGF-β and 17 times smaller for IL-8. For further improving the sensing efficiency for cancer biomarker analysis via DBCO – Ab-N_3 immobilization approach, detection was focused on nano-plasmonics i.e., nanohole array (NHA) integration which has been showcased to improve sensitivity parameters [70–73] and will be discussed in detail in Chapter 5.

3.5. Conclusions and Perspectives:

For fabrication of efficient plasmonic immunosensors, surface chemistry is of paramount importance. For click chemistry, DBCO as an active group is stable, reproducible, homogenous and is a suitable option for oriented coupling. DBCO PEGs/OH Alkyls have been showcased as "one-step” surface functionalization approach requiring no added activation steps. Qualitative characterization was performed through CA goniometry and AFM and comprehensive quantitative confirmation was highlighted through PM-IRRAS, XPS and ARXPS and depth profile simulations. Characterization of two different click chemistries namely thiol-yne approach via Ab-SH and SPAAC through Ab-N_3 was showcased for DBCO surfaces with either alkylated chains (DBCO/OH Alkyls) and/or PEGylated chains (DBCO PEGs/OH Alkyls). Between these surfaces, highest signal response was characterized for Ab-N_3 immobilized on DBCO PEGs/OH Alkyls.

In addition, for selection of optimal immobilization approach, comparative analysis for biosensing characterization was performed between SPAAC approach for DBCO PEGs/OH Alkyls and conventional C/NHS chemistry for NHS/OH Alkyls. Based on our characterization, favourable signal responses were analysed for Ab-N_3 - DBCO PEGs/OH Alkyls, highlighting site-specific, oriented, and directed nature of conjugation. Multiple target injections at varying concentrations were characterized along with analysis of reaction rates (ON/OFF kinetics), and calculations for target surface coverage. These results indicated DBCO PEGs/OH Alkyls monolayer to be stable for multiple target injections, and capable of regeneration and target recognition for Ab-N_3 immobilized on the surface to be concentration dependent.

Different cancer biomarkers such as interleukin-6 (IL-6), interleukin-8 (IL-8) and tumour growth factor – beta (TGF-β) were selected for biosensing application using DBCO – Ab-N_3 approach in complex culture media, however, these minute proteins were difficult to detect using conventional SPRi setup. After unable to detect such biomarkers, the focus was shifted towards: (i) characterization of different spacing ratios for DBCO PEGs 2k surfaces, where 1/0 (where no OH PEGs diluents are mixed), 1/1 (equal part functional (DBCO PEGs 2k) and diluent monolayer (OH PEGs 2k) mixed) and 1/4 (one-part DBCO PEGs 2k and four part OH PEGs 2k are mixed) approaches, and (ii) performing target recognition through nanohole array (NHA) based plasmonic sensors.

Between the spacing ratios, optimal monolayer orientation was exhibited for 1/4 DBCO/OH PEGs 2k, however as these analyses were performed in RMIT rather than INL/ECL were unable to characterize biomarker detection via this approach on the conventional SPRi setup. However, this surface approach i.e., 1/4 DBCO/OH PEGs 2k was employed for biosensing experiments through NHA-plasmonic setup at RMIT which have exhibited improved sensitivity over the conventional SPRi setup [74–76]. Cancer biomarker through NHA setup will further be discussed in detail in Chapter 5.

References:

1. S. Huertas, C., Soler, M., Estévez, M. C. & Lechuga, L. M. One-step immobilization of antibodies and DNA on gold sensor surfaces via poly-Adenine oligonucleotide approach. *Anal. Chem.* acs.analchem.0c02619 (2020) doi:10.1021/acs.analchem.0c02619.
2. Han, X., Liu, K. & Sun, C. Plasmonics for biosensing. *Materials (Basel).* **12**, (2019).
3. Jin, C. *et al.* Plasmonic nanosensors for point-of-care biomarker detection. *Mater. Today Bio* 100263 (2022) doi:10.1016/j.mtbio.2022.100263.
4. Park, J. H., Cho, Y. W. & Kim, T. H. Recent Advances in Surface Plasmon Resonance Sensors for Sensitive Optical Detection of Pathogens. *Biosensors* **12**, (2022).

5. Chumsae, C., Gaza-Bulseco, G. & Liu, H. Identification and localization of unpaired cysteine residues in monoclonal antibodies by fluorescence labeling and mass spectrometry. *Anal. Chem.* **81**, 6449–6457 (2009).
6. Zhang, Q. & Flynn, G. C. Cysteine racemization on IgG heavy and light chains. *J. Biol. Chem.* **288**, 34325–34335 (2013).
7. Vidarsson, G., Dekkers, G. & Rispens, T. IgG subclasses and allotypes: From structure to effector functions. *Front. Immunol.* **5**, 1–17 (2014).
8. Soler, M., Huertas, C. S. & Lechuga, L. M. Label-free plasmonic biosensors for point-of-care diagnostics: a review. *Expert Rev. Mol. Diagn.* **19**, 71–81 (2019).
9. Chiodi, E., Marn, A. M., Geib, M. T. & Selim Ünlü, M. The role of surface chemistry in the efficacy of protein and dna microarrays for label-free detection: An overview. *Polymers (Basel).* **13**, 1–21 (2021).
10. Gao, S., Guisán, J. M. & Rocha-Martin, J. Oriented immobilization of antibodies onto sensing platforms - A critical review. *Anal. Chim. Acta* **1189**, (2022).
11. Yang, L., Biswas, M. E. & Chen, P. Study of binding between Protein A and immunoglobulin G using a surface tension probe. *Biophys. J.* **84**, 509–522 (2003).
12. Asav, E. Development of a functional impedimetric immunosensor for accurate detection of thyroid-stimulating hormone. *Turkish J. Chem.* **45**, 819–834 (2021).
13. Ahmad, A. & Moore, E. Electrochemical immunosensor modified with self-assembled monolayer of 11-mercaptoundecanoic acid on gold electrodes for detection of benzo[a]pyrene in water. *Analyst* **137**, 5839–5844 (2012).
14. Fenoy, G. E. *et al.* Interface Engineering of “Clickable” Organic Electrochemical Transistors toward Biosensing Devices. *ACS Appl. Mater. Interfaces* **15**, 10885–10896 (2023).
15. Escorihuela, J., Marcelis, A. T. M. & Zuilhof, H. Metal-Free Click Chemistry Reactions on Surfaces. *Adv. Mater. Interfaces* **2**, 1–42 (2015).
16. Yoshimoto, K., Hirase, T., Nemoto, S., Harta, T. & Nagasaki, Y. Facile construction of sulfanyl-terminated poly(ethylene glycol)-brushed layer on a gold surface for protein immobilization by the combined use of sulfanyl-ended telechelic and semitelechelic poly(ethylene glycol)s. *Langmuir* **24**, 9623–9629 (2008).
17. Tamada, K. *et al.* Structure of SAMs generated from functionalized thiols on gold. *Thin Solid Films* **327–329**, 150–155 (1998).
18. Collman, J. P., Devaraj, N. K., Eberspacher, T. P. A. & Chidsey, C. E. D. Mixed azide-terminated monolayers: A platform for modifying electrode surfaces. *Langmuir* **22**, 2457–2464 (2006).
19. Yoshimoto, K. *et al.* Studies on the adsorption property and structure of polyamine-ended poly(ethylene glycol) derivatives on a gold surface by surface plasmon resonance and angle-resolved X-ray photoelectron spectroscopy. *Langmuir* **25**, 12243–12249 (2009).
20. Yoshimoto, K., Nishio, M., Sugasawa, H. & Nagasaki, Y. Direct observation of adsorption-induced inactivation of antibody fragments surrounded by mixed-PEG layer on a gold surface. *J. Am. Chem. Soc.* **132**, 7982–7989 (2010).
21. Xu, F. J. *et al.* Spatially well-defined binary brushes of poly(ethylene glycol)s for

micropatterning of active proteins on anti-fouling surfaces. *Biosens. Bioelectron.* **24**, 773–780 (2008).

22. Liu, B. *et al.* Design and mechanisms of antifouling materials for surface plasmon resonance sensors. *Acta Biomater.* **40**, 100–118 (2016).
23. Lecot, S. *et al.* Arrangement of Monofunctional Silane Molecules on Silica Surfaces: Influence of Alkyl Chain Length, Head-Group Charge, and Surface Coverage, from Molecular Dynamics Simulations, X-ray Photoelectron Spectroscopy, and Fourier Transform Infrared Spectroscopy. *J. Phys. Chem. C* **124**, 20125–20134 (2020).
24. Emilsson, G. *et al.* Strongly stretched protein resistant poly(ethylene glycol) brushes prepared by grafting-to. *ACS Appl. Mater. Interfaces* **7**, 7505–7515 (2015).
25. Palazon, F. *et al.* Carbodiimide/NHS derivatization of COOH-terminated SAMs: Activation or byproduct formation? *Langmuir* **30**, 4545–4550 (2014).
26. Norouzi, P., Nezamoddini, M. & Safarnejad, M. R. Antibody-oriented immobilization for newcastle disease virus detection using label free electrochemical immunosensor. *Chem. Pap.* **75**, 3061–3072 (2021).
27. Walsh, S. J. *et al.* Site-selective modification strategies in antibody-drug conjugates. *Chem. Soc. Rev.* **50**, 1305–1353 (2021).
28. Wong, L. S., Khan, F. & Micklefield, J. Selective Covalent Protein Immobilization: Strategies and Applications. 4025–4053 (2009).
29. Devaraj, N. K. & Finn, M. G. Introduction: Click Chemistry. *Chem. Rev.* **121**, 6697–6698 (2021).
30. Kolb, H. C., Finn, M. G. & Sharpless, K. B. Click Chemistry: Diverse Chemical Function from a Few Good Reactions. *Angew. Chemie - Int. Ed.* **40**, 2004–2021 (2001).
31. Spiteri, C. & Moses, J. E. Copper-catalyzed azide-alkyne cycloaddition: Regioselective synthesis of 1,4,5-trisubstituted 1,2,3-triazoles. *Angew. Chemie - Int. Ed.* **49**, 31–33 (2010).
32. Sletten, E. M. & Bertozzi, C. R. From mechanism to mouse: A tale of two bioorthogonal reactions. *Acc. Chem. Res.* **44**, 666–676 (2011).
33. MacKenzie, D. A., Sherratt, A. R., Chigrinova, M., Cheung, L. L. W. & Pezacki, J. P. Strain-promoted cycloadditions involving nitrones and alkynes-rapid tunable reactions for bioorthogonal labeling. *Curr. Opin. Chem. Biol.* **21**, 81–88 (2014).
34. Blackman;, M. L., Maksim Royzen; & Fox, J. M. The Tetrazine Ligation: Fast Bioconjugation based on Inverse- electron-demand Diels-Alder Reactivity. *J Am Chem Soc.* **130**, 13518–13519 (2009).
35. Devaraj, N. K., Weissleder, R. & Hilderbrand, S. A. Tetrazine-Based Cycloadditions: Application to Pretargeted Live Cell Imaging. *Bioconjug Chem.* **19**, 1–7 (2008).
36. Stöckmann, H., Neves, A. A., Stairs, S., Brindle, K. M. & Leeper, F. J. Exploring isonitrile-based click chemistry for ligation with biomolecules. *Org. Biomol. Chem.* **9**, 7303–7305 (2011).
37. Kashemirov, B. A. *et al.* Fluorescently labeled risedronate and related analogues: 'Magic linker' synthesis. *Bioconjug. Chem.* **19**, 2308–2310 (2008).
38. Wang, X. *et al.* Additive manufacturing of ceramics from preceramic polymers: A versatile

stereolithographic approach assisted by thiol-ene click chemistry. *Addit. Manuf.* **27**, 80–90 (2019).

39. Mohammad Mahdi Dadfar, S., Sekula-Neuner, S., Trouillet, V. & Hirtz, M. A Comparative Study of Thiol-Terminated Surface Modification by Click Reactions: Thiol-yne Coupling versus Thiol-ene Michael Addition. *Adv. Mater. Interfaces* **5**, 1–9 (2018).
40. Ruizendaal, L., Pujari, S. P., Gevaerts, V., Paulusse, J. M. J. & Zuilhof, H. Biofunctional silicon nanoparticles by means of thiol-ene click chemistry. *Chem. - An Asian J.* **6**, 2776–2786 (2011).
41. Pola, R., Braunová, A., Laga, R., Pechar, M. & Ulbrich, K. Click chemistry as a powerful and chemoselective tool for the attachment of targeting ligands to polymer drug carriers. *Polym. Chem.* **5**, 1340–1350 (2014).
42. Rojas-Sánchez, L., Sokolova, V., Riebe, S., Voskuhl, J. & Epple, M. Covalent Surface Functionalization of Calcium Phosphate Nanoparticles with Fluorescent Dyes by Copper-Catalysed and by Strain-Promoted Azide-Alkyne Click Chemistry. *ChemNanoMat* **5**, 436–446 (2019).
43. Dadfar, S. M. M., Sekula-Neuner, S., Bog, U., Trouillet, V. & Hirtz, M. Site-specific surface functionalization via microchannel cantilever spotting (µCS): Comparison between Azide–alkyne and thiol–alkyne click chemistry reactions. *Small* **14**, 1–10 (2018).
44. Kim, E. Biomedical applications of copper-free click chemistry: in vitro, in vivo, and ex vivo. **10**, (2019).
45. Gordon, C. G. *et al.* Reactivity of biarylazacyclooctynones in copper-free click chemistry. *J. Am. Chem. Soc.* **134**, 9199–9208 (2012).
46. Colombo, M. *et al.* Site-Specific Conjugation of ScFvs Antibodies to Nanoparticles by Bioorthogonal Strain-Promoted Alkyne-Nitrone Cycloaddition. *Angew. Chemie* **124**, 511–514 (2012).
47. Koo, H. *et al.* Bioorthogonal Copper-Free Click Chemistry In Vivo for Tumor-Targeted Delivery of Nanoparticles. *Angew. Chemie* **124**, 12006–12010 (2012).
48. Meghani, N. M., Amin, H. H. & Lee, B. J. Mechanistic applications of click chemistry for pharmaceutical drug discovery and drug delivery. *Drug Discov. Today* **22**, 1604–1619 (2017).
49. Rossin, R. & Robillard, M. S. Pretargeted imaging using bioorthogonal chemistry in mice. *Curr. Opin. Chem. Biol.* **21**, 161–169 (2014).
50. Lee, S. *et al.* Chemical tumor-targeting of nanoparticles based on metabolic glycoengineering and click chemistry. *ACS Nano* **8**, 2048–2063 (2014).
51. Kosaka, T. *et al.* Bioorthogonal Photoreactive Surfaces for Single-Cell Analysis of Intercellular Communications. *J. Am. Chem. Soc.* **144**, 17980–17988 (2022).
52. Yuan, D. *et al.* Site-Selective Lysine Acetylation of Human Immunoglobulin G for Immunoliposomes and Bispecific Antibody Complexes. *J. Am. Chem. Soc.* **144**, 18494–18503 (2022).
53. Gobbo, P. *et al.* Versatile strained alkyne modified water-soluble AuNPs for interfacial strain promoted azide-alkyne cycloaddition (I-SPAAC). *J. Mater. Chem. B* **2**, 1764–1769 (2014).
54. Chen, J., Rizvi, A., Patterson, J. P. & Hawker, C. J. Discrete Libraries of Amphiphilic

Poly(ethylene glycol) Graft Copolymers: Synthesis, Assembly, and Bioactivity. *J. Am. Chem. Soc.* **144**, 19466–19474 (2022).

55. Gobbo, P., Novoa, S., Biesinger, M. C. & Workentin, M. S. Interfacial strain-promoted alkyne-azide cycloaddition (I-SPAAC) for the synthesis of nanomaterial hybrids. *Chem. Commun.* **49**, 3982–3984 (2013).
56. Gai, M. *et al.* A bio-orthogonal functionalization strategy for site-specific coupling of antibodies on vesicle surfaces after self-assembly. *Polym. Chem.* **11**, 527–540 (2020).
57. Wang, X., Gobbo, P., Suchy, M., Workentin, M. S. & Hudson, R. H. E. Peptide-decorated gold nanoparticles via strain-promoted azide-alkyne cycloaddition and post assembly deprotection. *RSC Adv.* **4**, 43087–43091 (2014).
58. Fan, J. & Yang, W. Electrochemical DNA/aptamer biosensors based on SPAAC for detection of DNA and protein. *Sensors Actuators B Chem.* **353**, 131100 (2022).
59. Zhang, C., Dai, P., Vinogradov, A. A., Gates, Z. P. & Pentelute, B. L. Site - Selective Cysteine–Cyclooctyne Conjugation. *Angew. Chemie* **130**, 6569–6573 (2018).
60. Ariyasu, S., Hayashi, H., Xing, B. & Chiba, S. Site-Specific Dual Functionalization of Cysteine Residue in Peptides and Proteins with 2-Azidoacrylates. *Bioconjug. Chem.* **28**, 897–902 (2017).
61. Crivianu-gaita, V., Romaschin, A. & Thompson, M. High efficiency reduction capability for the formation of Fab ' antibody fragments from F (ab) 2 units. *Biochem. Biophys. Reports* **2**, 23–28 (2015).
62. Syed, N. *et al.* Printing two-dimensional gallium phosphate out of liquid metal. *Nat. Commun.* **9**, (2018).
63. Iwasaki, H., Nishitani, R. & Nakamura, S. Determination of Depth Profiles by Angular Dependent X-Ray Photoelectron Spectra. *Japanese J. Appl. Physics, Part 1 Regul. Pap. Short Notes Rev. Pap.* **17**, 1519–1523 (1978).
64. Paynter, R. W. & Rondeau, M. Comparison of regularization methods for the inversion of ARXPS data. *J. Electron Spectros. Relat. Phenomena* **184**, 43–51 (2011).
65. Cumpson, P. J. Angle-resolved XPS depth-profiling strategies. *Appl. Surf. Sci.* **144**–**145**, 16–20 (1999).
66. Al-Ani, A. *et al.* The influence of PEG-thiol derivatives on controlling cellular and bacterial interactions with gold surfaces. *Appl. Surf. Sci.* **462**, 980–990 (2018).
67. Kaneko, S., Urata, C., Sato, T., Hönes, R. & Hozumi, A. Smooth and Transparent Films Showing Paradoxical Surface Properties: The Lower the Static Contact Angle, the Better the Water Sliding Performance. *Langmuir* **35**, 6822–6829 (2019).
68. Yang, B. *et al.* Evaluation of Dibenzocyclooctyne and Bicyclononyne Click Reaction on Azido-Functionalized Antifouling Polymer Brushes via Microspotting. **2102325**, 1–10 (2022).
69. Tan, Y. H., Liu, M., Nolting, B., Go, J. G. & Gervay-hague, J. A Nanoengineering Approach for Investigation and Regulation of Protein Immobilization. **2**, 2374–2384 (2015).
70. Chen, K. *et al.* Rayleigh anomaly-enabled mode hybridization in gold nanohole arrays by scalable colloidal lithography for highly-sensitive biosensing. *Nanophotonics* **11**, 507–517 (2022).

71. Gomez-Cruz, J. *et al.* Cost-effective flow-through nanohole array-based biosensing platform for the label-free detection of uropathogenic E. coli in real time. *Biosens. Bioelectron.* **106**, 105–110 (2018).

72. Cetin, A. E. *et al.* Plasmonic Nanohole Arrays on a Robust Hybrid Substrate for Highly Sensitive Label-Free Biosensing. *ACS Photonics* **2**, 1167–1174 (2015).

73. Li, X. *et al.* Plasmonic nanohole array biosensor for label-free and real-time analysis of live cell secretion. *Lab Chip* **17**, 2208–2217 (2017).

74. Wang, X. *et al.* Large-Scale Plasmonic Hybrid Framework with Built-In Nanohole Array as Multifunctional Optical Sensing Platforms. *Small* **16**, 1–10 (2020).

75. Prasad, A., Choi, J., Jia, Z., Park, S. & Gartia, M. R. Nanohole array plasmonic biosensors: Emerging point-of-care applications. *Biosens. Bioelectron.* **130**, 185–203 (2019).

76. Chen, Z. *et al.* Enhanced extraordinary optical transmission and refractive-index sensing sensitivity in tapered plasmonic nanohole arrays. *Nanotechnology* **30**, (2019).

Chapter 4

Fabrication of Complex Pneumatically Actuated Microfluidic devices for Optimal trapping of cancer cells

4.1. Introduction:

Microfluidics entails the science of fluidic manipulation at micron and submicron scale. At these scales, the Reynold's number is typically very low, the viscous forces of the fluid are stronger than atmospheric inertia and the flows are laminar [1]. This allows microfluidics to be precise and reproducible and allow simulation with high confidence. Microfluidic devices are fabricated made using microfabrication techniques.

Early research focused on miniaturizing chromatographic and capillary systems [2–4], along with conventional laboratory handling and processing techniques [5]. Microfluidics have showcased applications from single/multi cell analysis to drug analysis to advanced therapeutic biosensing to high throughput screening and point-of-care diagnostics [6,7], while providing functionalities such as reduced diffusion/analysis times by at least million-fold through miniaturization. Laminar flow allows precise manipulation of micrometre-scale targets such as cells or microbeads. In addition, they allow the handling of small volume quantities, in the range of a few pL to a few nL, which facilitates the analysis of rare or expensive samples and accelerates the processes, thus improving the cost-effectiveness of the analysis. Thus, further pioneering integrated setups like lab-on-a-chip (LOC) or point-of-care systems.

Microfluidic devices offer an avenue for integration where multiple functions such as mixing, sorting, trapping, sensing and more could be incorporated into a single device, making the fabrication portable, versatile, and robust for point-of-care setups [8,9]. Thus, "lab-on-a-chip" microfluidic systems are becoming attractive solutions in the healthcare sector. Various materials have been explored in fabrication of microfluidic systems such as glass, cyclic olefin polymers (COP), Polycarbonate, 3D-printable polymers, thermoplastic based polymethylmethacrylate (PMMA, photosensitive resists SU-8 and silicon-based elastomer polydimethylsiloxane (PDMS) [10,11]. Thermoplastics such as PMMAs or COPs offer optical transparency, high mechanical strength and rigidity, good thermal stability, and low water adsorption. However, PMMA based microfluidic devices can be brittle, have low impact and chemical resistance, and have issues of mechanical stress. In addition, additional instrumentation is needed for fabrication [7].

And while these different methods have shown promise in commercial manufacture of microfluidic devices. PDMS offers similar optical transparency and thermal stability, simpler fabrication even on non-planar surfaces due to its deformability and flexibility, along with being comparatively cost-efficient [7]. In addition, PDMS is chemically stable, generally biocompatible, porous in nature for gases and solvents [6,7]. Based on their pros and cons, various groups have opted for PDMS based microfluidic devices for cell trapping and sorting [12] and biomarker analysis [13].

4.1.1. Overview:

As discussed previously, for our application, the project objective is to trap and culture cancer cells under flow so that we can analyse their biomarker secretions in real-time. To manifest this objective, a complex multilayered microfluidic design is required with multiple valves for flow manipulation and trap functions as shown in Fig. 4.1.1. To allow an analysis of the secretion over several hours, or even several days, the trapped cells must be kept alive over this period, which implies renewing their medium. Furthermore, to monitor cell secretions over a long duration, we have chosen to integrate plasmonic nanohole arrays (NHA) due to their relative simplicity of fabrication compatible interrogation strategies as discussed previously. Plasmonic nanohole arrays (NHA) are described in chapter 5.

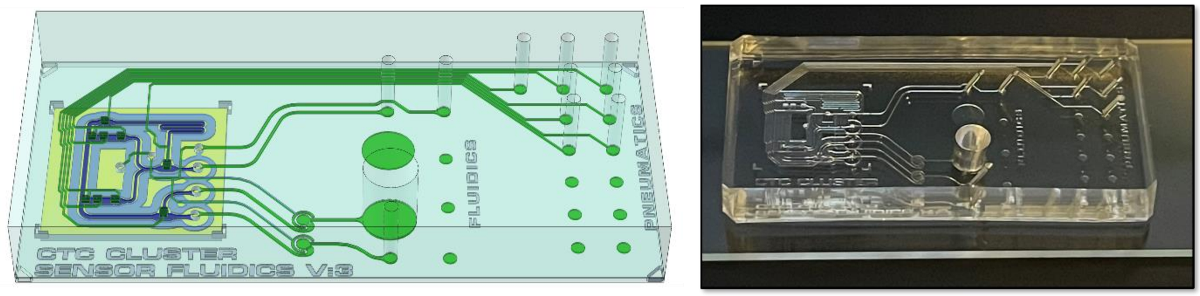

Figure 4.1.1.: Microfluidic device design for CTC Cluster V3 and fabricated device through moulding protocol on microscopic glass slide substrate.

For trapping application, pneumatic valves and trap units were fabricated through moulding protocol and controlled via simple manual syringe pump system where positioning of the syringe plungers gave us the freedom for opening and closing the valves. This was designed to not only trap the cancer cells such as CTCs, but also release or retain biomarkers secreted by the trapped cells for analysis. As such devices have multilayered configuration, negatively pressured vacuum sealing was employed around the trapping/sensing area to efficiently push the PDMS based microfluidics onto the substrate providing an avenue for reusability for device characterization of the fluidic systems. In addition, this vacuum sealing was imperative for valve actuation. For further limiting bubble formation during analysis, pillar-based bubble traps were adapted from Lochovsky and group, and integrated. Such traps further pushed aberrant bubbles formed during fluidic handling to be dissipated onto the PDMS which is porous for gases/bubbles [14].

This chapter focuses on the fabrication of such complex microfluidic systems as highlighted in Fig. 4.1.1. capable of trapping cancer cells. In addition, characterization of such devices is showcased through valve actuation for fluidic pathway optimization and trap unit functionality for trapping efficiency. Initial characterization of various valves based on their size, alignment and structure is further presented and fluidic pathway characterization, flow rates are measured in different configurations. Afterwards, primary trapping is presented with microbeads and then metastatic breast cancer cell line MCF7 are shown to be trapped within the device. And to have an idea about the range of biomarkers that could be secreted from such trapped cancer cells, enzyme linked immunosorbent assays (ELISA) for associated biomarkers such as fibronectin and interleukin-6 (IL-6) is performed.

4.2. State of the Art:

4.2.1. Integrated Biosensors for lab-on-a-chip (LOC) development:

Development of lab-on-chip (LOC) systems stemmed from the integration of biosensing element with a microfluidic platform for directed analysis of biological interactions. Different microfluidic functions like injection, reaction and separation can be coupled onto a single compact device offering optimal onsite functionality.

Such systems, offer higher stability with optimal onsite functionality. In addition, device characteristics focusing on real-time and improved limit of detections, and importantly portability can be provided through such integration. There are numerous research groups focusing on developing such lab-on-chip systems for multiple biosensing application. Different types of biosensors with piezoelectric, electrochemical, and optical transducers that have been discussed in detail in Chapter 2, are generally coupled with microfluidic platform for cancer cell and associated biomarker analysis. However, based on our application, label-free optical biosensors offer flexibility for integration with PDMS based microfluidic devices [13].

For multiplexed detection of cancer biomarkers in low concentration, various optical biosensing modalities ranging from fluorescence and luminescence based, to surface enhanced Raman scattering (SERS) to surface plasmon resonance (SPR) based to localized surface plasmon resonance (LSPR) and nanohole array (NHA) based approaches have been applied [13]. One of the examples relied on a modular microfluidic biosensor approach integrated with quantum dots (QDs) for multiplexed detection of various cancer markers [15] i.e., carcinoembryonic antigen (CEA), cancer antigen 125 (CA125) and receptor tyrosine-protein kinase (Her-2/Neu or C-erbB-2). For analysis, a sandwiched immunoassay coupled with QD-labelled detecting antibody was used where the cancer antigens bind and captured by microporous agarose bead array within the chip. The performance of this system was showcased with integrated sample pre-treatment along with biomarker detection in biological samples such as serum and saliva [15].

Another example relied on an aptamer/graphene oxide (GO) based Förster resonance energy transfer (FRET) approach where multiple cancer cell samples were analysed at the same time by parallel homogenous detection to develop a multiplexed cancer cell sensor chip [16]. These integrated lab-on-chip systems for cancer biomarker sensing have been showcased in Fig. 4.1.2. As mentioned previously in Section 2.4.3., comparative analysis highlighted for label-based optical sensors employed for such integrated devices have their short comings such as bleaching, non-specific labelling and false results which in turn, reduces their overall efficiency.

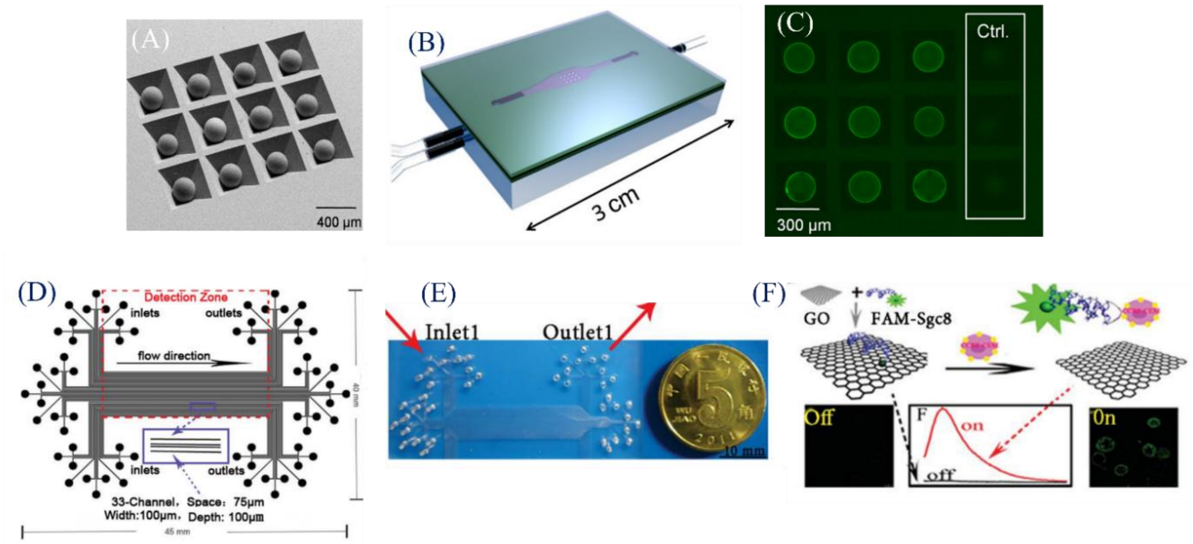

Figure 4.1.2.: Examples of Integrated biosensing-microfluidic devices for cancer biomarker sensing **(A)** SEM photomicrograph of beads in anisotropicaly etched silicon chip. **(B)** Sealed lab-on-chip assembly. **(C)** Fluorescent image of beads after immunoassay including negative controls as imaged with one second of CCD camera integration (exposure) time [15]. **(D)** Schematic setup of Graphene oxide-based FRET apta-sensing microfluidic chip and **(E)** the photograph of the GO-

based FRET apta-sensing microfluidic chip. Scale bar: 10 mm. **(F)** The principle of a 'signal-on' apta-sensor for detecting CCRF-CEM cells by assaying the cell-induced fluorescence recovery of GO/FAM-Sgc8 [16].

4.2.2. Trapping and Culturing cells in lab-on-a-chip (LOC):

One of the effective biological applications microfluidic technologies has in its arsenal is directly manipulating and analysing single cells or multi cell clusters. Microchannel dimensions at µm and sub-µm level for media exchange, ambient temperature and humidity can be precisely controlled within the vicinity of captured cells of interest, making device handling and analysis more flexible and easier.

Compared to conventional approaches, microfluidics can optimally perform single-cell and multi-cell analysis from effectively sorting to trapping and then culturing cells of interest. Thus such approaches can then be applied for several biological applications such as cell-migration, drug metabolism and toxicity testing along with high-throughput screening on a cellular level [12].

It can be performed on physical (like size, mechanical or electrical properties) or biological properties of the cells. For single cell culturing, initial approach focuses on sorting cells of interest and then trapping them in integrated specialized functional structures. Different approaches have been developed for cultured cells using various shapes and structuration.

One research group focused on a continuous cell-culture platform with eight U-shaped micro sieves in each cell chamber. The fluidic velocities were substantially lowered for the surrounding apertures due to these micro sieves which optimally trapped the cells without flushing them after trypsinization. In addition, for this microfluidic iteration, each chamber was capable of repeatedly growing cells to confluence and subsequent trypsinization and recovery was possible [17].

Similar approach of U-shaped trapping sites with continuous perfusion were used as a mean for hydrodynamic cell-trapping method with flow conditions for formation of compact spheroids. For this iteration, manipulation of flow rate controlled the speed and size of the spheroid formation and provided a way for anti-cancer drug assays [18]. In our group at INL, previous work focused on negative depletion of CTC though white blood cells (WBCs) immunomagnetic trapping. Neodymium magnet (NdFeB) particles were mixed in PDMS to create self-assembled micro-magnets integrated within a microfluidic device to act as micro-traps [19,20]. These examples for cell trapping through microfluidic systems have been showcased in Fig. 4.1.3. While existing approaches achieve impressive results, we require an approach that allows for fluidic isolation, in order to retain low concentration biomarkers secreted from our cells of interest [21].

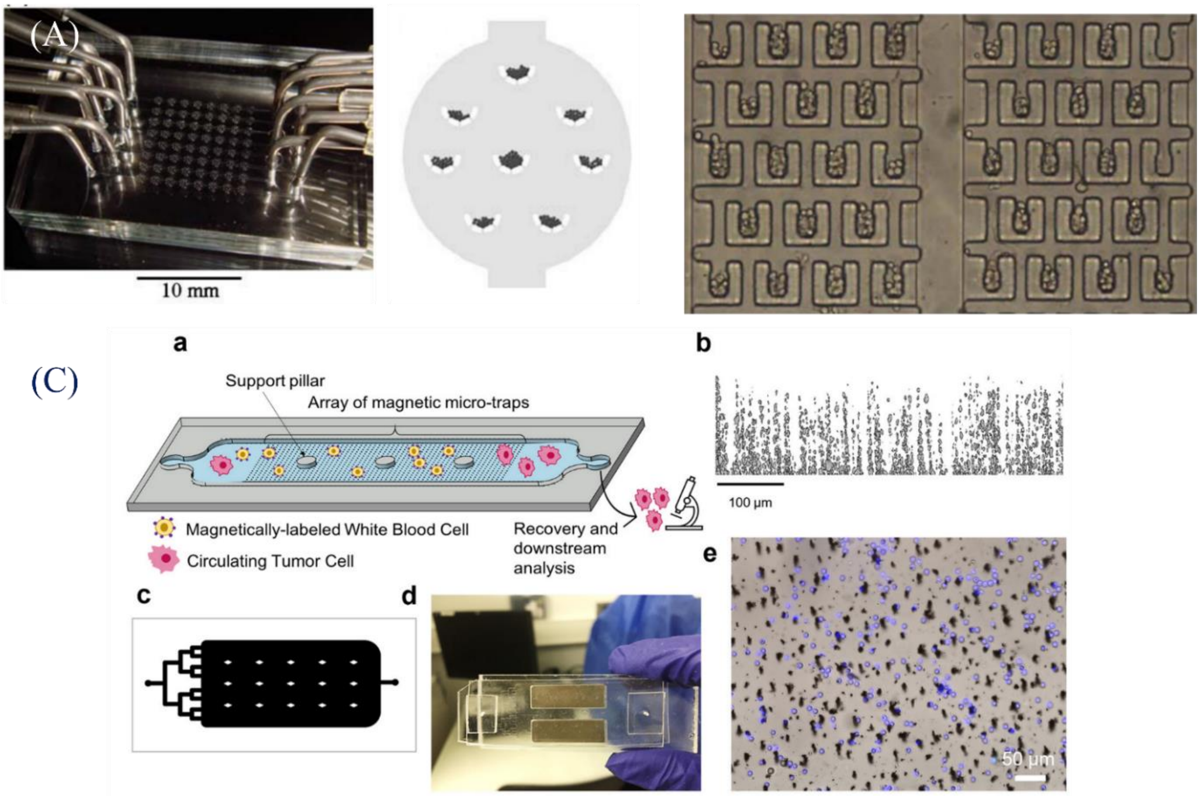

Figure 4.1.3.: **(A)** Image of the microfluidic device with fluid interconnects and simulation results for cell capture based on an input cell density of 106 cells ml^{-1}, a flow rate of 1 µL min^{-1} through the chamber, and a total flow time of 1.5 min [17]. **(B)** Spheroid array uniformity (a) The image taken right after MCF7 cell loading illustrates that the cells filled up the trap space uniformly [18]. **(C)** MagPure chip design and principle. (a) Schematic of the device for the negative selection of CTCs. Magnetically labeled WBCs are captured on magnetic micro-traps while CTCs are collected for downstream analysis. (b) Cross-section view of the composite membrane, located below the channel's floor, integrating chain-like NdFeB microstructures (magnetic micro-traps). (c) Design of the trapping chamber (0.1 × 20 × 40 mm3) which consists of cascade input channels and one single straight output channel and diamond-shaped support pillars (2 × 1mm2). All channels are 970 μm wide. (d) Picture of the compact system with the two milli-magnets located below the trapping chamber. (e) Composite microscopy image of captured WBCs on magnetic micro-traps integrated into the MagPure chip [22].

4.2.3. Valve integration in microfluidic device (or Lab-on-a-chip):

For actively trapping, culturing, and analysing cells, complex fluidic manipulation is required which could be achieved by valve integration within microfluidic systems. In addition, such valve based systems allow for wider applications in single and multi-cell trapping and sequencing for multiplexed immunoassays and biosensors [23]. Furthermore, such systems allow greater level of automation specifically for cell micro-culturing (cell culturing at micro and sub-micro levels in microfluidic devices).

Research from early 2000s focused on the fabrication of complex microfluidic systems integrating actuatable valves [24–26]. Early researchers focused on the control, with valves, of a high-density array of pico-litre chambers with multiple compartments. The principle of pneumatic systems focuses on on-chip control where microvalves can be opened and closed on demand. The principle of pneumatic systems is based on the application of negative or positive pressure to open or close on demand microfluidic channels. For such microfluidic designs, pneumatic routing lines and fluidic channels must be integrated for device functionality. Fundamental components of an integrated microfluidic circuit comprise of valves, pumps, and channels for optimal fluidic manipulation.

Such circuits and devices depend on the specific microfluidic function (separation, trapping, mixing and injection among others) and performance criteria focuses on size, channel dimensions (ranging from 10s to 100s microns, dead volume, valve actuation pressure and device scalability. Such microfluidic multiplexors increased fluidic processing power with minimal controlled inputs as presented in Fig. 4.1.4. These microfluidic arrays were designed in a way, where each fluidic channel was controlled by its own individual valve control channel.

For functionality of such Quake valves, a 'control' layer is coupled with a harboured channel for valve actuation while 'flow' layer of either air or liquid was situated on top that contained a controllable channel network within [26]. Fluidic manipulations for biological assays were performed within the flow layer and a valve was created when the control channel crosses the flow channel. For channel deflection on the membrane junction, hydraulic actuation was employed [26].

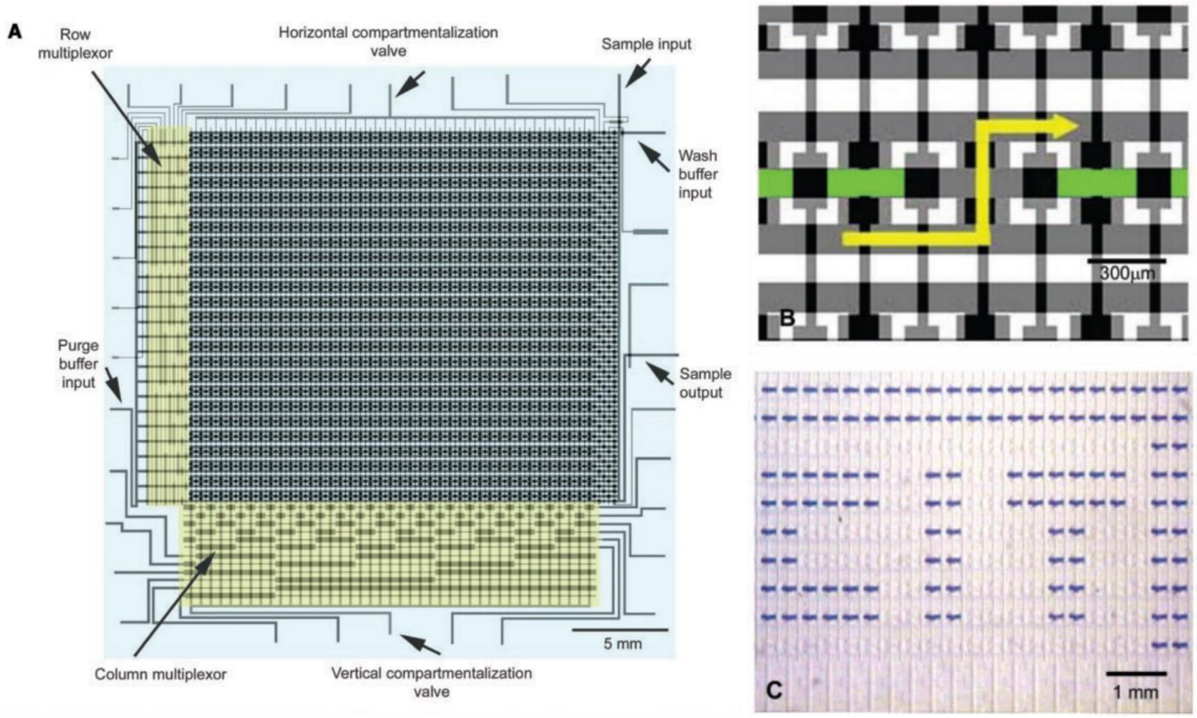

Figure 4.1.4.: Fabrication and actuation of early valves **(A)** Mask design for the microfluidic memory storage device. The chip contains an array of 25 ⫻ 40 chambers, each of which has a volume of ∕250 pl. Each chamber can be individually addressed using the column and row multiplexors. The contents of each memory location can be selectively programmed to be either blue dye (sample input) or water (wash buffer input). **(B)** Purging mechanics for a single chamber within a selected row of the chip. Each row contains three parallel microchannels. A specific chamber is purged as follows: (i) Pressurized fluid is introduced in the purge buffer input. (ii) The row multiplexor directs the fluid to the lower channel of the selected row. (iii) The column

multiplexor releases the vertical valves of the chamber, allowing the pressurized fluid to flow through the chamber and purge its contents. **(C)** Demonstration of microfluidic memory display: Individual chambers are selectively purged [26].

To further improve functionality and integration of these Quake valves, different aspects like controllable pneumatic actuation was focused on by various researchers. Our group at RMIT specifically focused on lifting gate valves that achieve similar functionality by limiting fabrication complexity. Compared with Quake valves, lifting gate valves are normally closed, and provide better fluidic isolation [21,27–30]. Such devices should be simple to use, can provide automated operations and be compatible for scalable fabrication. In addition, performance for such platforms be vital with dynamic functionality and proper fluidic isolation [8,27].

As mentioned above, our group followed up on the research entailing pneumatically actuated valves by focusing on simpler fabrication and easier interface alignment which could be further exploited for sensor integration. Compared with conventional method, fabrication methods focusing on moulding protocol pioneered by Szydzik and group at RMIT, offer flexibility and provide exceptional multifaceted fluidic handling. In addition, such techniques exhibited large degree of on-chip control. Numerous biosensing and lab-on-a-chip applications have been showcased previously for automation based pneumatic microfluidic systems [21,27,28,31].

Our biological application focuses on trapping cancer cells under flow and to achieve our target, we focused on actuation of pneumatic valves. These valves provide an avenue where in closed configuration, cells and biomarkers secreted directly from trapped cells are isolated for analysis within a discrete volume. One of the key challenges of such configuration, is the shear stress imparted on cells overflow and dilutions in biomarker concentrations flushed during medium exchange. Multilayer microfluidic structures and pneumatic valves for regulation of pressurised fluidic flow, were fabricated using reusable moulds patterned with high resolution maskless photolithography.

Application of the pneumatically actuated on chip valves in use as flow regulators of pressure driven fluids in a droplet slug-based system have been highlighted in Fig. 4.1.5 [31]. This system is an initial proof-of-concept prototype where pneumatic valves actively modulate coloured water dispensed into each droplet. Such designs are planned for investigating the effects of various drug concentrations and combinations on the morphology of blood cells under flow [31]. Controlled interconnects and isolated overpasses were required for valve control and actuation shown in Fig. 4.1.5 [31].

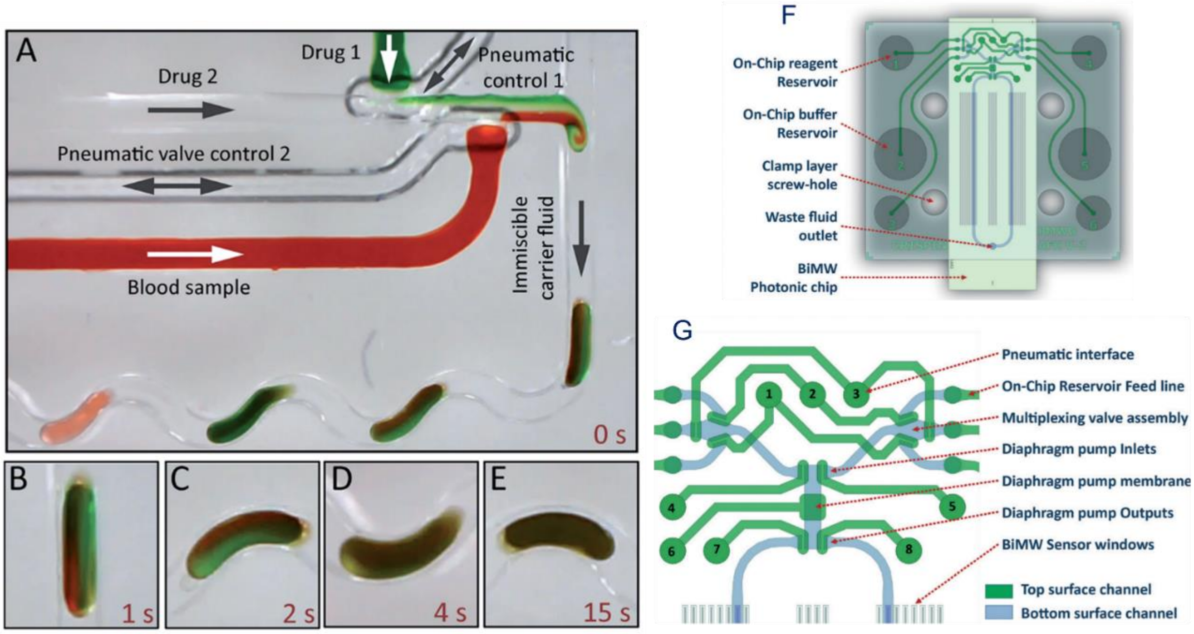

Figure 4.1.5.: (**A**) Application of the pneumatically actuated on chip valves. (**B**–**E**) show mixing of reagents within a slug at various time points Schematic of the automated microfluidic module and its various components. (**F**) Highlights locations of the primary fluidic reservoirs and overall alignment of the microfluidic and the photonic sensor, while (**G**) demonstrates an enlarged schematic of the various active microfluidic components, with features on the top surface of the injection moulded PDMS slab shown in green, and the bottom layer shown in blue [32].

The following section will highlight the materials and methods for fabrication of our microfluidic platform for cancer cell trapping.

4.3. Materials and Methods:

4.3.1. Microfluidic device fabrication:

For fabrication of PDMS microfluidic devices, similar protocols outlined in [21,27–29] were followed, where highlighted in Fig. 4.2.1., complementary moulds were realised using photolithographic methods. Multilayer designs were patterned onto two different silicon wafers. The top wafer had indentations for pneumatic and fluidic routing, actuation chambers and viaduct pathways, while the bottom mould consists of all the structures intended to contact the sensor platform, including channels, valves, traps units and bypass.

The multilayer design incorporating pneumatic lifting gate valves and their associated actuation systems were design with Solidworks - and patterned into Su8 3050 using a maskless photolithography tool (Heidelberg Instruments MLA150). Additionally, peg/hole alignment structures were integrated onto the design for manual alignment of complementary moulds. As showcased in Fig. 4.2.1. (A) top and (B) bottom layers were patterned onto two different mould halves of 4-inch, 500 µm thick silicon wafer substrate.

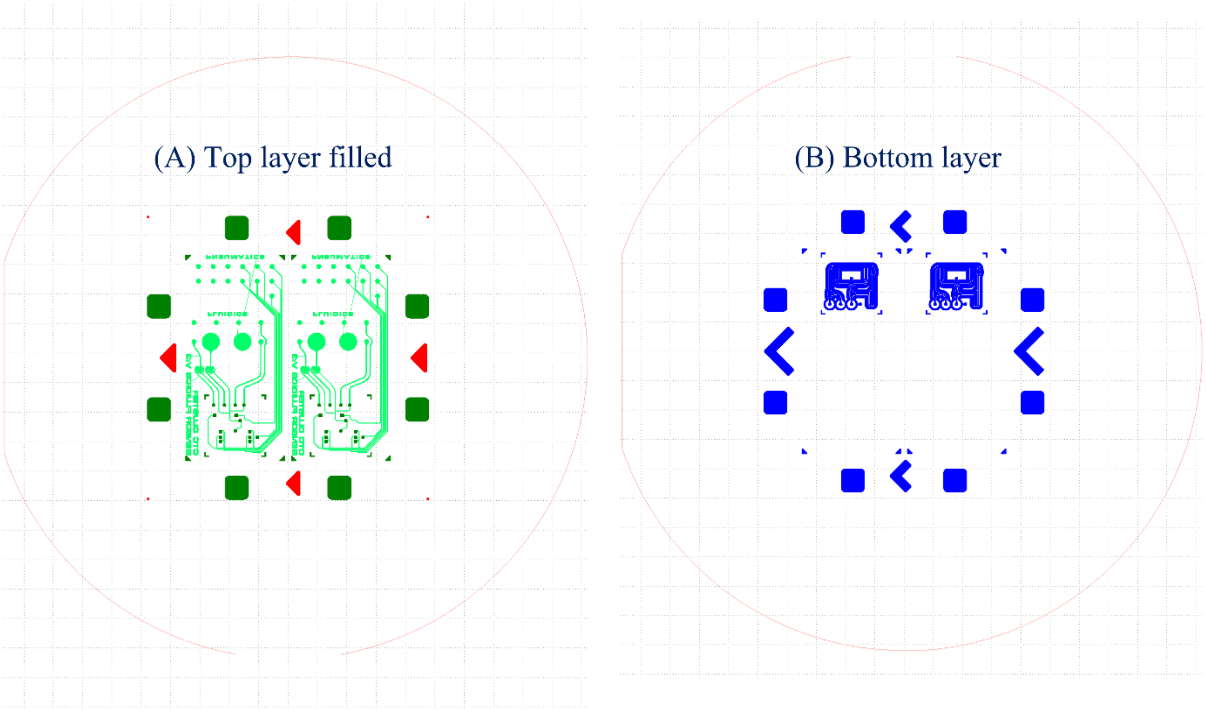

Figure 4.2.1.: Schematic of lithography moulds for CTC Cluster V3; **(A)** top layer filled and **(B)** bottom layer designed at RMIT.

Silicon wafers provided optimal adhesion of photoresist. SU-8 3050 series photoresist (MicroChem Corp) was used to produce channel structures on the mould with a height of 100 and 75 µm. Commercial silanes (1H,1H,2H,2H-Perfluorooctyltriethoxysilane, Sigma Aldrich) [33] were covalently attached on the surface providing passivated and non-reactive surface that facilitates mould release.

The aligned top and bottom layers have been presented in Fig. 4.2.2. The use of lithography allows generation of high resolution for valve gates and achieving small trap feature size; however, this process is labour-intensive and require cleanroom facilities.

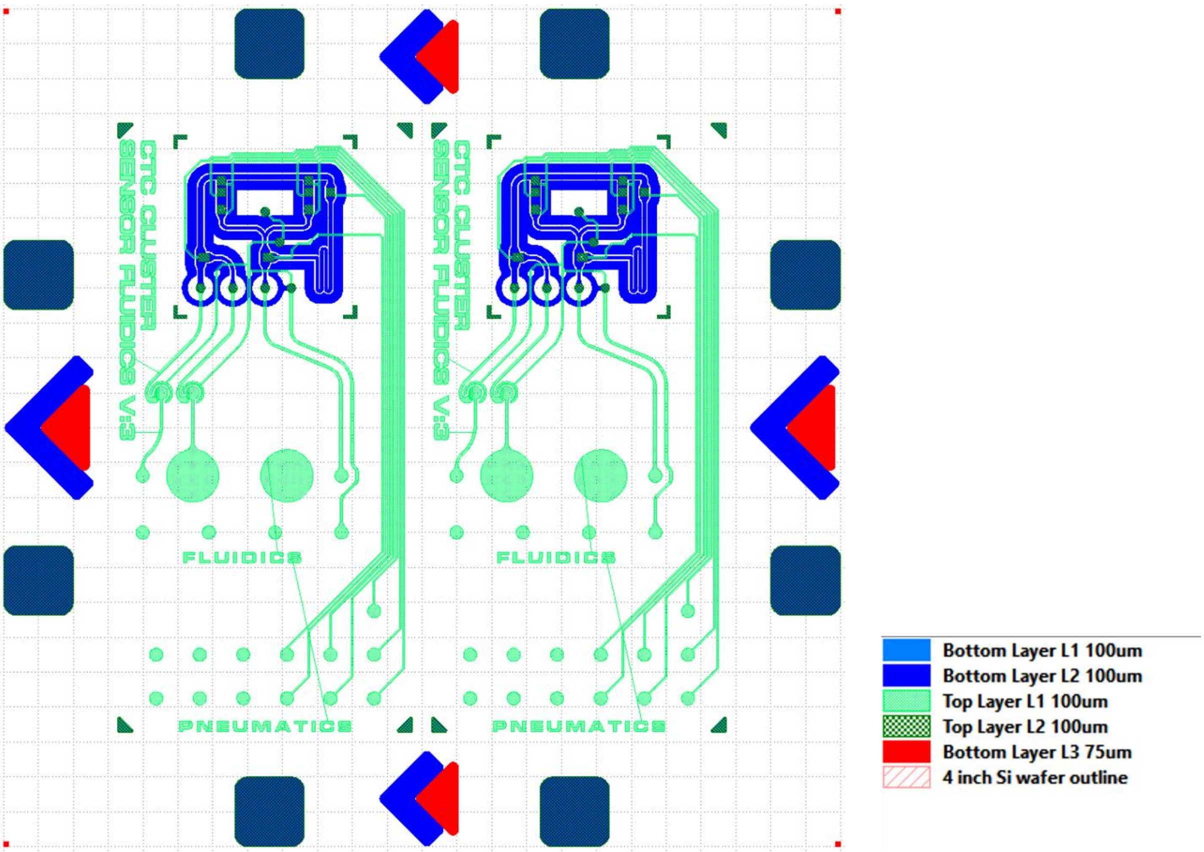

Figure 4.2.2.: Schematic of lithography mould for CTC Cluster V3 where both top and bottom layers are aligned with different depth thickness for layers highlighted.

4.3.2. Moulding protocol:

PDMS slab components were fabricated using PDMS Moulding technique, which was already published in peer-reviewed journals [9,27,34].

a. Standard 1:10 ratio of PDMS pre-polymer (Sylgard 184, Dow Corning USA) with curing agent: PDMS is mixed and degassed.
b. Further degassing of the pre-polymer solution is performed for additional 30 minutes under high vacuum (~ 0.2 millibar) like those used in plasma treatment units. This limits bubble formation trapped within the gas-impermeable mould structures, which can further absorb onto the highly degassed PDMS pre-polymer.
c. Sufficient solution of degassed pre-polymer PDMS was spread on the top mould and bottom mould of the encapsulated structure. Use of increase volume rather than less was preferred as this ensures bubble formation to be minimized and not adhered to the mould structure can flow out from between the moulds
d. Contact is made with the top mould half and the bottom mould half. Mould halves with pre-polymer were placed on top of each other until contact is made. Alignment is achieved automatically through use of alignment pin and slot structures patterned into the top and bottom moulds respectively. This was done to interface with the channel structures as shown in Fig. 4.2.1.

e. Moulds were placed on an angle (approx. 10 degrees) with a small weight on the top wafer (approx. 50grams) allowing locking of peg/holes structures while applying sufficient pressure for firm contact between the two mould spacer structures.
f. Following alignment, mould structures were placed in an oven at 130˚C curing temperature for 30 mins.
g. After moulds are removed from the oven during cooling, mould separation begins to occur spontaneously. Firstly, passivated top mould half is removed through gentle insertion of soft tool such as plastic tweezers or fingernails between the mould halves.
h. Following mould release, the PDMS slab was cut to size and peeled. Afterwards, appropriately aligned pneumatic interface holes (0.75 mm) and on-chip fluidic reservoirs were biopsy punched through an approximately 4-5 mm thick interface slab.
i. Finally, the moulded slab and punched interface slab were aligned and then plasma bonded with 1 min O2 plasma (Harrick plasma).

4.3.3. Flow rate control:

As described previously, the device is integrated with a vacuum chuck, which seals the completed device to the glass surface. The vacuum chuck functions via negative pressure, where syringe of 50 mL volume, which functions at levels below 0.5 bar to make an optimal seal. This makes the device reusable for preliminary testing, which could be very useful for the initial characterization of biosensors.

For valve actuation, negative pressure was applied via simple manual syringe pump system. Syringes of 1 mL capacity with rubber plungers were used. Specifically for trapping through sieve valves was performed through different configuration on the syringe pumps highlighted in Fig. 4.2.3. by partially opening or closing and completely opening and closing the valves.

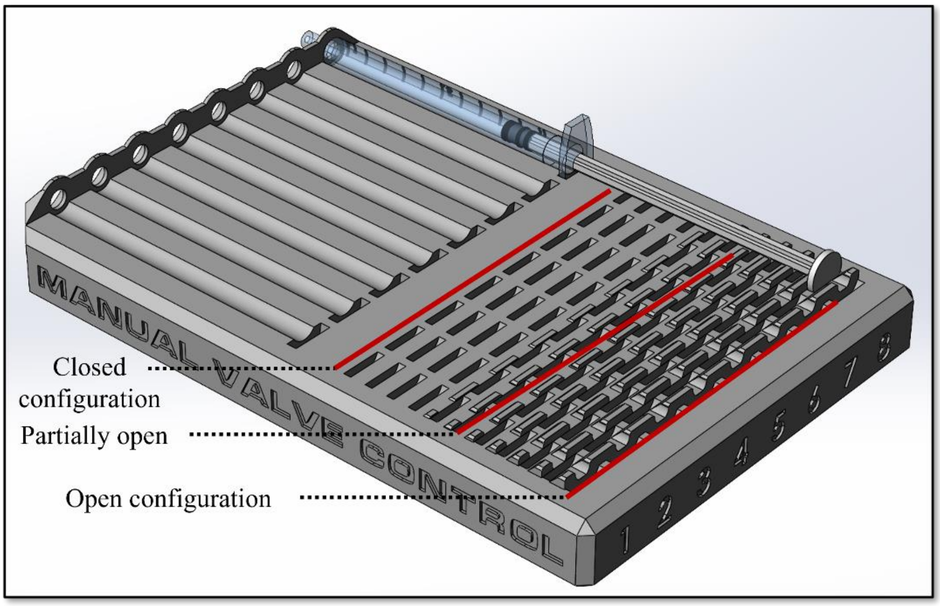

Figure 4.2.3.: Schematic of manual syringe pump fabricated at InPAC, RMIT university for valve actuation. Configurations of syringe locations for open, partially open/close, and close settings are highlighted.

A basic negative pressure pump was also used to drive fluid flow - a 50ml falcon tube was sealed with tubing connectors interfaces with a lure connector and the fluidic device, where aspiration of syringes ranging from 1 mL to 5 mL were used to establish flow as highlighted in Fig. 4.2.4.

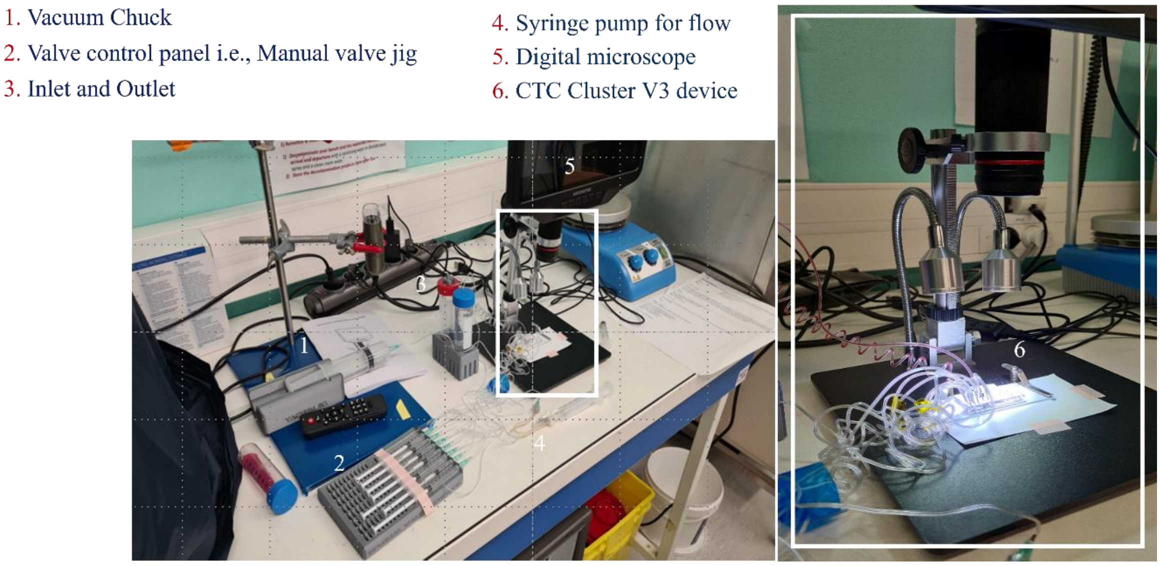

Figure 4.2.4.: Schematic for device setup highlighted with 1. Vacuum chuck, 2. Valve control panel, 3. Inlet and Outlet, 4. Syringe pump, 5. Digital microscope and 6. CTC Cluster V3 for bead characterization.

For co-flow manipulations at ECL/INL, 1 mL Eppendorf tubes were used for cell introductions and this microfluidic system was tuned using additional gravity driven flow. The Eppendorf tube for optimal co-flow had to be on level or a bit higher from the initial device height for additional gravity induced flow. If not aligned properly, backflow into the Eppendorf tube was observed if the tube is below the device height at P=0, thus a slight positive pressure was required for optimal laminar co-flow to fine tune the overall system at ECL/INL.

For characterization of flow rates, multiple measurements were performed for different fluidic pathways by valve manipulation through injection of coloured dyes. Flow rates were specifically calculated by measuring how much fluid from defined volume through a falcon tube was passed through the microfluidic system over time.

4.3.4. Sample Preparation:

4.3.4.1. Bead suspension:

Polystyrene microbeads of 50 to 100 microns in diameter supplied by Biovalley were used as models in the first steps of characterization of the trapping efficiency in the chambers. This characterization was performed both at RMIT and INL with

1-100 beads per µL suspended in PBS1X and 1% Gibco™™ Pluronic™ F-68 solution. Before bead introduction, BSA solution was injected for surface passivation of the microfluidic channels. Since beads tend to sediment in the tubes, prior to introduction, beads were actively resuspended using pipettes as to dislodge the from the bottom of the Eppendorf tubes. After trapping, beads were then released to check the functionality of valved gates.

4.3.4.2. Cell Suspension preparation:

Two different kinds of cells were used: MCF7 metastatic breast cancer cells and SK-OV-3 metastatic ovarian cancer cells that were both procured from ATCC cell banks. MCF7 cells were used to characterize the performance of the microfluidic device while SK-OV-3 cells were used for ELISA tests.

4.3.4.2.1. MCF7 cells:

Dulbecco's Modified Eagle Medium (DMEM) were brought from Gibco™. The medium was further characterized using 10% foetal bovine serum of final volume preparation and 1% penicillin-streptomycin to limit bacterial growth. MCF7 cells were prepared before each experiment by Dr. Magalie Faivre and then sub-cultured before trapping experiments at UCBL. For sub-culturing of MCF7 cells as shown in Fig. 4.2.4., ATCC protocol for cell handling was followed before cell trapping:

a. Corning® T-75 flasks were used for subculturing and volumes used for this protocol were for such flasks.
b. It is necessary if floating cells are presented as shown in Fig. 4.2.2. to be transferred for first two subcultures as shown in the protocol. Cell transfer is not required for following transfers for floating cells for subsequent subcultures.
c. Transfer the culture medium from the initial cell flasks to a centrifuge tube. Prepare 0.25% (w/v) Trypsin – 0.53 mM EDTA solution for brief rinsing of the cell layer to remove serum traces from the cells containing trypsin inhibitor.
d. Add 2-3 mL of this solution to the flask and observe cells under inverted microscope until cells are dispersed.
e. This takes around 5 to 15 minutes. For optimal dispersal and dislodgement place the flask with the cells in 37 ° C incubator.
f. Aspirate cells gently by pipetting and introduce 6 to 8 mL of complete growth medium.
g. Transfer the cell suspension to centrifuge tube with the initial medium from step (a).
h. Centrifuge at 125x g for 5 to 10 minutes, subsequently discarding the supernatant.
i. In the fresh growth medium, resuspend the cell pellet obtained in the previous step.
j. Add appropriate cell suspension aliquots to the new culture vessels and incubate the cultures at 37° C. Subculturing was performed every 48 hrs for optimal growth.

Sub-cultivation Ratio: A sub-cultivation ratio of 1:3 to 1:6 is recommended

Medium Renewal: 2 to 3 times per week

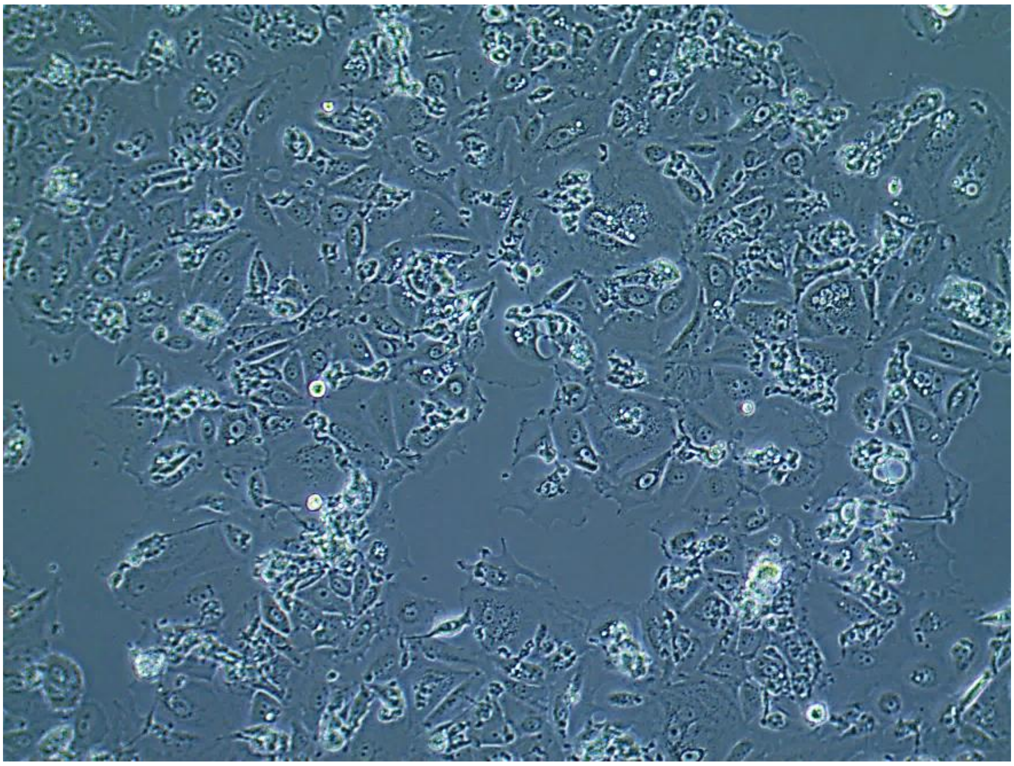

Figure 4.2.5.: MCF7 Metastatic Breast cancer cell line under confocal microscope at 20X observation.

4.3.4.2.2. SK-OV-3 cells:

SK-OV-3 cells were prepared before each biomarker secretion experiments by Dr April Kartikasari at RMIT Bundoora campus. ATCC protocol for sub-culturing of SK-OV-3 cells as presented in Fig. 4.2.5. were followed before ELISA:

a. Discard initial culture medium, the cells should be as shown in Fig.4.2.3.
b. Rinse the cell layer briefly with 0.25% (w/v) Trypsin – 0.53 mM EDTA solution. This is performed to remove all serum traces from the cells that contain trypsin inhibitor.
c. Add 2-3 mL of this Trypsin-EDTA solution and observe the cells under inverted microscope until cell layer is completely dispersed. This takes around 5-15 minutes.
d. To minimize clumping, avoid agitating cells by hitting or shaking the flask while waiting for the cell detachment.
e. For optimal removal of cells and facilitate dispersal, place the cells at 37 ° C. Corning® T-75 flasks were used for subculturing.
f. Aspirate cells by gentle pipetting and add 6 to 8 mL of complete growth medium and introduce appropriate cell suspension aliquots to new culture vessels.
g. Incubate the cells at 37 ° C. Subculturing was performed every 48 hrs.

Sub-cultivation Ratio: A sub-cultivation ratio of 1:2 to 1:6 is recommended
Medium Renewal: 2 to 3 times per week

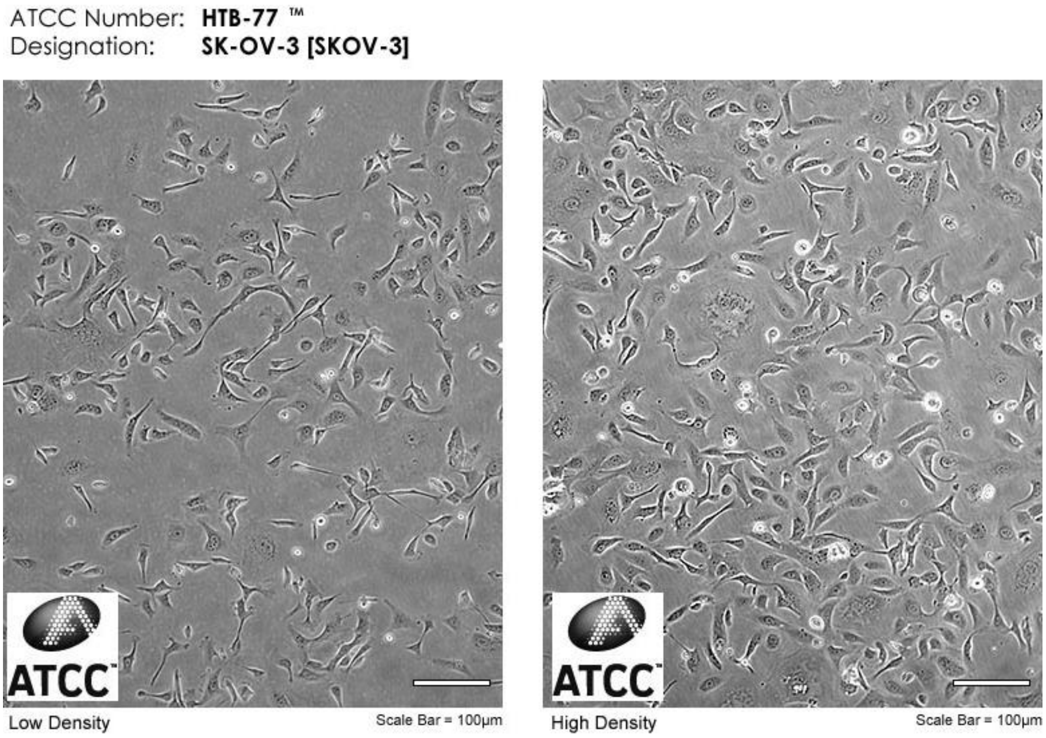

Figure 4.2.6.: SK-OV-3 Metastatic Ovarian cancer cell line under confocal microscope.

4.3.4.3. ELISA: SK-OV-3 cells

4.3.4.3.1. Principle:

The principle of Enzyme Linked Immunosorbent Assays (ELISA) focuses on exploitation of monoclonal antibodies specific for specific proteins of interest for quantitative measurements in supernatants, buffered solutions, serum, plasma, and other body fluids. For sandwich ELISA, characteristic monoclonal antibodies are coated on the wells and samples containing proteins of interest are coupled once introduced in the well. For 2-step incubation, initial incubation focuses on specificity between samples and the biotinylated monoclonal antibodies. Streptavidin-HRP (HRP: Horseradish peroxidase) enzyme complex is introduced for the second step after washing, and subsequently washed. Coloured reaction is analysed after the addition of TMB solution (3,3', 5,5; -tetramethylbenzidine) that binds to the attached enzyme complex. The presence of interested protein depends on the intensity of this reaction that is directly proportional to concentration of the protein in the sample.

For cell number calculations, cells grown in 6 well plates with 2 mL total volume, the cells were $1.7x10^6$ while the cells grown in T75 flasks with 10 mL total volume were around $6.1x10^6$. For cells grown in T75 flask, trypsinization was performed to dislodge the cells in addition to lipopolysaccharide (LPS) stimulation for immunoactivity.

4.3.4.3.2. Kit specifications: Fibronectin

Fibronectin secretion in SK-OV3 cells were characterized by using the Human Fibronectin ELISA Kit (ab219046). It is one-wash 90-minute protocol with sensitivity of up to 20.6 pg/mL and range of 125 pg/mL to 8000 pg/mL. This ELISA kit could be used for cell culture extracts and supernatants, plasma and milk, serum, and tissue extracts. For our experiments, analysis was performed on cell culture extracts and supernatants. It is a colorimetric based sandwiched assay that is reactive for human and rhesus monkey species. General protocol for the kit were followed.

4.3.4.3.3. Kit specifications: Interleukin-6

For Interleukin-6, like fibronectin, ELISA kit was procured by Abcam, titled Human IL-6 ELISA Kit High Sensitivity (ab46042). Kit sensitivity is around 0.8 pg/mL and range are between 1.56 pg/mL to 50 pg/mL. This kit is suitable for cell culture supernatant, plasma, and serum. It is a colorimetric based sandwiched assay that is reactive for humans. General protocol for the kit were followed.

4.4. Results and Discussions:

4.4.1. Device Description:

The objective of the CTC Cluster V3, an integrated optofluidic device is to trap cancer cells having size greater than 10 microns in diameter, actively perfuse them with culture medium for several hours and detect directly secreted biomarkers with an optical sensor. It is the culmination of two design upgrades (V1 and V2).

The device is made up of three sections: Pneumatics, Fluidics and Sensor contact area. Pneumatics consisted of seven interfaces in total, focusing on 4 castellated or V-gate isolation valves and 3 sieve valves. Fluidics are made up of a media inlet/input and waster outlet/output for flow control, CTC cluster reservoir for co-flow integration used to regenerate medium and vac chuck interface for temporarily pushing the device onto the substrate. In addition, the fluidic compartment contained bubble traps to minimize bubble formation during flow operation. The trapping function for the device are incorporated within the sensor contact area consisting of valve controls for the inlet and outlet along with two trap units for cell trapping.

The device is integrated with two trapping chambers having 50 nL volume capacity, and V-gated isolation valves highlighted in Fig. 4.3.1. As mentioned previously, the configuration was designed in a way to trap cells and then perfuse media to keep the cells viable for a long time. The device is fabricated by moulding protocol where channels, valves and trap unit designs were patterned through maskless lithography, as describe previously. In addition, the device design consisted of two layers (top layer and bottom layer) along with the substrate layer which in our case are glass slides, where the device is temporarily sucked onto the substrate.

The top layer has a deep upper section that is bonded onto the bottom layer by permanently bonding through plasma treatment. Bottom layer on the other hand consists of design indentations for microfluidic features around the trapping and sensing area. Both these layers are then pushed onto the substrate layer via negative pressure.

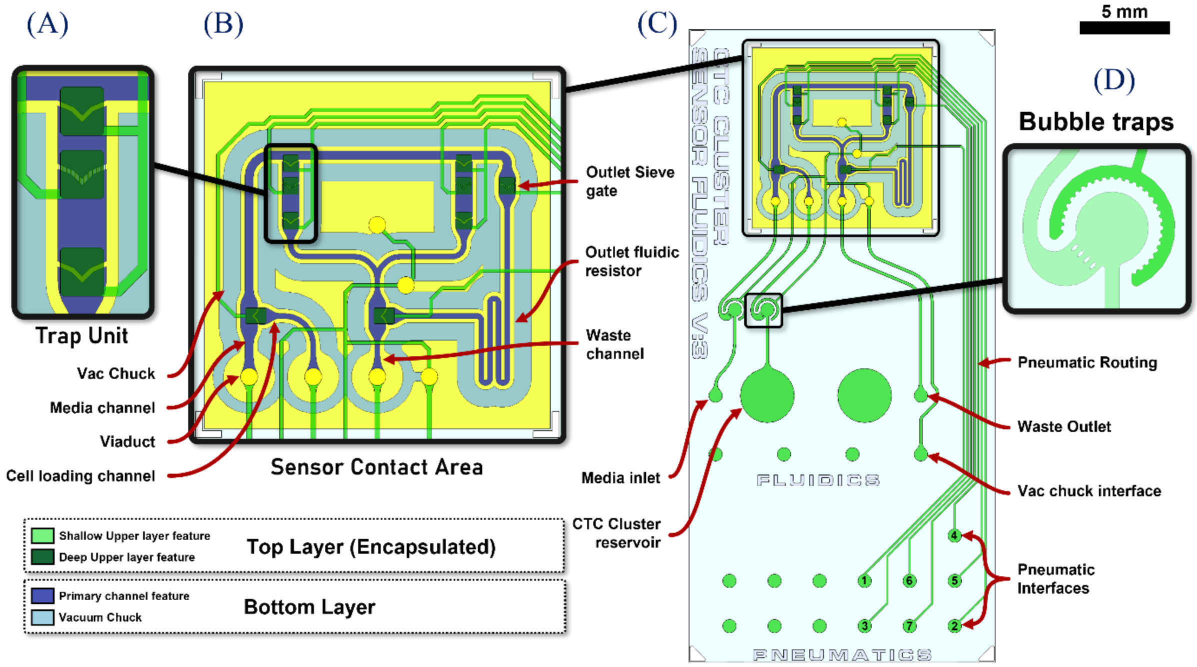

Figure 4.3.1.: Design overview for CTC Cluster V3 with the fluidics integrated with the **(A)** trap units, **(B)** sensor contact area **(C)** pneumatic routing to control the valves for fluid introduction within the trap units and **(D)** bubble traps. Top layer and bottom layer along with the area actively chucking by the vacuum are highlighted. From V2, certain modifications were made. The length of the bypass was decreased from 150 to 100 µm to increase fluidic resistance along with the sieve valve was incorporated on the bypass line. The perforation area on the sieve valves was further increased and the configuration was changed to V-shaped to address this issue. Similar valve configuration and pneumatics were incorporated as in V2.

As discussed above, different valves were incorporated (Fig. 4.3.1.): (i) four large V-shaped isolation valves for flow operation, (ii) three partially open sieve valves. Each trap unit has integrated sieve valves for trapping cells, along with two V gated valves to isolate the secretions for direct analysis. One of the sieve valves acts as an outlet fluidic resistor to increase the fluidic resistance on the serpentine as to direct the flow mostly through trap units. In addition, for cell trapping, the sieve valves were realized with micropillars with at least 10 microns separation. Each channel has height around 150 µm. The following sections entails the characterization of CTC Cluster V3 device focusing on actuation and sieve valves, fluidic pathway, trap units and bubble traps.

4.4.2. Characterization of Actuation and Sieve Valves:

For optimal fluidic manipulation and trapping, optimization of different valve configuration was analysed. Characteristics range from valve size such as large and small concertina valves to valve alignment to valve design i.e., W-, straight or V- gate were focused on. For fluidic manipulation, large concertina valves with W-gated with the following dimensions: length: 350 µm, Width: 350 µm, Area: 0.12 mm^2 and Gate width: 400 µm were tested.

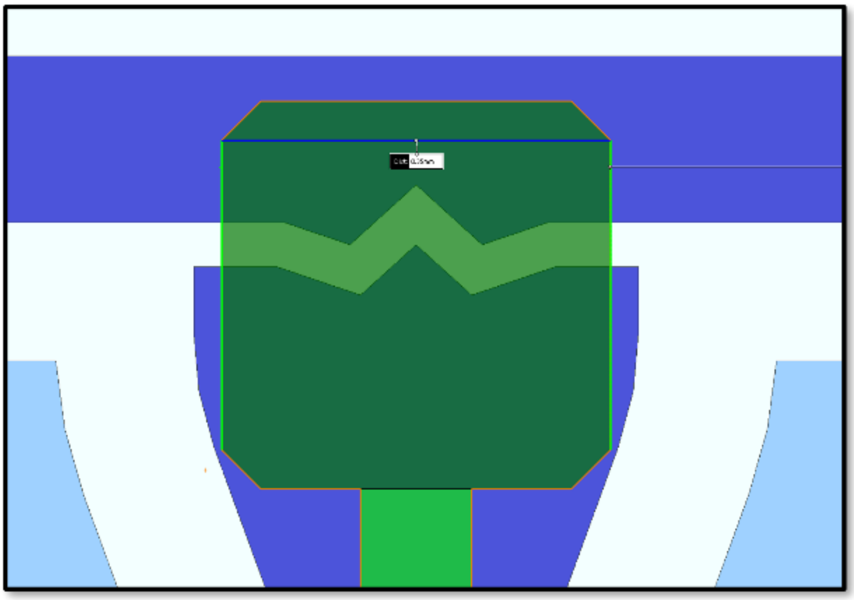

Figure 4.3.2.: Design schematic of W-shaped large chamber concertina valves and large chamber valves were utilized for large actuation chambers. Following are the dimensions for large chamber valves: Length: 350 µm, Width: 350 µm, Area: 0.12 mm2 and Gate width: 400 µm.

As showcased in Fig. 4.3.3., alignment and misalignment of large W-shaped chamber valves were presented for comparative analysis. The valve alignment is imperative for opening/closing time as exhibited in Fig. 4.3.4. For misaligned large chambers, misalignment of 25 µm has been analysed. Fluidic comparison for large chamber alignment presented 2.5 times slower opening time for misaligned valves compared to well aligned ones.

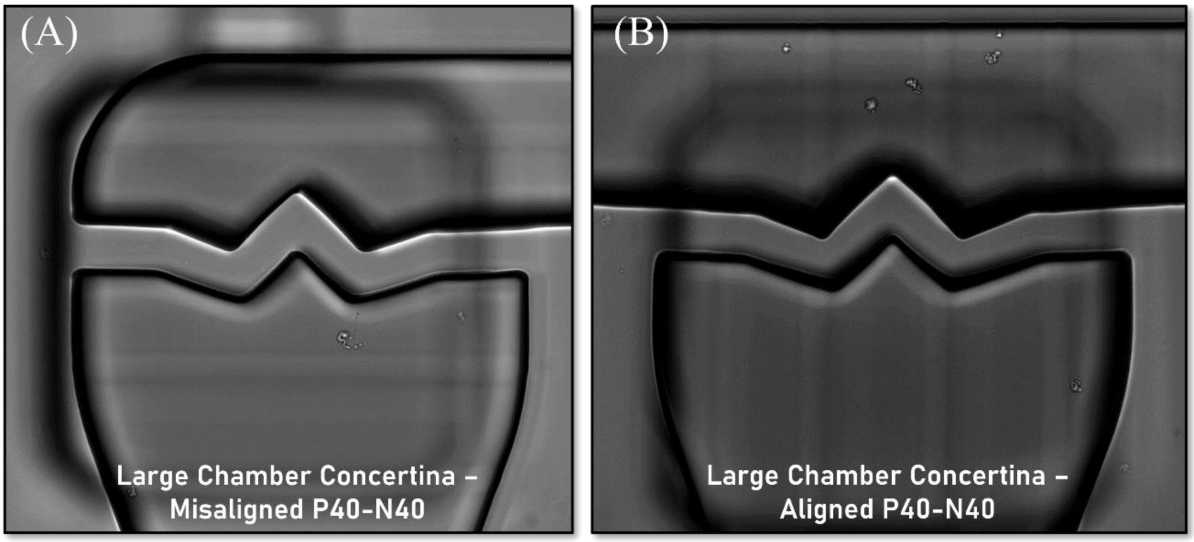

Figure 4.3.3.: Alignment comparison for large chamber W-shaped valves, **(A)** misaligned and **(B)** aligned.

Open times of 250 to 50 msec was exhibited for misaligned chambers while for well aligned chambers, open times ranged from 150 to 50 msec. Negative pressure of 40-50 kPa is required for valve functionality for opening the valves completely and around 80 kPa would close them completely. As showcased for both misaligned and well aligned valves, alignment of the top and bottom layer is imperative for proper valve functionality as opening time vary significantly.

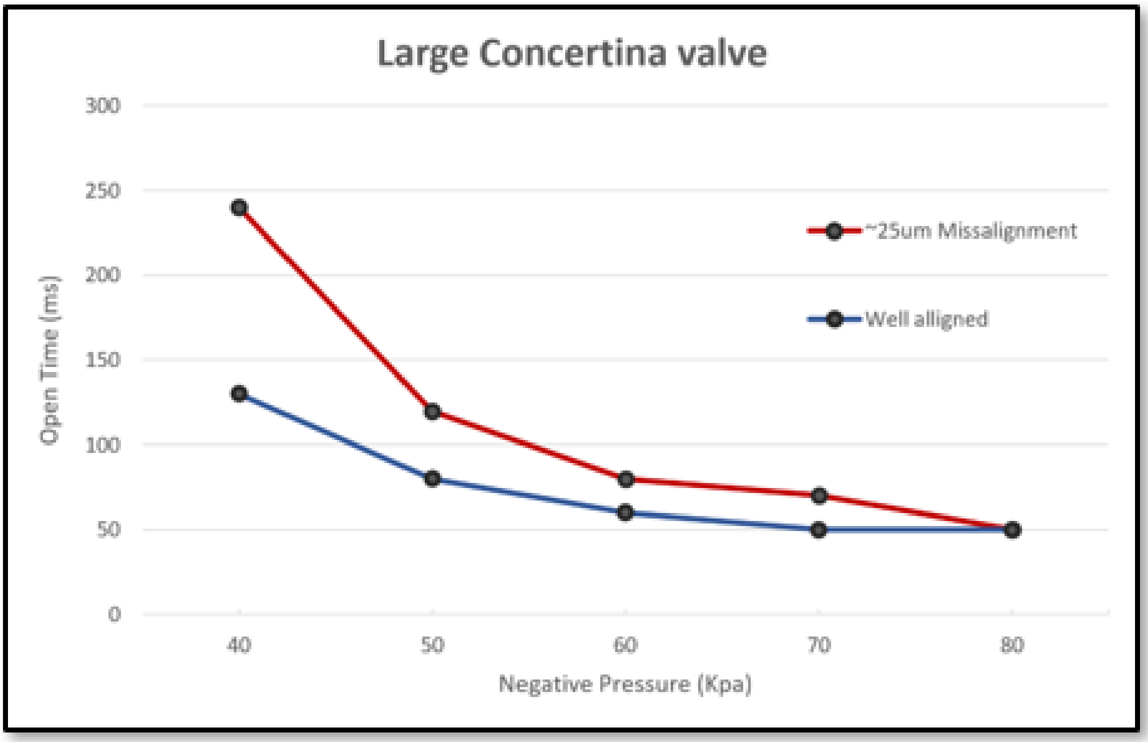

Figure 4.3.4.: Fluidic comparison of alignment for W-shaped large chamber concertina valves, red: misaligned and blue: aligned. Open times for 25 µm misaligned valves are between 250 to 50 msec while for well aligned one are less than 150 to 50 msec. For valve activity, negative pressure of 40 kPa is required for opening the valves completely while 80 kPa would close them and as can be seen for both misaligned and aligned valves, opening times vary significantly.

For lifting gate valve design for trapping, two different configurations were explored: straight perforated and V-shaped. The designs were in consideration for characterizing cell trapping and release efficiency and fluidic resistance throughout the system. Straight lifted gate comprised of 10 µm deep perforation layer as showcased in Fig. 4.3.5. (Isometric and top down). These valves were incorporated with actuation chamber for sieve valve functionality for opening and closing the valves.

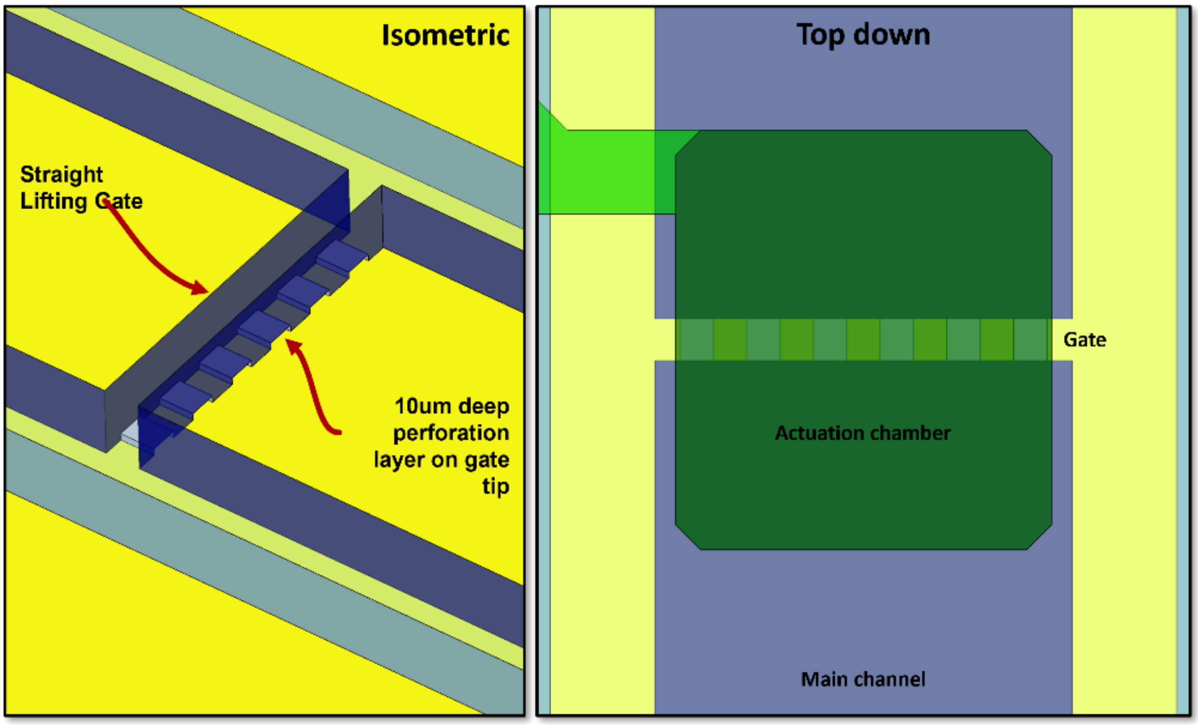

Figure 4.3.5.: Schematic design for straight perforated lifting gate. Isometric and top-down view. Perforation layer is 10 µm deep on the gate tip which will allows the cells to pass through when released. This geometry approximates a Sieve valve with the addition of an actuation chamber.

As presented in Fig. 4.3.6., V-shaped lifting gates have perforation layer of 30 µm deep on the gate tip. Experimentations on gate performance characterized at RMIT by Crispin and specifications of such valves can be adapted as to trap cells with diameter larger than 10µm. These valves showcased easier bead release through the sieve valves via the V-shaped compared to the straight gates. In addition, qualitative characterization of valve functionality showcased easier release of trapping function for V-shaped gates compared to the straight ones. Fluidic resistance was further lowered due to these modifications of gap-to-pillar ratios.

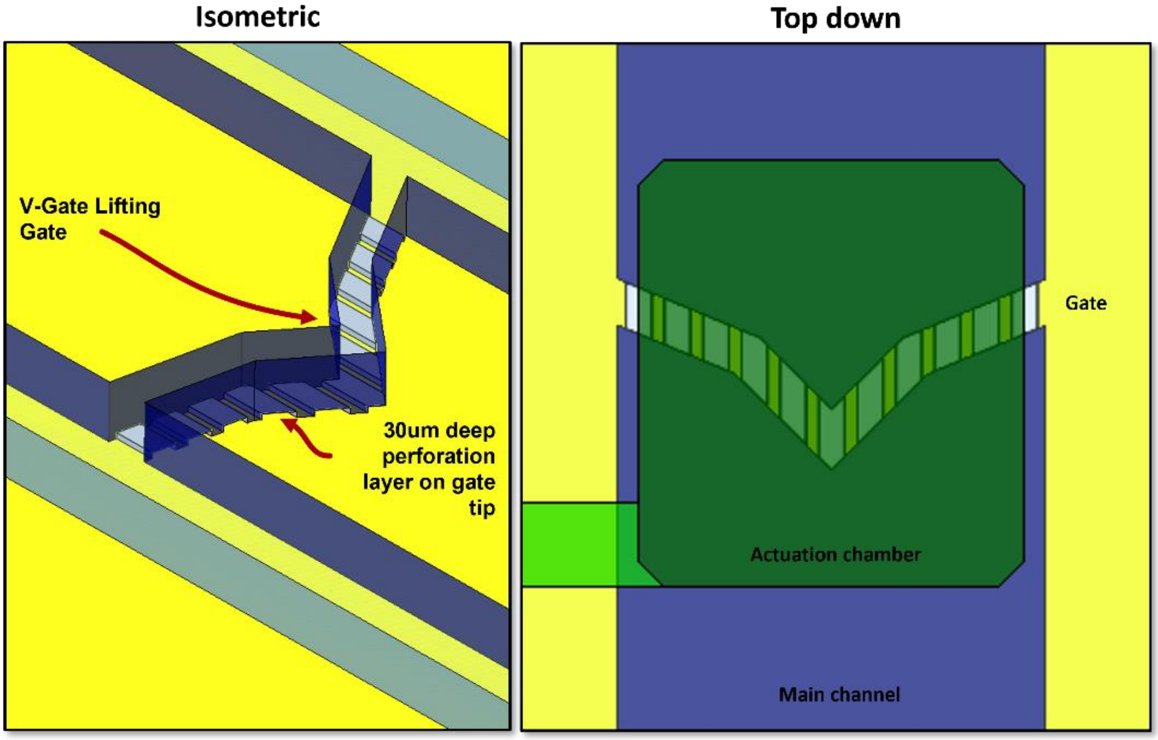

Figure 4.3.6.: Schematic design for V-shaped lifting gate. Isometric and top-down view. Perforation layer is 30 µm deep on the gate tip which will allows the cells to pass through when released. Fluidic resistance is lowered through modifications of gap-to-pillar ratio.

In conclusion for fluidic manipulation, compared with the small chamber concertina valves, large chamber concertina valves were selected. And compared with concertina valves, V-shaped perforated gates were opted as they open more easily, providing more functional freedom and additional optimization for efficient cell trapping of lifting gates. Thus, similar V-shaped gates were selected for fluidic manipulation. In addition, to match the fluidic resistance of the traps, fluidic resistance of the outlet is tuned to be higher than the traps through use of a fluidic resistor (sieve valve along the serpentine). This further ensures that the flow coming from the CTC cluster inlet is directed wholly to the trap, while the buffer passes through the outlet thereby increasing trapping efficiency. In the following sub-section further focuses on the fluidic resistance for optimal trapping functionality.

4.4.3. Analysis of Fluidic Pathway:

Following experiments were focused on understanding the fluidic manipulation through the system. Optimization is required for higher flow to pass through the trap units rather than the serpentine for further increasing the trapping efficiency.

Comparative analysis was performed for V1, V2 and V3 device iterations. For these device designs, fluidic resistance (R) was measured for two different pathways R1 and R2. R1 is the fluidic resistance pathway through the serpentine while R2 is the fluidic pathway through the trap units for CTC Cluster designs. Qualitative characterization by measuring the fluidic resistances R1 and R2 performed at RMIT.

For initial V1 design, R1 path length was calculated to be approximately 15 mm compared to R2 path length, which was around 2.8 mm. Calculated fluidic resistances for R1 was around 0.35 mbar*min/ μL and R2 was approximately 0.07 mbar*min/ μL based on Eq. 4.3.1., where w is the channel width, h is thickness and L is the pathway length.

$$R = \frac{1}{1-0.63\left(\frac{h}{w}\right)}\frac{12\mu L}{h^3 w} \quad \text{(Eq. 4.3.1.)}$$

However, when considering the resistance for the trap units for V1 and V2, most of the flow bypasses the trap units. To overcome this issue, we matched the fluidic resistance of the traps through inclusion of a tertiary trap on the outlet bypass as showcased in Fig. 4.3.7. This has the added benefit of trapping any uncaught cells that don't make it into the traps, so that they can be recycled rather than sent to waste.

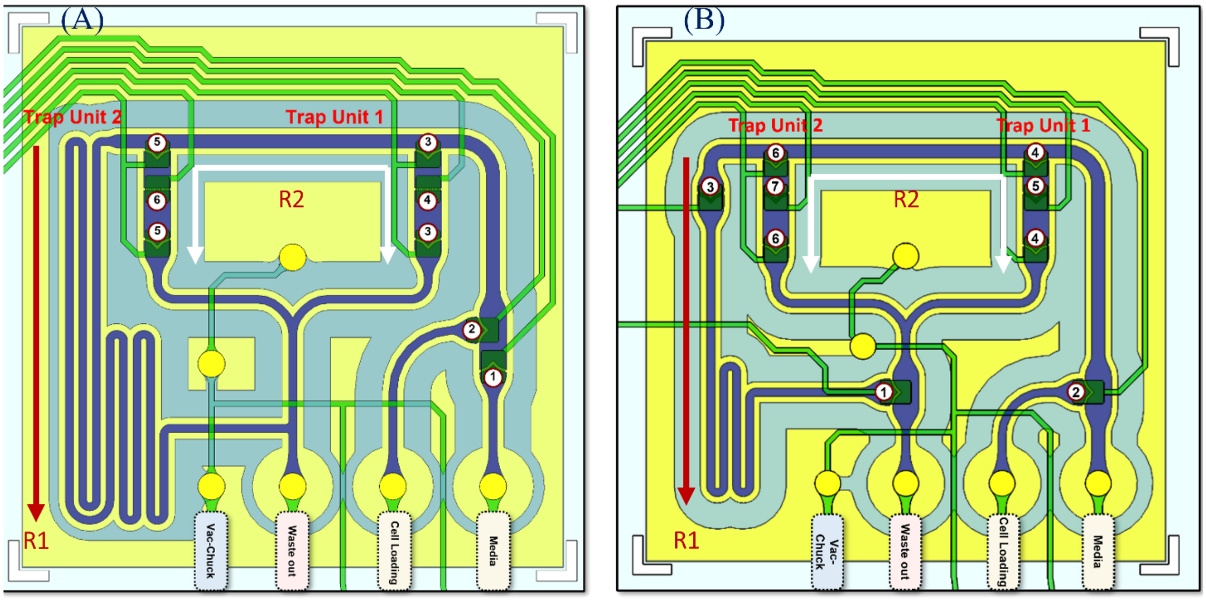

Figure 4.3.7.: **(A)** Schematic for the pneumatic routing for the fluidic interface of V2 (mirrored). Media inlet, cell loading reservoir, waste outlet and vac chuck. For each trap unit, there is a loading gate, perforated lifting gated valve and isolation gate. Valve 1: Media loading, Valve 2: Cell loading, Valve 3: Loading/isolation gate trap unit 1, Valve 4: Perforated lifting gate trap unit 1, Valve 5: Loading/isolation gate trap unit 2, Valve 6: Perforated lifting gate trap unit 2. **(B)** Schematic for the pneumatic routing for the fluidic interface of V3 (mirrored). Media inlet, cell loading reservoir, waste outlet and vac chuck. For each trap unit, there is a loading gate, perforated lifting gated valve and isolation gate. Valve 1: Bypass for the waste outlet, Valve 2: Media/Cell loading, Valve 3: Bypass for the main channel, Valve 4: Perforated lifting gate trap unit 1, Valve 5: Loading/isolation gate trap unit 1, Valve 6: Perforated lifting gate trap unit 2, Valve 7: Loading/isolation gate trap unit 2. For both V2 and V3, R1 highlighted as red and R2 highlighted as white.

Between V2 and V3 configuration, valve 1 was moved to the outlet for the later version. This allows increased trapping efficiency and direct media exchange while limiting marker dilution due to mixing for the whole system.

Table 4.3.1.: Valve configuration for V2 and V3 CTC Cluster design.

Valve	V2	V3
1	Media loading	Bypass Waste outlet
2	Cell loading	Media/Cell loading
3	Loading/Isolation gate trap unit 1	Bypass Main channel
4	Perforated lifting gate trap unit 1	Perforated lifting gate trap unit 1
5	Loading/Isolation gate trap unit 2	Loading/Isolation gate trap unit 1
6	Perforated lifting gate trap unit 2	Perforated lifting gate trap unit 2
7	-	Loading/Isolation gate trap unit 2

4.4.4. Characterization of Trap Units and Bubble traps:

Each trap unit consists of a loading gate, trapping area and isolation gate, and is connected to the main channel and surrounded by the vac chuck gasket. The trapping area is comprised of cell isolation chamber and V-gated perforated lifting gate trap controlled through pneumatic actuation. The perforated lifting gates were used to trap cells and the sensor area is incorporated with a volume of around 50-55 nL as shown in Fig. 4.3.8. More precisely, the loading gate diverts a fraction of the flow from the main channel to the trapping area and the lifting gate below the sensor area allows isolation and releasing the cells after analysis.

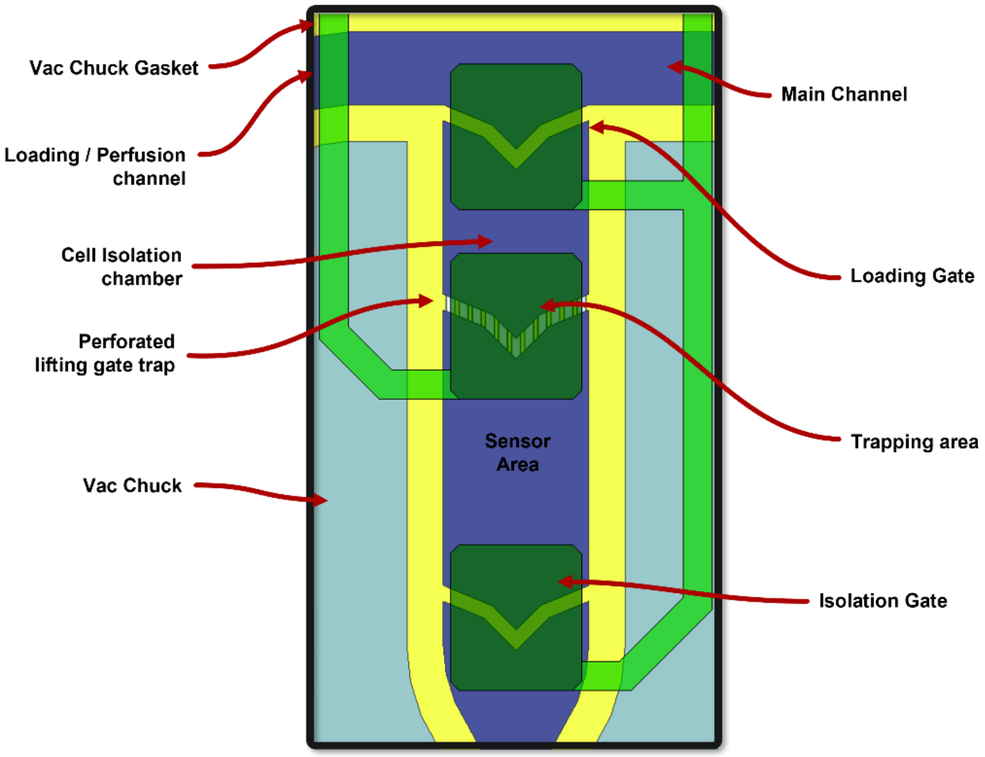

Figure 4.3.8.: V3 Trap Unit design. Each trap unit has a loading and isolation gate along with perforated lifting gate to trap the cells and allow the passage of markers secreted by the cell clusters onto the sensor area. Loading gate diverts the flow from the main channel to the sensor area and the trapping area is incorporated with lifting gates for trapping and releasing the cells after analysis. Calculated sensor chamber volume is around 53 nL.

For on-chip microfluidic and cell culturing, gas bubbles within the flow are challenging. Bubble formation have been shown to increase stress on wall shear within a microfluidic channel by an multiple orders of magnitude specifically in a liquid perfused microsystem, which can further impair biosensing functions [14]. Bubble traps are ingenious solution to limiting this drawback and requires a footprint of less than ten sq. mm. Bubble traps employed for our device have been showcased to remove approximately 4000 bubbles in one day where nitrogen bubbles were consistently removed at a rate of 0.14 µL/min [14].

The principle of bubble traps focuses on closely spaced pillars that confine the air pockets to the circular chamber and prevent them from entering the outflow channel. The pillars are elliptical and are placed at the exit of the chamber and were separated by 50 µm. This is done to prevent the bubbles exceeding the gap size diameter to leave the chamber. The collective sum of all the gaps should be greater than the width of the inflow channel. Flow resistance increased post pillar marginally unless a trapped bubble is large for blocking the chamber. Gas permeation through the PDMS wall actively remove the bubbles within the chamber into the vacuum channel lining the three quarter of the cylindrical chamber's (radius r=1 mm) circumference.

Bubble traps having a circular chamber of 750 µm diameter with an inter-channel wall contains cylindrical support elements (radius 100 µm) equidistantly placed as showcased in Fig. 4.3.9.

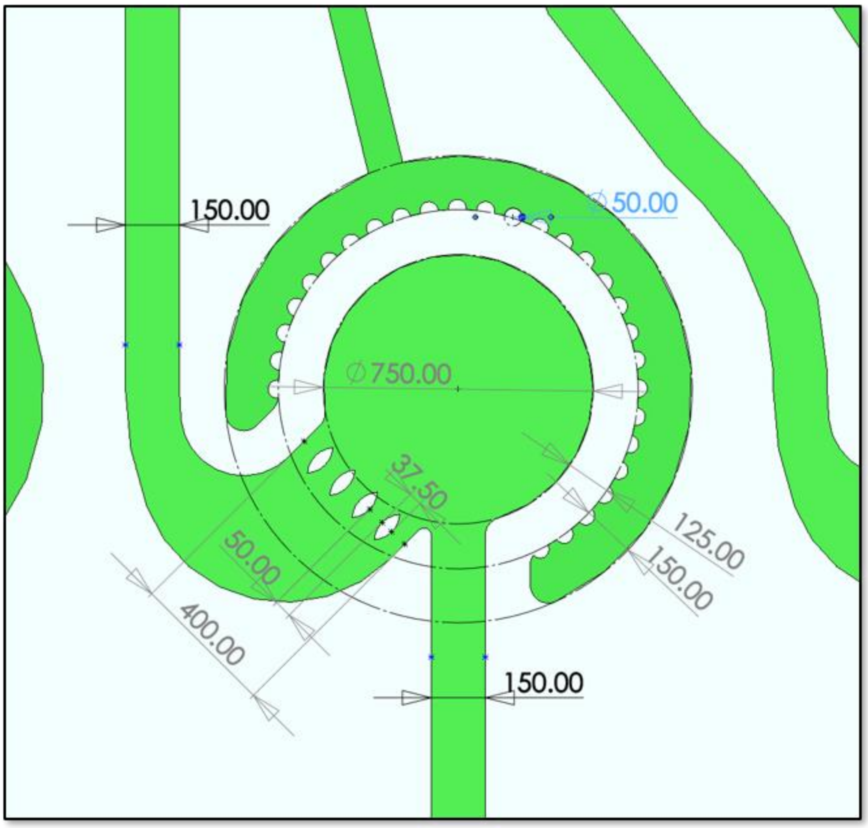

Figure 4.3.9.: Design schematic for bubble traps. Flow is introduced through the bubble traps and move on towards the valves and the trapping area. The bubble traps are integrated with grooves and ridges that can separate the air pocket from the fluid and dissipate in the PDMS fabricated microfluidics as PDMS is gas permeable and porous in nature. In addition, some pillars are integrated within the channel to further limit bubble formation through change in flow or flow rate distension.

Each bubble traps were incorporated within the inlet and CTC reservoir channel. At the outlet of the bubble trap channel, four lenticular shaped pillars are adjusted for trapping air pockets. They are around 37.5 µm in size and are distanced at 50 µm between each other inspired by Lochovsky and group [14]. For our experiments, multiple bubbles being formed because of flow changes specifically during co-flow were dissipated within the porous PDMS device showcasing their functionality for longer experiments.

4.4.5. Comparative analysis of Flow rates:

As discussed in the experimental section, for fluidic manipulation and valve actuation, manual syringe pumps were used as presented in Fig. 4.2.2. Characterization of these syringe pumps were analysed by measuring the flow rate at different configurations. These configurations and flow rates measured in triplicates were compiled in Table 4.3.2. for single flow and Table 4.3.3. for co-flow when the reservoir channel is opened. The reservoir channel is integrated within the device for introducing cells and media exchange along with the introduction of drugs for analysis.

The valve numbers are highlighted in Fig. 4.3.10. for single flow and 4.3.11. for co-flow configuration. Initial characterization was performed by opening V1 valve and then opening completely V1 and V4 and finally opening V1, V4 and V6. When only V1 is open, the fluid bypassed the trap units as shown in Fig. 4.3.10. (A) and went through the fluidic outlet. As exhibited in Fig. 4.3.10. (B), the fluid went through the trap unit 1, when V1 and V4 were opened and some of the fluid passed through the outlet. And when V1, V4 and V6 were opened fluid mostly went through both trap units 1 and 2 as presented in Fig. 4.3.10. (C).

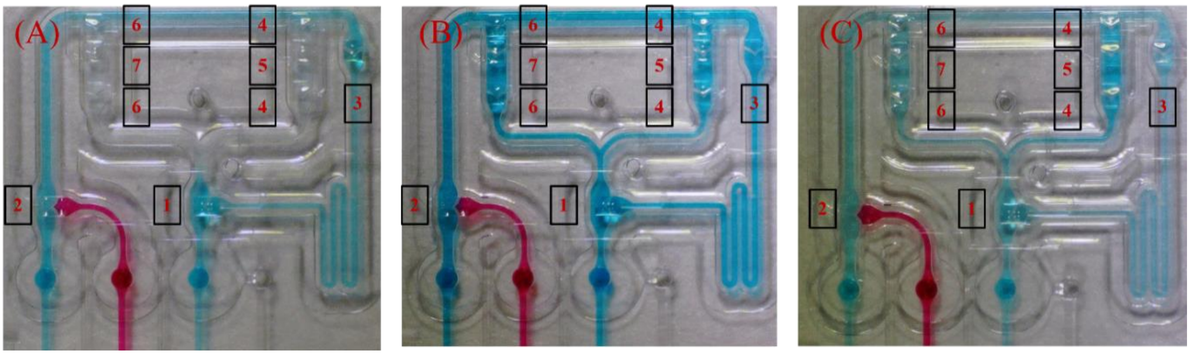

Figure 4.3.10.: Flow rate characterization at different valve configuration **(A)**, only V1 was open, where only one or either trap unit 1 or 2 might be used for trapping. **(B)**, when both V1 and V4 were opened where both the trap units would be used for trapping and **(C)**, when all 3 V1, V4 and V6 were opened in the case of flushing the system.

However, for our experimentations at different configurations the flow rates were between 4 µL/min to 11.6 µL/min. When only V1 was opened, flow rate of the V3 system was around 4 µL/min, while it further increased to 7 µL/min when both V1 and V4 were opened, where flow was moving only through trap unit 1. It further increased to 11.6 µL/min when flow was moving through trap units 1 and 2 where, V1, V4 and V6 were opened. For these experiments the sieve valves V3 (for fluidic manipulation) and V5 and V7 (for trapping efficiency) were kept in partially open/close position.

Table 4.3.2.: Flow rate characterization for V1, V1/V4 and V1/V4/V6. For V1, around 4 µL/min was measured and for V1/V4, the flow rate of the system increased to 7 µL/min. When all three V1, V4 and V6 were opened for flushing, flow rate of 11.6 µL/min was observed.

Valve configuration	V1	V1/V4	V1/V4/V6
Flow rate (µL/min)	4	7	11.6

For characterization of co-flow, when laminar concurrent flow was passing the system, V2 valve was opened. In addition, inlets and outlets needed to be arranged at either similar height or adjusted higher than the inlet tubes for optimal co-flow.

Like before, flow rates were analysed at different configurations. As exhibited in Fig. 4.3.11. (A), both V1 and V2 valves were opened, which was highlighted by a distinct co-flow between the different coloured dyes. When V2 and V6 were opened, fluid in co-flow configuration pass through the trap unit 1 as shown in Fig. 4.3.11. (B). And when V2, V4 and V6 were opened, fluid went through both trap units 1 and 2 as shown above however in co-flow configuration as presented in Fig. 4.3.11. (C).

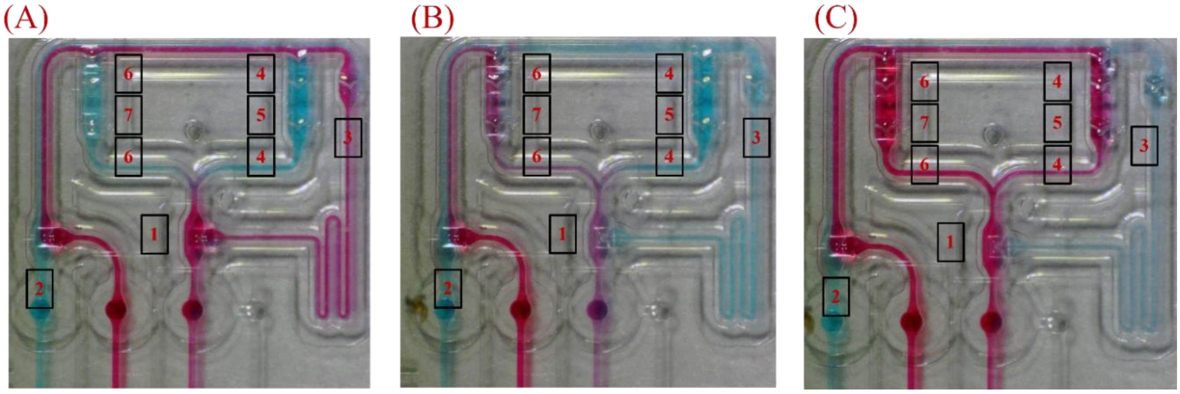

Figure 4.3.11.: Flow rate characterization at different valve configuration during co-flow **(A)**, when both V1 and V2 were opened, the flow was bit higher as expected and for **(B)**, when trapping from trap unit 1 would be performed, open configuration for V2 and V4. **(C)**, when both trap units 1 and 2 would be employed for trapping the flow rate, in multi-trap configuration.

Flow rate of the microfluidic system increased from 4 µL/min to 5.7 µL/min in co-flow configuration when only V1 was opened. However, it was around 7 µL/min in both single flow and co-flow configuration when either V1/V4 and V2/V4 were opened. Compared to single flow going through both trap units, in co-flow for similar valve configuration, flow rate was around 8.8 µL/min.

These experiments were conducted in triplicates and in conclusion, for co-flow manipulation compared with normal flow, we expected the flow rate to be higher, as we have less inlet resistance (where blue is the inlet flow coming from the Eppendorf, while pink is from the on-chip reservoir with no tubing).

Table 4.3.3.: Flow rate characterization for V1/V2, V2/V4 and V2/V4/V6. For V1, around 5.7 µL/min was measured and for V2/V4, the flow rate of the system increased to 7 µL/min. When all three V2, V4 and V6 were opened for multi-trapping, flow rate of 8.8 µL/min was observed.

Valve configuration	V1/V2	V2/V4	V2/V4/V6
Flow rate (µL/min)	5.7	7	8.8

In conclusion, for both normal flow and co-flow, flow rates were characterized in different configuration for flow bypass, through one and then both trap units simultaneously. Calculated flow rates for single flow were 4-11 µL/min, while for co-flow manipulation, these measurements significantly decreased to around 6-9 µL/min. Such differences could be due to fine tuning the system by manually applying additional pressure on the inlet and outlet position.

For optimal/gentle cell trapping within the trap units, controllable low flow rates are needed as cells unlike beads are not rigid and can pass through the valves if the flow is too high. The manual syringe pump system for valve actuation and flow control highlighted here have shown to be easy to handle. While compared with an automated system, such a manual system might not be as precise, but it offers more on-hand control for initial characterization and further provides an avenue for minimizing pressure build up within the system.

4.4.6. Characterization of Trapping efficiency:

Following characterization of flow rates for the device, beads of different sizes varying from 50-100 microns, slightly bigger than normal cells were trapped for preliminary functionality of the microsystem. Initial entrapment was performed with single trap units and afterwards, multi trap units were used. For the whole experimental setup from laminar co-flow to beads bypass to single and multi-bead trapping scan the QR codes (A., B., C., and D.) presented in Fig. 4.3.12. Further details are mentioned in the video captions.

(A) (B) (C) (D)

Figure 4.3.12.: **(A)** Laminar co-flow showcasing trap unit functionality in co-flow orientation. **(B)** Bead bypass before single and multi-bead trapping. **(C)** Single bead trapping through trap unit 1 in co-flow orientation. **(D)** Multi bead trapping with both trap units 1 and 2 in co-flow orientation. All the videos are 2X speed.

For single bead trapping, valves 1 and 3 were opened to have a channel for fluidic resistance, while valves 4 and 5 were actuated so the beads would be trapped in the trap unit. In addition to these valves, valves 6 and 7 were further opened after single bead trapping to showcase multi bead trapping. Screenshots of both single and multi-bead trapping has been showcased in Fig. 4.3.13. In conclusion, these experimentations showcased optimal single and co-flow manipulation within the V3 design. In addition, trapping of beads within one trap unit and both trap units were presented as well highlighting the prospect of trapping cancer cells within this system which is further illustrated in the following sub-section.

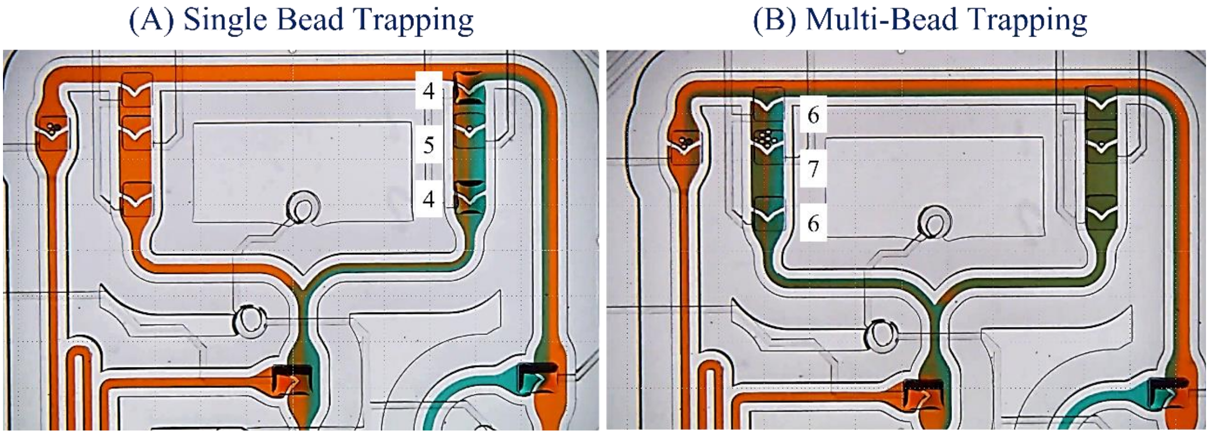

Figure 4.3.13.: Beads of 100 microns diameter were trapped in trap unit 1 for **(A)** Single bead trapping, for **(B)** Multi bead trapping where both trap units trapped beads. The valves actuation for trap unit 1 and trap unit 2 were highlighted.

Following bead trapping, characterization of trap units was performed by trapping cancer cells. MCF7 metastatic breast cancer cells were introduced in the device reservoir as shown in Fig. 4.3.14. For optimal viability, the cells were sub-cultured the same day. Freshly prepared culture medium was used as running buffer to keep the cell alive for longer period. For further characterization of valve actuation for trap units, cells were trapped and released. It was observed that several cells deformed and passed through unlike beads due to their elasticity. When we had enough cells trapped, overnight perfusion was done to analyse their viability within the device. The medium was changed continuously at the lowest flow rate possible where outlet V3 were closed.

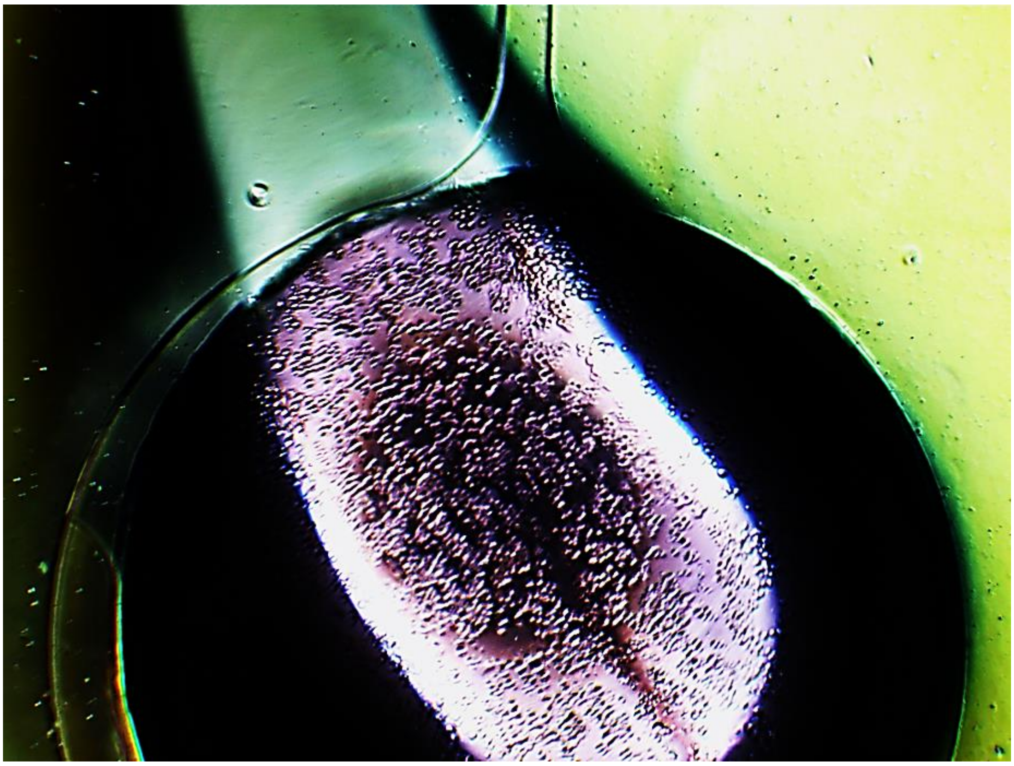

Figure 4.3.14.: MCF7 cells under 20X observation in cell reservoir of CTC Cluster V3. Cells under the reservoir starts to sedimented to the bottom layer of the device, to promote the transportation of cells through the device, the cells after introduction to the reservoir were further agitated in suspension before opening the valve for cell trapping.

As shown in Fig. 4.3.15. (A), multiple number of cells were trapped on top of each other within the trap unit. Initial observation indicated up to 50-100 cells being stacked on top of each other vs ~1000 cells being introduced (5-10% cell trapping efficiency). Upon further analysis, some cells were observed to be within the pillars. Based on the morphology of such cancer cells and due to their plasticity, some of the cells were observed to pass through the pillars.

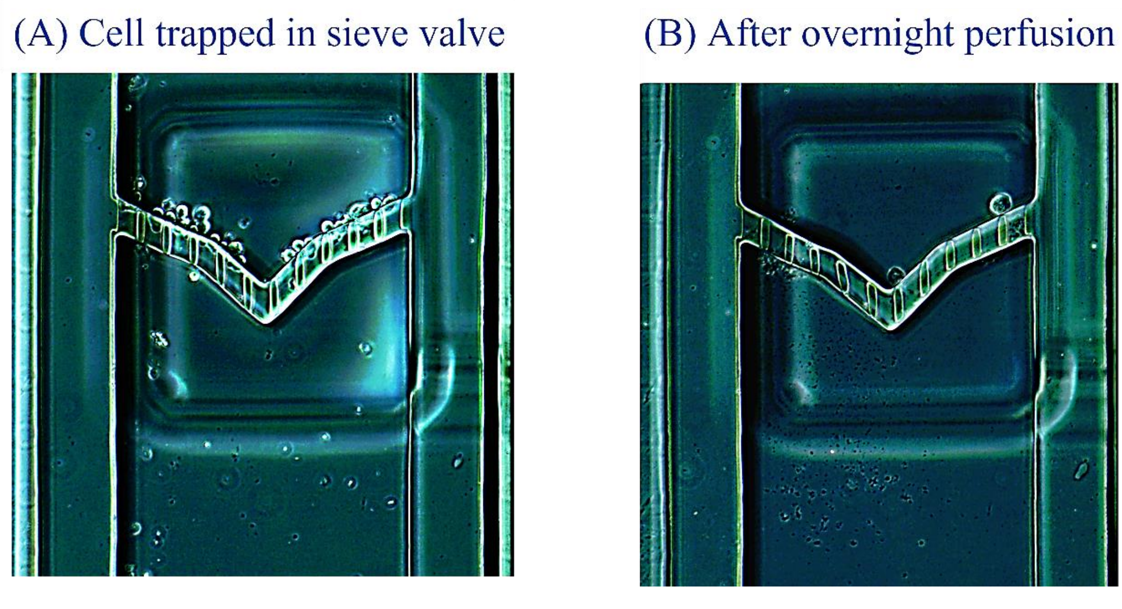

Figure 4.3.15.: **(A)** MCF7 cells being trapped within the Trap unit 1 under constant flow at 7 µL/min in the V1/V2 valve configuration. In real-time as the cells are elastic in nature, most of the cells squeeze through the pillars integrated within the sieve valves, however some of the cells were trapped and piled on top of each other for observation under perfusion. **(B)** The trapped MCF7 cells were then observed at regular intervals and then overnight analysis was performed. After 24 hours, trapped cells were dead as when the valves were opened, cell fragments from the trapped cells were prominent.

For long-term analysis, around 20-25 cells were trapped and observed at regular 30 min intervals for 3 hours at room temperature and then overnight in the incubator at 37° C, by closing the V2 and only opening V1 partially for overnight perfusion. After 24 hours, all the cells from our observation were dead as when the V4/V5 were opened, cell fragments from the trapped cells were seen prominently as exhibited in Fig. 4.3.15. (B). Initial thoughts of the cells being passed through the device were alleviated by seeing these fragments. The device's inability to keep the cells alive could be due to low CO_2 presence and temperature required of 37 ° C.

In conclusion, the device was able to trap cancer cells under flow and medium perfusion was performed through co-flow configuration. However, future work needs to be focused on (i) modifying the depth of the perfusion layer on the V-shaped lifting gate in the trapping unit to increase the efficiency of cell trapping, (ii) keeping the cells alive for longer period up to 24-48 hours, by either (iii) adapting the device to be placed in the incubator and/or (iv) integrating a water jacket for O_2/CO_2 exchange and temperature control, however such modifications will make the device more complex.

4.4.7. Detection of biomarker secretions through ELISA:

Prior to integration of biosensing modality within the optofluidic device, analysis of biomarker secretion was performed for trapped cells within the trap units. For measurement of cancer biomarker secretions, fibronectin, and interleukin-6 (IL-6) were selected. Between the two, fibronectin was analysed initially due to its large molecular weight compared with the IL-6, which might influence biosensing using plasmonic sensing such as SPR or NHA.

For small volume measurements, analysis was performed for cells that were trypsin-ised in T75 flasks and cells grown in 6 well plates. Cell cultivation times were taken into consideration as well where analysis for T75 cells were performed after 48 hrs and for 6 well plates, measurements were done for 2 hr and 24 hr intervals. In addition, to analyse secretion uptake for SK-OV-3 cells, lipopolysaccharides (LPS) were introduced. As LPS is an immunoreactive agent, and immune related biomarkers such as IL-6 should have increased secretion uptake compared to non-immune related biomarkers such as fibronectin. For controls, DMEM culture medium was analysed.

For both fibronectin and IL-6 calculations, direct cell suspensions from SK-OV-3 cells grown in T75 flasks named 'Susp' and cells grown in 6-well plates named 'cells' were compared. Cell numbers for susp were 6.1×10^6 cells and for SK-OV-3 cells were 1.7×10^6 and for T75 flasks, the volume was set at 10 mL, while for 6 well plates, each well had 2 mL. ELISA was performed for cell suspension +/- LPS after 48 hr and for SK-OV-3 cells that were sub-cultured +/- LPS for 2 hr and 24 hr.

Controls were measured by analysing only the DMEM medium. For fibronectin, control was measured at 1.1 ng/mL and +/-LPS for cell suspensions did not showcase significant difference. Similar trend was highlighted for cells grown in 6 well plates.

Table 4.3.4.: ELISA for Fibronectin marker secretion for SK-OV-3 metastatic ovarian cancer cells.

Analysis type	**Cultivation time (hr)**	**Biomarker secretions ± St. dev. (ng/mL)**
Control		
DMEM culture medium	-	1.1 ± 0.2
T75 flasks: 6.1 x 10^6 cells		
Cell susp. + LPS	48 hr	1.6 ± 0.1
Cell susp. -LPS	48 hr	1.7 ± 0.1
6-well plates: 1.7 x 10^6 cells		
Cells + LPS	2 hr	2.8 ± 1.4
Cells – LPS	2 hr	3.6 ± 1.4
Cells	24 hr	3.3 ± 2.7

As exhibited in Table 4.3.4., LPS was shown not to upregulate fibronectin secretions uptake. Significant increase in fibronectin secretions were observed for cells grown in 6-well plates for 2 hr and then 24 hr compared with the cells grown in T75 flasks. Such increase could be due to the functionality of fibronectin, that is used by cells to attach on the substrate layer.

Similar analyses were performed for IL-6 biomarker secretions using the same cell solutions as shown in Table. 4.3.5. Control exhibited around 28.3 pg/mL marker secretion and trypsin-ised cells activated with LPS (susp in T75) exhibited significant difference compared with the cells without LPS activation (around 2 times as high). This further highlights the role of LPS as an immune active agent for increased marker secretion as hypothesized for IL-6, an immune biomarker.

Table 4.3.5.: ELISA for IL-6 marker secretion for SK-OV-3 metastatic ovarian cancer cells.

Analysis type	**Cultivation time (hr)**	**Biomarker secretions ± St. dev. (pg/mL)**
Control		
DMEM culture medium	-	28.3 ± 6.7
T75 flasks: 6.1 x 10^6 cells		
Cell susp. + LPS	48 hr	63.7 ± 10.2
Cell susp. -LPS	48 hr	33.4 ± 7.2
6-well plates: 1.7 x 10^6 cells		
Cells + LPS	2 hr	82.9 ± 12.1

Cells – LPS	2 hr	82.9 ± 12.1
Cells	24 hr	82.9 ± 12.1

Similar calculations were observed for +/-LPS cells grown in 6 well plates. However, signal saturation was observed at 82.9 pg/mL as the secretion from the cells were much higher than the sensitivity of the ELISA kit due to the ultrasensitive nature of the IL-6 kit vs Fibronectin kit. This showcased increased markers were secreted at the beginning around 2 hr mark till 24 hr mark, highlighting the fact for marker analysis immediately after trapping, as we can hypothesized the cells communicate by secreting such biomarkers.

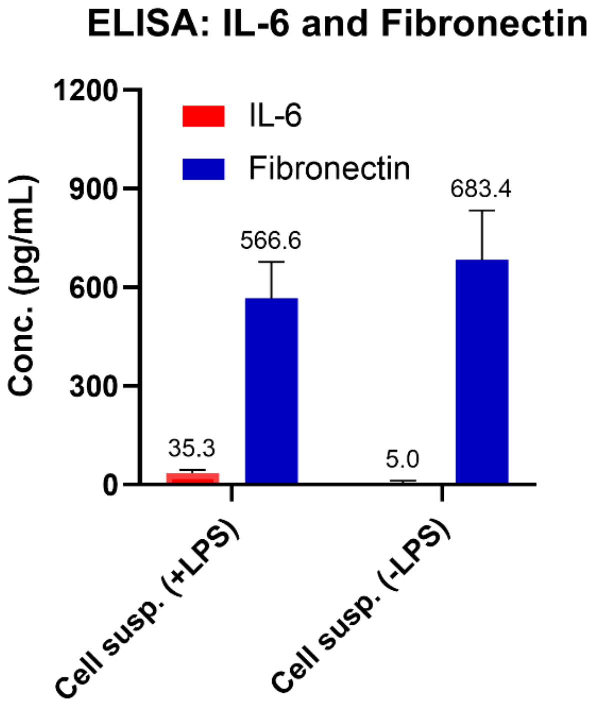

Figure 4.3.16.: ELISA Signal (Secretion – Control) for Fibronectin and IL-6 secretion for Susp SK-OV-3 cells +/- LPS after 48 hrs. As shown, the marker secretion varies significantly between fibronectin and IL-6. For +LPS, IL-6 was observed at 35.3 pg/mL while fibronectin at 566.6 pg/mL and for -LPS, IL-6 was measured at 5.0 pg/mL and fibronectin at 683.4 pg/mL. Based on these measurements, the marker secretion of trapped cells within the trap units of CTC Cluster V3 can be interpolated to have an idea for the sensitivity that has to be reached for sensing these marker secretions through the nanohole array (NHA) plasmonic setup.

Comparative analysis between fibronectin and IL-6 was exhibited in Fig. 4.3.16. for signal-to-noise (S/N) ratio of SK-OV-3 cell suspensions grown in T75 flasks. Significant differences were highlighted between fibronectin and IL-6 secretions, where fibronectin concentrations were comparatively 20 times higher than IL-6.

As mentioned above, no significant difference was observed for fibronectin secretions for LPS activity. However, for IL-6, +LPS signal was around 7 times higher than -LPS. Such analysis was performed for characterising marker secretions of trapped cells within trap units of CTC Cluster

V3, which we can interpolate to have an expected sensitivity range for the integrated NHA-microfluidic system, highlighted in Table 4.3.6.

Significant decrease in marker secretion is to be expected due to the volume dilution of the trap units having 50 nL capacity, while increasing cell number would increase the marker secretion. For trap unit volume (~50 nL), with around 10 cells, fibronectin secretion +LPS/-LPS were approx. 130-160 pg/nL. IL-6 secretions for similar conditions were comparatively significantly lowered around 1-8 pg/nL.

Table 4.3.6.: Compiled marker secretions with cluster volume.

Biomarker secretion	**Fibronectin**		**Interleukin-6**	
	+LPS	**-LPS**	**+LPS**	**-LPS**
pg/ nL per 1 cell	666.5	804	41.5	5.8
pg/ 50 nL per 10 cells	133.3	160.8	8.3	1.1

In conclusion, for both fibronectin and IL-6, biomarker secretions were characterized through ELISA for different volume, cultivation times and LPS activation. For fibronectin, increased biomarker was secreted at 2 hr and 24 hr cultivation time compared to 48 hr. In addition, no significant difference in marker secretion was observed for +/-LPS activation. Unlike fibronectin, for IL-6 significant increase in marker secretion was exhibited, around 7 times higher uptake. Between the two cancer associated markers, significant increase in marker secretion was observed for fibronectin compared to IL-6. This could be due to large molecular weight of fibronectin compared to IL-6 and in addition, secretion of fibronectin is imperative for cell attachment on the substrate for early analysis 2-24 hr cultivation time. Significant difference between +LPS and -LPS was observed for IL-6. For biosensing applications through integrated optofluidic setup, marker secretion between 133-160 pg/50 nL should be expected for fibronectin while for IL-6, 1.1 pg/50 nL could be observed for -LPS cells and 8.3 pg/50 nL for LPS activated cells. Sensitivity ranges for nanohole plasmonic arrays to integrated should be within lower pg/nL range to be able to analyse marker secretion in real-time for cancer associated markers for cancer cells trapped within the device. This is further highlighted in Chapter 4.

4.5. Conclusions and Perspectives:

CTCs and their associated biomarkers have been considered for rapid cancer diagnostics, prognosis and monitoring for liquid biopsies and personalized cancer medicine. Numerous research projects are underway for development of microsystems for sorting, isolating, and analysing CTCs. Such devices focus on: (i) recovery of live CTCs (ii) obtaining high purity i.e., few remaining while blood cells, and (iii) clinical compatibility. This is a great challenge due to CTCs scarcity, (as a reminder 1-10 CTCs vs 10^8 other blood cells in 1 mL of blood) and heterogeneity of their biomarker expression. The principle for such microfluidic devices focuses on variations in CTC size compared to the blood cells as well as physical properties like electrical charge and density along with their biological characteristics like specific surface marker expression.

One of the biological problems affecting researchers is real-time analysis and direct characterization of CTCs. CTCs and their associated biomarkers can act as reliable markers for metastatic stage and early-stage cancer diagnostics [35,36]. In recent years, microfluidic systems have showcased exceptional characteristics for separation and trapping CTCs from minute biological volumes. Different microfluidic devices awaiting U.S. Food and Drug Administration (FDA) clearance and have been in pipeline for commercialization like CTC isolation, ClearCell® FX1 (Biolidics Limited, Mapex, Singapore), Parsortix® (ANGLE plc, Surrey, UK), and VTX-1 (Vortex Biosciences, Menlo Park, CA, USA). For such optimal technologies, high recovery rates and sample throughput for downstream processing is needed to collect viable and heterogenous CTCs, which down the line could be critical clinical information [37].

Microfluidics on the other hand provide an avenue for integration with different analytical platforms specifically biosensing technologies. Such integrated systems could be capable of performing real-time analysis of secreted biomarkers secreted directly by CTCs. In recent years, microfluidic devices with chambers have been employed for such analysis. Moreover, micro-chambers like nano wells with precise fluidic control achieve large number of reagent vessels with low sample volume requirements. However, such nanostructures are relatively small for filling different reagents i.e., medium for cell viability and drugs for biological activity at the same time for analysis of either individual cancer cells or spheroids [23]. In contrast, a more sophisticated approach with valve integration could be targeted for complex fluidic manipulation capable of performing optimal cell trapping and subsequent biomarker analysis. In addition, valve based systems provide wider applications in single and multi-cell trapping and sequencing for multiplexed immunoassays and biosensors [23]. For cell micro-culturing, such systems allow greater level of automation.

In this chapter, we have presented an integrated valve-based microfluidic system fabricated through moulding protocol for trapping cancer cells. A practical method for the fabrication of complex 3D valves with actuation circuits and trap units with sieve channels have been showcased. Furthermore, moulds prepared for this fabrication method are reusable and have the capability to incorporate valve membranes and hybrid integrated systems specifically optical biosensors for lab-on-a-chip platform having high optical resolution.

We worked on three different iterations of CTC Cluster device. Initial characterization for different W-gate, straight and V-gated valves was showcased where V-gated valves highlighted the optimal functionality. Moreover, between V2 and V3, the microfluidic circuit was optimised so that most of the flow passes through the trap units rather than the bypass. Afterwards, flow rates for the micro-system in different single flow and co-flow configuration were calculated to be around 4-11 µL/min. Significant difference highlighted between single and co-flow fluidic rates could be due to the gravitational pressure we imparted on the system for laminar flow.

In addition, trapping efficiency was highlighted for both microbeads and MCF7 cells for single and multiple trap units. However, due to lack of an active perfusion system, the cells were not kept alive for a longer period (~24 hrs). This highlights the need for added modifications that can actively control gas exchange, temperature and replenish medium for micro-culturing and subsequently improving cell viability within such a system.

In conclusion, this trapping system showcased here presents a lot of promise for real-time trapping, however, further improvements are needed focusing on controllable flow rates and device automation. This will allow the cells to be trapped in a gentler fashion limiting cell shearing through the sieve traps. CTC Cluster V3 presented here was used for solely trapping cancer cells under flow, however modifications are required before an optical biosensor such as a nanohole array can be integrated. However, the next chapter, Chap 5: NHA optofluidic sensing focuses on the integration with such complex microfluidic circuits.

References:

1. Cristea, C., Florea, A., Tertiș, M. & Săndulescu, R. Immunosensors. *InTech Open* (2015) doi:10.5772/60524.
2. Becker, H. & Gärtner, C. Polymer microfabrication technologies for microfluidic systems. 89–111 (2008) doi:10.1007/s00216-007-1692-2.
3. Zhang, D., Men, L., Chen, Q. & Science, A. Microfabrication and Applications of Opto-Microfluidic Sensors. 5360–5382 (2011) doi:10.3390/s110505360.
4. Qin, D., Xia, Y. & Whitesides, G. M. Soft lithography for micro- and nanoscale patterning. *Nat. Protoc.* **5**, 491–502 (2010).
5. Das, C., Wang, G. & Nguyen, C. A Low-Cost, Accurate, and High-Precision Fluid Dispensing System for Microscale Application. *SLAS Technol.* **22**, 144–152 (2017).
6. Yeo, L. Y., Chang, H. C., Chan, P. P. Y. & Friend, J. R. Microfluidic devices for bioapplications. *Small* vol. 7 12–48 (2011).
7. Kulkarni, M. B., Ayachit, N. H. & Aminabhavi, T. M. Biosensors and Microfluidic Biosensors: From Fabrication to Application. *Biosensors* **12**, (2022).
8. Descamps, L., Roy, D. Le & Tomba, C. Magnetic Polymers for Magnetophoretic Separation in Microfluidic Devices. (2021).
9. Szydzik, C. *et al.* Fabrication of complex PDMS microfluidic structures and embedded functional substrates by one-step injection moulding. *RSC Adv.* **6**, 87988–87994 (2016).
10. Ren, K., Zhou, J. & Wu, H. Materials for Microfluidic Chip Fabrication. **46**, (2013).
11. Ren, K., Chen, Y. & Wu, H. New materials for microfluidics in biology. *Curr. Opin. Biotechnol.* **25**, 78–85 (2014).
12. Gao, D. *et al.* Recent developments in microfluidic devices for in vitro cell culture for cell-biology research. *TrAC - Trends Anal. Chem.* **35**, 150–164 (2012).
13. Liao, Z. *et al.* Microfluidic chip coupled with optical biosensors for simultaneous detection of multiple analytes: A review. *Biosens. Bioelectron.* **126**, 697–706 (2019).
14. Lochovsky, C., Yasotharan, S. & Günther, A. Bubbles no more: In-plane trapping and removal of bubbles in microfluidic devices. *Lab Chip* **12**, 595–601 (2012).
15. Jokerst, J. V. *et al.* Nano-bio-chips for high performance multiplexed protein detection: Determinations of cancer biomarkers in serum and saliva using quantum dot bioconjugate labels. *Biosens. Bioelectron.* **24**, 3622–3629 (2009).
16. Cao, L. *et al.* Visual and high-throughput detection of cancer cells using a graphene oxide-based FRET aptasensing microfluidic chip. *Lab Chip* **12**, 4864–4869 (2012).
17. Zhang, B., Kim, M.-C., Thorsen, T. & Wang, Z. A self-contained microfluidic cell culture system. *Biomed. Microdevices* **11**, 1233–1237 (2009).
18. Wu, L. Y., Di Carlo, D. & Lee, L. P. Microfluidic self-assembly of tumor spheroids for anticancer drug discovery. *Biomed. Microdevices* **10**, 197–202 (2008).

19. Descamps, L. *et al.* Self-assembled permanent micro-magnets in a polymer-based microfluidic device for magnetic cell sorting. *Cells* **10**, (2021).
20. Mekkaoui, S., Descamps, L., Audry, M. C., Deman, A. L. & Le Roy, D. Nanonewton Magnetophoretic Microtrap Array for Microsystems. *Langmuir* **36**, 14546–14553 (2020).
21. Li, X. *et al.* Label-Free Optofluidic Nanobiosensor Enables Real-Time Analysis of Single-Cell Cytokine Secretion. *Small* **14**, 1–11 (2018).
22. Descamps, L. *et al.* MagPure chip: an immunomagnetic-based microfluidic device for high purification of circulating tumor cells from liquid biopsies. 4151–4166 (2022) doi:10.1039/d2lc00443g.
23. Mathur, L., Ballinger, M., Utharala, R. & Merten, C. A. Microfluidics as an Enabling Technology for Personalized Cancer Therapy. *Small* **16**, (2020).
24. Unger, M. A., Chou, H. P., Thorsen, T., Scherer, A. & Quake, S. R. Monolithic microfabricated valves and pumps by multilayer soft lithography. *Science (80-.).* **288**, 113–116 (2000).
25. Studer, V. *et al.* Scaling properties of a low-actuation pressure microfluidic valve. *J. Appl. Phys.* **95**, 393–398 (2004).
26. Quake, S. R. Microfluidic Large-Scale.pdf. *Science* **298**, 580–584 (2002).
27. Thurgood, P., Baratchi, S., Szydzik, C., Mitchell, A. & Khoshmanesh, K. Porous PDMS structures for the storage and release of aqueous solutions into fluidic environments. *Lab Chip* **17**, 2517–2527 (2017).
28. Szydzik, C., Khoshmanesh, K., Mitchell, A. & Karnutsch, C. Microfluidic platform for separation and extraction of plasma from whole blood using dielectrophoresis. *Biomicrofluidics* **9**, 1–16 (2015).
29. Xiaokang Li, Maria Soler, Crispin Szydzik, Khashayar Khoshmanesh, Julien Schmidt, George Coukos, Arnan Mitchell, and H. A. Label - Free Optofluidic Nanobiosensor Enables Real - Time Analysis of Single - Cell Cytokine Secretion. *Small* (2018) doi:10.1002/smll.201800698.
30. Szydzik, C. *et al.* Fabrication of complex PDMS microfluidic structures and embedded functional substrates by one-step injection moulding. 87988–87994 (2016) doi:10.1039/c6ra20688c.
31. Szydzik, C. *et al.* Fabrication of complex PDMS microfluidic structures and embedded functional substrates by one-step injection moulding. *RSC Adv.* **6**, 87988–87994 (2016).
32. Szydzik, C. *et al.* Lab on a Chip combining interferometric sensors and injection Photonic background. 2793–2804 (2017) doi:10.1039/c7lc00524e.
33. Duffy, D. C., McDonald, J. C., Schueller, O. J. A. & Whitesides, G. M. Rapid prototyping of microfluidic systems in poly(dimethylsiloxane). *Anal. Chem.* **70**, 4974–4984 (1998).
34. Szydzik, C. *et al.* An automated optofluidic biosensor platform combining interferometric sensors and injection moulded microfluidics. *Lab Chip* **17**, 2793–2804 (2017).
35. Yin, J., Deng, J., Du, C., Zhang, W. & Jiang, X. Microfluidics-based approaches for separation and analysis of circulating tumor cells. *TrAC - Trends Anal. Chem.* **117**, 84–100 (2019).
36. Belotti, Y. & Lim, C. T. Microfluidics for Liquid Biopsies: Recent Advances, Current Challenges, and Future Directions. *Anal. Chem.* **93**, 4727–4738 (2021).
37. Descamps, L., Roy, D. Le & Deman, A. Microfluidic-Based Technologies for CTC Isolation :

A Review of 10 Years of Intense Efforts towards Liquid Biopsy. (2022).

Chapter 5

Plasmonic Nanohole array sensing for cancer biomarker through an Integrated Opto-fluidic system

5.1. Introduction:

For healthcare dogma, diagnosis is an initial crucial step and early detection for precise disease identification is fundamental for disease progression and therapy efficacies that could affect the ultimate outcome for the patient. Conventional diagnosis relies on detection and quantification of biomarkers whose altered levels are indicators for diseased state [1,2].

Analysis of such biomarkers is used for monitoring therapy response and evolution of patient state. Typical techniques in clinical diagnostics include biomolecular assays such as enzyme linked immunosorbent assay (ELISA), chemiluminescence immunoassays (CLIA), polymerase chain reaction (PCR) coupled with fluorescence or chromatographic approaches and mass spectrometry among others [1,2]. Such standardized approaches provide outstanding sensitivity and specificity and detect large libraries of biomarkers. Recently, automation and modernization of these techniques have further reduced time consumption, labour demand and manual errors. However, such systems face shortcomings related to need of specialized technicians, centralized laboratories, and overall high financial cost hamper efficient and rapid on-site performance of diagnostic assays [1,2].

Plasmonic biosensors have the potential to take charge in the evolution of medical analytics focusing on reliable and ultrasensitive point of care (POC) diagnostics. Among different plasmonic systems, Surface Plasmon Resonance (SPR) and its derivatives – e.g., SPR imaging (SPRi) and localized SPR (LSPR) have showcased exceptional capabilities focusing on label-free detection and real-time monitoring with minimal reagent and sample consumption, time conscious, and user-friendly operation devices [2].

Plasmonic biosensors are refractometric in nature relying on the manipulation of the evanescent field upon light interaction under determined conditions such as wavelength, incidence angle, polarization, among others. Coherent oscillations due to excitations of the conductive electrons on metal surfaces creates an evanescent field where electromagnetic waves penetrates the adjacent dielectric medium with decaying intensity [3,4]. This evanescent field is highly sensitive to refractive index changes on the metal-dielectric interface induced by mass change or media composition directly translated for variations in certain optical properties like reflectivity, resonance angle and wavelength. For a biological interaction, when a target analyte is recognized by a biorecognition element immobilized on the sensor surface leads to such variations that can be analysed in real-time providing direct and quantifiable detection of the bio-interaction without requirements of external labels. For an optimal plasmonic signal, sensograms display an association phase followed by a steady state and a dissociation phase in a concentration-dependent manner for optimal assessment and evaluation of affinity and kinetic parameters.

Conventional SPR based sensors have exhibited technical sensitivity to be around 10^{-5} to 10^{-6} refractive index units (RIUs) and range between 0.5 and 1 pg/mm^{-2} for standardized biomolecular assays [2,4]. SPR based biosensors have been widely applied in research laboratories and pharmaceutical industry, with multiple commercial setups available for kinetics and affinity studies. However, such sensors have yet to be adopted in clinical settings where a handful of vital challenges identified specifically sensor surface biofunctionalization, high-throughput analysis capability and POC device integration miring their progress for implementation as *in vitro* diagnostic devices. Current research has been focused on such directions with advents in novel chemistries, nanotechnologies, and biotechnology approaches. Recent reports have addressed not only faster and sensitive detection of conventional biomarkers but for newly discovered targets that can improve early disease identification and precise therapy monitoring. In this chapter, I will focus on the different plasmonic approaches for cancer biosensing applications specifically focusing on plasmon propagation through nanohole arrays (NHA), recent research on their comprehensive perspective for application in medical diagnostics.

5.1.1. Overview:

Here we presented an integrated setup used for the detection of cancer biomarkers via a label-free optical biosensing modality coupled within a pneumatically actuated microfluidic device. For the biosensing modality, we opted for a plasmonic transducer based on nanostructured surfaces i.e., nanohole arrays (NHA) to further enhance sensitivity. NHA films were acquired from a company and further deposited with gold (Au) via E-beam deposition at RMIT University. For characterization of biosensing efficiency, these Au deposited NHA were coupled in a pneumatically actuated microfluidic device fabricated through moulding protocol and cancer associated biomarkers i.e., Interleukin-6 (IL-6) and Tumour Necrosis Factor Receptor 2 (TNFR2) were targeted. Copper free click chemistry was used to selectively immobilize azide activated anti-IL-6 on DBCO/OH PEGs 2k (1:4 ratio) functionalized Au-NHA surface as showcased in Fig. 5.1.1.

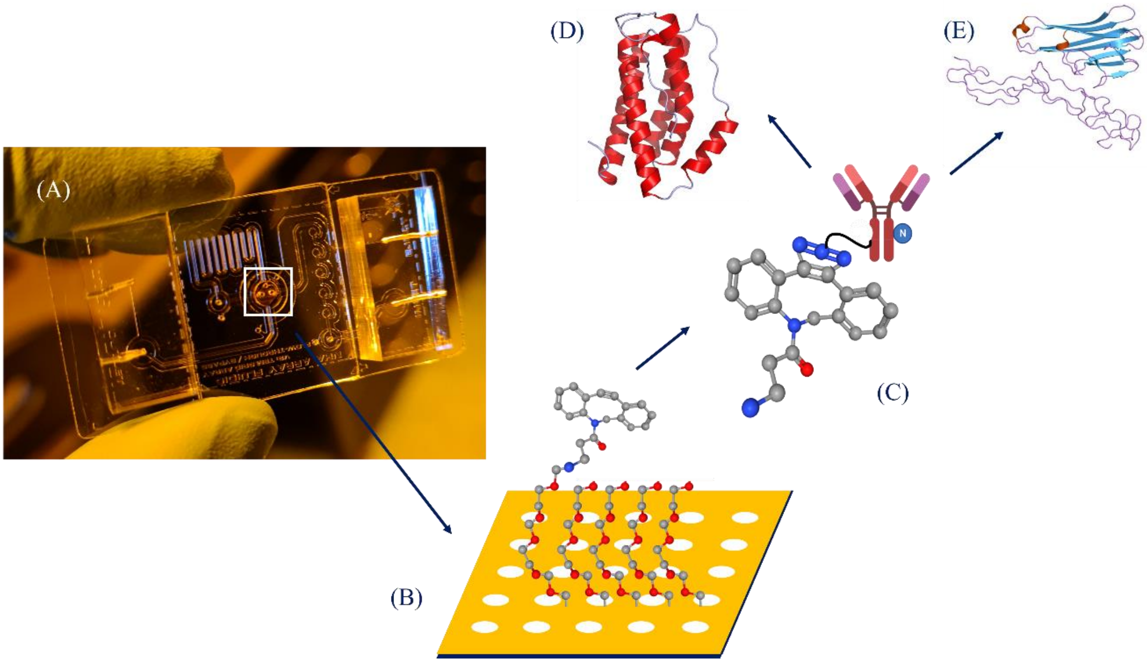

Figure 5.1.1.: Schematic of **(A)** Integrated opto-fluidic setup with nanohole array (NHA) highlighted functionalized with **(B)** 1/4 DBCO/OH PEGs 2k functional monolayer and further immobilized with **(C)** azide activated Ab-N$_3$ antibody. Conjugation of Ab-N$_3$ with DBCO/OH PEGs via SPAAC in site-specific and oriented fashion for specific **(D)** Interleukin-6 (IL-6) and non-specific for **(E)** tumour necrosis factor 2 receptor soluble (TNFR2) marker detection.

For characterization of this integrated opto-fluidic device and signal interactions, a modular opto-spectroscopic system was fabricated. Initially, qualitative characterization was performed for NHAs through a dual focused ion beam/scanning electron microscope FIB/SEM system, and then optical and fluidic characterization was showcased for the integrated system. Optimization of the opto-spectroscopic system was demonstrated for optimal objective selection followed by bulk sensitivity characterization using glycerol dilutions to establish sensitivity parameters i.e., limit of detection (LOD) and quantification (LOQ) and range. Afterwards, biosensing efficiency was exhibited in depth for specific and non-specific signal interactions for IL-6 and TNFR2 and further comparative analysis was performed.

5.2. State of the art:

5.2.1. Principle of Plasmonics and Surface plasmon:

Plasmon are defined as excitation on a bosonic quasiparticle level due to the oscillations occurring at a specific frequency signifying quantum plasmonic oscillation [5,6]. According to the Fermi liquid model, plasmon can be considered as charged electron cloud, systematically being displaced from their equilibrium position around a positively charged ionic lattice. Such propagations can be excited by an external electric field of the electromagnetic radiations on the surface [5] as exhibited in Fig. 5.1.3. (A) and (B). On an appropriate angle termed incidence angle, the wave vector parallel to the surface couples efficiently with the free electron gas/cloud with the light incidence in attenuated total reflection known as Otto or Kretschmann configuration as showcased in Fig. 5.1.2. for both conventional and nano-structured surface.

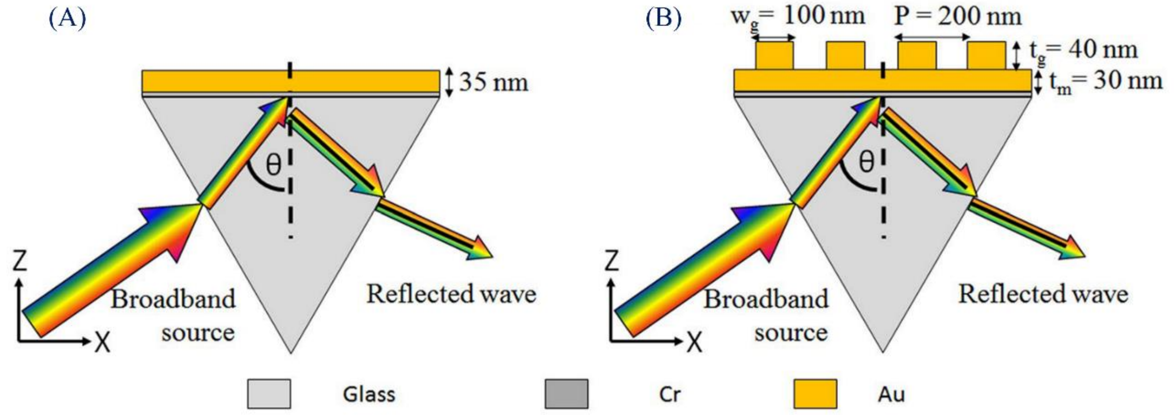

Figure 5.1.2.: Schematic of **(A)** Conventional and **(B)** Plasmonic nanograting based Kretschmann configuration. A 2 nm Cr adhesion layer followed by a 35 nm thick gold film is deposited on the prism. Rectangular gold nano-gratings with a thickness (tg) of 40 nm, a period (P) of 200 nm and a width (wg) of 100 nm are fabricated on top of 30 nm thick gold film [7].

Such excitations are defined as propagating surface plasmon polaritons (PSPPs) [6] and on metallic surfaces with or without nano-structuration, such polaritons can polarize the conducting electrons and penetrate metal surface resulting in localized surface plasmon (LSPs) demonstrated in Fig. 5.1.3. (C).

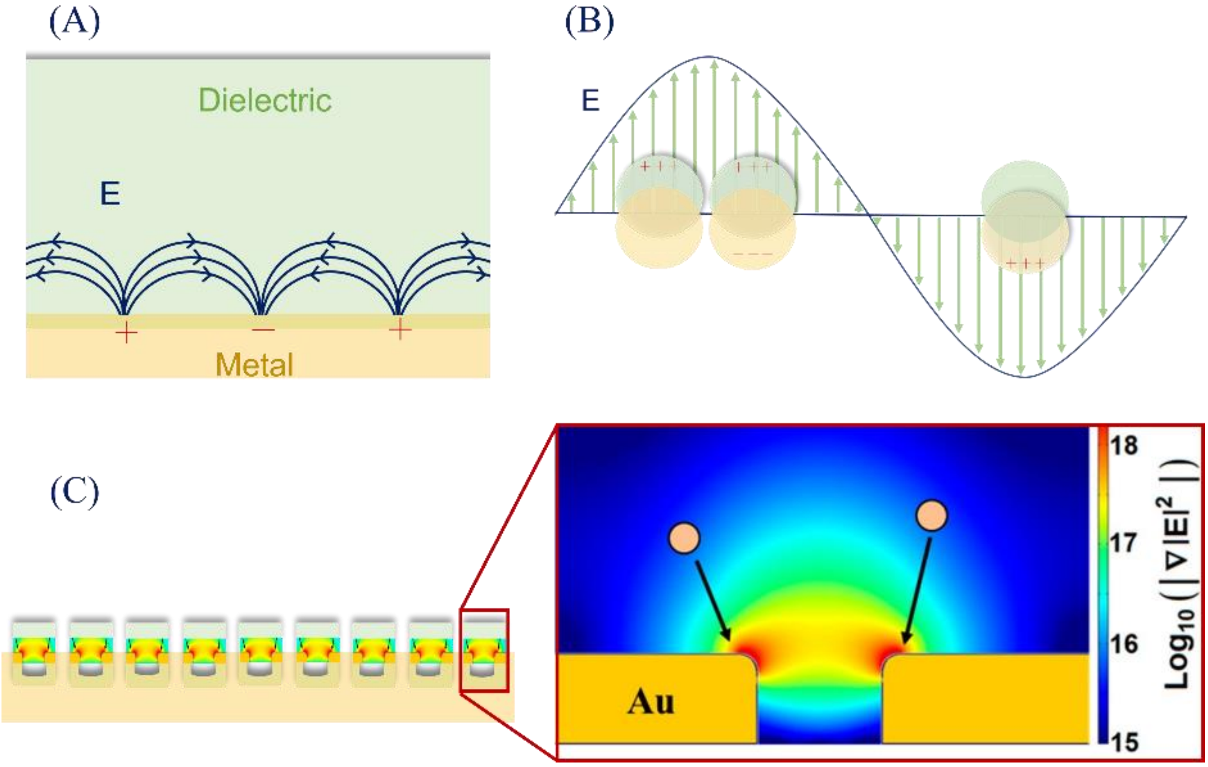

Figure 5.1.3.: Schematic of plasmon excitation in bulk and localized on surfaces **(A)** Electron beam excitation of bulk plasmon and propagating surface plasmon polaritons (PSPP) excitation through evanescent light field (top). **(B)** Localized surface plasmon (LSP) excitation through light propagation in free space or dielectric media. **(C)** LSPs in gold-nanohole array (Au NHA) model [8].

At the interface of a 'plasmonic' metal and a dielectric, systems of equations for surface plasmon resonance can be actuated. This actuation can be highlighted as eq. 5.1.1., where the propagation of wave vector k can be defined in electric and magnetic fields [9,10], where, ε_u is the dielectric constant of the metal [Ampere.sec/Volt.meter (As/Vm)] and ε_m is the dielectric of the environment [As].

$$k = \frac{w}{c}\frac{\sqrt{\varepsilon_u * \varepsilon_m}}{\sqrt{\varepsilon_u + \varepsilon_m}} \qquad \text{(Eq. 5.1.1)}$$

For large wave vectors, following equation Eq. 5.1.2. must be considered, where ωsp is the surface plasmon frequency [s^{-1}]. Characteristic frequency of such plasmon ωsp is 10^{15} s^{-1}.

$$\omega sp = \frac{\omega p}{\sqrt{1+\varepsilon_m}} \qquad \text{(Eq. 5.1.2.)}$$

In current case, according to Eq. 5.1.3., surface plasmon at constant frequency have a wave vector larger than wave vector of light in vacuum, thus the argument of the root is larger than 1. Thus, wave vector of light in vacuum k can be explained in Eq. 5.1.3., where w is angular frequency [s^{-1}] and c is the speed of light ~$3*10^8$ m/s [11].

$$k = \frac{\omega}{c} \qquad \text{(Eq. 5.1.3.)}$$

An increase in the wave vector of light is required for excitation of such surface plasmon. This is achieved by a prism 5.1.4. or diffraction grating highlighted in Eq. 5.1.5. [12,13] resulting in the intersection of the light with the dispersion relative to the surface plasmon on the interface between metal and bulk material achieving plasmonic excitation [5,14]. For both Eq. 5.1.4. and 5.1.5., p is the counting index $\mathrm{p} \in N$ of the prism, a is the lattice constant [m], θ is the incidence angle relative to the surface normal [°] and $n\mathrm{Pr}$ is the optical density of the prism.

$$kges, Pr = \frac{2\pi}{\lambda} * nPr * \sin(\theta) \qquad \text{(Eq. 5.1.4.)}$$

$$kges, BG = \frac{2\pi}{\lambda} + \sin(\theta) \pm p * a \qquad \text{(Eq. 5.1.5.)}$$

$$a = \frac{2\pi}{d}$$ (Eq. 5.1.6.), where d is the period of the diffraction grating [m]

In case of prism coupling such as commercial conventional SPRi setups i.e., Horiba's used previously for characterization of biological immobilization, wave vector of light is determined by the angle of incidence relative to the interface and optical density of the prism. For diffraction grating, an integer multiple of the lattice constant is added to the wavelength dependent component [15]. The associated lattice constant has been highlighted above in Eq. 5.1.4. and 5.1.5.

5.2.2. Propagation of Localized Surface Plasmon:

In contrast to PSPPS, localized surface plasmon (LSPs), are much smaller sized plasmon, on the nanoscale they could be smaller than wavelength of photon. LSPs are non-propagating excitations because of the resulting plasmonic oscillations distributed over the whole region [5,6,12]. The coherent electronic displacement for a restoring force is generated through positively charged lattice. Thus, attracting the polarized electrons towards the lattice such as nanostructures and nanoparticles can behave as 'nanoantenna', thus such systems can be considered as mass-spring harmonic oscillators driven by the energy resonant light wave. For such systems, electron cloud oscillates like simple dipole in parallel to the electric field of the electromagnetic radiation as highlighted in Fig. 5.1.1 (C) [16–18]. For propagations of LSPs, resonant light must be in frequency with the plasmonic oscillations, and the associated extinction coefficient has a dependence on the wavelength described by Mie theory [19,20] and highlighted in Eq. 5.1.6., where $\varepsilon_{\mathrm{m}'}\lambda$ and $\varepsilon_{\mathrm{m}}\lambda$ is the real and imaginary component of the dielectric constant of the metal respectively [As/Vm], d is the diameter [m] and λ is the wavelength [m].

$$E(\lambda) = \frac{24\pi N d^3 \varepsilon_{\mathrm{d}}{}^{3/2}}{\lambda \ln(10)} \frac{\varepsilon_{\mathrm{m}}\lambda}{(\varepsilon_{\mathrm{m}}(\lambda)+2\varepsilon_{\mathrm{u}}(\lambda))^2+(\varepsilon_{\mathrm{m}}(\lambda))^2} \qquad \text{(Eq. 5.1.6.)}$$

A simple spring-mass oscillator can be used to explain the Coulomb restoring force between lattice atoms and electrons. This concept of plasmonic systems have been described several times to attain conceptual and physical (semi-quantitative) understanding [16–18]. For example, the electron cloud distortion by an electric field can be explained by metal polarizability for spherical gold nanoparticles with size smaller than the wavelength of light (quasi-static approximation) [6,20].

Metallic films with sub-wavelength nanoholes have been reported to have enhanced plasmonic transmissions. This transmission is specifically high for certain wavelengths attributed to different plasmonic modes on the nanohole arrays (NHA) as presented in Fig. 5.1.4. [21].

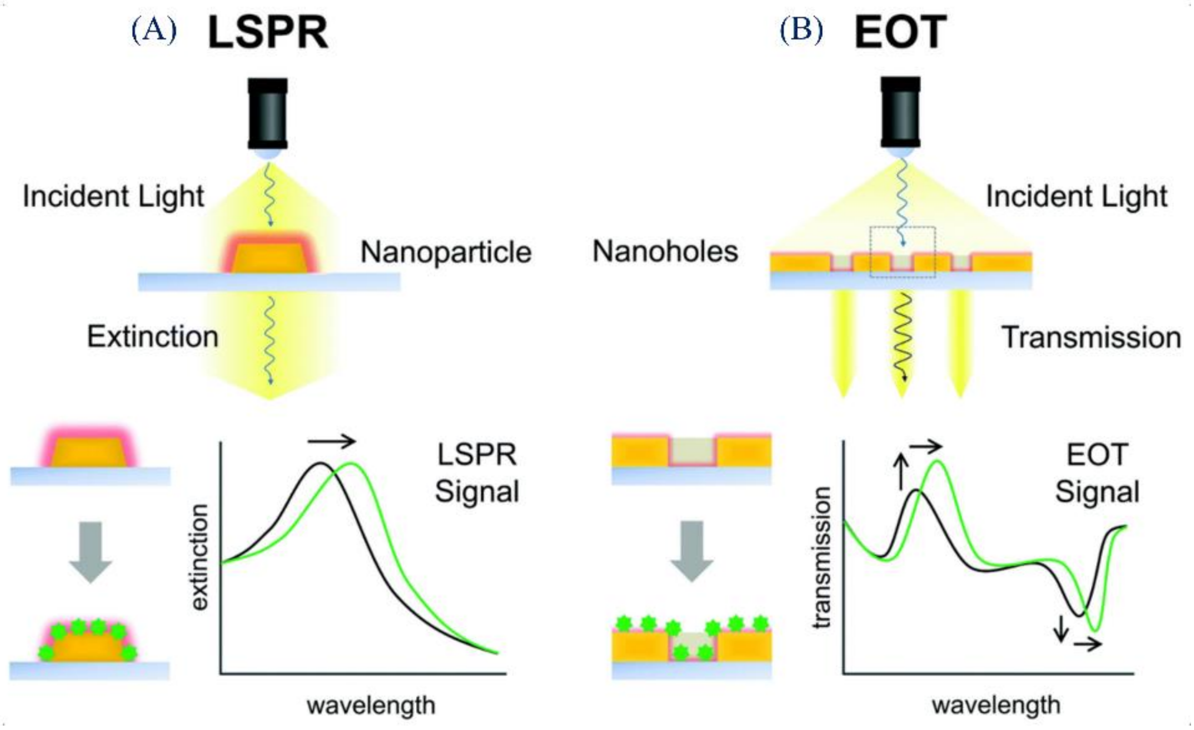

Figure 5.1.4.: Schematic illustration of principles of the plasmonic metallic nanostructure-based biosensors. The sensing strategies for a nanoparticle structures array is based on **(A)** LSPR extinction spectrum sensing, while for nanohole or cavity array, it is based through an **(B)** extraordinary optical transmission (EOT) spectrum, where electron clouds are highlighted as green dots [22,23].

Nanohole arrays (NHA) due to their interesting optical physico-chemical properties could be applied in numerous fields as optical bandpass filter for biosensing applications using surface plasmon resonance. The wavelength attributed for enhanced transmissions on NHA can be exploited for biosensing applications [24] via Otto/Kretschmann configuration explained earlier. More specifically refractive index shifts and surface sensitivity on thin solution layer are observed for such applications. Compared to non-structured metallic surface, NHA on metallic surfaces offers enhanced electrical field generation due to excitation from incident light for an active plasmonic mode of the nanoholes [24].

5.2.3. Elaboration of Nanohole Arrays (NHA) and plasmonic characterization:

Most NHA are exhibited to be cylindrical or circular hole shapes at specific periodicity. The hole shape, diameter and periodicity exhibit different optical properties, however the optimal shape and configuration for SPR sensors have yet to be showcased. Fabrication of NHA was first reported in by Masuda and Fukuda [25] through use of anodized alumina structure using the replication process showcased in Fig. 5.1.5. Afterwards, numerous protocols have been established for generation of nanohole arrays, however these strategies can be classified as serial such as milling techniques or parallel in nature i.e., lithographic techniques. Among these methodologies, excellent reproducibility has been highlighted through focus ion beam (FIB) milling specifically focusing on shape and diameter of nanoholes [24,26–28].

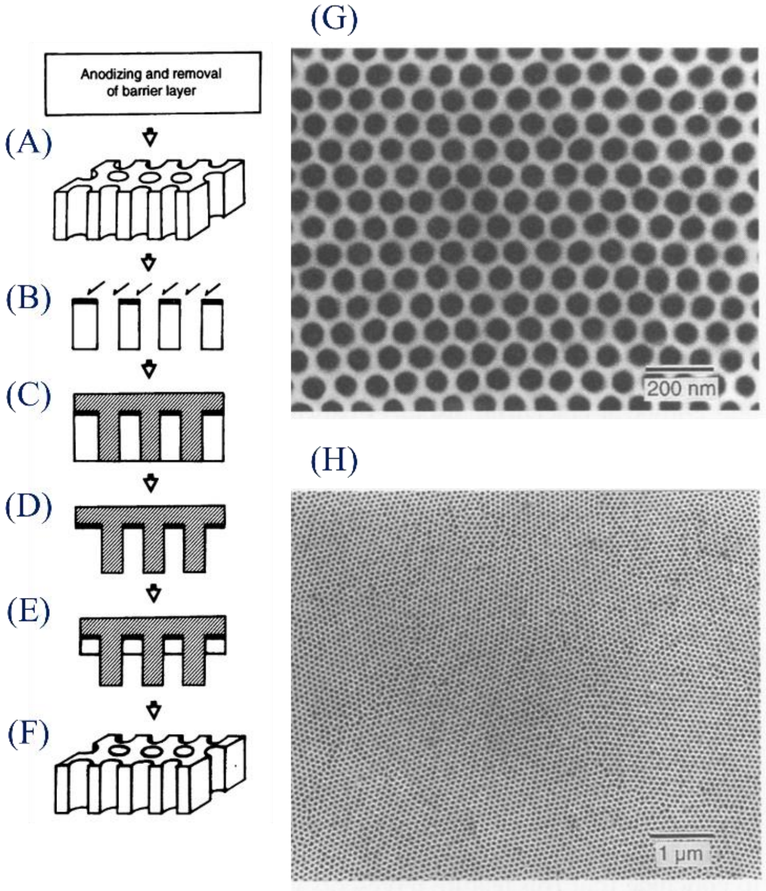

Figure 5.1.5.: Schematic diagram of the process for the fabrication of the metal nanohole array: **(A)** porous alumina with through holes (mother structure), **(B)** metal deposition with vacuum evaporation, **(C)** injection and polymerization of methyl methacrylate, **(D)** poly (methyl methacrylate) negative type, **(E)** electroless metal deposition, and **(F)** metal hole array. SEM photographs of the Pt nanohole array: **(G)** view of the surface (higher magnification), **(H)** view of the surface (lower magnification) [25].

Conversely, FIB is costly and require long processing time for milling for arrays larger than 100x100 µm, making it less practical. Lithographic techniques such as soft embossing with pre-prepared masks using E-beam lithography have alleviated some of the drawbacks associated with FIB milling [24,29,30]. Fabrication rate with area covered with nanoholes can be increased by this approach by using an imprinting mask that can be printed on a surface multiple time where such holes are covered with lossless metals such as gold to generate NHA.

Another protocol focuses on phase-shifting photolithography, etching, electron beam deposition and lifting (PEEL). Removable cylindrical pillars are generated through this technique that leads to the fabrication of NHA after lift-oof of nanopillars. All these techniques can offer tunability and reproducibility for diameter and shape for massive parallel fabrication of NHA. For lithographic techniques, different masks or templates with different physical parameters are required to fabricate NHA of different shapes and periodicity [31].

The analytical properties for NHA comprises of overall sensitivity and sensitivity to the monolayer formation, spectral position of the plasmonic band and resolution of refractive index measurements as refractive index sensitivity have been used to construct biosensors. The optical properties of NHA must be established for assessing such nanostructures as biosensors. Similar properties to nanoparticles were observed for NHA where transition between LSPs to propagating surface plasmon over the whole surface were observed. The optical response changes from localized SPR signal to extended surface plasmon was established on periodic NHA [24].

For unetched samples, typical LSPR absorption was analysed that showcased initial red shift with increasing etch time. At the transition point of the NHA, LSPR absorption band disappeared from 450-800 nm spectral range and a new plasmonic band was visible at around 480 nm as highlighted in Fig. 5.1.6. for different configurations. This further highlights a simple method for hole diameter tunability i.e., **(A)** variations in metal height, **(B)** gratings and **(C)** grating heights [7].

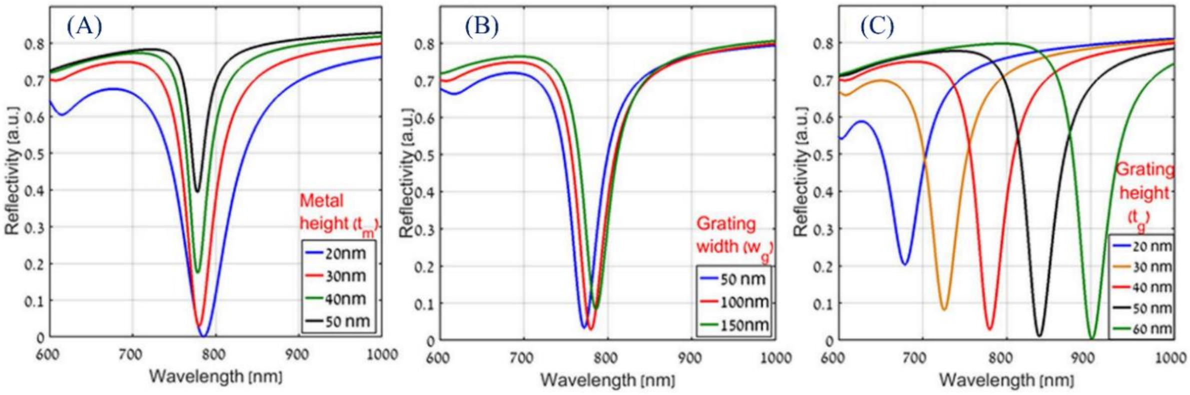

Figure 5.1.6.: Calculated reflectivity as a function of wavelength for plasmonic nanograting based Kretschmann configuration at an incident angle of 82° for a grating period of 200 nm with **(A)** variation in thin metal height (tm) **(B)** variation in grating width (wg) and **(C)** variation in grating height (tg) respectively [7].

For periodic Au-NHA fabricated through various methodologies have been showcased to accomplish this 480 nm plasmonic band periodicity [7,32–34]. For calculation of plasmonic wavelength in ordered NHA and hexagonal arrays have been highlighted in Eq. 5.1.7. and 5.1.8., where P is the array periodicity, ε_m is dielectric constants of the metal and ε_s is the of the solution in contact with the NHA and $\lambda_{SPR}(i,j)$ is the plasmonic wavelength for the Bragg resonance orders (i,j). The experimental spectrum for NHA matches closely with the finite difference time-domain (FDTD) calculation [35].

$$\lambda_{SPR}(i,j) = \sqrt{\frac{\varepsilon_m * \varepsilon_s}{\varepsilon_m + \varepsilon_s} \frac{P}{\sqrt{i^2 + j^2}}} \qquad \text{(Eq. 5.1.7.)}$$

$$\lambda_{SPR}(i,j) = \sqrt{\frac{\varepsilon_m * \varepsilon_s}{\varepsilon_m + \varepsilon_s} \frac{P}{\sqrt{\frac{4}{3}(i^2 + ij + j^2)}}} \qquad \text{(Eq. 5.1.8.)}$$

The correlation to the solution/nanohole interface was showcased for the plasmonic peak at the lower wavelength and the peak at higher wavelength was defined to glass/nanohole interface. Accordingly, around 226 nm/RIU have been showcased for the sensitivity to the solution refractive index of the lower wavelength peak while sensitivity for glass/nanohole plasmonic peak is an order magnitude lower [33]. Compared with the FIB-milled nanoholes, the sensitivity to the refractive index is a bit lower around 333 nm/RIU. Conversely, FIB manufactured nanoholes have a square array of

150 nm holes compared with the 320 nm holes hexagonal array obtained through modified lithography as highlighted in Fig. 5.1.7.

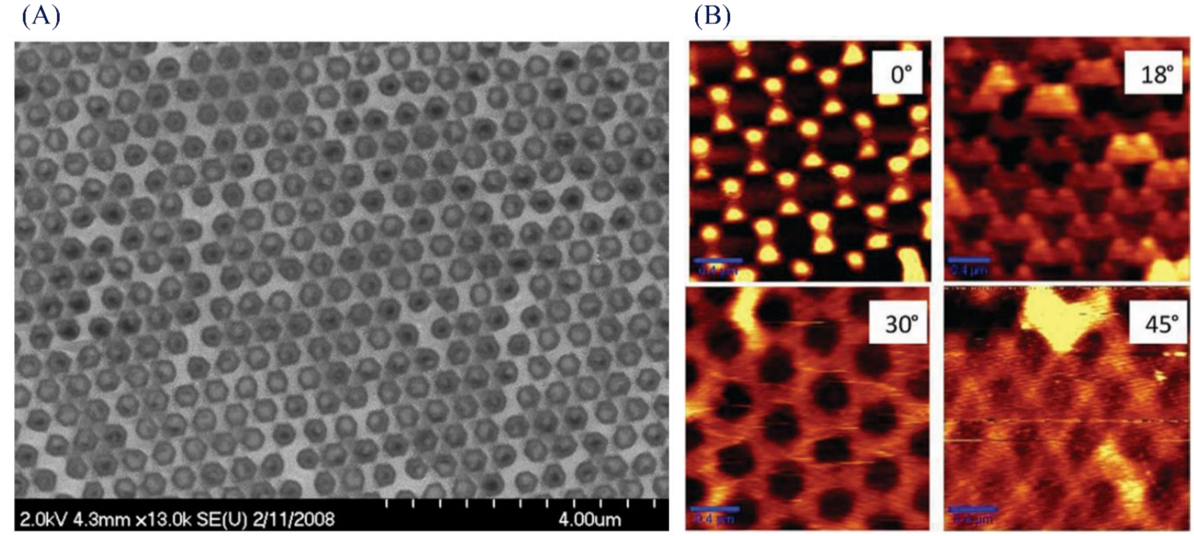

Figure 5.1.7.: **(A)** SEM image of a nanohole array at a deposition angle of 30° . The nanoholes are hexagonally shaped and the SEM image demonstrated that nanosphere lithography (NSL) coupled with glancing angle deposition (GLAD) produces relatively few defects on the nanohole array. **(B)** AFM images in contact mode for nanostructures at different deposition angles. The scan size is 2 µm x 2 µm for each image [33].

The sensitivity difference highlighted here based on two different fabrication approach may be due to different physical parameters of the NHA. In addition, sensitivity to the formation of an organic thiol monolayer was analysed with periodic NHA with an observable wavelength shift of the order of 1-2 nm [33]. Compared with the periodic NHA, LSPR on differently structured arrays are significantly lower up to 40 nm discussed in detail in Fig. 5.1.8.

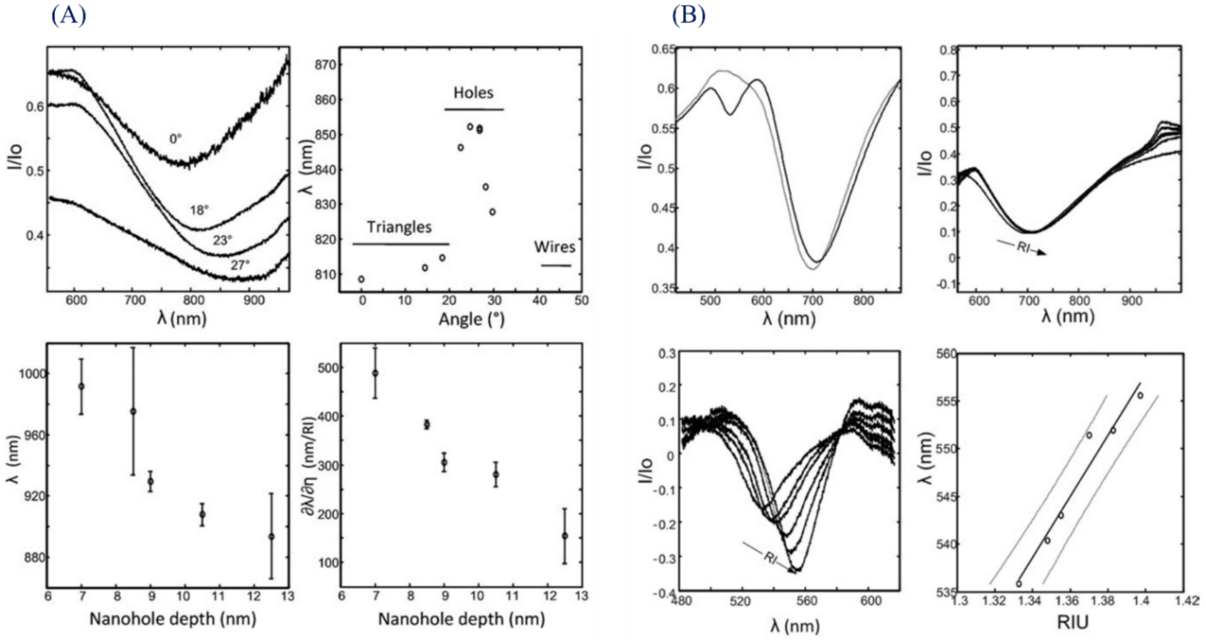

Figure 5.1.8.: **(A)** (top left) Spectra of nanostructures produced with GLAD. The deposition angle for nanotriangles is at 0° , a deposition angle of 18° and 23° results in interconnected triangles

and a deposition angle of 27° results in a hexagonal nanohole array. (Top right) The excitation wave- length in water is shown for the surface plasmon (SP) of nanostructures prepared by GLAD at different deposition angle. (Bottom left) The excitation wavelength in methanol is depicted for the SP of nanoholes prepared with GLAD (27°) at different nanoholes depth. (Bottom right) The sensitivity of nanohole arrays prepared at 27° decreases for nanoholes of increasing depth. **(B)** (top right) Transmission spectrum of a plasma treated nanohole array, two absorption bands at 552 nm and 718 nm are observed in water (black) and a single absorption is observed in air (gray). (Top right) Transmission spectra of sucrose solutions with the absorption band at 718 nm. Increasing the refractive index of the solution minimally changes the absorption peak. (Bottom left) Transmission spectra of sucrose solution with the absorption peak at 552 nm. Increasing the refractive index of the sucrose solution significantly changes the position of the absorption band. (Bottom right) Calibration of the refractive index sensitivity of the nanohole arrays prepared by plasma treatment of the nanosphere monolayer. The peak at 552 nm (represented here) has a sensitivity of 226 ±45 nm RIU^{-1}, while the peak at 718 nm has a sensitivity of 27 ± 5 nm RIU^{-1} [33].

5.2.4. Analytical and Optical properties of NHA for Biosensing Applications:

Refractive index (RI) resolution is another analytical parameter to focus on in addition to sensitivity and improving RI resolution results in improved detection limits. Typically, magnitude of 10^{-4} is achieved for ordered NHA [24,33] similar to the order of conventional SPR. However different groups focusing on SPR biosensing have highlighted RI resolutions of 10^{-5} to 10^{-6} focusing on data analysis methodologies to improve signal-to-noise (S/N) ratio [24,33]. Better S/N can be achieved for NHA by reducing the shot noise combined with calculating centroid wavelength of the plasmonic response. Alternatively, NHA of higher sensitivities can be achieved with sharp plasmonic bands which will further improve RI resolution like 10^{-6} to 10^{-7} range [36].

Compared with the conventional SPR based sensing methods, NHA highlight a growing niche providing device integration, smaller labour foot-print, increased multiplexing potential and simplified collinear optical detection where binding of analytes is determined directly from light transmitted through the holes [37]. In contrast to traditional SPR, the top metallic surface is necessarily not the dominant sensing surface for NHA where, molecular analyte binding that occurs on the inner surface of the nanoholes can dominate the sensor signal response. Thus, to enhance the analyte transport to the in-hole sensing surface, flow-through compared with flow-over NHA sensing format shows promise. For flow-over NHA that are dead ended, such configuration relies on cross-stream transport of analytes within microchannel flow typical for surface-based biosensors. However, flow-through NHA configuration capitulates on the unique nature of nanohole plasmonic sensing elements as ‘nanochannels’. An array of such nanochannels in parallel provide sieving action for the analyte in contrast to the surface-based sensors discussed in detail in Fig. 5.1.9.

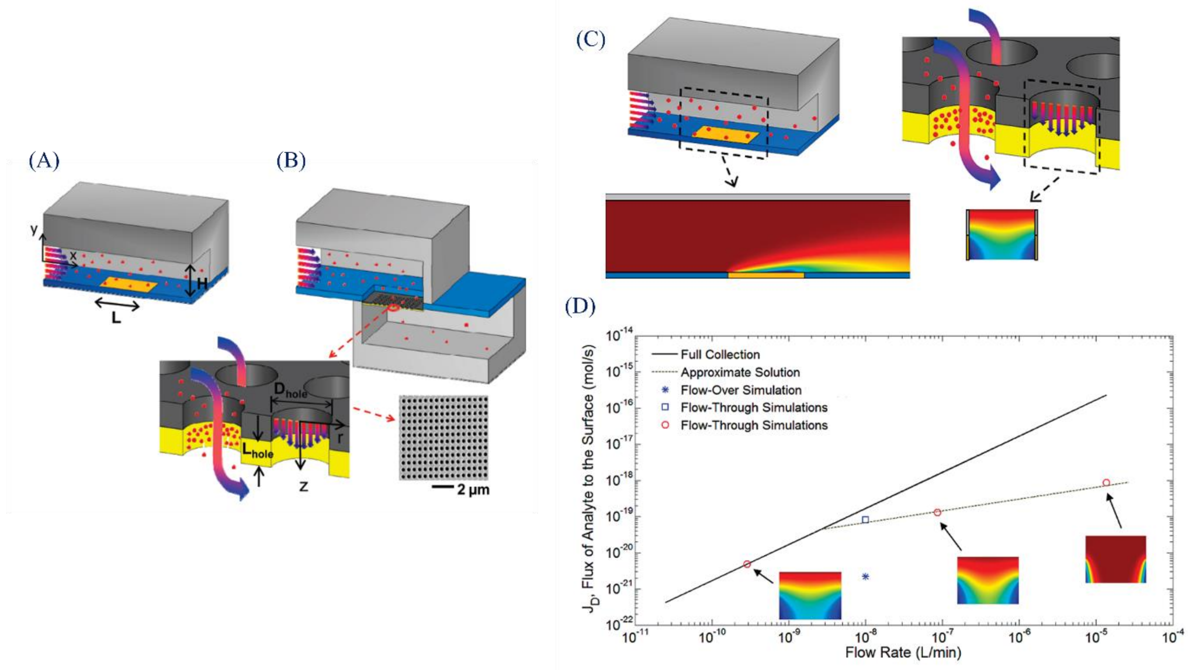

Figure 5.1.9.: Schematic representation of the two sensing formats considered in this work: **(A)** a typical flow-over format with a square surface-based sensor within a microfluidic channel, and **(B)** the flow- through nanohole array format where analyte solution passes from one microchannel to another via an array of nanoholes/nanochannels in parallel. Comparison of transport in flow-over and flow-through sensing formats. **(C)** Schematic of the flow-over format (left) and flow-through format (right). Simulation results indicate analyte collection in the flow-over sensor (L = H = 20 µm), and a flow-through nanohole (D= 300 nm, L_{hole} = 100 nm) array of equivalent sensing area. Both are provided the same flow rate (Q = 10 nL/min), D = 1 × 10^{-10}m^{2}s^{-1} and the surface concentration was fixed ($c_S(t) = 0$) to consider transport in isolation from binding kinetics. **(D)** Extension of results shown in **(C)** plotted as total molecular flux to the sensing surface, JD, versus flow rate. The continuous line indicates the fundamental limit where all incoming analyte molecules are transported to the sensing surface. The dashed line represents the flux estimated using the solution for mass transfer to a two-dimensional sensor as given by Ackerberg et al. Values corresponding to microchannel and nanohole cases from **(C)** are plotted, as indicated as in the legend, and sample flow-through computational results are shown inset [37].

Experimental results showcased flow-through biosensing configuration does not relatively improve the RI resolution compared with the flow-over approach showcased in Fig. 5.1.10. However, it has been highlighted to significantly improve analysis and response time to monitor analyte sensing [37–39].

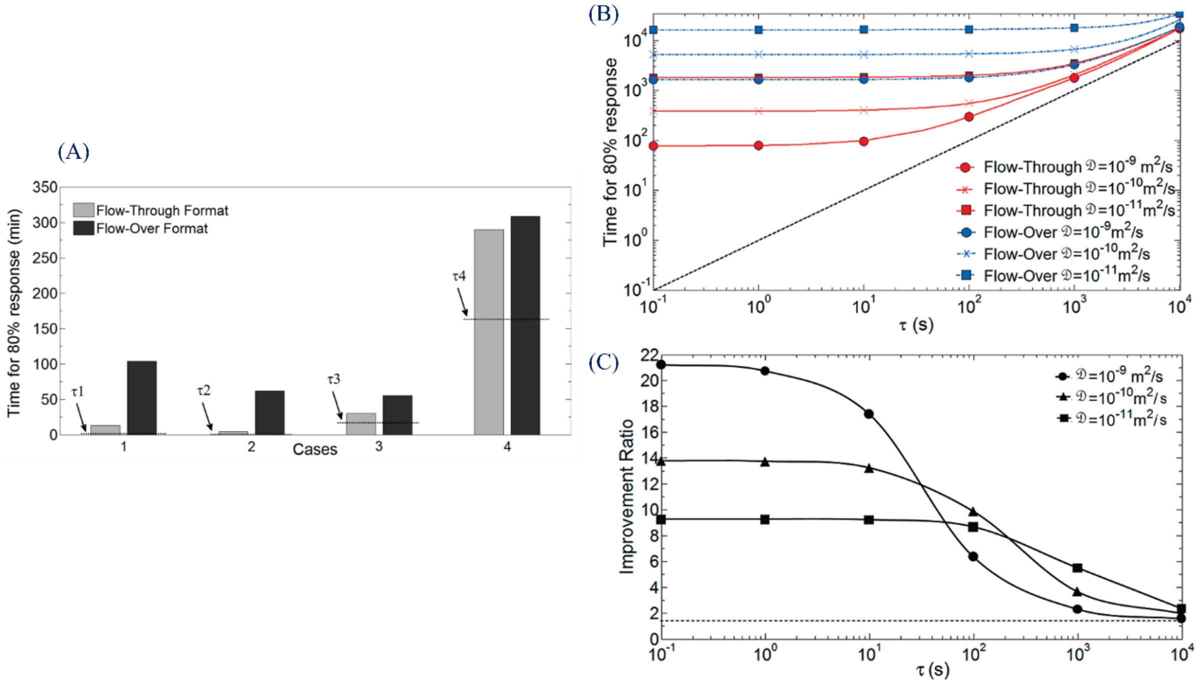

Figure 5.1.10.: **(A)** Comparison of flow-over and flow-through sensing formats for four analyte systems. Time for 80% of the equilibrium analyte concentration to be adsorbed to the surface is plotted for both sensing formats. The sensors had equivalent sensing area with geometries as employed in Figure 5.1.8, and both systems were provided 10 nL/ min. The flow-through format provides significant gains for Analyte Systems 1 and 2, however, only a modest benefit was achieved in Systems 3 and 4. Particularly in Analyte System 4, the benefit of flow- through transport is obscured by the long characteristic time binding time. Characteristic binding time scale for each case is shown as a dashed line as indicated. **(B)** Response time improvement of the flow-through sensing format as a function of characteristic binding time scale, τ . The results shown in **(B)** were obtained from simulations using the COMSOL model described in the text, and varying k_{on} from 10^2 to 10^7 $M^{-1}s^{-1}$ for three different molecule sizes. In all cases, c_0 is higher than $1/K_A$ to ensure saturation of the sensing surface. The flow-through format provides maximum benefit at $\tau \leq 10^2$ s. As τ increases, all the response curves approach the limit $t = \tau$. In **(C)**, the results from **(B)** are shown as a flow-through-to-flow-over response time improvement factor. The highest benefit, around 20-fold, is achieved for rapidly diffusing analyte and smaller τ values; and between 10- to 20-fold for values representing typical biosensing applications [37].

However, for microfluidic integration flow-through is more complicated compared with flow-over configuration which can be achieved via a single channel. Operating parameters and binding kinetics of the specific analyte system fare given potential benefit by flow-through sensing. Quantification and generalization of binding kinetics through flow-through configuration have been showcased in Eq. 5.1.9. and 5.1.10., considering analytes transport to active sites occurring rapidly than binding kinetics, rate of change of surface concentration of analyte adsorbed on the sensing surface c_s for first-order Langmuir kinetics:

$$\frac{\partial c_s}{\partial t} = k_{on} c_0 (b_0 - c_s) - k_{off} c_s \qquad \text{(Eq. 5.1.9)}$$

Where k_{on} is the adsorption constant, k_{off} is the desorption constant, c_0 is the concentration of analytes in bulk and b_0 is the total concentration on the surface of active potential binding sites. Eq. 5.1.11. is derived from Eq. 5.1.10., with an analytical expression for surface concentration adsorbed species, where c_s^{Eq} is the equilibrium for surface concentration termed by Langmuir adsorption equation. In addition, K_{A} is the affinity constant, and τ is the time scale characterizing the required time for sensor to reach equilibrium concentration. Thus, τ is used to quantify and compare various analyte systems for binding kinetics [37].

$$c_s(t) = c_s^{\mathrm{Eq}}(1 - e^{-t/\tau}), c_s^{\mathrm{Eq}} = \frac{b_0 c_0 k_{\mathrm{on}}}{k_{\mathrm{on}} c_0 + k_{\mathrm{off}}}, K_{\mathrm{A}} = \frac{k_{\mathrm{on}}}{k_{\mathrm{off}}}, \tau = (k_{\mathrm{on}} c_0 + k_{\mathrm{off}})^{-1} \quad \text{(Eq. 5.1.10.)}$$

Different groups have used nanohole arrays for different bio-applications focusing on detection of various biomarkers. Wong and group showcased high throughput and high yield fabrication of gold NHA using nanopattern nickel mould fabrication and UV imprinting. This fabrication protocol achieved almost 100% yield from nanoimprinting to gold lift-off. This gold nanohole array demonstrated prostate specific antigen (PSA) detection by a sandwich fluorescence assay with detection limit of 100 pg/mL while non-structured gold film demonstrated 1 ng/mL as exhibited in Fig. 5.1.11 [40].

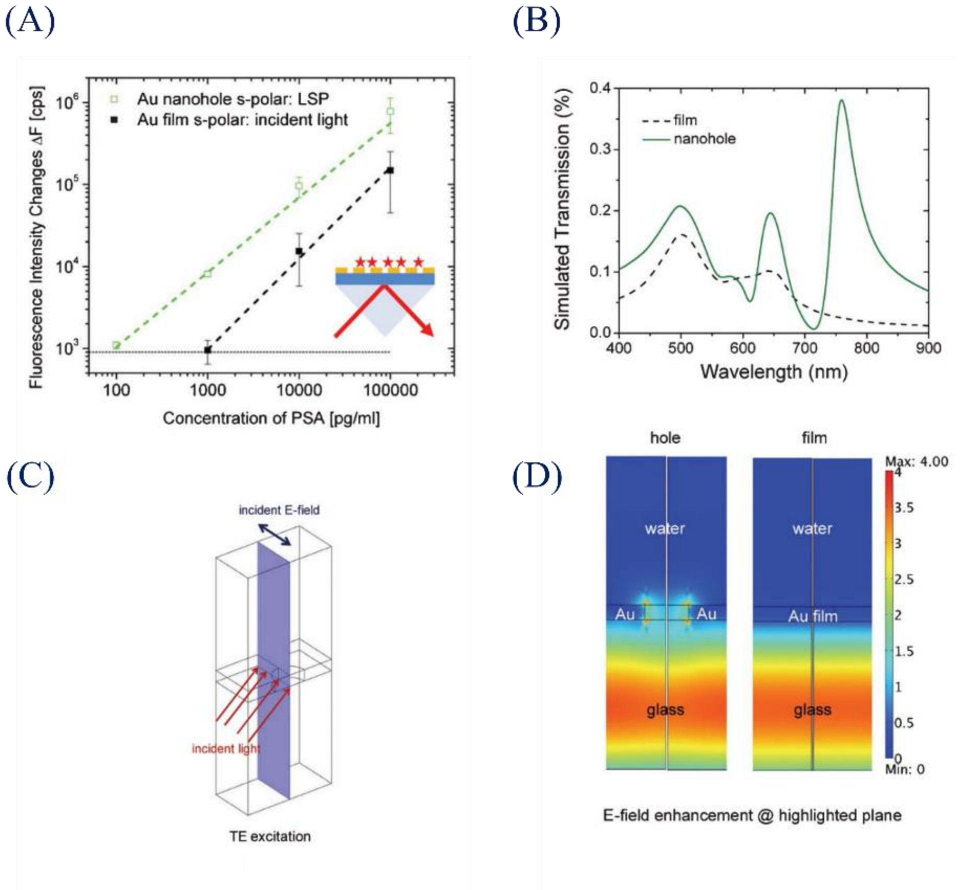

Figure 5.1.11.: **(A)** Fluorescence detection on a gold nanohole array (p = 400 nm, square length = 140 nm, T = 50 nm) and gold film (T = 50 nm) for a sandwich immunoassay of PSA at concentrations from 100 pg/mL to 100 ng/mL, where the 633 nm light is shed at 71° (the angle between the normal of the glass surface and the light beam) using total internal reflectance (TIR) fluorescence spectroscopy in TE mode. **(B)** A half of a cell for plasmonic field simulation with

angular incidence. **(C)** Transmission spectra and **(D)** plasmonic field distributions of the gold nanohole array and gold film on glass under the same conditions as in the experiments [40].

Escobedo *et al.*, presented another nanohole array-based biosensors integrated with a microfluidic concentration gradient generator for image detection and quantification of ovarian cancer biomarkers. A microfluidic stepped diffusive mixing was fabricated to create calibration curves on controlled concentrations. Image intensity and comparison with calibration curves was focused for quantification of samples with unknown concentration. Initially, this setup was employed for the immobilization of ovarian cancer marker antibodies and subsequent quantification of r-PAX8, an ovarian cancer marker. LOD of around 5 nM and a dynamic range from 0.25 to 9.0 μg/mL were achieved and the proposed biosensor demonstrated on-chip self-generating calibration curves as presented in Fig. 5.1.12 [41].

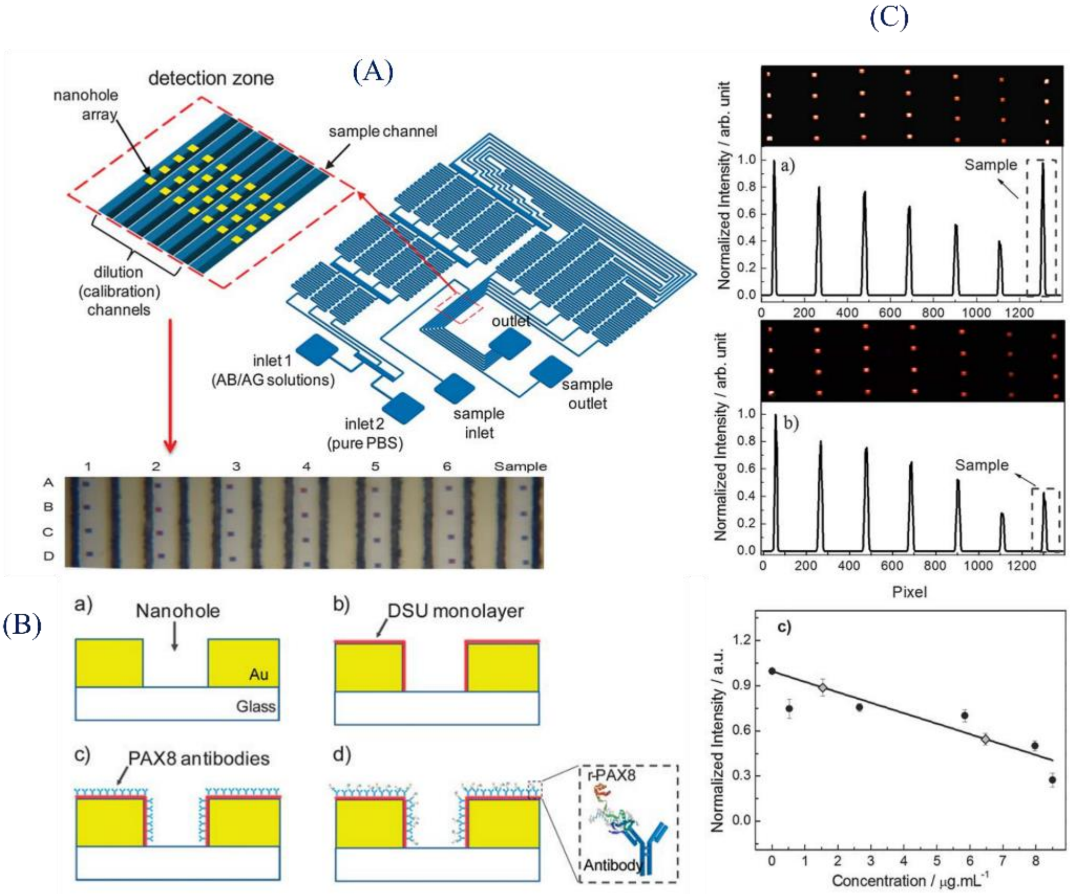

Figure 5.1.12.: **(A)** Schematics of the microfluidic chip used to both generate a concentration gradient for calibration and to introduce an "unknown" concentration of the ovarian cancer markers. **(B)** General schematics of ovarian cancer biomarker detection using nano- hole arrays. (a) Schematic representation of one of the multiple nanoholes in a nanohole array-based sensor, (b) Au sensor surface is coated with dithiobissuccinimidyl undecanoate (DSU) monolayer, (c) A layer of antibody for the r-PAX8 ovarian cancer biomarker (antigen) is deposited onto the DSU monolayer. (d) r-PAX8 specifically binds to the antibody on the surface of the sensor, generating a plasmonic signal response. **(C)** Normalized intensities after flowing r-PAX8 (antigen) solution onto a gold surface modified with PAX8 antibody. (a) Results when the nominal "unknown"

sample concentration of r-PAX8 was 2.00 µg/mL (low concentration end); (b) results when the nominal “unknown” sample concentration of r-PAX8 was 5.30 µg/mL (high concentration end), (c) average intensities obtained from all the arrays in each microchannel as a function of the concentration obtained through the dilution factors (R^2=0.926) [41].

Further progress on NHA integration for bio-application was demonstrated by Sun and group. A fully automated point-of-care (POC) system for quick quantitative procalcitonin (PCT) for sepsis diagnosis was developed. This system specifically focuses on localized surface plasmon resonance (LSPR) enhanced quantum dot (QD) emission in a sandwich assay of “capture PCT antibody/PCT/detection PCT antibody labelled with QD” on a gold nanoarray chip. Gold nanostructures were fabricated that were able to generate plasmonic cloud at resonant wavelength coincident with excitation wavelength of fluorescent dyes as highlighted in Fig. 5.1.13. Gold nanochip was fabricated by E-beam lithography and was integrated into the microfluidic chip with analyte sampling and bioassay reagent flow controlled by LabVIEW program.

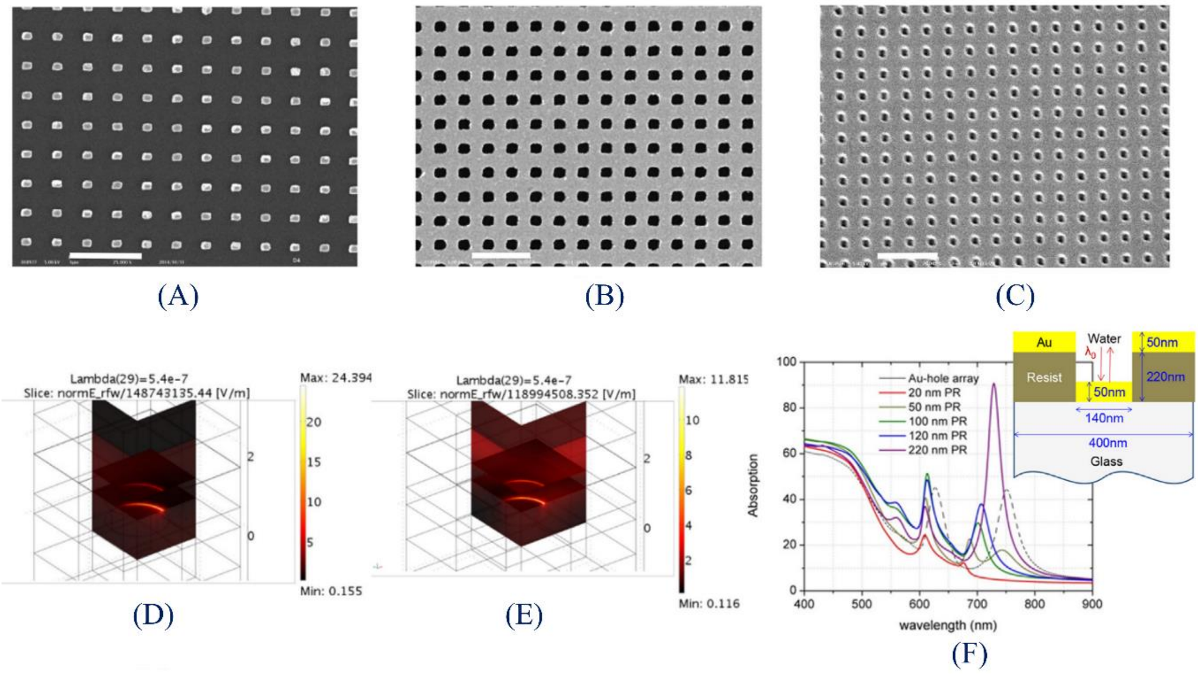

(A) (B) (C) (D) (E) (F)

Figure 5.1.13.: SEM images of **(A)** gold nanopillar array on glass, **(B)** gold nanohole array on glass and **(C)** gold nanohole array on PMMA, the metal layer is with 5 nm of chromium and 45nm of gold. The scale bars are 1 µm. The simulations of the plasmonic electromagnetic field at the wavelength of 540nm for gold nanopillar and nanohole array (assumed the size to be 140 nm diameter, chip immersed in water with light sheds from the top) are shown in **(D)** and **(E)**. **(F)** is the absorption spectral simulation of a gold nanohole array on photoresist (PR), whose situation is like their gold nanohole array on PMMA [42].

A CCD camera and a laser source was incorporated for the detection of QD emission. The microfluidic chip is inserted into the POC system upon analyte detection where blood sample loading, antibody recognition, dye-labelling, fluorescent detection, and data analysis was conducted automatically within 30 min at a test sensitivity of 0.5 ng/mL suitable for clinical diagnosis of sepsis through PCT biomarker highlighted in Fig. 5.1.14. [42].

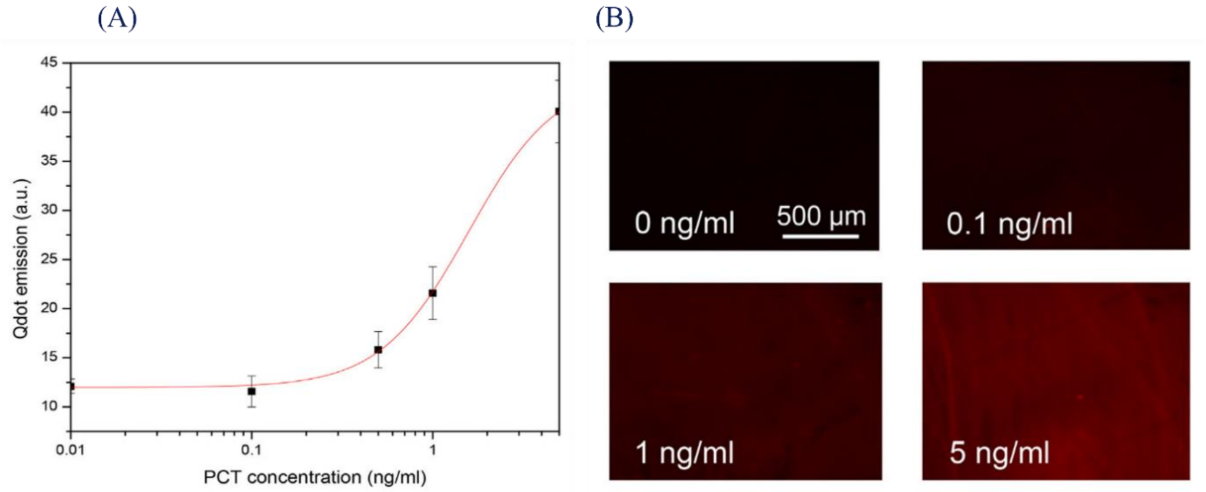

Figure 5.1.14.: **(A)** Fluorescent emission vs. concentrations of PCT on the gold nanopillar array, detected by the POC system. **(B)** Images of PCT immunoassay results taken by fluorescent microscope (scale bar is the same for all images) [42].

Cetin and group developed such a lightweight and field-portable biosensor employing a plasmonic chip based on nanohole arrays integrated to a lens free-imaging framework for label-free detection of viruses. A CMOS (complementary metal–oxide–semiconductor) camera is integrated with a high quantum efficiency in the spectral window of interest to monitor diffraction field patterns of nanohole arrays under the uniform illumination of an LED (light-emitting diode) source specifically spectrally tuned to the plasmonic mode supported by the nanohole arrays as showcased in Fig. 5.1.15. This handheld setup demonstrated the label-free detection of H1N1 viruses, e.g., swine flu, at medically relevant concentrations around as low as 10^3 $TCID_{50}$/mL (LOD), weighing only 70 g and 12 cm tall and capable of being employed in the field for rapid diagnosis [43].

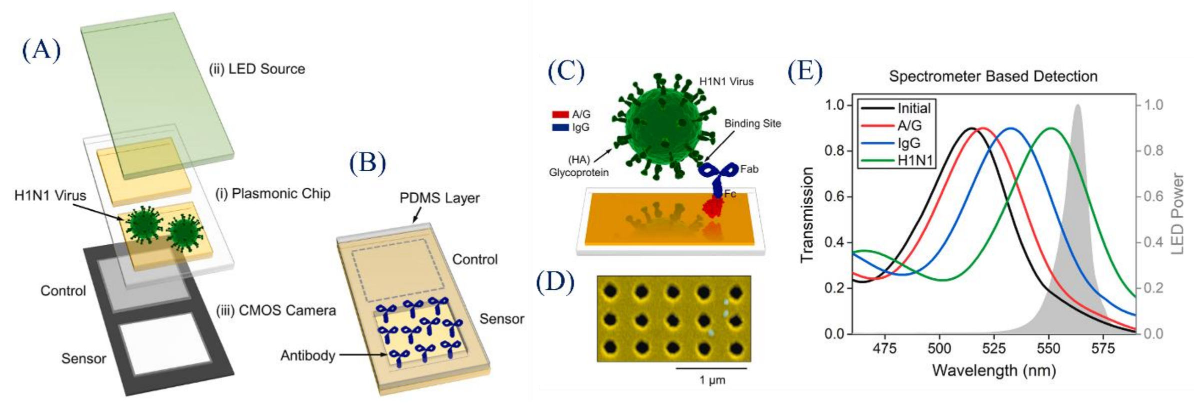

Figure 5.1.15.: Photograph and schematic illustration of **(A)**, **(B)** the handheld plasmonic biosensor. Sample preparation kit divides the plasmonic chip into sensor and control regions, which have different diffraction field intensities under the same LED illumination captured by the CMOS camera. **(C)** Schematic illustration of the virus (green) attachment on the Au surface using protein A/G (red) and virus antibody (blue). **(D)** SEM image of the H1N1 viruses on the surface of the Au nanoholes. **(E)** EOT response of the nanohole arrays before (black) and after the

attachment of protein A/G (red), protein IgG (blue) and H1N1 virus (green). Gray denotes the output power spectrum of the LED light source used in the portable biosensor platform [43].

The following section will focus on the materials and methods highlighting the chemical and biological products used along with different techniques used for fabrication, characterization, and analysis of our gold nanohole arrays and the opto-spectroscopic setup.

5.3. Materials and Methods:

5.3.1. Biological and Chemical products:

Glycerol 99%, Acetone 99.5%, Dichloromethane 99.8%, and Methanol 99.9% were purchased from Sigma-Aldrich. DBCO PEG thiol (DBCO-PEGs 2k) and OH PEG thiol (OH-PEGs 2k) was purchased from Nanocs (USA).

Phosphate Buffer Saline pH 7.4 (PBS) and Bovine Serum Albumin 98% (BSA) were purchased from Sigma-Aldrich while Tween® 20 was acquired from Carl Roth. SiteClick™ Antibody Azido Modification Kit (N_3) was purchased from Thermo Fisher. Interleukin-6 (IL-6; ref: 206-IL) and Tumour necrosis factor (TNF) receptor type II (TNFR2; aa 24-206; ref: 1089-R2) were procured from R&D systems and Anti-IL-6 (EPR21711; ref: ab233706) were procured from AbCam (USA).

5.3.2. Elaboration and Characterization of NHA:

5.3.2.1. Nanohole Array (NHA) metamaterial fabrication:

TEM grids for NHA meta-surfaces were acquired from PELCO Holey Si3N4 Support Films for TEM (Ted Pella Inc., USA). This film is a 450 µm x 450µm self-standing squared window with a 3mm diameter frame and a thickness of 200nm. The working window is fabricated with a closely packed hexagonal arrangement of circular holes with 200 nm diameter having periodicity of 400 nm.

Physical deposition of 100 nm thin gold (Au) layer on these Si3N4 support films was performed through E-beam evaporation (PVB75 Thermal Evaporator Kurt J. Lesker, USA) with a 5 nm initial layer of Chromium (Cr) being deposited before to coat the grids so to enable the adhesion of Au on the Si3N4 films.

5.3.2.2. Scanning Electron Microscopy (SEM) and Focused Ion Beam (FIB):

The periodic nature of NHA deposited with 100 nm Au layer was characterized using a Scios 2 DualBeam Focused ion beam/Scanning electron microscope (FIB/SEM) for ultra-high resolution and high-quality sample preparation. Gallium (Ga) ion beam according to the specifications was used to cut cross sections for FIB characterization, whereas for SEM scans, the setup was operated at 2kV and current between 6-13 pA with a working distance (WD) between 4-7 nm.

5.3.3. Characterization of Integrated NHA-Microfluidic setup:

5.3.3.1. Device Fabrication and Characterization of the microfluidic system:

The moulds for the integrated NHA-microfluidic device were designed and fabricated at Micro Nano Research Facility (MNRF), RMIT University as shown in Fig. 5.2.1. The devices were actuated in similar fashion to the CTC Cluster V1-V3 shown in Chapter 4 for microfluidic design done in Solidworks, and fabrication done using the same PDMS moulding protocol.

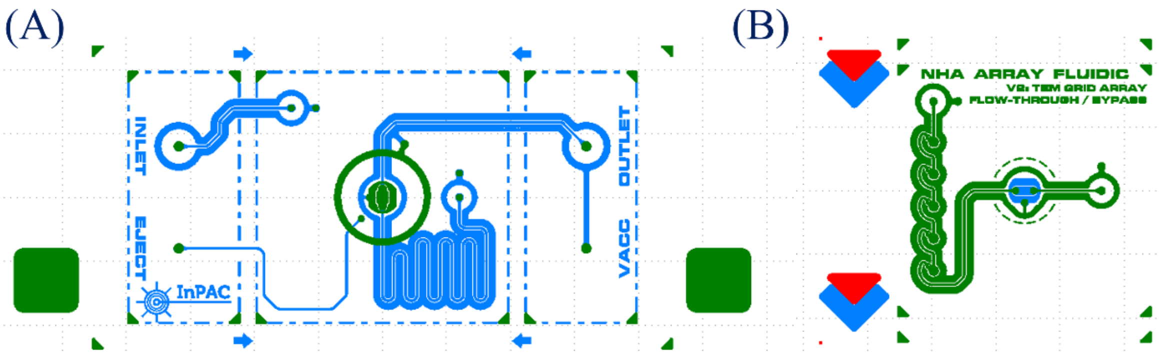

Figure 5.2.1.: Lithography mask for the moulds of the integrated Au-NHA microfluidic device. **(A)** Bottom layer of the microfluidic device with inlet, eject valves on the left side, outlet, and vac chuck outlet on the right side with NHA sensing area and serpentine for fluidic flow moving underneath the sensors and then connected to the outlet. **(B)** Top layer with connectors from the inlet, bubble trap arrays and connection to the NHA sensing area for flow to be going on top and through the NHA.

The schematic for the aligned device with the NHA under the microfluidic system has been highlighted in Fig. 5.2.2. (A). For fluidic manipulation, TEM grid was susceptible to bubble formation on the NHA under flow due to an air pocket between the films. To overcome this drawback, design considered flow-over as well as flow-through configuration as presented in Fig. 5.2.2. (B).

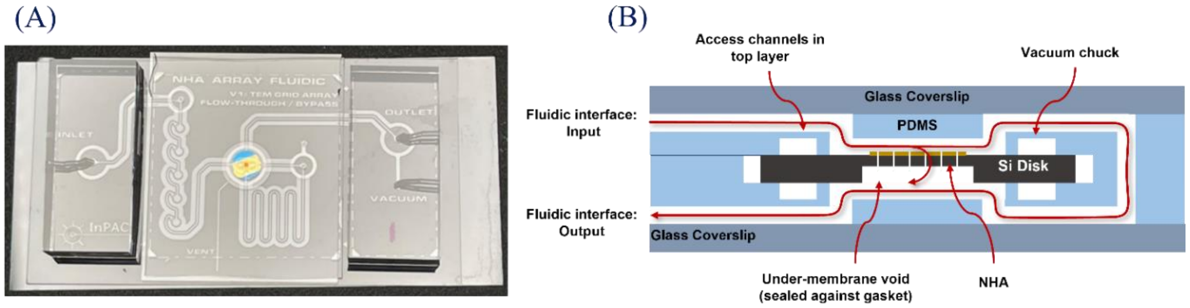

Figure 5.2.2.: Aligned microfluidic device with the Au-NHA and microfluidic path for biomolecule detection. **(A)** Aligned integrated Au-NHA microfluidic device with the NHA sensing area on SiN surface (blue), presumably because of its depth around that wavelenght, with gold deposited over it in a strip - the sensor is plasmonic and peaks at red – (red). **(B)** Microfluidic flow pathway highlighting the flow to move on top and through the NHA and afterwards, moving beneath as well to minimize bubble formations on the NHA.

This crossflow filtration approach was employed to ensure full fluidic access on both sides of the sensor. In literature, flow configuration for such plasmonic NHA are dead ended. This means that debris are trapped on the NHA acting as a filter and in addition, making the resistance very high, thus flow must be low in order not to break the array [37,44,45]. For our configuration, we achieve high flow because there is a path around the array thus, we are not limited to slow sensing. More so, with this crossflow filter, the NHA are not dead ended and portion of flow over the NHA will clear the debris.

5.3.3.2. Analysis of Optical setup and data processing:

Custom made opto-spectroscopic setup was composed of 30mm optical cage system (Thorlabs, Inc., USA) holding the free-space optical components. The opto-fluidic device with the NHA plasmonic sensor is illuminated with a collimated broadband light (MBB1L3: 470-850 nm Mounted Broadband LED, Thorlabs, Inc. USA) at normal incidence. For the facilitation of correct illumination of the NHA and collection of transmitted signals, a custom-made microfluidic holder was attached onto the alignment stage (Physik Instrumente (PI) GmbH & Co. KG, Germany) as highlighted in Fig. 5.2.3.

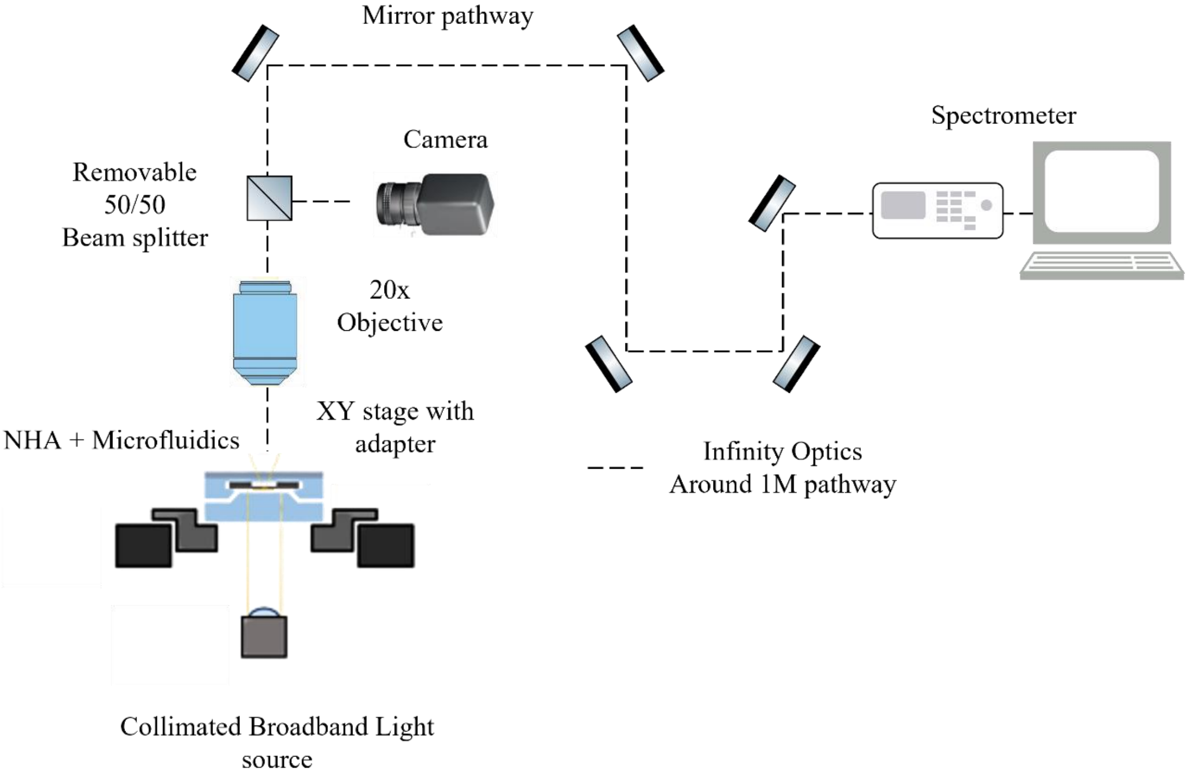

Figure 5.2.3.: Schematic of the opto-spectroscopic setup for analysis of integrated NHA microfluidic system. Collimated broadband light source, XY-stage for the microfluidic device along with an objective, a beam splitter and mirror pathway for optical direction towards the spectrometer. Beam splitter is integrated within the setup as to observe NHA via a camera.

For signal collection from the NHA, a 20X with a numerical aperture (N.A.) of 0.4 objective was used. The transmitted light from NHA was directed to the input slit of the spectrometer with an aperture of 500 μm via a series of mirrors (Thorlabs, USA). Andor Kymera 193i spectrometer was adjusted to the spectral range of 604-735 nm and this was collected by an electron multiplying CCD (Andor iXon Ultra 897). In addition, it has a grating of 300 l/mm providing spectral resolution of 500 nm full width at half max (FWHM) blaze.

The spectroscopic signals were obtained with an exposure time of 0.5 sec and recorded by a Python-based script. This script analysed the NHA signal on each interval and recorded the resonance peak within the defined spectral range mentioned above. This resonance is then analysed to corroborate the peak centroid within a fixed wavelength window of FWHM and plotted in real-time through a sensogram. This sensogram displayed centroid shifting of the signal over time produced by the changes in the refractive indices of the samples.

5.3.4. Chemical functionalization of NHA: 1/4 DBCO/OH PEGs 2k:

1/4 DBCO/OH PEGs 2k were obtained by immersing clean gold NHA in 0.04 mM DBCO-PEGs 2k and 0.16 mM OH PEGs 2k in degassed ethanol solution. This has been covered in detail in Chapter 3, Section: Materials and Methods: Gold substrate preparation and Chemical functionalization of gold surfaces. Incubation was done overnight under dark condition at room temperature. Functionalized NHA samples were than washed with ethanol for 2 x 10 min under gentle stream (no ultrasonication) and then soaked in deionized water for 5 min before drying with gentle nitrogen flow.

5.3.5. Antibody immobilization of functionalized NHA:

Anti-IL-6 was activated with azide function using the SiteClick™ Antibody Azido Modification Kit (N3). The final concentration of the activated antibody was 0.35 mg/mL as confirmed by OPTIZEN NanoQ (Mecasys, South Korea) and it was stored at 4° C untill immobilization.

Immediately after the chemical functionalization of NHA, N3 activated anti-IL was immobilized on the NHA through the integrated opto-fluidic system by initial injection at 10 μL/min follow by decrease to 2 μL/min. Afterwards, 1 μg/mL of human IL-6 was injected at a flow rate of 10 μL/min. In addition, 1 μg/mL of human TNFR2 at was injected for non-specific signal interaction as the molecular weights of both IL-6 and TNFR2 is similar.

5.4. Results and Discussions:

Qualitative NHA characterization was performed through Dual FIB/SEM setup. In addition, to assess functionality of these NHA plasmonic sensors, a modular opto-spectral system was fabricated, and initial characterization was performed by using different objectives with various field of view (FOV), ranging from 4X to 50X. Comparative analysis between transmission spectra was performed for the selection of optimal objective. Subsequently, NHA bulk sensitivities were performed in duplicate where glycerol solutions ranging from 20% to 15% to 10% to 5% to 2.5% and 1% were injected in descending order. The spectral shift from these bulk refractive index variations were used to measure baseline, slope, limit of detection (LOD) and limit of quantification (LOQ) for the integrated opto-fluidic system. More so, specific signal interaction was measured for cancer biomarkers i.e., IL-6 for specific and TNFR2 for non-specific interaction onto Ab-N_3 – DBCO/OH PEGs 2k 1/4 surface functionalization.

5.4.1. Qualitative characterization of NHA:

SEM images of the NHA were obtained after depositing support-Cr and top-Au layers. Different scans were taken from different locations on the Au-NHA sample.

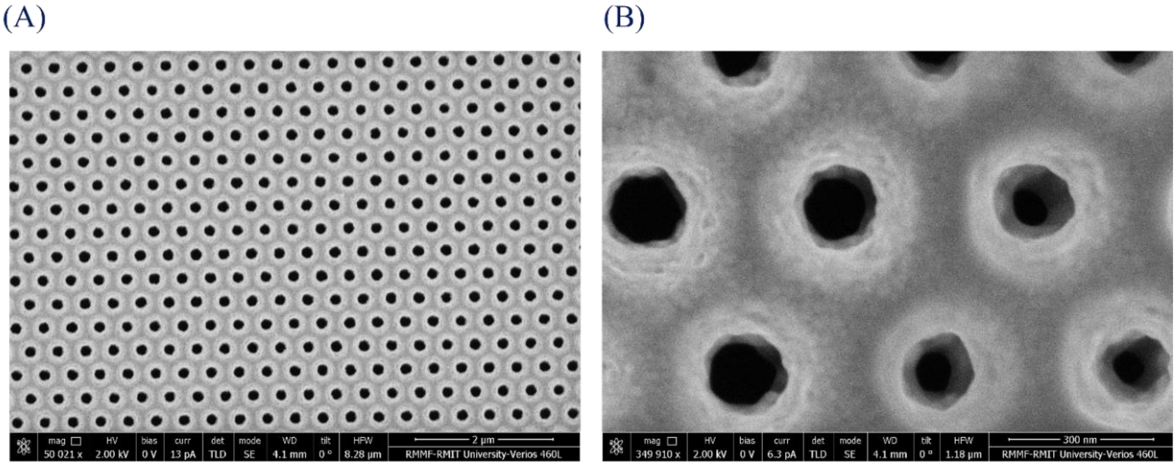

Figure 5.3.1.: SEM micro scans at different magnifications. **(A)** Micro scan of NHA at 50,000X magnification. **(B)** Micro scan of NHA at 350,000X magnification.

As highlighted in Fig. 5.3.1, the holes are arranged in a hexagonal grid array equidistant from each other based on the manufacturer's specifications. Measurements were performed after Au deposition to present a clear picture on the hole-array dimensions. The distance between the holes after deposition were around 405.2 ± 9.4 nm, in agreement with the TEM grid specifications as shown in Fig. 5.3.1. (A). However, hole diameter for deposited Au NHA measured from Fig 5.3.1. (B), to be around 110.02 ± 12.5 nm, which were significantly smaller than 200 nm TEM grid specification. This could be explained by the Cr and then subsequent Au layer covering the hole significantly after E-beam deposition.

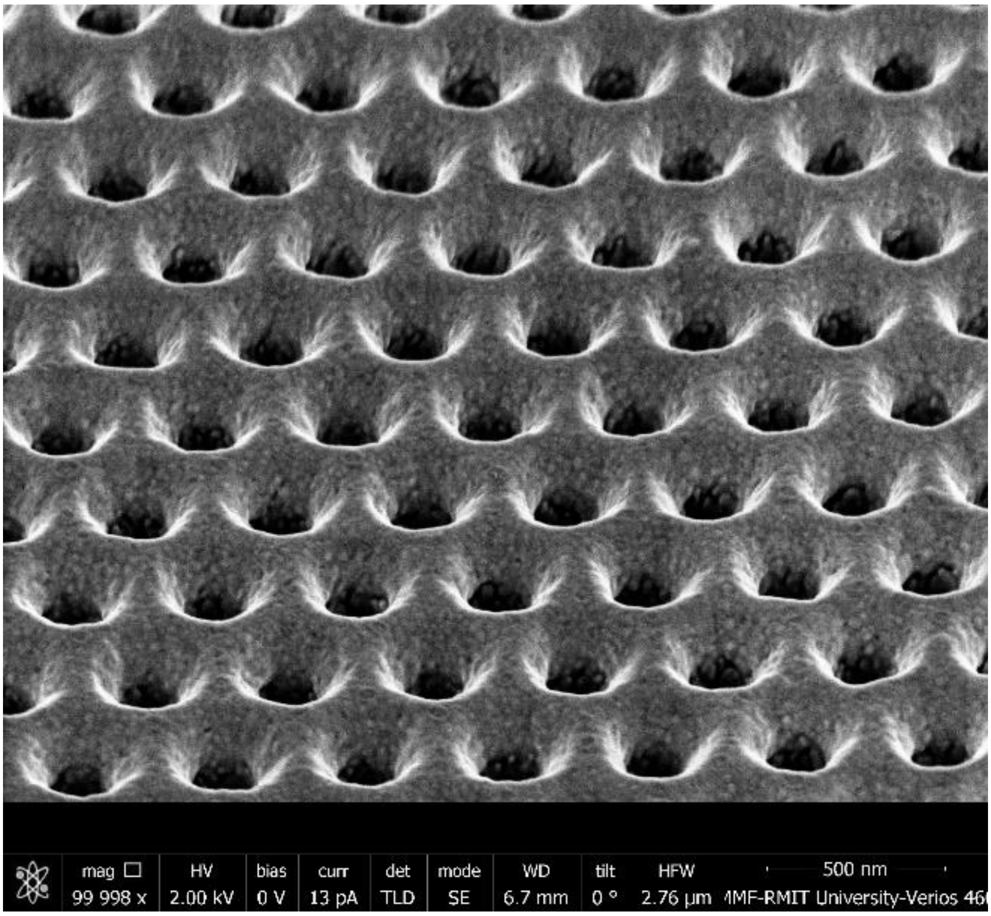

Figure 5.3.2.: Tilted SEM scan of NHA at 100,000X magnification, 40° where surface deposition on the NHA TEM grid can be observed in detail where gold can be seen further seeping within the holes and the surrounding area.

To further verify the quality of the holes after Au deposition, tilted SEM scan at 40° was carried out and presented a comprehensive picture of the agglomerated Au globules. These globules can be seen covering the nanoholes and seeping within the holes as shown in Fig. 5.3.2. Between holes, Au was expected to make sharper structures due to smoother deposition, however, blunt cones/pillars were observed. This could be due to how Au is deposited as thin film on the nanoholes and for further confirmation, FIB was performed.

NHA cross-section through FIB has been highlighted in Fig. 5.3.3. to characterize deposition depth and behaviour of Au over the nanohole surface. The deposition depths were measured to be 135.2 ± 13.9 (Fig. 5.3.3. (B)). which was significantly higher than the calculated depth (100 nm for Au and 5 nm for Cr). which could be due to E-beam deposition specifically on smooth deposition, targeted thickness, and protocol accuracy. It has been showcased that compared with different deposition techniques, E-beam deposition might not be smoothest [46].

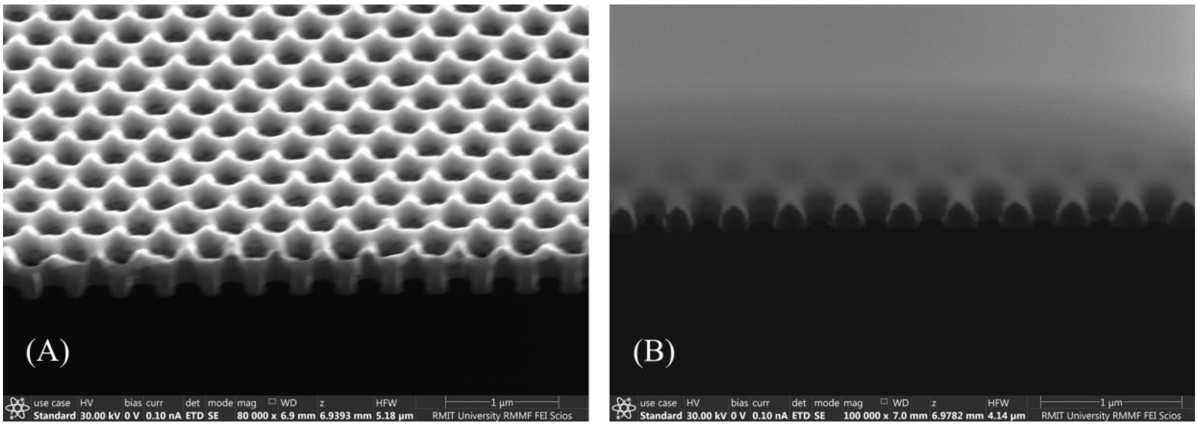

Figure 5.3.3.: FIB scans at different magnifications. **(A)** FIB scan of NHA at 80,000X magnification. **(B)** FIB scan of NHA at 100,000X magnification.

As can be seen on tilted FIB scans at 40° (Fig. 5.3.4), Au deposits form blunt cones around the TEM hole grids, which in addition, can further be observed to seep in the holes as expected. These cone shaped structures could be due to parameters of E-beam deposition for gold thin film deposition, where variations could arise between non-structured surfaces and nanohole arrays (resulting in comparatively rougher than expected surface). This could affect the overall biosensing performance of the NHA.

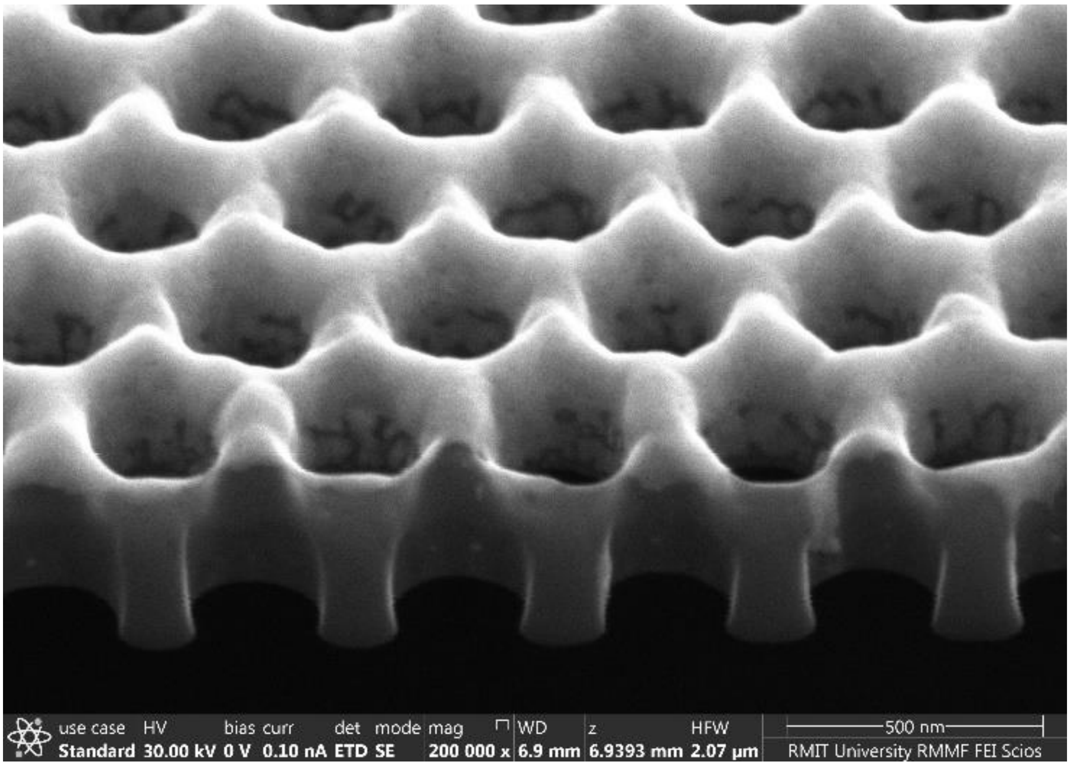

Figure 5.3.4.: Tilted 40° FIB scan of NHA at 200,000X magnification, where gold can be observed seeping within the holes for measuring optimal depth.

In conclusion, we performed characterization of these NHA after gold film deposition via FIB/SEM setup. However, compared with the literature review and nanohole arrays fabricated from other researchers, our fabrication protocol lacks the surface homogeneity. Specifically, we have observed irregular deposition depths as mentioned previously along with artefacts like cone-shaped structures which could affect their opto-sensing performance. The following sub-section focuses on such characterization, initially focusing on the optimal objective selection based on our biological applications.

5.4.2. Opto-fluidic characterization of the integrated Au-NHA microfluidic system:

5.4.2.1. Device setup:

Initial characterization of the optical-spectroscopic system focused on the selection of the objective parameters. i.e., magnification, numerical aperture and working distance suitable for our NHA sensing. The optical-spectroscopic system comprised of a XY- moveable stage as showcased in Fig. 5.3.5. where the Au-NHA is integrated within the microfluidic chip as exhibited in Fig. 5.3.6. (A). The collimated light is directed onto the Au-NHA from beneath and the transmitted light is aligned onto the objective with a selectable beam path, of which one path is for taking pictures while the other is for spectroscopic analysis.

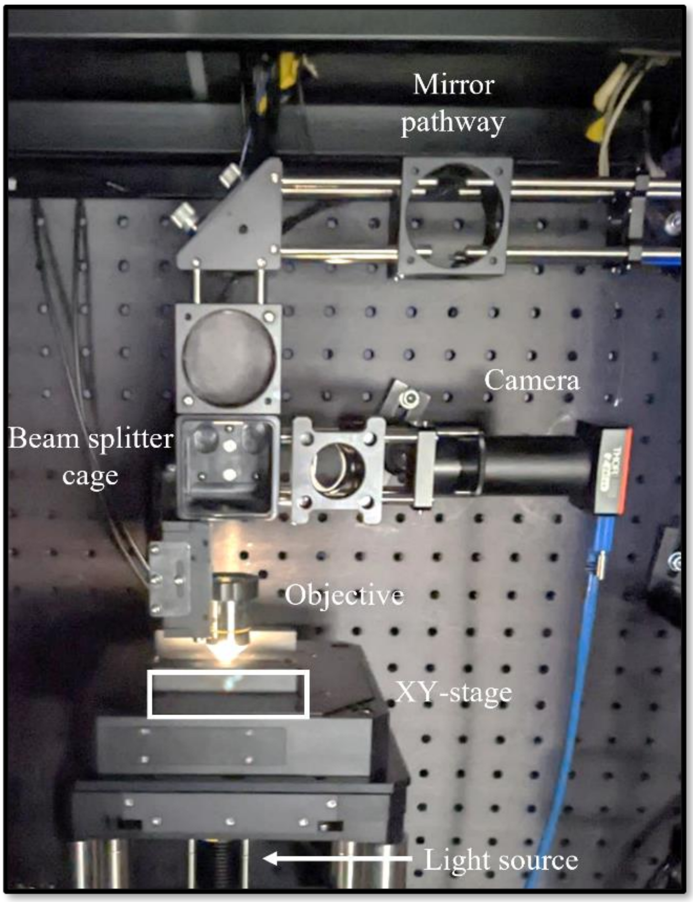

Figure 5.3.5.: Image of the opto-spectroscopic setup and integrated NHA microfluidic system showcasing light source, stage, objective, beam splitter, camera and mirror pathway highlighted.

The integrated Au-NHA microfluidic chip consists of an inlet and an outlet, a vacuum chuck for clamping the top layer and bottom layer with the Au-NHA in between to prevent leakages, and an eject inlet to release the top layer from the bottom layer for extraction of Au-NHA after signal interaction for regeneration. The microfluidic chip is connected to an external syringe pump via the inlet. The liquid in the syringe pump flows through a channel containing a bubble trap array for minimizing bubble formation as presented in Fig. 5.3.6. (B).

The system has both flow-over and flow-through configuration discussed above to limit bubble formations on the Au-NHA film. The liquid will pass over as well as going through Au-NHA by moving along the serpentine and directed towards the outlet. This serpentine act as the fluidic resistor to ensure good portion of the flow is encouraged to pass through the NHA. Without the serpentine, we can assume the fluidic resistance of the NHA to be high, which could result in bad sensing. We can observe this resistor is working as the trapped debris is trapped and then further removed from the NHA surface as flow is passing through and over it.

As showcased in Fig. 5.3.6. (B) to limit bubble formations on the Au-NHA film. The Au-NHA is aligned within the top and bottom layer and placed in the middle of the chip in contact with the microfluidic interfaces as exhibited in Fig 5.3.6. (C) top-side and (D) under-side. In addition, TEM grid film can be seen from the shadow patterned specifically in Fig. 5.3.6. (C).

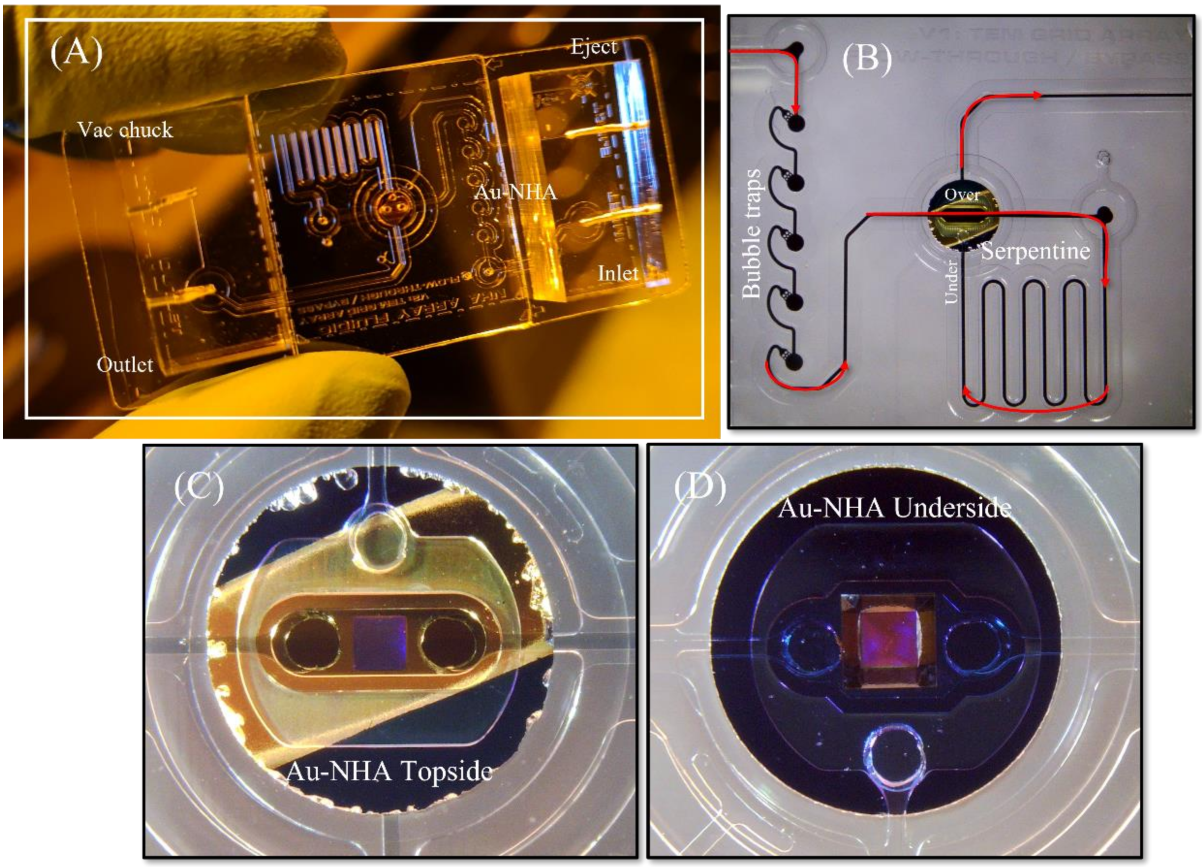

Figure 5.3.6.: **(A)** Integrated NHA microfluidic system with vac chuck, outlet, eject and inlet highlighted along with the Au-NHA integrated within the microfluidic chip. Magnified image of the Au-NHA microfluidic chip. **(B)** Flow pathway for the integrated microfluidic device. **(C)** Au-NHA topside integrated within the microfluidic chip. **(D)** Au-NHA underside integrated within the microfluidic chip.

5.4.2.2. Characterization of Optimal Objective:

Selection of optimal objective for the opto-spectroscopic system is imperative for setup functionality. Optical objectives ranging from 4X to 10X to 20X and 50X were characterized. For our specification, the light needs to be focused directly on the Au-NHA, resulting as a high intensity transmitted signal for post-processing. Images from different objectives have been showcased in Fig. 5.3.7. (A) 4X with numerical aperture (NA) of 0.13 and field of view (FOV) of 3100 µm, (B) 10X with NA of 0.25 and FOV of 1200 µm and (C) 20X, NA 0.4 and FOV 600 µm. For 4X and 10X objective, Au-NHA was observed under air displaying a yellow colour, whereas a red shift is observed on the Au-NHA after flow with 20X objective.

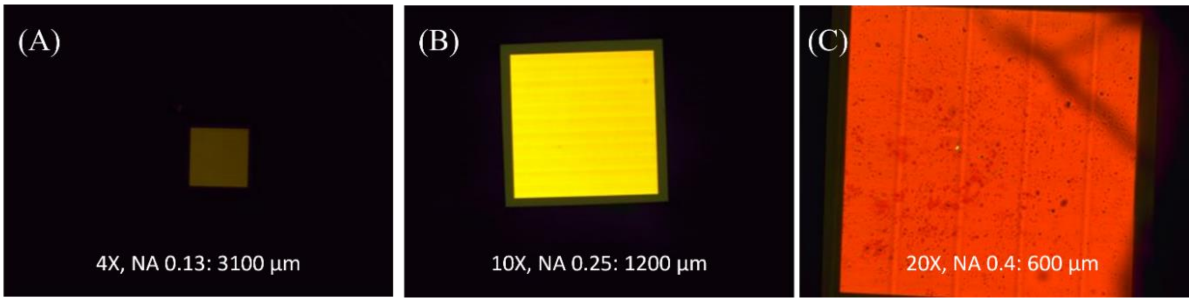

Figure 5.3.7.: Scans of Au-NHA with different objectives at various FOV. **(A)** Au-NHA at 4X NA 0.13 and 3100 µm FOV. **(B)** Au-NHA at 10X NA 0.25 and 1200 µm FOV. **(C)** Au-NHA at 20X NA 0.4 and 600 µm FOV.

Analysis of transmitted Au-NHA signals from different objectives was performed under flow using deionized water and reference lamp signal, presented in Fig. 5.3.8. for 4X, 10X, 20X and 50X at 500 µm grating slit size. Highest transmitted intensity was observed under 4X objective while lowest was observed for 50X as expected. In addition, transmitted signal from 10X and 20X was comparatively lowered than 4X due to the abhorrent light being collected with a larger FOV. Intensity difference of around 0.2 a.u. between 10X and 20X could be due to close working distance (WD) of 10X, where less abhorrent light would be captured. More so, additional matching oil requirements of 10X for optimal focusing could further explain this outlier.

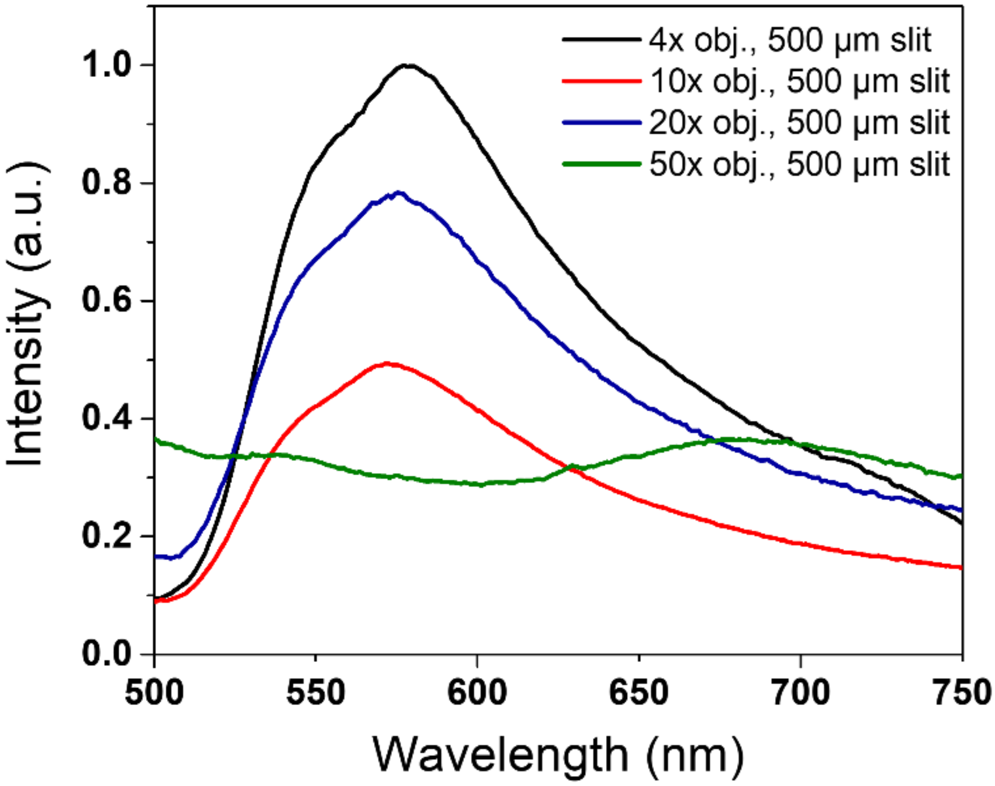

Figure 5.3.8.: Transmitted signals from Au-NHA at different objectives ranging from 4X to 10X to 20X and 50X at 500 μm slit opened.

Between the transmitted signal for 4X, 10X and 20X, a prominent Gaussian with a shoulder can be observed between 500-650 nm window. However, transmitted signal for 50X presented no such Gaussian peaks between this window. This is due to zoomed in FOV, which is within the dimension specifications of the NHA (hole diameter: 200 nm; periodicity: 400 nm), where plasmonic interaction on the top layer might be from individual hole rather than collective signal from the hole array. Based on our optical specifications, 20X objective was selected where transmitted signal predominantly focused on Au-NHA and collected at an optimal FOV (600-1000 μm).

5.4.2.3. Characterization of bulk sensitivities:

Bulk sensitivity measurements were performed for the integrated opto-fluidic setup with periodic injection of different glycerol dilutions as presented in Fig. 5.3.9. The sensogram was monitored over time between the optical window mentioned above.

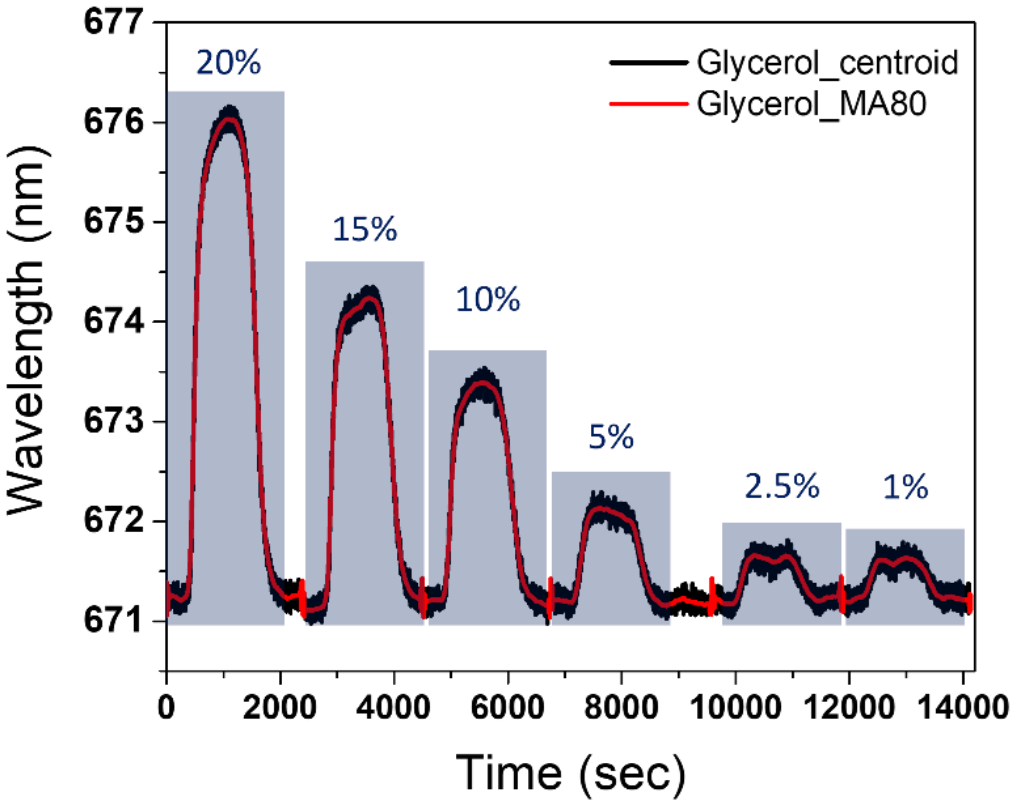

Figure 5.3.9.: Bulk sensitivity measurements through glycerol injections at various concentrations starting from 20% to 15% to 10% and 5% to 2.5% to 1%. Measurements are performed by tracking the centroid highlighted as glycerol_centroid and the moving average (MA) of 80 showcased as glycerol_MA80.

Wavelength shifts after each dilution injection has been compiled in Table 5.3.1., where differences in glycerol concentrations cause variations in bulk refractive index on the sensor surface.

Table 5.3.1.: Concentration of glycerol dilutions, refractive index units (RIUs) and subsequent wavelength shift observed from the bulk sensitivity measurements.

Glycerol dilution	RIUs	Wavelength shift
20%	1.3637	5 nm
15%	1.3533	3.5 nm
10%	1.3483	2.5 nm
5%	1.3403	1.5 nm
2.5%	1.3369	1 nm
1%	1.3366	< 1 nm

Based on these centroid method measurements, baseline (σ), S-bulk (slope), LOD and LOQ were calculated. For parity, this experiment was performed twice using two different Au-NHA. Results are presented in Table 5.3.2.

Table 5.3.2.: Parameters for measuring the setup sensitivity via bulk measurements through glycerol injections. LOD and LOQ highlighted for the integrated NHA microfluidic system. The measurements were performed twice using two different NHA via centroid tracking and the average sensitivities have been further highlighted.

Tracking method	LOD	LOQ
Centroid_06.09.2022	6.76×10^{-5}	2.25×10^{-4}
Centroid_09.09.2022	1.19×10^{-4}	3.97×10^{-4}
Centroid avg.	9.33×10^{-5}	3.11×10^{-4}

Calculated LOD is in the average range of 1.2×10^{-4} to 6.8×10^{-5} and LOQ in the range of 2.2×10^{-4} to 4×10^{-4} which is similar to published data for integrated plasmonic-NHA setups for biomolecule detection, [28,47–52]. However, some studies presented much better LOD and LOQ (between 10^{-5} to 10^{-7}) [28,47–52], which could be attributed to the fabrication protocol of Au-NHA. Indeed, in these studies, ion etching is employed to obtain homogenous and ordered arrays, whereas in our work, E-beam was used leading to lower resolution of NHA elaboration as presented in Section 5.3.2.

5.4.3. Biosensing efficiency of NHA-Optical setup:

Interleukin-6 (IL-6, MW: 21 kDa) was selected for characterization of biosensing efficiency of our integrated Au-NHA microfluidic system. Au-NHA were cleaned and functionalized *ex situ* with DBCO/OH PEGs 2k in 1/4 spacing ratio and then integrated within the microfluidic device. The experiments were performed in PBS 1X buffer and for initial characterization of the opto-spectroscopic system and optimal flow/fluidic manipulation, PBS 5X was injected as showcased in Fig. 5.3.10 (A).

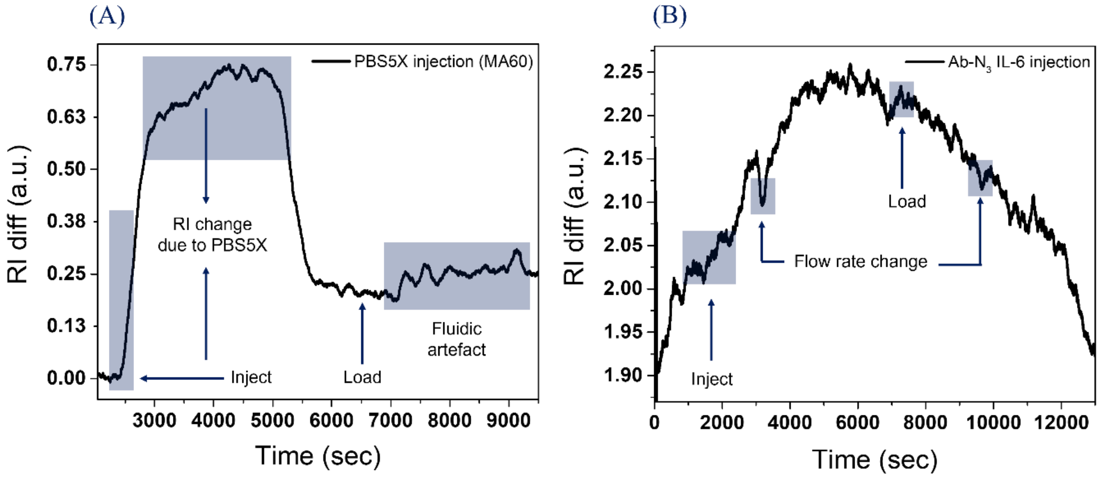

Figure 5.3.10.: Signal shift for PBS 5X and Ab immobilization. **(A)** Initial signal of PBS 5X with DBCO/OH PEGs 2k functionalized on gold nanohole arrays (Au-NHA) with refractive index (RI) shift highlighted along with the fluidic artefact observed from our setup. **(B)** Ab-N_3 Anti-IL-6 immobilization on DBCO/OH PEGs functionalized Au-NHA highlighted with showcasing changes in flow rate from 10 µL/min to 2 µL/min.

Following injection, refractive index (RI) shifts of around 7.2x10^{-3} a.u., but the signal did not return to the baseline (Δ RI of around 1.9x10^{-1} between inject and load) as for the conventional SPR setup. This phenomenon could be due to deposition of PBS salts on the nano-structuration in small amount. Then at 7000-9000 sec, the slight Δ RI increase of 5.8x10^{-2} could also be attributed to PBS salt depositions. To recover the initial baseline, the system was kept running but due to bubble formation, the baseline was set to 1.9 a.u. as presented in Fig. 5.3.10. (B), before azide activated Anti-IL-6 injection.

As highlighted in Fig. 5.3.10., initial flow rate was set at 10 µL/min, then decreased to 2 µL/min so that maximum number of antibodies have sufficient time to immobilize on the top NHA layer as highlighted in Fig. 5.3.10. (B). The efficient immobilization process of Ab-N3 could be confirmed by the presence of an association phase (RI increase) followed by a steady state (constant RI) then by a dissociation phase (RI decrease to a higher baseline than the initial one). However, on Fig. 5.3.10. (B) we can observe a slight increase of ~0.20 a.u. Δ RI in signal shift after Ab-N3 injection, immediately followed by the decrease of the signal.

This result indicate that azide activated anti-IL-6 immobilization on the functionalized NHA surface under flow was not as efficient as expected in the experimental condition tested. For optimal coupling, the surface needs to be saturated with the antibodies for sufficient time. However, the minimal signal shift indicated between injection and load, might suggest that low level of antibodies are immobilized on the surface. Hence, the experiment was further carried out by injecting human IL-6 at initial concentration of 1 µg/mL.

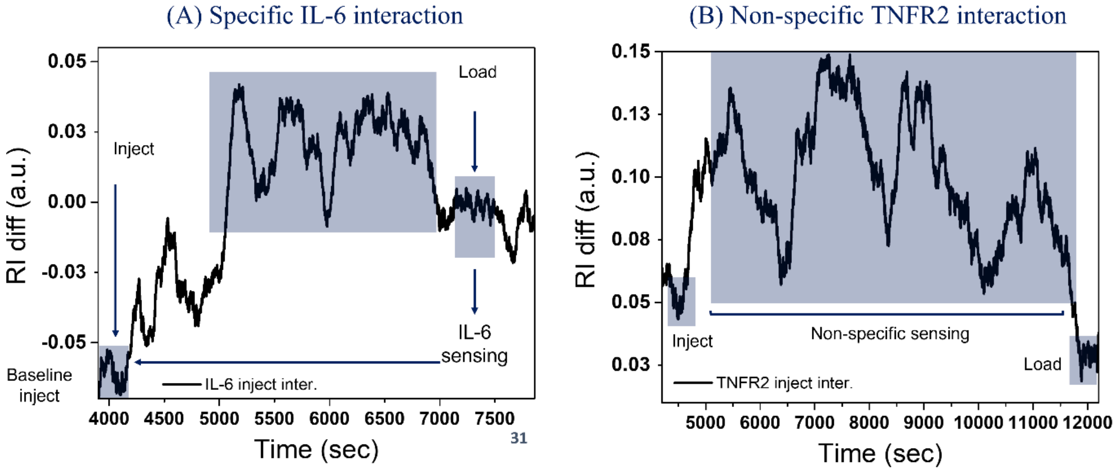

Figure 5.3.11.: Analysis of signal interactions through integrated Au-NHA microfluidic system. **(A)** Specific signal interaction of human IL-6 at 1 µg/mL concentration. **(B)** Non-specific signal interaction of human TNFR2 at 1 µg/mL concentration.

The specific signal interaction for IL-6 with immobilized Anti-IL-6 has been presented in Fig. 5.3.11. (A). For this signal interaction, the spectroscopic system was rebooted, with the initial baseline at ~0 a.u. being re-achieved. After injection of Human IL-6, a specific signal interaction corresponding to the association phase was observed until the dissociation phase (load phase at 7500 sec.). The ΔRI obtained is about $5x10^{-2}$ which is lower than expected considering the IL-6 concentration tested (1 µg/mL). However, this signal interaction was confirmed to be specific, as injection of tumour necrosis factor (TNF) receptor type II (TNFR2; MW: ~25 kDa), led to non-specific signal (Fig. 5.3.11. (B)).

TNFR2 is another cancer associated biomarker with no reported interaction with anti-IL-6 antibody. Indeed, the signal obtained following TNFR2 injection is characteristic from non-specific interaction.

While distinct difference between IL-6 and TNFR2 signals was established, due to time and system constraints, further characterization could not have been performed. Comparative ΔRI analysis between IL-6 and TNFR2 provide a promising picture for the approach but further modifications are needed to make this setup sensitive for real-time analysis. The hypothetical range of 5 to 35 pg/mL for IL-6 has been highlighted in Chapter 4 for detection of biomarker secretions in real-time from cancer cells. This is an order of E-06 compared to what was achieved using this integrated system. We have showcased ΔRI of 5×10^{-2} for 1 µg/mL IL-6 concentration and further calculated ΔRI shift of 2.5×10^{-7} to 1.7×10^{-6} could be required to optimally detect IL-6 in the pg/mL range. Based on our bulk sensitivity measurements and biosensing characterization, the LOD and LOQ analysed above i.e., 10^{-4} to 10^{-5} is only sensitive for detection of µg/mL range, however, minimum order of 10^{-7} and 10^{-8} for LOD/LOQ is needed for optimal analysis.

5.5. Conclusions and Perspectives:

This chapter focused on the integration of a plasmonic nanohole array (NHA) sensor with a complex microfluidic device for the detection of ultra-low biomolecules associated with cancer and metastasis. Fabrication of these NHA and further deposition with Cr and Au was presented to elucidate their potential for plasmonic sensing. Surface characterization of these Au-NHAs was performed via SEM and FIB dual analysis, to analyse the performance of gold deposition on surface topology. Biomedical application of these Au-NHA is intertwined with their optimal integration with a microfluidic system. As discussed in Chapter 4, for our microfluidic devices, moulding protocol has been utilized to fabricate complex devices with multi-layers to couple the Au-NHA within the device for characterization and analysis. To establish this integrated Au-NHA microfluidic system to support spectral and sharp optical responses with regards to variations in surface conditions, a modular opto-spectroscopic system was fabricated.

After comprehensive characterization of the topography of Au-NHA and spectral ranges for opto-spectroscopic system, bulk sensitivity for the integrated setup was measured by glycerol injections at different concentrations. The optical response for the Au-NHA was easy to track for reliable monitoring of spectral variations due to concentration interactions. The detection and quantification limit for our biosensing platform demonstrated within the range of 10^{-4} to 10^{-5}. Specific signal interaction and binding kinetics was presented for IL-6 at µg/mL concentrations albeit with certain systemic drawbacks from the optical system and the subsequent signal processing for low signal-to-noise ratio, where further improvements need to be focused on. Similarly, to signal interaction of IL-6, non-specific signal interaction for TNFR2 was demonstrated with similar signal processing issue, where overtime the signal increased gradually which needs to be further assessed.

In conclusion, this integrated Au-NHA microfluidic system was presented for analysis of cancer associated biomarkers i.e., IL-6 and TNFR2 at initial 1 µg/mL concentration. In my opinion objectively, this setup was mired with operational constraints. Initial characterization of Au-NHA through FIB/SEM could paint a more comprehensive picture where different approaches like ion-deposition could be focused for efficient and smooth Au-deposition on the hole arrays. Because of this inefficient deposition, surface regeneration was compromised due to the chromium layer being etched off after HCl injection. More so, the innate nature of the NHA film before deposition made it prone for bubble formation which was addressed by the complex microfluidic design. This complicated circuit alleviated initial issues but for long term experiment such a system might not be suitable. In addition, for signal processing, as can be seen from specific and non-specific interactions, the noise is significantly higher under flow compared to the conventional SPR setup which could be due to the signal processing being employed which for such a system is in its infancy. Further research on optimal NHA deposition and signal processing for further minimizing the noise is required to make such an integrated system capable of performing real-time analysis at smaller concentrations.

However, based on our interpolated measurements for IL-6 concentration analysis for single and multi-cell secretions, this integrated setup might not be able to detect such ultra-low analyte ranges. We calculated around 41.5 pg/nL IL-6 concentration for a single cell, which further decreased to around 8 pg/nL for 10 cells in a 50 nL trap chamber volume presented in detail in Chapter 4. For further improving the biosensing capability of such an integrated system, focus needs to be shifted towards optimal deposition of Au on nanohole arrays. As highlighted above, different research groups have showed analytes being detected at ultra-low concentrations, the common thread among them all was optimal fabrication and characterization of NHA. After Au deposition, precise and regular nanoholes are to be achieved, biomarker concentrations ranging for sub pg/mL to ng/mL can be detected in biological samples [28,47–52]. In conclusion, we have however, showed the promise of an integrated opto-fluidic NHA system that could be utilised not only for biomarker detection but be incorporated with additional microfluidic trapping function to detection of direct secretions for not only single cancer cell i.e., CTCs but to analyse multiple cancer cells i.e., CTC-Clusters.

Recent advances in cancer research, is increasingly focusing on single and multi-cell analyses to decode not only tumour heterogeneity but to further understand what parameters are regulated for cancer spread. Extraordinary optical transmission (EOT) / plasmonic based technologies have come to the forefront that can be applied in depth for this bio-application focusing on discriminating normal and cancer cells specifically focusing on their biomarker secretions at the single cell and multi-cell level with rapid, label-free, and overall simple modality. These integrated approaches can be used further down the line for cancer patients to analyse their secretions directly at the cell-level to further promote personalized diagnostics and medicine. The biomedical application of such plasmonic systems can be improved by performing further studies with multiple samples of different cancer origin at different stages.

References:

1. Soler, M., Huertas, C. S. & Lechuga, L. M. Label-free plasmonic biosensors for point-of-care diagnostics: a review. *Expert Rev. Mol. Diagn.* **19**, 71–81 (2019).
2. Soler, Maria and Huertas, C. S. Label-Free Plasmonic Biosensors in Clinical Diagnostics. **4**, 383–401 (2023).
3. Homola, J. & Piliarik, M. *Surface Plasmon Resonance (SPR) Sensors*. (2006). doi:10.1007/5346_014.
4. Soler, M., Huertas, C. S. & Lechuga, L. M. Label-free plasmonic biosensors for point-of-care diagnostics: a review. *Expert Rev. Mol. Diagn.* **19**, 71–81 (2019).
5. Stefan A. Maier. *Plasmonics: Fundamentals and Applications*. *วารสารวิชาการมหาวิทยาลัยอีสเทิร์นเอเซีย* vol. 4 (Springer International Publishing, 2007).
6. Uwe Kreibig Michael Vollmer. *Optical Properties of Metal Clusters*. *Springer Series in Materials Science* vol. 5 (Springer International Publishing, 1995).
7. Arora, P., Talker, E., Mazurski, N. & Levy, U. Dispersion engineering with plasmonic nano structures for enhanced surface plasmon resonance sensing. *Sci. Rep.* **8**, 1–9 (2018).
8. Barik, A. *et al.* Dielectrophoresis-enhanced plasmonic sensing with gold nanohole arrays. *Nano Lett.* **14**, 2006–2012 (2014).
9. Su, K. H. *et al.* Local refractive index dependence of plasmon resonance spectra from individual nanoparticles. *Nano Lett.* **3**, 485–491 (2003).
10. Hutter, E. & Fendler, J. H. Exploitation of localized surface plasmon resonance. *Adv. Mater.* **16**, 1685–1706 (2004).
11. Willets, K. A. & Van Duyne, R. P. Localized surface plasmon resonance spectroscopy and sensing. *Annu. Rev. Phys. Chem.* **58**, 267–297 (2007).
12. Homola, J., Yee, S. S. & Gauglitz, G. Surface plasmon resonance sensors: review. *Sensors*

Actuators, B Chem. **54**, 3–15 (1999).

13. Pitarke, J. M., Silkin, V. M., Chulkov, E. V. & Echenique, P. M. Theory of surface plasmons and surface-plasmon polaritons. *Reports Prog. Phys.* **70**, 1–87 (2007).
14. Schröter, U. & Heitmann, D. Grating couplers for surface plasmons excited on thin metal films in the kretschmann-raether configuration. *Phys. Rev. B - Condens. Matter Mater. Phys.* **60**, 4992–4999 (1999).
15. Schasfoort, R. B. M. Chapter 1. Introduction to Surface Plasmon Resonance. *Handb. Surf. Plasmon Reson.* 1–26 (2017) doi:10.1039/9781788010283-00001.
16. Zuloaga, J. & Nordlander, P. On the energy shift between near-field and far-field peak intensities in localized plasmon systems. *Nano Lett.* **11**, 1280–1283 (2011).
17. Celebrano, M. *et al.* Mode matching in multiresonant plasmonic nanoantennas for enhanced second harmonic generation. *Nat. Nanotechnol.* **10**, 412–417 (2015).
18. Amendola, V., Pilot, R., Frasconi, M., Maragò, O. M. & Iatì, M. A. Surface plasmon resonance in gold nanoparticles: A review. *J. Phys. Condens. Matter* **29**, (2017).
19. Stuart, D. A., Haes, A. J., McFarland, A. D., Nie, S. & Van Duyne, R. P. Refractive-index-sensitive, plasmon-resonant-scattering, and surface-enhanced Raman-scattering nanoparticles and arrays as biological sensing platforms. *Plasmon. Biol. Med.* **5327**, 60 (2004).
20. Mayer, K. M. & Hafner, J. H. Localized surface plasmon resonance sensors. *Chem. Rev.* **111**, 3828–3857 (2011).
21. Ebbesen, T. W., Lezec, H. J., Ghaemi, H. F., Thio, T. & Wolff, P. A. Extraordinary opticale desire to use and control photons in a manner analogous to the control of electrons in solids has inspired great interest in such topics as the localization of light, microcavity quantum electrodynamics and nest- field optics. A fun. *Nature* **391**, 667–669 (1998).
22. Liu, Y. & Zhang, X. Microfluidics-Based Plasmonic Biosensing System Based on Patterned Plasmonic Nanostructure Arrays. (2021).
23. Cho, N., Jackman, J. A., Ferhan, R. & Cho, N. Nanoplasmonic sensors for biointerfacial science. **46**, (2017).
24. Masson, J. F., Murray-Méthot, M. P. & Live, L. S. Nanohole arrays in chemical analysis: Manufacturing methods and applications. *Analyst* **135**, 1483–1489 (2010).
25. Masuda, H. & Fukuda, K. Ordered metal nanohole arrays made by a two-step replication of honeycomb structures of anodic alumina. *Science (80-.).* **268**, 1466–1468 (1995).
26. Sinton, D., Gordon, R. & Brolo, A. G. Nanohole arrays in metal films as optofluidic elements: Progress and potential. *Microfluid. Nanofluidics* **4**, 107–116 (2008).
27. Yang, T. & Ho, H. P. A phase-sensitive surface plasmon resonance sensor based on the enhanced light transmission through arrays of nanoholes in gold films. *2008 IEEE Int. Conf. Electron Devices Solid-State Circuits, EDSSC* 4813–4815 (2008) doi:10.1109/EDSSC.2008.4760727.
28. Lesuffleur, A., Im, H., Lindquist, N. C. & Oh, S. H. Periodic nanohole arrays with shape-enhanced plasmon resonance as real-time biosensors. *Appl. Phys. Lett.* **90**, (2007).
29. Sharpe, J. C., Mitchell, J. S., Lin, L., Sedoglavich, N. & Blaikie, R. J. Gold nanohole array

substrates as immunobiosensors. *Anal. Chem.* **80**, 2244–2249 (2008).

30. Ji, J., O'Connell, J. G., Carter, D. J. D. & Larson, D. N. High-throughput nanohole array based system to monitor multiple binding events in real time. *Anal. Chem.* **80**, 2491–2498 (2008).
31. Henzie, J., Lee, J., Lee, M. H., Hasan, W. & Odom, T. W. Nanofabrication of plasmonic structures. *Annu. Rev. Phys. Chem.* **60**, 147–165 (2009).
32. Canpean, V. & Astilean, S. Multifunctional plasmonic sensors on low-cost subwavelength metallic nanoholes arrays. *Lab Chip* **9**, 3574–3579 (2009).
33. Murray-Methot, M. P., Menegazzo, N. & Masson, J. F. Analytical and physical optimization of nanohole-array sensors prepared by modified nanosphere lithography. *Analyst* **133**, 1714–1721 (2008).
34. Lee, S. H., Bantz, K. C., Lindquist, N. C., Oh, S. H. & Haynes, C. L. Self-assembled plasmonic nanohole arrays. *Langmuir* **25**, 13685–13693 (2009).
35. Lee, H. J., Nedelkov, D. & Corn, R. M. Surface plasmon resonance imaging measurements of antibody arrays for the multiplexed detection of low molecular weight protein biomarkers. *Anal. Chem.* **78**, 6504–6510 (2006).
36. Dahlin, A. B., Tegenfeldt, J. O. & Höök, F. Improving the Instrumental Resolution of Sensors Based on Localized Surface Plasmon Resonance interfacial refractive index of nanoscale noble metal generic data analysis algorithms and a simple experimen- comparable to that of state-of-the art SPR systems. *Anal. Chem.* **78**, 4416–4423 (2006).
37. Escobedo, C., Brolo, A. G., Gordon, R. & Sinton, D. Flow-through vs flow-over: Analysis of transport and binding in nanohole array plasmonic biosensors. *Anal. Chem.* **82**, 10015–10020 (2010).
38. Jonsson, M. P., Dahlin, A. B., Feuz, L., Petronis, S. & Höök, F. Locally functionalized short-range ordered nanoplasmonic pores for bioanalytical sensing. *Anal. Chem.* **82**, 2087–2094 (2010).
39. Yanik, A. A., Huang, M., Artar, A., Chang, T. Y. & Altug, H. Integrated nanoplasmonic-nanofluidic biosensors with targeted delivery of analytes. *Appl. Phys. Lett.* **96**, 2008–2011 (2010).
40. Wong, T. I. *et al.* Lab on a Chip High throughput and high yield nanofabrication of precisely designed gold nanohole arrays for fluorescence enhanced detection of biomarkers. 2405–2413 (2013) doi:10.1039/c3lc41396a.
41. Escobedo, C. *et al.* Quantification of ovarian cancer markers with integrated microfluidic concentration gradient and imaging nanohole surface plasmon resonance. 1450–1458 (2013) doi:10.1039/c3an36616b.
42. Sun, L. L. *et al.* Localized surface plasmon resonance based point-of-care system for sepsis diagnosis. *Mater. Sci. Energy Technol.* **3**, 274–281 (2020).
43. Cetin, A. E., Kocer, Z. A., Topkaya, S. N. & Yazici, Z. A. Handheld plasmonic biosensor for virus detection in field-settings. *Sensors Actuators, B Chem.* **344**, 130301 (2021).
44. Chen, Z. *et al.* Enhanced extraordinary optical transmission and refractive-index sensing sensitivity in tapered plasmonic nanohole arrays. *Nanotechnology* **30**, (2019).
45. Masson, J. F., Murray-Methot, M. P. & Live, L. S. Nanohole arrays in chemical analysis :

manufacturing methods and applications. 1483–1489 (2010) doi:10.1039/c0an00053a.

46. Anders, A. A structure zone diagram including plasma-based deposition and ion etching. *Thin Solid Films* **518**, 4087–4090 (2010).

47. Zheng, P. *et al.* A gold nanohole array based surface-enhanced Raman scattering biosensor for detection of silver(i) and mercury(ii) in human saliva. *Nanoscale* **7**, 11005–11012 (2015).

48. Cetin, A. E. *et al.* Plasmonic Nanohole Arrays on a Robust Hybrid Substrate for Highly Sensitive Label-Free Biosensing. *ACS Photonics* **2**, 1167–1174 (2015).

49. Li, X. *et al.* Label-Free Optofluidic Nanobiosensor Enables Real-Time Analysis of Single-Cell Cytokine Secretion. *Small* **14**, (2018).

50. Li, X. *et al.* Plasmonic nanohole array biosensor for label-free and real-time analysis of live cell secretion. *Lab Chip* **17**, 2208–2217 (2017).

51. Monteiro, J. P., de Oliveira, J. H., Radovanovic, E., Brolo, A. G. & Girotto, E. M. Microfluidic Plasmonic Biosensor for Breast Cancer Antigen Detection. *Plasmonics* **11**, 45–51 (2016).

52. Franco, A. *et al.* A label-free optical system with a nanohole array biosensor for discriminating live single cancer cells from normal cells. *Nanophotonics* **11**, 315–328 (2022).

Chapter 6

Conclusions and future perspectives

My PhD project focused on analysing secreted cancer-associated biomarkers in a real-time and multiplexed fashion. Based on the literature review, it has been presented that different cancer biomarkers like certain cytokines, secreted proteins involved in cell signalling are significantly upregulated in various tumours playing a vital role in evading the immune response. Interleukins, a specific class of cytokines, are secreted when the tumour growth is either in epithelial or mesenchymal state. Among theminterleukin-6 (IL-6) and interleukin-8 (IL-8) have been shown to play a vital role in cancer cell progression [1,2]. In addition, such interleukin classes have been identified to upregulate metastasis via CTCs propagation [3,4] specifically for both lung and prostate cancer along with breast and ovarian tumours. Along with IL-6 and IL-8, TGF-β and fibronectin have been highlighted as common CTC secreted biomarkers playing vital roles in epithelial to mesenchymal (EMT) and mesenchymal to epithelial (MET) transitions.

Thus, in this work, I had to focus on fabricating an integrated opto-fluidic Lab-on-a-Chip (LOC) setup capable of performing CTC trapping and direct analysis of biomarker secretions from the captured CTCs and cluster-CTCs. This LOC was comprised of two components: (i) microfluidic compartment for efficient cell trapping and (ii) biosensing part for cell secretions analysis. In addition, for fabrication of an optimal biosensing setup, surface modification is of paramount importance, so during my project I also worked on (iii) fabricating a surface immobilization approach capable of directed, site-specific and oriented conjugation of antibodies on sensor surface for target recognition.

For developing such a surface modification approach, click chemistry was exploited, where dibenzocyclooctyne (DBCO) group was selected as an active group, which is stable and reproducible, and is a suitable option for oriented coupling through either strain promoted azide-alkyne cycloaddition (SPAAC) or thiol-yne reaction.

Initial characterization performed between DBCO surfaces with either alkylayted (DBCO/OH Alkyls) and PEGylated chain (DBCO PEGs/OH Alkyls) showcased complementarity and optimal functionalization for DBCO PEGs/OH Alkyls over DBCO/OH Alkyls. In addition, two copper free click chemistries i.e., thiol-yne chemistry (Ab-SH) and SPAAC (Ab-N_3) was analysed for antibody immobilization where Ab-N3 showcased optimal coupling on DBCO PEGs/OH Alkyls functional monolayers. More specifically, SPRi signal for Ab-N3 for 2.3 times higher for DBCO PEGs/OH Alkyl over DBCO/OH Alkyls. More so, for these immobilizations, reaction kinetics for DBCO PEGs/OH Alkyls was 4.5 times faster than DBCO/OH Alkyls.

Then, comparative analysis of biosensing characterization was performed between SPAAC approach for DBCO PEGs/OH Alkyls and conventional C/NHS chemistry for NHS/OH Alkyls for the selection of immobilization approach which would be employed for biosensor fabrication. Based on our results, –azide-activated antibody immobilized onto DBCO PEGs/OH Alkyls presented favourable signal responses around 2.3 times higher than NHS/OH Alkyls, highlighting site-specific, oriented, and directed nature of conjugation.

More so, monolayer stability was exhibited through multiple target injections at varying concentrations where surface saturation was exhibited at 0.44 – 0.49 mm^2/a.u. after 4 μg/mL target injection onwards. Furthermore, optimal monolayer coverage highlighted around 1.6×10^9 antibodies to be captured by Ab-N_3 on DBCO PEGs/OH Alkyls. Such results indicated DBCO

PEGs/OH Alkyls monolayer to be stable, capable of regeneration and concentration dependent target recognition. However, using conventional SPRi setup we were not able to detect interleukin-6 (IL-6), interleukin-8 (IL-8) and tumour growth factor – beta (TGF-β) interactions with their specific azide-activated antibodies immobilized onto DBCO PEGs/OH Alkyls monolayer.

Thus DBCO/OH PEGs 2k surfaces were functionalized at various ratio to improve surface modification. In addition, surface characterization of these monolayers at RMIT, highlighted 1/4 DBCO/OH PEGs 2k presented the optimal monolayer orientation unlike 1/1 DBCO/OH PEGs 2k that was used for characterization of biomarker sensing through SPRi setup.

Then, I focused on trapping CTCs through a complex microfluidic system. To achieve our goal, we employed valve-based systems that provide wider applications in single and multi-cell trapping along with downstream analysis through a biosensing modality. More so, for cell micro-culturing, such microfluidic systems provide greater level of automation.

I fabricated an integrated microfluidic system actuated through a PDMS moulding protocol specifically focusing on monolithic features like 3D pneumatic valves with actuation circuits and trap units with sieve valves for cell trapping. Such features reduced fabrication error and achieve device functionality for rapid prototyping, where moulds prepared for fabrication were reusable and further incorporated valve membranes and hybrid integrated systems like NHA. The device titled CTC Cluster V3 was characterized initially for flow manipulation. Afterwards, polystyrene beads and then subsequently, metastatic breast MCF7 cancer cells were trapped within the device in real-time. Despite continuous medium perfusion, the cells died within the device probably due to lack of gas exchange (O_2/CO_2 exchange) to keep them functional.

In addition, ELISA was performed for different cancer biomarkers like fibronectin and IL-6 for metastatic ovarian SK-OV-3 cells. These calculations were extrapolated for the trap unit volume i.e., ~50 nL, where range of 650 to 800 pg/nL/cell was observed for fibronectin and while for IL-6, around 6 – 40 pg/nL/cell was exhibited. These calculations the concentrations which can be detected secreted directly from the trapped cells.

I showcased such devices were capable of passive release of stored mediums and drugs for optimal cell trapping and culturing for keeping the cells alive for longer experiments. The intricate device design provided single as well as multiple trapping capabilities with multiple trap units and such valves were able to manipulate the flow through the microfluidic circuit. The trapping system presented in my project showcased a lot of promise for real-time trapping, however in my opinion, further improvements are needed, specifically controllable flow rates where cells can be trapped in a gentler fashion limiting cell shearing through the sieve traps. In addition, for my system, I used manual actuation to control valve functionality and manual syringe pumps were used for flow manipulation, thus, more automation is urgently required to decrease manual handling. More so, certain modifications are required focusing on (i) active gas/medium perfusion system is required for long-term overnight experiments for biological viability of trapped cells and (ii) integration of NHA for analysis of secreted biomarkers.

Before integrating a NHA onto the CTC Cluster V3, NHA must be initially characterized. These NHA were acquired from a company and deposited with thin chromium (Cr) and gold (Au) films at RMIT to elucidate their potential for plasmonic sensing. Dual SEM/FIB system was utilized to characterize these deposited NHA. After Au deposition on NHA, dimensions for hole distances agreed with the acquired TEM grid (~400 nm), however the hole size significantly decreased from 200 nm to around 110 nm.

In addition, deposition depths were measured to be approx. 135 nm significantly higher than calculated depth (100 nm for Au and 5 nm for Cr), which could be due to E-beam deposition employed. These discrepancies because of irregular deposition might affect their opto-sensing performance. In my opinion, different approaches like ion-deposition might be employed for more efficient and smooth Au film deposition on such nano-structuration.

Afterwards, these NHA were integrated within a microfluidic system actuated through moulding protocol like CTC Cluster V3 mentioned above. This system had multiple top and bottom layer with the NHA perched in between and this integrated device was then characterized through a modular opto-spectroscopic system. Initial bulk sensitivities for this setup were measured by glycerol injections at different concentrations. The optical response for these Au-NHA was easily tracked for reliable monitoring of spectral variations due to concentration interactions. The detection and quantification limit for our biosensing platform demonstrated range between 10^{-4} to 10^{-5}.

Au-NHA functionalized with 1/4 DBCO/OH PEGs 2k and then with azide activated Anti-IL-6 antibodies were evaluated for real-time, label-free detection of biomolecular binding kinetics for IL-6 at µg/mL concentrations. More so, non-specificity of the signal interaction was demonstrated through TNFR2 injection at similar concentrations.

The device design was quite intricate as the flow had to be manipulated over as well as through the NHA to limit bubble formation, which further complicated the analysis specifically for long term experimentation. The signal interactions are significantly noisier under flow compared to the conventional SPRi setup. This could also be due to the signal processing being employed is still in its infancy and more research needs to be directed on this avenue as well.

As mentioned above, ELISA calculations for IL-6 specifically showed maximum concentrations to be around 40 pg/nL per cell which decreased further to 8 pg/nL per 10 cells which might be secreted directly in the trap chamber of the microfluidic device. However, based on the sensitivity measurements we acquired from our integrated optical-NHA sensing system, such a platform might not be able to detect such ultra-low analyte ranges (between sub ng/mL to pg/mL).

For further improving biosensing capability of such an integrated system, focus needs to be shifted towards optimal deposition and further signal processing. Different research groups have showcased ultra-low concentrations of analytes being detected where the common thread among them all was optimal fabrication and characterization of NHA. After Au deposition, if precise and regular nanoholes are to be actuated, biomarker concentrations ranging between sub ng/mL to pg/mL can be detected in biological samples [5–11].

In conclusion, however, I have showcased the promise of an integrated opto-fluidic NHA system that could be utilised not only for biomarker detection but be incorporated with additional microfluidic trapping function to detection of direct secretions for not only single cancer cell i.e., CTCs but to analyse multiple cancer cells i.e., CTC-Clusters. I can envisage a future where once such systems are optimized can be used for cancer patient samples. In addition, such CTCs can be exploited through a single micro-system for specific isolation and separation with subsequent analysis of biomarkers directly secreted by the trapped cells to provide a picture of the metastatic stage. Thus, such personalized healthcare systems based on integrated biosensors and different technologies seem to be an achievable possibility. For cancer diagnostics, lab-on-a-chip (LOC) systems offer an avenue steadily gaining momentum for point-of-care (POC) systems. Such systems could be capable of tracking and monitoring cancer cells in real-time, with further providing information that could alleviate therapeutic success rates. Furthermore, such devices can provide comprehensive picture for staging, detailed molecular profiling and monitoring disease remission and possible recurrence.

References:

1. Ueda, T., Shimada, E. & Urakawa, T. Serum levels of cytokines in patients with colorectal cancer: Possible involvement of interleukin-6 and interleukin-8 in hematogenous metastasis. *J. Gastroenterol.* **29**, 423–429 (1994).
2. Tawara, K., Oxford, J. T. & Jorcyk, C. L. Clinical significance of interleukin (IL)-6 in cancer metastasis to bone:Potential of anti-IL-6 therapies. *Cancer Manag. Res.* **3**, 177–189 (2011).
3. Liu, T. *et al.* Self-seeding circulating tumor cells promote the proliferation and metastasis of human osteosarcoma by upregulating interleukin-8. *Cell Death Dis.* **10**, (2019).
4. Wang, C. Q. *et al.* Interleukin-6 enhances cancer stemness and promotes metastasis of hepatocellular carcinoma via up-regulating osteopontin expression. *Am. J. Cancer Res.* **6**, 1873–1889 (2016).
5. Lesuffleur, A., Im, H., Lindquist, N. C. & Oh, S. H. Periodic nanohole arrays with shape-enhanced plasmon resonance as real-time biosensors. *Appl. Phys. Lett.* **90**, (2007).
6. Zheng, P. *et al.* A gold nanohole array based surface-enhanced Raman scattering biosensor for detection of silver(i) and mercury(ii) in human saliva. *Nanoscale* **7**, 11005–11012 (2015).
7. Cetin, A. E. *et al.* Plasmonic Nanohole Arrays on a Robust Hybrid Substrate for Highly Sensitive Label-Free Biosensing. *ACS Photonics* **2**, 1167–1174 (2015).
8. Li, X. *et al.* Label-Free Optofluidic Nanobiosensor Enables Real-Time Analysis of Single-Cell Cytokine Secretion. *Small* **14**, (2018).
9. Li, X. *et al.* Plasmonic nanohole array biosensor for label-free and real-time analysis of live cell secretion. *Lab Chip* **17**, 2208–2217 (2017).
10. Monteiro, J. P., de Oliveira, J. H., Radovanovic, E., Brolo, A. G. & Girotto, E. M. Microfluidic Plasmonic Biosensor for Breast Cancer Antigen Detection. *Plasmonics* **11**, 45–51 (2016).
11. Franco, A. *et al.* A label-free optical system with a nanohole array biosensor for discriminating live single cancer cells from normal cells. *Nanophotonics* **11**, 315–328 (2022).

Résumé de la thèse en français

Étude en temps réel d'échantillons biologiques modèles sur plateforme microfluidique dédiée couplée à un biocapteur multiplexé : un pas vers le Lab-on-Chip pour les clusters CTC

1. Introduction:

Le cancer est défini comme une prolifération incontrôlée de cellules persistantes et non fonctionnelles dans une partie de l'organisme. Certaines de ces cellules se détachent et se séparent de la masse tumorale primaire, rejoignent la circulation sanguine et se fixent à une autre partie de l'organisme, entraînant la propagation de la tumeur et des métastases. Ces cellules sont appelées cellules tumorales circulantes (CTC), et des recherches récentes ont montré un lien entre ces cellules et une croissance métastatique agressive et la propagation du cancer [1]. Une progression agressive de la maladie et une survie globale (SG) plus courte ont été observées chez des patients présentant un nombre élevé de CTC [1]. Les CTC ainsi que l'ADN tumoral circulant (ctDNA) et les exosomes peuvent être utilisés comme « biopsies liquides » pour la détection et l'intervention précoces contre le cancer. Par rapport aux biopsies tissulaires conventionnelles, qui sont la norme de référence en matière de diagnostic des cancers, ces biopsies liquides sont moins invasives et peuvent être utilisées pour un meilleur dépistage, diagnostic et suivi du cancer. [2].

Le principal obstacle scientifique à l'analyse des CTC en tant que biopsies liquides est leur isolation efficace et la détection spécifique en temps réel de divers biomarqueurs associés. De plus, les CTC expriment différents biomarqueurs en fonction du stade de progression du cancer. Ainsi leur analyse peut donner une image plus large de l'état et de la progression de la maladie, conduisant aussi au développement de nouvelles façons de diagnostiquer et de traiter le cancer. Pour ce faire, l'analyse des CTC peut être divisée en (i) isolement et piégeage des CTC, et (ii) caractérisation des biomarqueurs CTC. Des configurations ou des kits commerciaux sont utilisés pour le tri initial des CTC, puis des tests immunologiques conventionnels et des tests génétiques peuvent être utilisés pour une analyse plus poussée des CTC et des biomarqueurs associés. Toutes ces méthodes doivent être utilisées séquentiellement pour obtenir un diagnostic sûr pour un patient. Toutes ces analyses sont extrêmement chronophage et nécessite en outre des volumes d'échantillons importants et répétés, ce qui entraîne des coûts opérationnels globalement élevés.

Des appareils commerciaux comme le CELLSEARCH® , seul dispositif approuvé par la FDA, et différents kits comme l'isolement des cellules tumorales épithéliales (ISET) peuvent être utilisés pour la numération des CTC. Cependant ces dispositifs ne permettent pas d'analyser la sécrétion de biomarqueurs de différentes sous-populations. En fait, ces outils n'isolent pas toutes les sous-populations de CTC, mais ciblent uniquement les cellules épithéliales [3,4]. Pour surmonter certains des inconvénients liés à l'isolement et au tri des CTC, des recherches récentes se sont concentrées sur la technologie microfluidique qui a connu des progres rapides. La microfluidique est un domaine multidisciplinaire qui se concentre sur l'étude du comportement des fluides à une échelle extrêmement petite (généralement submillimétrique) où l'action capillaire régit le transport de masse. En biologie, la microfluidique est utilisée dans de nombreuses applications comme les puces à ADN, les microarrays pour la PCR, les Lab-On-a-Chip, les microarrays pour le criblage de médicaments et la culture de cellules. Pour l'isolement des CTC, un piégeage efficace tout en gardant leur intégrité biologique est impératif.

Les dispositifs microfluidiques sont bien adaptés au piégeage des CTC car ils sont portables et nécessitent de petits volumes d'échantillons, ce qui minimise les coûts. De plus, ces dispositifs peuvent être automatisés, ce qui réduit la main-d'œuvre opérationnelle globale.

Différents matériaux tels que le silicium, le verre, le poly(méthacrylate de méthyle) (PMMA), le polydiméthylsiloxane (PDMS) et d'autres polymères peuvent être utilisés pour la fabrication de dispositifs microfluidiques [5,6]. Cependant, pour les applications biologiques, le PDMS est une excellente option en raison de sa nature biocompatible (permet la culture cellulaire et l'imagerie par fluorescence) et de sa transparence optique (permet la détection à des longueurs d'onde entre 1100 et 240 nm). De plus, le PDMS est peu coûteux, facile à manipuler et peut être scellé de manière irréversible afin d'éviter les fuites, grâce à un traitement au plasma. Enfin, la nature élastique du PDMS permet la conception et la reproduction de diverses structures 3D complexes pour une approche modulaire.

La fabrication de dispositifs en PDMS peut être réalisée soit par lithographie douce, soit par photo- ou UV-lithographie, soit par lithographie par faisceau d'électrons [7]. Cependant, nous nous sommes concentrés sur la technique de moulage du PDMSutilisant des motifs complexes gravés sur des substrats ou des moules réutilisables par photolithographie haute résolution. Ce type de fabrication est relativement bon marché et les dispositifs peuvent être répliqués [8,9], comme cela sera présenté dans le chapitre 4.

Pour l'analyse des biomarqueurs CTC, les méthodes de laboratoire standard comprennent l'immunofluorescence, l'immunohistochimie (IHC), le dosage immuno-enzymatique (ELISA) et les tests génétiques. Bien que ces méthodes standards soient sensibles et spécifiques, elles présentent certains inconvénients tels que le temps et nécessitent souvent un équipement coûteux et des opérateurs expérimentés. En particulier, pour les stades précoces du cancer, l'IHC et l'ELISA ne sont pas suffisamment sensibles en raison de la faible concentration de biomarqueurs. Pour palier à ces inconvénients, la technologie des biocapteurs est devenue une alternative de premier plan car elle permet une analyse multiplexée et en temps réel tout en offrant la possibilité d'intégration avec une plate-forme microfluidique.

Cependant, pour la fabrication de tout biocapteur, l'immobilisation de l'élément de bio-reconnaissance sur des substrats solides comme une surface métallique telle que l'or (Au) et/ou le verre est capitale. Ainsi, l'optimisation de la modification de surface par fonctionnalisation chimique et l'immobilisation biologique doivent être étudiées. L'immobilisation covalente par activation carbodiimide/NHS est une approche conventionnelle dans laquelle les monocouches chimiques fonctionnalisées sur le substrat doivent porter des groupes fonctionnels terminaux tels que -COOH, -NH2 et -NHS ester. Ensuite, ces groupes fonctionnels réagissent avec des molécules biologiques telles que des anticorps, des protéines et des acides nucléiques (NA). Cependant, ce couplage nécessite des conditions de pH et de température spécifiques, ce qui conduit à de faibles rendements d'immobilisation et à une perte d'acitivité biologique des molecules immobilisées [10].

Pour surmonter ces problèmes, la chimie du click sans cuivre est une approche récente intéressante qui fait référence à un groupe de réactions chimiques utilisées pour la conjugaison spécifique de biomolécules. Ces réactions sont rapides, polyvalentes, simples à réaliser, faciles à purifier, stéréospécifiques et ne produisent que des sous-produits inoffensifs, ce qui les rend adaptées à la manipulation de biomolécules. La chimie du click peut être classée en différentes réactions comme l'azide-alcyne catalysé par le cuivre (CuAAC), l'azide-alcyne non catalyse par le cuivre (SPAAC), les cycloadditions alcyne-nitrone (SPANC), les réactions thiol-ène et thiol-yne, entre autres, qui seront discutées en détaildans le chapitre 3.

1. Aperçu de la these

Pour mon projet de doctorat, je me suis concentré sur la fabrication d'un laboratoire sur puce (LOC), intégrant une plateforme microfluidique capable d'effectuer le piégeage des CTC avec un biocapteur pour l'analyse de l'expression des biomarqueurs CTC. Un tel microsystème permettra d'analyser les CTC des patients et de réaliser des études de chimiosensibilité sur les CTC. Ce projet fait partie d'une cotutelle internationale entre l'Ecole Centrale de Lyon (ECL) et le Royal Melbourne Institute of Technology (RMIT) sous l'égide de l'Union Européenne et du cadre Marie Curie. Mes travaux sont répartis entre les deux laboratoires: (i) Dispositifs pour la santé et l'environnement (DSE), Institut des Nanotechnologies de Lyon (INL) à l'ECL et Université Claude Bernard Lyon-1 ; (ii) le Centre intégré de photonique et d'applications (InPAC) du RMIT.

Cette thèse est divisée en 5 parties. **Le chapitre 2** présentera l’état de l'art concernant le diagnostic général du cancer en se concentrant spécifiquement sur les CTC, les caractéristiques et les méthodes conventionnelles utilisées pour leur analyse. En outre, ce chapitre présentera la physiologie générale et les biomarqueurs communs pour les CTC ainsi que les biomarqueurs associés au CTC spécifiquement dans le cas du cancer du poumon et du cancer de la prostate. Enfin, les modalités de biodétection telles que les approches massiques / piézoélectriques, électrochimiques et optiques spécifiques à ces biomarqueurs seront présentées, ainsi qu'une analyse comparative approfondie sera effectuée pour ces éléments transducteurs.

Le chapitre 3 se concentrera sur l'étape initiale de fabrication d'un biocapteur, la modification de surface pour une immobilisation site-spécifique et orientée d'anticorps pour la reconnaissance efficace de cible spécifique. Une analyse comparative entre deux réactions de chimie click, la cycloaddition azide-alcyne sans cuivre (SPAAC) et la réaction thiol-yne, a été réalisée pour des surfaces d’or fonctionnalisées par des chaînes alkylées et PEGylées. De plus, une caractérisation approfondie a été effectuée entre la réaction de chimie click optimale et le couplage par l’approche carbodiimide/NHS conventionnelle. Différentes stratégies d'espacement utilisant divers rapports de diluant PEGylé comme 1/0, 1/1 et 1/4 avec les monocouches fonctionnelles ont été réalisées. Ensuite, l'efficacité d'immobilisation des anticorps non modifiés avec un couplage carbodiimide/NHS et des anticorps modifiés (Ab-N3 et Ab-SH) spécifiques des chimies click SPAAC et thiol-yne respectivement a été caractérisée. La modification optimale a été sélectionnée en se concentrant sur l’immobilisation dirigées et orientés des anticorps sur la surface fonctionnalisée.

Le chapitre 4 présente la fabrication d'un dispositif microfluidique complexe pour le piégeage des CTC. Une telle plate-forme microfluidique avec des vannes pneumatiques et des unités de piègeage a été mise en oeuvre grâce à la technique de moulage. L'analyse de la littérature porte sur l'actionnement des vannes pneumatiques pour les dispositifs microfluidiques ainsi que sur les techniques de moulage. La caractérisation initiale des vannes pneumatiques a été réalisée à travers différentes itérations du dispositif. La caractérisation du débit dans le microsystème fluidique a été réalisé par la manipulationdebit et le piégeage des microbilles puis par celui de cellules. Enfin, des évaluations sur les sécrétions de différents biomarqueurs ont été effectués pour les cellules cancéreuses.

Le chapitre 5 décrit le développement d'une configuration intégrée du biocapteur à une plate-forme microfluidique capable d'effectuer une detection spécifique en temps réel du biomarqueur interleukine-6 (IL-6). Il s’agit d’un biocapteur à détection optique sans marquage utilisant des réseaux de nanotrous plasmoniques en or (NHA) fabriqués par dépôt de faisceau électronique. Ils ont été caractérisés par microscope électronique à balayage double (SEM) et faisceau d'ions focalisé (FIB). L'évaluation de la sensibilité initiale des NHA a été réalisée au moyen d’un montage opto-spectroscopique permettant d’analyser les changements d'indice de réfraction dûs à des variations de concentrations de glycérol.

Et enfin, **le chapitre 6** se concentrera sur la synthèse de l’état de l’art présenté au chapitre 2 et les résultats obtenus dans les chapitres 3, 4 et 5. Enfin, les perspectives futures et mes propositions sur l'amélioration de ce qui a été réalisé jusqu'à présent seronnt présentées.

2. Fonctionnalisation de surface de l'immuno-capteur plasmonique : chimie du click versus chimie du carbodiimide/NHS

Les immuno-capteurs plasmoniques sont généralement composés d'or sous forme de film ou de nanoparticules, et dont les éléments de bio-reconnaissance (les anticorps) sont greffés sur la surface pour détecter des analytes basés sur la reconnaissance anticorps/antigène. Ces biocapteurs font appel à une approche sans marquage en exploitant le principe de la résonance plasmonique de surface (SPR) [11,12]. Lors de la reconnaissance de la cible par les anticorps immobilisés, l'indice de réfraction de surface change et induit des modifications électromagnétiques sur les conditions de résonance propagées sous forme de plasmons comme décrit dans la figure 1. Les performances de ces dispositifs dépendent à la fois de leur sensibilité aux changements d'indice de réfraction et de la fonctionnalisation de surface pour capturer efficacement et spécifiquement l'antigène d'intérêt tout en limitant l'adsorption non spécifique.

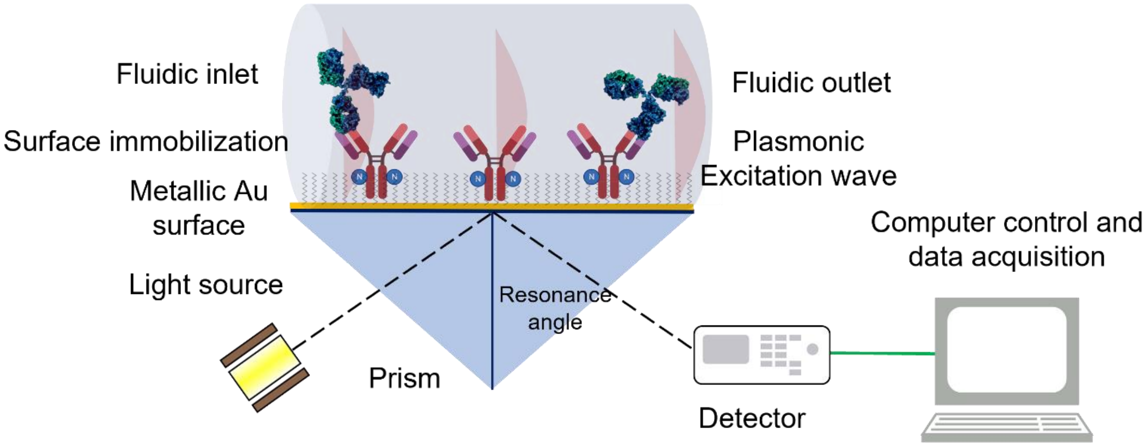

Figure 1.: Schéma et principe de l'imagerie par résonance plasmonique de surface (SPRi).

Pour la fabrication d'immuno-capteurs plasmoniques efficaces, la fonctionnalisation chimique de la surface d'or est une étape clé. Une mauvaise fonctionnalisation peut conduire à une désorption de l'anticorps (Ab) entraînant une adsorption non spécifique d'autres composés présenes dans l'échantillon telles que des cellules, des marqueurs et des protéines non spécifiques. La fonctionnalisation chimique repose sur l'agencement de monocouches auto-assemblées (SAM) de molécules organiques de manière orientée. Ces molécules organiques sont généralement constituées de chaînes d'hydrocarbures, portant un groupe thiol (-SH) à une extrémité qui se lie à l'or par des liaisons Au-S via la réaction d'oxydoréduction, tandis qu'un groupe fonctionnel à l'autre extrémité peut établir des liaisons avec l'anticorps.

Pour la bio-reconnaissance de différentes cibles protéiques, différentes classes d'immunoglobulines (Ig) d'anticorps (Ac) peuvent être sélectionnées telles que IgA, IgD, IgE, IgG et IgM mais dont IgG est l'immunoglobuline la plus couramment utilisée. Les anticorps IgG contiennent environ 9 cystéines qui sont des sites potentiels de réaction/immobilisation. La structure de l'IgG se compose des fragments Fc et Fab ainsi que de chaînes légères et lourdes. Un seul anticorps est composé de plusieurs acides aminés qui portent différents groupes fonctionnels comme -NH2, -COOH et -OH entre autres sur leur chaîne latérale. De tels groupes sont exploités pour l'immobilisation et la fonctionnalisation de surface.

2.1.Aperçu:

Comme mentionné précédemment, pour mon projet, je me suis concentré sur deux stratégies différentes (i) la chimie du click sans cuivre soit par couplage thiol-yne ou SPAAC en utilisant le groupe dibenzocyclooctyne (DBCO) et (ii) la chimie conventionnelle C/NHS pour une analyse comparative. Ces stratégies ont été analysées pour développer une immobilisation d'anticorps site-spécifique et orientée sur des surfaces d'or fonctionnalisées. Pour la chimie C/NHS, des concentrations molaires 1/1 de NHS-/COOH-Alkyls mélangés avec des OH-Alkyls ont été préparées, tandis que pour la chimie click sans cuivre, deux surfaces fonctionnalisées ont été comparées: 1/1 DBCO/OH Alkyls avec des chaînes alkylées et 1/1 DBCO PEGs/OH Alkyls avec des chaînes PEGylées comme indiqué sur la Fig. 2. (A).

Les groupes fonctionnels pour l'immobilisation d'anticorps IgG1 sont été présentés sur la Fig. 2. (B). Le groupe NHS sur les NHS/OH Alkyls est spécifiques des fonctions NH2 des Ab et le groupe

DBCO sur DBCO/OH Alkyls et DBCO PEGs /OH Alkyls est spécifique des fonctions -SH sur l'Ab-SH fragmenté (thiol-yne) et -N3 (azide) sur l'Ab-N3 activé par l'azide (SPAAC) pour le couplage covalent d'anticorps, décrit plus en détail au chapitre 3.

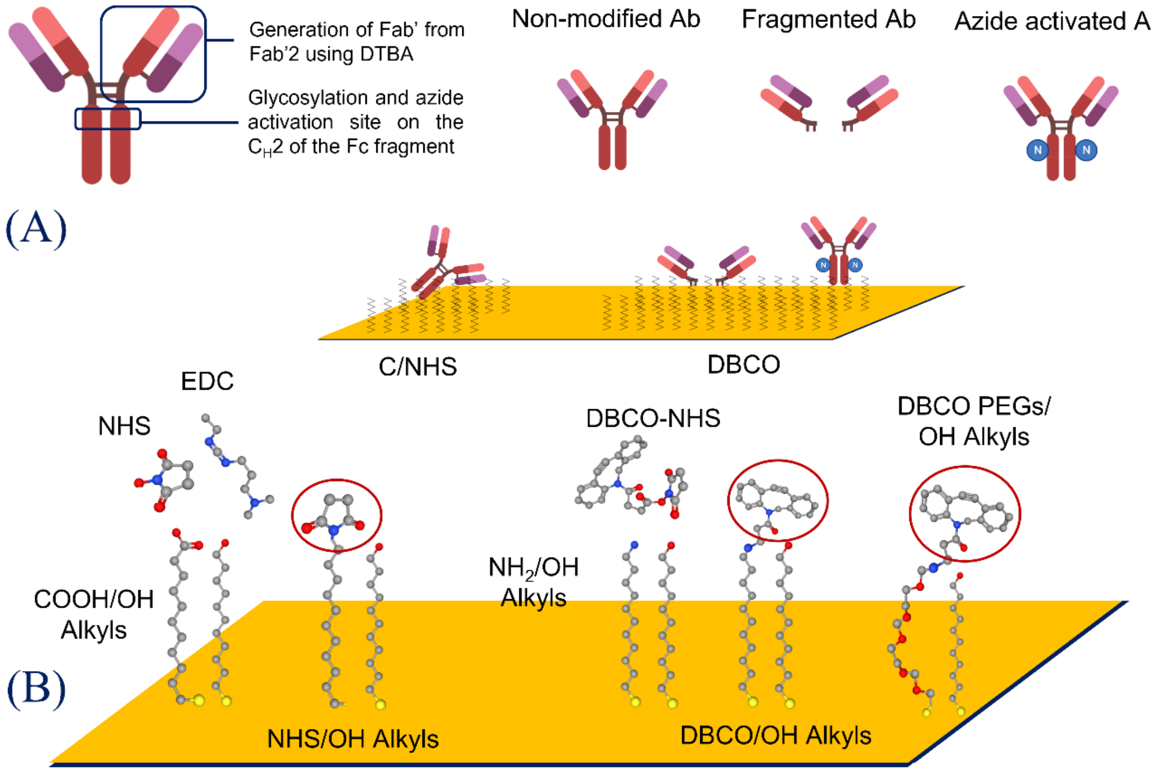

Figure 2.: Stratégies de fonctionnalisation de surface : **(A)** Les groupes fonctionnels pour l'immobilisation d'anticorps (Ab) sont mis en évidence pour toutes les surfaces. L'Ab non modifié est immobilisé sur une surface fonctionnalisée carbodiimide/NHS (C/NHS). L'anticorps fragmenté (Ab-SH) et l'anticorps activé par l'azide (Ab-N3) sont immobilisés sur des surfaces fonctionnalisées DBCO. **(B)** Structure chimique des surfaces d'or fonctionnalisées. La surface NHS/OH Alkyls est obtenue après activation EDC/NHS de monocouches mixtes COOH/OH Alkyls ; La surface DBCO/OH Alkyls est obtenue après greffage DBCO-NHS sur des monocouches mixtes NH2/OH Alkyls ; La surface DBCO PEGs/OH Alkyls est obtenue directement par fonctionnalisation monocouche mixte DBCO PEGs/OH Alkyls.

2.2.Analyse comparative de l'efficacité d'immobilisation des anticorps entre les surfaces C/NHS et DBCO-SPAAC :

Les interactions ont été mesurées sous forme de rapport signal sur bruit (S / N) en divisant le signal de l'interaction spécifique par celui de l'interaction non spécifique (plots PBS1X) comme présenté sur la figure 3. (A). Sur NHS/OH Alkyls, pour les deux types d'anticorps immobilisés (Ab et Ab-N3), aucune tendance distincte n'a été observée car les mêmes groupes fonctionnels sur les anticorps sont impliqués dans la reaction (groups –NH2) entraînant une immobilisation aléatoire et non orientée. Il est également possible que l'adsorption non spécifique sur la surface soit équivalente pour les deux types d'anticorps.

Cependant, sur DBCO PEGs/OH Alkyls, le S/N pour Ab-N3 a mis en évidence une conjugaison site-spécifique et dirigée de l'anticorps avec le groupe DBCO de la surface fonctionnalisée. L'immobilisation d'anticorps sur les surfaces DBCO PEG/OH Alkyls ont présenté une réponse de signal 2,8 fois plus élevée que sur les surfaces NHS/OH Alkyls. Cela indique une meilleure orientation des anticorps couplés sur la surface de manière dirigée pour Ab-N3 sur DBCO PEGs/OH Alkyls par rapport à Ab ou Ab-N3 sur NHS/OH Alkyls.

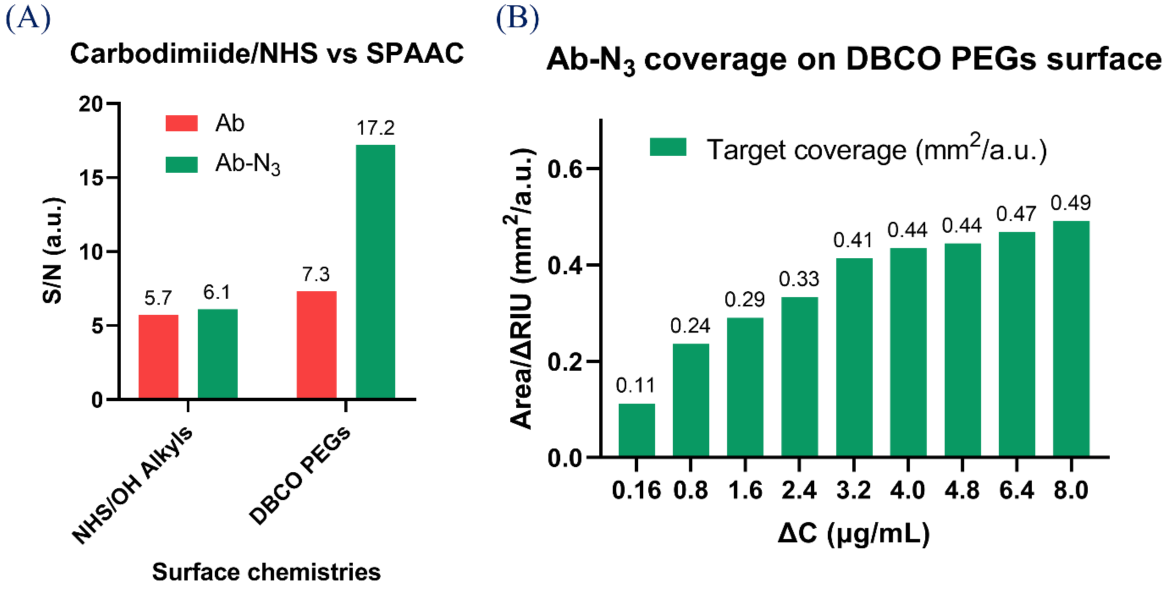

Figure 3. : (A) Analyse comparative du rapport signal sur bruit (S/N) des performances de biodétection. L'IgG1 polyclonal de chèvre anti-souris a été utilisé comme cible pour la détection par l'Ac non modifiés et l'Ac-N3 activés par l'azoture immobilisés sur la surface NHS/OH Alkyls pour la chimie carbodiimide/NHS et sur la surface DBCO PEG/OH Alkyls pour la chimie click SPAAC. S/N a été calculé en divisant le signal de détection spécifique (Ab et Ab-N3) par le signal non spécifique (PBS1X). (B) Analyse de la couverture cible pour Ab-N3 sur les monocouches DBCO PEGs/OH Alkyls. Pour mesurer la couverture minimale de la cible, le changement d'indice de réfraction global après interaction avec la concentration a été pris en compte.

Une caractérisation supplémentaire sur la stabilité de la monocouche DBCO PEGs / OH Alkyls couplés à Ab-N3 a été réalisée. Les résultats obtenus pour des injections multiples à des concentrations variables d'anticorps cible de 0,16 μg/mL à 8 μg/mL sont présentées sur la Fig. 3. (B). Pour determiner la couverture cible minimale, une zone d'intérêt de ~ 0,15 mm2 a été sélectionnée et les calculs ont été effectués en mesurant le changement de RI induit par la reconnaissance spécifique avec la concentration de cibles correspondante. Après chaque injection de cible, la surface a été régénérée en utilisant du HCl 10 mM.

En conclusion, la reconnaissance concentration-dépendante de la cible ainsi que la saturation de la surface par la cible mettent en évidence la stabilité de la monocouche DBCO PEG/OH Alkyls fonctyionnalisée par Ab-N3 pour de multiples interactions. La section suivante mettra en évidence l'application de cette approche DBCO PEGs / OH Alkyls avec immobilisation d'anticorps actives par l'azide pour la biodétection des marqueurs du cancer.

3. Fabrication de dispositifs microfluidiques complexes actionnés pneumatiquement pour le piégeage optimal des cellules cancéreuses :

La microfluidique est la science de la manipulation de fluides à l'échelle micrométrique et submicronique. Pour le développement de dispositifs microfluidiques, des techniques de microfabrication sont utilisées. La plupart des systèmes microfluidiques fonctionnent dans des régimes d'écoulement laminaire où le nombre de Reynold est généralement maintenu très bas, dans lequel les forces visqueuses du fluide sont plus fortes que l'inertie atmosphérique [13]. Cela permet à la microfluidique d'être précise et reproductible et de permettre une simulation avec une grande confiance.

Les premières études se concentraient sur la miniaturisation des systèmes d'électrophorèse chromatographique et capillaire ainsi que sur les technologies microélectroniques [8,14,15]. Récemment, la recherche a fait des pas de géant pour révolutionner les processus conventionnels axés sur la manipulation et le traitement en laboratoire [16]. Les dispositifs microfluidiques offrent la perspective de réduire considérablement les volumes d'échantillons et d'effectuer des analyses à moindre coût et temps [17]. Par rapport à la manipulation fluidique conventionnelle, la manipulation microfluidique présente des avantages uniques, en particulier l'intégration pour des applications biologiques.

Les dimensions des canaux allant de quelques microns à 100 microns avec flux laminaire permettent une manipulation et une analyse précises. De plus, ils permettent la manipulation de petites quantités volumiques, de l'ordre de quelques pL à quelques nL, ce qui facilite l'analyse d'échantillons rares ou coûteux et accélère les processus, améliorant ainsi la rentabilité de l'analyse.

Les dispositifs microfluidiques offrent une voie d'intégration où plusieurs fonctions telles que le mélange, le tri, le piégeage, la détection et plus encore pourraient être incorporées dans un seul dispositif, le rendant portable, polyvalent et robuste pour une utilisation au lit du malade [5,18]. Ainsi, les systèmes microfluidiques "lab-on-a-chip" deviennent des solutions attractives dans le secteur de la santé. Divers matériaux ont été explorés dans la fabrication de systèmes microfluidiques tels que le verre, les polymères d'oléfines cycliques (COP), le polycarbonate, avec des techniques de fabrication comme l'impression 3D, le polyméthylméthacrylate à base thermoplastique (PMMA), les résines photosensibles SU-8 et le polydiméthylsiloxane élastomère à base de silicium (PDMS) [19,20]. Les thermoplastiques tels que les PMMA offrent une transparence optique, une résistance et une rigidité mécaniques élevées, une bonne stabilité thermique et une faible adsorption d'eau. De plus, des instruments supplémentaires sont nécessaires pour la fabrication [21].

Et bien que ces différentes méthodes se soient révélées prometteuses dans la fabrication commerciale de dispositifs microfluidiques, le PDMS reste le premier choix du point de vue du prototypage. Le PDMS offre une transparence optique et une stabilité thermique similaires, une fabrication plus simple même sur des surfaces non planes en raison de sa déformabilité et de sa flexibilité, tout en étant relativement rentable [21]. De plus, le PDMS est chimiquement stable, généralement biocompatible, de nature poreuse pour les gaz et les solvants [17,21]. Sur la base de leurs avantages et inconvénients, divers groupes ont opté pour des dispositifs microfluidiques à base de PDMS pour le piégeage et le tri des cellules [22] et pour l'analyse de biomarqueurs [23].

3.1.Aperçu:

Comme discuté précédemment, pour notre application, l'objectif du projet est de piéger et de cultiver des cellules cancéreuses sous flux afin que nous puissions analyser leurs sécrétions de biomarqueurs en temps réel. Pour atteindre cet objectif, un système microfluidique multicouche complexe est nécessaire comprenant plusieurs vannes pour la manipulation du débit et les fonctions de piégeage, comme illustré à la Fig. 5. Les cellules piégées doivent être maintenues en vie pendant plusieurs heures, voire plusieurs jours, pour un temps d'analyse plus long ce qui implique un dispositif de perfusion actif pour le renouvellement du milieu de culture. Le biocapteur à détection optique sans marquage NHA basée sur une transmission optique extraordinaire (EOT) doit être intégrée dans le dispositive microfluidique pour analyser les biomarqueurs sécrétés par les celleules piégées.

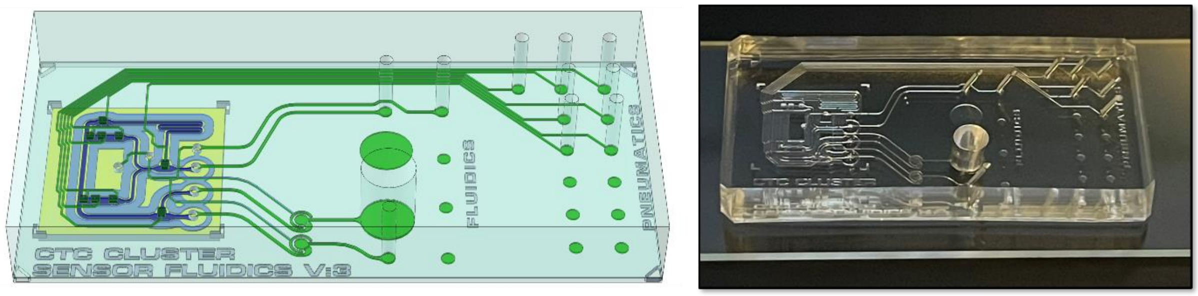

Figure 4.: Conception d'un dispositif microfluidique pour CTC Cluster V3 et dispositif fabriqué par la technique de moulage sur un substrat de lame de verre de microscope.

Pour l'application de piégeage, des vannes pneumatiques et des unités de pièegeage ont été fabriquées selon la technqiue de moulage et contrôlées via un système de pompe à seringue manuelle permettant d'ouvrir et de fermer les vannes. Cela a été conçu non seulement pour piéger les cellules cancéreuses telles que les CTC, mais également pour libérer les biomarqueurs sécrétés par les cellules piégées pour l'analyse. Pour ma thèse, je me suis concentré sur la fabrication de systèmes microfluidiques complexes tels que décrits sur la figure 4.. La caractérisation initiale des différentes vannes, l'optimisation de la voie fluidique et la fonctionnalité de l'unité de pièegeage ont été réalisées. Ensuite, le piégeage avec des billes puis des cellules MCF7 a été présenté. De plus, pour caractériser la gamme de biomarqueurs sécrétés directement par les cellules, des tests ELISA sur les cellules SK-OV-3 et leurs sécrétions, c'est-à-dire la fibronectine et l'interleukine-6 (IL-6), sont discutées en détail au chapitre 4.

3.2.Piégeage des cellules cancéreuses MCF7 :

Comme le montre la Fig. 5. (A), plusieurs cellules ont été piégées dans l'unité de pièegeage. L'observation initiale a indiqué jusqu'à 50 cellules empilées les unes sur les autres. Après une analyse plus approfondie, certaines cellules ont été observées à l'intérieur des piliers. Sur la base de la morphologie de ces cellules cancéreuses et en raison de leur plasticité, on a observé que certaines des cellules traversaient les piliers.

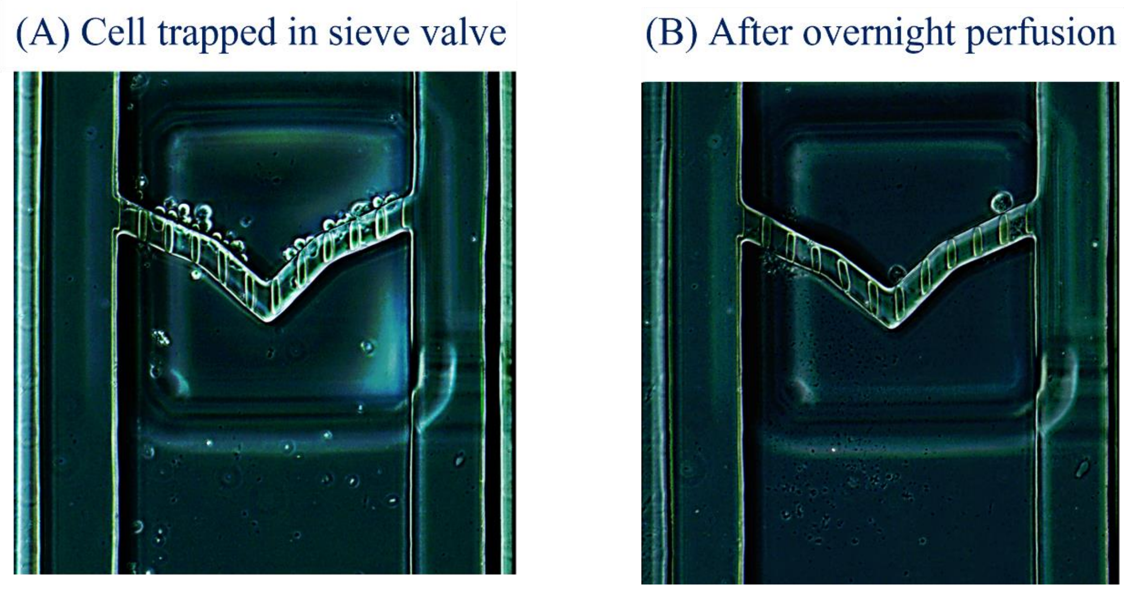

Figure 5. : (A) Cellules MCF7 piégées dans l'unité Trap 1 sous un débit constant à 7 µL/min dans la configuration de vanne V1/V2. En temps réel, comme les cellules sont de nature élastique, la plupart des cellules se faufilent à travers les piliers intégrés dans les vannes à tamis, mais certaines des cellules ont été piégées et empilées les unes sur les autres. (B) Les cellules MCF7 piégées ont ensuite été observées à intervalles réguliers, puis une analyse pendant la nuit a été effectuée. Après 24 heures, les cellules piégées étaient mortes car lorsque les vannes ont été ouvertes, les fragments cellulaires des cellules piégées étaient présents.

Pour une analyse à long terme, environ 20 à 25 cellules ont été piégées et observées à des intervalles réguliers de 30 minutes pendant 3 heures, puis pendant la nuit en fermant la vanne V2 et en n'ouvrant que la vanne V1 partiellement pour une perfusion du milieu de culture nocturne. Après 24 heures, toutes les cellules étaient mortes. En effet, lorsque les vannes V4/V5 ont été ouvertes, des fragments de cellules ont été observés, comme illustré sur la Fig. 8. (B). L'incapacité de l'appareil à maintenir les cellules en vie pourrait être due à une faible présence de CO2 et à une température requise de 37 ° C.

En conclusion, le dispositif microfluidique est capable de piéger de manière efficace les cellules cancéreuses sous flux et une perfusion moyenne a été réalisée via une configuration de co-flux. Cependant, les travaux futurs doivent se concentrer sur le maintien de ces cellules en vie suffisamment longtemps pour l'observation et l'analyse des marqueurs. Pour l'échange de CO2, une couche d'eau pourrait être intégrée dans l'appareil, mais cela rendrait la fonctionnalité de l'appareil plus complexe. De plus, cette couche d'eau serait capable de maintenir la température requise pour conserver les cellules en vie pendant toute la durée de l'analyse.

4. Détection de biomarqueur du cancer grâce à un réseau de nanotrous plasmoniques en système opto-fluidique intégré:

En santé, le diagnostic est une première étape cruciale et la détection précoce permettant l’identification précise de la maladie est fondamentale pour estimer la progression de la maladie et l'efficacité du traitement. Le diagnostic conventionnel repose sur la détection et la quantification de biomarqueurs dont les niveaux altérés sont des indicateurs de l'état pathologique du patient.

L'analyse de ces biomarqueurs est utilisée pour surveiller la réponse thérapeutique et l'évolution de l'état du patient [24,25]. Les techniques classique de diagnostic clinique comprennent les dosages biomoléculaires tels que le dosage immuno-enzymatique (ELISA), les dosages immunologiques par chimiluminescence (CLIA), la réaction en chaîne par polymérase (PCR) couplée à des approches de fluorescence ou chromatographiques et à la spectrométrie de masse [24,25].

Ces approches standardisées offrent une sensibilité et une spécificité exceptionnelles et détectent de grandes bibliothèques de biomarqueurs. Récemment, l'automatisation et la modernisation de ces techniques ont encore réduit la consommation de temps, la demande de main-d'œuvre et les erreurs manuelles [24,25]. Cependant, ces systèmes sont confrontés à des lacunes liées au besoin de techniciens spécialisés, de laboratoires centralisés et à un coût financier global élevé qui entravent la réalisation efficace et rapide sur site des tests de diagnostic. Les biocapteurs plasmoniques ont le potentiel de prendre en charge l'évolution de l'analyse médicale en se concentrant sur des diagnostics fiables et ultrasensibles au lit du malade (POC). Parmi les différents systèmes plasmoniques, la résonance plasmonique de surface (SPR) et ses dérivés - par exemple, l'imagerie SPR (SPRi) et la SPR localisée (LSPR) ont présenté des capacités exceptionnelles axées sur la détection sans marquage et l’analyse en temps réel avec une consommation minimale de réactifs et d'échantillons [24,25].

Les capteurs conventionnels basés sur la SPR ont montré une sensibilité technique d'environ 10-5 à 10-6 unités d'indice de réfraction (RIU) et une plage comprise entre 0,5 et 1 pg/mm-2 pour les dosages biomoléculaires standardisés [25,26]. Les biocapteurs basés sur la SPR ont été largement uilisés dans les laboratoires de recherche et l'industrie pharmaceutique, avec de multiples configurations commerciales disponibles pour les études de cinétique et d'affinité. Cependant, de tels capteurs n'ont pas encore été adoptés dans les milieux cliniques où des défis important ont identifié comme la biofonctionnalisation de la surface du capteur, la capacité d'analyse à haut débit et l'intégration de dispositifs POC empêchant leurs développements en tant que dispositifs de diagnostic *in vitro*. La recherche actuelle s'est concentrée sur ces problématiques avec notamment l'avènement de nouvelles chimies, les nanotechnologies et les approches biotechnologiques. Des rapports récents ont montré non seulement une détection plus rapide et sensible des biomarqueurs conventionnels, mais aussi la découverte de nouvelles cibles peuvant améliorer l'identification précoce des maladies et le suivi précis du traitement. Dans ce chapitre, je me concentrerai sur les différentes approches plasmoniques pour les applications de biodétection du cancer et plus spécifiquement sur la propagation du plasmon à travers des réseaux de nanotrous (NHA), ainsi que les recherches récentes sur leur perspective d’utilisation pour une application dans le diagnostic médical.

4.1.Aperçu:

Pour la modalité de biodétection, nous avons opté pour un transducteur plasmonique constitué de réseaux de nanotrous (NHA) afin d’améliorer la sensibilité du biocapteur. Les réseaux NHA ont été obtenus auprès d'une société, puis recouvert d’une fine couche d’'or (Au) via un dépôt par faisceau d'électrons au RMIT. Ces NHA recouverts de Au ont ensuite été focntionnalisés par des PEG DBCO / OH 2k (1/4). Puis l’anticorps anti-IL-6 activé par un azide a été immobilise sur la surface fonctionnaliséecomme indiqué sur la Fig. 6. L'efficacité de la biodétection a été caractérisée par mesure de l'interaction spécifique pour l'IL-6 comparativement à l'interaction non spécifique pour le récepteur du facteur de nécrose tumorale 2 (TNFR2).pour

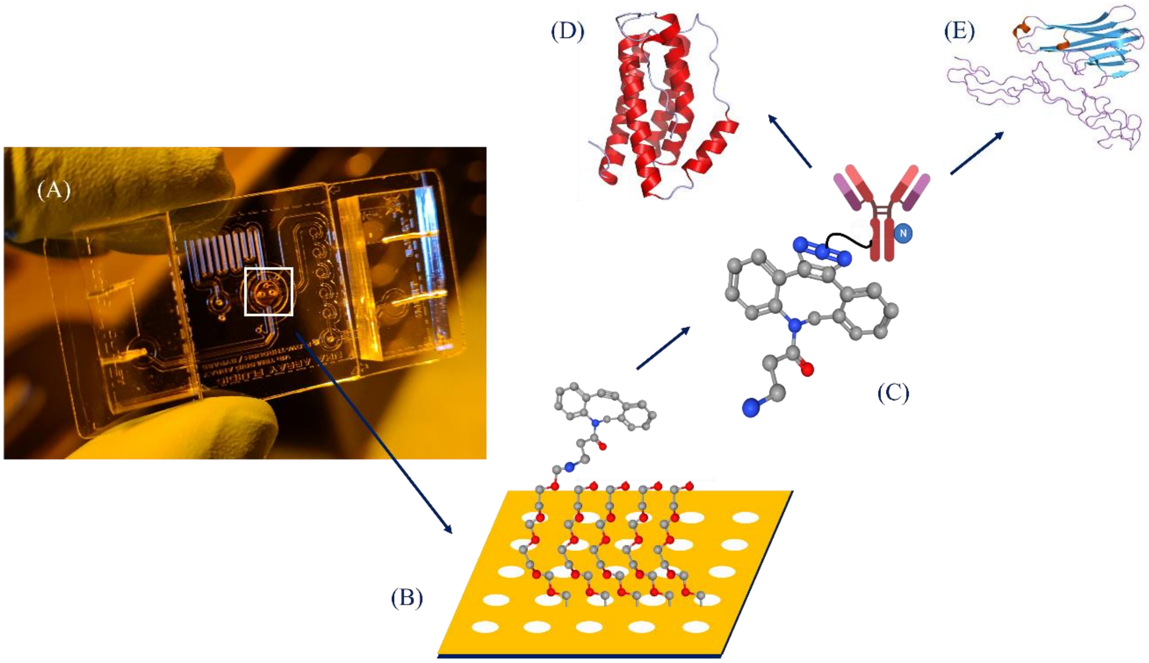

Figure 6.: Schéma de (A) Configuration opto-fluidique intégrée avec réseau de nanotrous (NHA) fonctionnalisé avec (B) une monocouche 1/4 DBCO/OH PEGs 2k et avec (C) l'anticorps active avec l'azoture Ab-N3. (D) representation 3D de l'interleukine-6 (IL-6) et (E) representation 3D du récepteur du facteur de nécrose tumorale 2 (TNFR2).

4.2.Efficacité de biodétection optique sans marquage avec le réseaux de NHA-Optical :

Les résultats présentés sur la Fig. 7 indiquent une interaction spécifique entre l'IL-6 et l'anticorps anti-IL-6 immobilisé sur la surface du biocapteur NHA et une interaction non spécifique pour TNFR2.

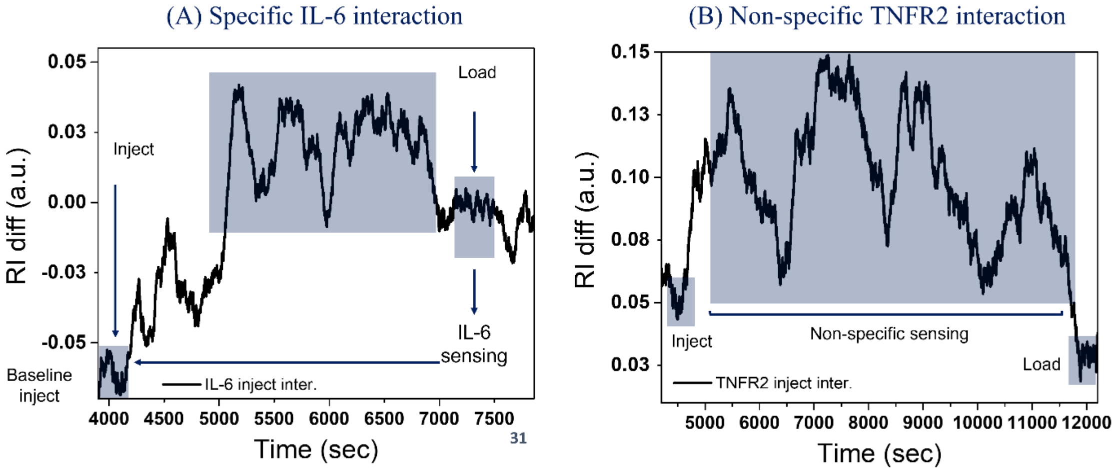

Figure 7. : Analyse des interactions du réseaux Au-NHA intégré dans un système microfluidique. (A) Interaction spécifique de l'IL-6 humaine à une concentration de 1 µg/mL. (B) Interaction non spécifique du TNFR2 humain à une concentration de 1 µg/mL.

Le TNFR2 est un autre biomarqueur associé au cancer sans interaction rapportée avec l'anticorps anti-IL-6. En effet, le signal obtenu suite à l'injection de TNFR2 est caractéristique d'une interaction non spécifique. Bien qu'une différence distincte entre les signaux IL-6 et TNFR2 ait été établie, en raison de contraintes de temps et de système, une caractérisation plus poussée n'a pas pu être effectuée. L'analyse comparative Δ RI entre l'IL-6 et le TNFR2 fournit une image prometteuse pour cette approche, mais des modifications sont nécessaires pour rendre cette configuration sensible à l'analyse en temps réel. La plage de concentrations théoriques pour la détection des sécrétions de biomarqueurs en temps réel à partir de cellules cancéreuses a été évaluée au chapitre 4 et est de 5 à 35 pg/mL pour l'IL-6. C'est un ordre de 10-6 inférieur par rapport à ce qui a été réalisé avec ce système intégré. Nous avons présenté un Δ RI de 5 x 10-2 pour une concentration d'IL-6 de 1 µg/mL et un décalage Δ RI calculé de 2,5 x 10-7 à 1,7 x 10-6 pourrait être nécessaire pour détecter de manière optimale l'IL-6 à des concentrations de l'ordre du pg/mL. Sur la base de nos mesures de sensibilité et de la caractérisation de la biodétection, la LOD et la LOQ analysées ci-dessus, c'est-à-dire que 10-4 à 10-5 ne sont sensibles que pour une détection de l'ordre du µg/mL. Un sensibilité minimum de 10-7 et 10-8 pour la LOD /LOQ serait nécessaire pour une analyse optimale.

5. Conclusions et perspectives

Mon projet de doctorat portait sur l'analyse en temps réel et de manière multiplexée de biomarqueurs sécrétés du cancer. Et pour concrétiser cette vision, j'ai dû me concentrer sur la fabrication d'une configuration opto-fluidique intégrée de type Lab-on-a-Chip (LOC) capable d'effectuer le piégeage des CTC et l'analyse directe des sécrétions de biomarqueurs des CTC capturés et des cluster de CTC. Ce LOC est composé de: (i) un compartiment microfluidique pour un piégeage efficace des cellules et (ii) un système de biodétection pour l'analyse des sécrétions cellulaires. Pour l'élaboration de ce dispositif, la modification de surface est d'une importance primordial. J'ai donc également travaillé sur (iii) la fabrication d'une approche d'immobilisation de surface capable d'une conjugaison dirigée, site-spécifique et orientée d'anticorps sur la surface du capteur pour une reconnaissance spécifique de cible.

Pour développer une telle approche de modification de surface, la chimie du click a été développée utilisant le groupe dibenzocyclooctyne (DBCO) comme groupe actif pour le couplage orienté via la cycloaddition azide-alcyne sans cuivre (SPAAC) ou la réaction thiol-yne. Dans un premier temps, j'ai effectué une analyse comparative entre des monocouches à terminaison DBCO ayant des chaînes alkylées (DBCO/OH Alkyls) ou PEGylées (DBCO PEGs/OH Alkyls). La caractérisation qualitative a été réalisée par goniométrie CA et AFM et une confirmation quantitative complète a été mise en évidence par PM-IRRAS, XPS et ARXPS et des simulations de profil de profondeur. La caractérisation de ces deux surfaces DBCO a été présentée pour l'approche thiol-yne via Ab-SH et SPAAC via Ab-N3 et entre ces monocouches, les meilleurs résultats ont été obtenus pour Ab-N3 immobilisé sur DBCO PEGs/OH Alkyls.

Une fois que l'approche optimale de la chimie du click a été présentée, une analyse comparative de la caractérisation de la biodétection a été effectuée entre l'approche SPAAC pour les DBCO PEG/OH Alkyls et la chimie conventionnelle C/NHS pour les NHS/OH Alkyls pour la sélection de l'approche d'immobilisation qui serait utilisée pour la fabrication du biocapteur . Sur la base de nos résultats, Ab-N3 - DBCO PEGs/OH Alkyls ont présenté des réponses de signal favorables mettant en évidence la nature site-spécifique, orientée et dirigée de l'immobilisation. De plus, la stabilité de la monocouche a été démontrée par de multiples injections cibles à des concentrations variables ainsi que par une analyse des taux de réaction (cinétique ON/OFF) et des calculs pour la couverture de la surface par les molecules cibles. Ces résultats ont indiqué que la monocouche DBCO PEGs/OH Alkyls était stable, capable de régénération et de reconnaissance concentration-dépendante de la cible.

Comme mentionné ci-dessus, l'interleukine-6 (IL-6), l'interleukine-8 (IL-8) et le facteur de croissance tumorale-bêta (TGF-β) ont été sélectionnés pour la caractérisation de l'efficacité de la biodétection à l'aide de l'approche DBCO - Ab-N3 dans des milieux de culture complexes. Cependant, en raison de la sensibilité de configuration SPRi conventionnelle, je n'ai pas pu détecter d'interaction spécifique de ces biomarqueurs. Je me suis alors concentré sur la caractérisation de différents rapports d'espacement pour les surfaces DBCO PEGs 2k afin d'améliorer cette modification de surface. J'ai pu mettre en evidence que le rapport 1/4 DBCO/OH PEGs 2k (monocouche fonctionnelle DBCO en une partie et diluants OH en quatre parties) présentait l'orientation optimale de la monocouche contrairement au rapport 1/1 qui a été utilisé pour la caractérisation de la détection de biomarqueurs via la configuration SPRi. J'ai également essayé d'améliorer la sensibilité de la détection en utilisant des capteurs plasmoniques basés sur un réseau de nanotrous (NHA) plutôt que sur la configuration SPRi conventionnelle.

Avant la fabrication d'un système intégré, je me suis concentré sur le piégeage des CTC dans un système microfluidique complexe. J'ai fabriqué un système microfluidique selon une technique de moulage PDMS comportant des vannes pneumatiques 3D avec des circuits d'actionnement et des unités de piégeage avec des vannes à tamis pour le piégeage des cellules. Le dispositif intitulé CTC Cluster V3 a été caractérisé initialement pour la manipulation de flux à la fois comme flux unique et co-flux. Ensuite, des billes de polystyrène, puis par la suite, des cellules cancéreuses ont été piégées dans le microsystème en temps réel.

Après avoir piégé ces cellules, j'ai essayé de les maintenir en culture par perfusion continue de milieu pendant une période de 3 heures, puis une nuit. Cependant, les cellules sont mortes dans le dispositif en raison d'un manque d'échange gazeux (O2/CO2 échange). J'ai également effectué des tests ELISA pour différents biomarqueurs du cancer et calculé les besoins en volume unitaire du piège, afin d'avoir une gamme de concentrations en biomarqueurs sécrétées directement par les cellules qui soit détectable.

Le système de piégeage présenté dans mon projet a présenté beaucoup de promesses pour le piégeage en temps réel, mais à mon avis, des améliorations sont nécessaires, notamment le contrôle des débits permettant un piégeage des cellules moins stressant, limitant le cisaillement des cellules à travers les pièges à tamis.

Avant d'intégrer le réseau NHA dans le CTC Cluster V3, il a été caractérisé pour évaluer son potentiel de détection plasmonique. Le système double SEM/FIB a été utilisé pour caractériser ces NHA. Ensuite, ces NHA ont été intégrés dans le système microfluidique CTC Cluster V3 mentionné ci-dessus, puis caractérisé par un système opto-spectroscopique modulaire. La limite de détection et de quantification pour notre plateforme de biodétection a évaluée avec des solutions de glycerol à différentes concentrations, et les résultats indiquent une plage comprise entre 10-4 et 10-5.

Ensuite, les Au-NHA ont été fonctionnalisés avec 1/4 DBCO/OH PEGs 2k, puis des anticorps anti-IL-6 Ab-N3 activés par l'azide ont été immobilisés sur la monocouche fonctionnelle pour effectuer une détection en temps réel et sans marquage de l'IL-6 à des concentrations en µg/mL. La non-spécificité de l'interaction a été démontrée par l'injection de TNFR2 à des concentrations similaires. Les résultats que j'ai obtenus pour les concentrations théoriques d'IL-6 semblent indiquer qu'un tel système intégré pourraient ne pas être en mesure de détecter de telles plages très faibles d'analytes (ng/mL et pg/mL). J'ai calculé environ 41,5 pg/nL d'IL-6 sécrétés pour une seule cellule, et environ 8 pg/nL pour 10 cellules dans un volume de chambre de piégeage de 50 nL. Pour améliorer encore la capacité de biodétection d'un tel système intégré, l'accent doit être mis sur le dépôt optimal de la couche d'or et le traitement ultérieur du signal. Différents groupes de recherche ont présenté des concentrations ultra-faibles d'analytes détectées grâce à la fabrication et la caractérisation optimales des réseaux NHA. Après le dépôt d'or, si des nanotrous précis et réguliers doivent être activés, des concentrations de biomarqueurs allant du ng/mL au pg/mL peuvent être détectées dans des échantillons biologiques [27–33].

En perspective, une fois ces systèmes optimisés, ils pourront être utilisés pour les échantillons de patients atteints de cancer. Ainsi, les CTC pouront être analysées via un seul microsystème permettant un isolement et une séparation spécifiques avec une analyse des biomarqueurs directement sécrétés par les cellules piégées afin d'obtenir une image complète du stade métastatique. De tels systèmes de médecine personnalisée basés sur des biocapteurs intégrés associant différentes technologies semblent être une bonne alternative. Pour le diagnostic du cancer, les laboratoires sur puce (LOC) offrent une voie qui prend de plus en plus d'ampleur pour developer des dispositif au lit du patient (POC).

References:

1. Alix-Panabières, C. & Pantel, K. Clinical prospects of liquid biopsies. *Nat. Biomed. Eng.* **1**, (2017).
2. Young, R. Circulating Tumor Cells in Lung Cancer. 655–660 (2012) doi:10.1159/000345182.
3. Nagrath, S. *et al.* Isolation of rare circulating tumour cells in cancer patients by microchip technology. *Nature* **450**, 1235–1239 (2007).
4. Khoo, B. L. *et al.* Expansion of patient-derived circulating tumor cells from liquid biopsies using a CTC microfluidic culture device. *Nat. Protoc.* **13**, 34–58 (2018).
5. Szydzik, C. *et al.* Fabrication of complex PDMS microfluidic structures and embedded functional substrates by one-step injection moulding. *RSC Adv.* **6**, 87988–87994 (2016).
6. Young, E. W. K. *et al.* NIH Public Access Author Manuscript Anal Chem. Author manuscript; available in PMC 2011 March 9. Published in final edited form as: Anal Chem . 2011 February 15; 83(4): 1408–1417. doi:10.1021/ac102897h. Rapid prototyping of arrayed microfluidic systems in. **83**, 1408–1417 (2011).
7. Bouaidat, S. *et al.* Surface-directed capillary system; theory, experiments and applications. *Lab Chip* **5**, 827–836 (2005).
8. Qin, D., Xia, Y. & Whitesides, G. M. Soft lithography for micro- and nanoscale patterning. *Nat. Protoc.* **5**, 491–502 (2010).
9. Rogers, J. A. & Nuzzo, R. G. Recent progress in soft lithography. *Mater. Today* **8**, 50–56

(2005).

10. Wickramathilaka, M. P. & Tao, B. Y. Characterization of covalent crosslinking strategies for synthesizing DNA-based bioconjugates. *J. Biol. Eng.* **13**, 8–17 (2019).
11. S. Huertas, C., Soler, M., Estévez, M. C. & Lechuga, L. M. One-step immobilization of antibodies and DNA on gold sensor surfaces via poly-Adenine oligonucleotide approach. *Anal. Chem.* acs.analchem.0c02619 (2020) doi:10.1021/acs.analchem.0c02619.
12. Han, X., Liu, K. & Sun, C. Plasmonics for biosensing. *Materials (Basel).* **12**, (2019).
13. Cristea, C., Florea, A., Tertiș, M. & Săndulescu, R. Immunosensors. *InTech Open* (2015) doi:10.5772/60524.
14. Becker, H. & Gärtner, C. Polymer microfabrication technologies for microfluidic systems. 89–111 (2008) doi:10.1007/s00216-007-1692-2.
15. Zhang, D., Men, L., Chen, Q. & Science, A. Microfabrication and Applications of Opto-Microfluidic Sensors. 5360–5382 (2011) doi:10.3390/s110505360.
16. Das, C., Wang, G. & Nguyen, C. A Low-Cost, Accurate, and High-Precision Fluid Dispensing System for Microscale Application. *SLAS Technol.* **22**, 144–152 (2017).
17. Yeo, L. Y., Chang, H. C., Chan, P. P. Y. & Friend, J. R. Microfluidic devices for bioapplications. *Small* vol. 7 12–48 (2011).
18. Descamps, L., Roy, D. Le & Tomba, C. Magnetic Polymers for Magnetophoretic Separation in Microfluidic Devices. (2021).
19. Ren, K., Zhou, J. & Wu, H. Materials for Microfluidic Chip Fabrication. **46**, (2013).
20. Ren, K., Chen, Y. & Wu, H. New materials for microfluidics in biology. *Curr. Opin. Biotechnol.* **25**, 78–85 (2014).
21. Kulkarni, M. B., Ayachit, N. H. & Aminabhavi, T. M. Biosensors and Microfluidic Biosensors: From Fabrication to Application. *Biosensors* **12**, (2022).
22. Gao, D. *et al.* Recent developments in microfluidic devices for in vitro cell culture for cell-biology research. *TrAC - Trends Anal. Chem.* **35**, 150–164 (2012).
23. Liao, Z. *et al.* Microfluidic chip coupled with optical biosensors for simultaneous detection of multiple analytes: A review. *Biosens. Bioelectron.* **126**, 697–706 (2019).
24. Soler, M., Huertas, C. S. & Lechuga, L. M. Label-free plasmonic biosensors for point-of-care diagnostics: a review. *Expert Rev. Mol. Diagn.* **19**, 71–81 (2019).
25. Soler, Maria and Huertas, C. S. Label-Free Plasmonic Biosensors in Clinical Diagnostics. **4**, 383–401 (2023).
26. Soler, M., Huertas, C. S. & Lechuga, L. M. Label-free plasmonic biosensors for point-of-care diagnostics: a review. *Expert Rev. Mol. Diagn.* **19**, 71–81 (2019).
27. Lesuffleur, A., Im, H., Lindquist, N. C. & Oh, S. H. Periodic nanohole arrays with shape-enhanced plasmon resonance as real-time biosensors. *Appl. Phys. Lett.* **90**, (2007).
28. Zheng, P. *et al.* A gold nanohole array based surface-enhanced Raman scattering biosensor for detection of silver(i) and mercury(ii) in human saliva. *Nanoscale* **7**, 11005–11012 (2015).
29. Cetin, A. E. *et al.* Plasmonic Nanohole Arrays on a Robust Hybrid Substrate for Highly Sensitive Label-Free Biosensing. *ACS Photonics* **2**, 1167–1174 (2015).
30. Li, X. *et al.* Label-Free Optofluidic Nanobiosensor Enables Real-Time Analysis of Single-Cell

Cytokine Secretion. *Small* **14**, (2018).

31. Li, X. *et al.* Plasmonic nanohole array biosensor for label-free and real-time analysis of live cell secretion. *Lab Chip* **17**, 2208–2217 (2017).

32. Monteiro, J. P., de Oliveira, J. H., Radovanovic, E., Brolo, A. G. & Girotto, E. M. Microfluidic Plasmonic Biosensor for Breast Cancer Antigen Detection. *Plasmonics* **11**, 45–51 (2016).

33. Franco, A. *et al.* A label-free optical system with a nanohole array biosensor for discriminating live single cancer cells from normal cells. *Nanophotonics* **11**, 315–328 (2022).

Real-time study of model biological samples on dedicated microfluidic platform coupled with multiplexed biosensor: one step towards Lab-on-Chip for CTC-clusters

Abstract

Cancer is the proliferation of purposeless cells taking place in any part of the body while the spread of cancer to different part via the circulation is defined as metastasis. In recent years, circulating tumour cells (CTCs) have come to the forefront for their role in metastatic progression. Their detection and analysis can provide valuable information for early cancer diagnosis, screening, and monitoring. The objective of this project is to develop an integrated biosensing-microfluidic setup that can trap and cultivate such rare cells for their biomarker analysis. For biosensing, label-free optical modality has been selected through plasmonic materials (gold, Au) and nano-structuration (nanohole array, NHA). The gold surfaces were functionalized with mixed alkylated/PEGylated monolayer allowing the covalent immobilization of anti-CTC biomarker antibodies. Two covalent immobilization strategies were studied: (i) novel site-specific via enzymatic activation, copper free strain promoted azide-alkyne click chemistry (SPAAC) using dibenzocyclooctyne and (ii) conventional carbodiimide/NHS chemistry via amine coupling for comparative analysis. Surface characterization was performed through XPS analysis, AFM, and Infra-Red spectroscopy. SPRi analysis was used to evaluate biosensing efficiency. Comparative analysis between conventional and copper free click chemistry exhibited SPAAC immobilized target recognition to be ~3 times higher. Thus, optimal coupling chemistry was demonstrated leading to site-specific and oriented antibody immobilization on functionalized gold surfaces. Then, to trap cancer cells, PDMS microfluidic device was fabricated via moulding protocol. Characterization for valve actuation and trap unit functionality was performed first using microbeads and then metastatic breast cancer MCF7 cell line. For analysis of biomarkers secreted directly by cancer cells, ELISA was performed for metastatic ovarian cancer SK-OV-3 cells for Interleukin-6 (IL-6) and fibronectin, where around 5-50 pg/nL for IL-6 and 600-800 pg/nL for fibronectin concentrations were analysed per cell. An integrated setup was developed with a label-free optical NHA biosensor coupled within a pneumatically actuated microfluidic device for directed real-time and multiplexed analysis of such biomarker concentrations. Cancer associated biomarkers i.e., IL-6 and soluble Tumour Necrosis Factor Receptor 2 (TNFR2) were injected into the integrated microsystem for characterization of biosensing efficiency using the optimal surface immobilization approach. We were able to highlight significant difference between specific IL-6 signal interaction vs non-specific TNFR2 signal interaction, however for subsequent lowered concentration (sub ng/mL to pg/mL), this setup is not sensitive enough to detect such small biomarkers. This could be due to inconsistencies showcased for the gold film deposition protocol employed for NHA fabrication, where significant difference between hole size and deposition depth was showcased. The system developed in this work provide an avenue for studying the effects of different chemotherapeutic drugs on cultured CTCs from cancer patient blood samples. The results obtained are expected to further contribute towards the development of precise cancer diagnosis and personalized treatments.

Keywords:

Circulating tumour cells (CTCs), Cancer biomarkers, Surface functionalization, Copper-free click chemistry, Antibody immobilization, Plasmonic biosensor, Nanohole arrays (NHA), Extraordinary optical transmission (EOT), Microfluidics, Pneumatic valves, Cell trapping

Titre: Étude en temps réel d'échantillons biologiques modèles sur plateforme microfluidique dédiée couplée à un biocapteur multiplexé : un pas vers le Lab-on-Chip pour les clusters CTC

Résumé:

Le cancer est dû à une proliferation incontrôlée de cellules dans une partie l'orgnisme, tandis qu'une métastase est la propagation du cancer à différentes parties de l'organisme via la circulation sanguine. Ces dernières années, les cellules tumorales circulantes (CTC) sont devenues incontournables pour leur rôle dans la progression métastatique. Ces cellules proviennent du site tumoral primaire et expriment des biomarqueurs spécifiques de la propagation du cancer. Leur détection et leur analyse peuvent fournir des informations précieuses pour le diagnostic, le dépistage précoce et la surveillance du cancer. L'objectif de ce projet est de développer un microsystème fluidique integrant un biocapteur permettant à la fois de piéger et cultiver ces cellules rares et d'analyser les biomarqueurs sécrétés. Le biocapteur sélectionné est basée sur une détection sans marquage utilisant des matériaux plasmoniques (or, Au) et la nanostructuration (matrice de nanotrous, NHA). Les surfaces d'or ont été fonctionnalisées avec une monocouche mixte alkylée/PEGylée permettant l'immobilisation covalente d'anticorps anti-biomarqueur de CTC. Deux stratégies d'immobilisation covalente ont été étudiées: (i) la chimie click sans cuivre utilisant du dibenzocyclooctyne (SPAAC) et une activation enzymatique site-spécifique, et (ii) la chimie conventionnelle carbodiimide/NHS via le couplage des amines pour l'analyse comparative. La caractérisation de surface a été réalisée par XPS, AFM et spectroscopie infra-rouge. L'analyse SPRi a été utilisée pour évaluer l'efficacité de la biodétection. Il a été démontré que la chimie click SPAAC conduit à une reconnaissance des cibles 3 fois plus élevée qu'avec la chimie conventionnelle. La chimie click SPAAC permet donc l'immobilisation d'anticorps site- spécifique et orientée sur les surfaces d'or fonctionnalisées.Ensuite, pour piéger les cellules cancéreuses, un dispositif microfluidique en PDMS a été fabriqué via un protocole de moulage. La caractérisation de l'actionnement des vannes et de la fonctionnalité de l'unité de piègeage a d'abord été réalisée à l'aide de microbilles, puis de la lignée cellulaire MCF7 du cancer du sein métastatique. Afin de verifier les concentrations de biomarqueurs sécrétés par les CTC, un dosage ELISA de l'Interleukine-6 (IL-6) et de la fibronectine a été réalisé sur les cellules de cancer métastatique ovarien SK-OV-3. Les résultats indiquent 5-50 pg/mL pour IL-6 et 600-800 pg/mL pour la fibronectine. Une configuration intégrée a été développée avec le biocapteur NHA dans le dispositif microfluidique pour la detection en temps reel et l’analyse multiplexe de ces concentrations de biomarqueurs. Des biomarqueurs associés au cancer, à savoir l'interleukine-6 (IL-6) et le récepteur soluble du facteur de nécrose tumorale 2 (TNFR2), ont été injectés dans le microsystème pour caractériser l'efficacité de la biodétection utilisant l'approche d'immobilisation optimale des anticorps anti-IL-6 sur la surface du biocapteur. Nous avons mis en evidence une difference significative entre la detection spécifique de IL-6 et la detection non spécifique de TNFR2. Cependant pour des concentrations de l’ordre du ng/mL ou pg/mL, notre dispositif n’est pas suffisamment sensible probablement à cause de la mauvaise qualité du dépôt d’or sur les NHA. Le système développé dans ce travail offre une voie pour étudier les effets de différents traitements chimiothérapeutiques sur les CTC en culture à partir d'échantillons de sang de patients cancéreux. Les résultats obtenus devraient contribuer au développement d'un diagnostic précis du cancer et de traitements personnalisés.

Mots clés:

Cellules tumorales circulantes (CTC), Biomarqueurs du cancer, Fonctionnalisation de surface, Chimie du clic sans cuivre, Immobilisation d'anticorps, Biocapteur plasmonique, Réseaux de nanotrous (NHA), Transmission optique extraordinaire (EOT), Microfluidique, Valves pneumatiques, Piégeage cellulaire

Appendix: Research output

List of publication(s) under peer review, emanating from the thesis work

Hussain, S. H., Huertas, C. S., Mitchell, A., Deman, A. L., & Laurenceau, E. (2022). Biosensors for circulating tumor cells (CTCs)-biomarker detection in lung and prostate cancer: Trends and prospects. Biosensors and Bioelectronics, 197, 113770.

List of manuscripts under preparation, emanating from this work:

Hussain, S.H., Gehin, T., Botella, C., Yeromonahos, C., Chevolot, Y., Szydzik, C., Huertas, C.S., Mitchell, A., Deman, A.L. and Laurenceau, E., Rapid, Site-Specific, and Oriented Surface Immobilization Approach Through Copper-Free Click Chemistry for Plasmonic Immunosensors. Available at SSRN 4397147.

List of national/international conferences where work done in this thesis was presented:

ASCOS (Oct 2022) Optical chemo- and biosensors focusing on signal transduction, interface architecture, molecular recognition, microfluidics, and sensor applications Universität Ulm and Universität Innsbruck, Obergurgl, AT

Colloque du LN2 (LN2 lab Symposium) (July 2022) CNRS, Université de Sherbrooke, Ecole centrale de Lyon UGA and INSA Annecy, Fr/On-line

Hussain, S.H., Gehin, T., Botella, C., Yeromonahos, C., Chevolot, Y., Szydzik, C., Huertas, C.S., Mitchell, A., Deman, A.L. and **Laurenceau, E.,**

SPIE (Apr 2022) Presented: Gold surface bioengineering: a chemical perspective SPIE Photonics Europe Strasbourg, FR/On-line

Hussain, S.H., Gehin, T., Botella, C., Yeromonahos, C., **Chevolot, Y**., Szydzik, C., Huertas, C.S., Mitchell, A., Deman, A.L. and Laurenceau, E.,

4th International Workshop of the IEEE Sensors France Chapter (Nov 2021) Presented: Label-free optical immunosensor for CTC biomarker analysis: Development of copper-free click chemistry for one-step and oriented antibody immobilization Sensor technologies: Health, Wellness & Environmental Applications Marseille, FR/Online

Hussain, S.H., Gehin, T., Botella, C., Yeromonahos, C., Chevolot, Y., Szydzik, C., Huertas, C.S., Mitchell, A., Deman, A.L. and Laurenceau, E.,

GdR B21(Sep 2021) Presented: Comparative analysis between conventional carbodiimide / NHS coupling and copper-free click chemistry: Surface characterization and biological efficiency Bioengineering and surface interfaces Toulouse, FR

Hussain, S.H., Gehin, T., Botella, C., Yeromonahos, C., Chevolot, Y., Szydzik, C., Huertas, C.S., Mitchell, A., Deman, A.L. and Laurenceau, E.,

BIOSENSORS 2021 (July 2021) Poster: Oriented antibody immobilization through site-specific copper free click chemistry for design of efficient immunosensors

Hussain, S.H., Gehin, T., Botella, C., Yeromonahos, C., Chevolot, Y., Szydzik, C., Huertas, C.S., Mitchell, A., Deman, A.L. and Laurenceau, E.,

BIOSENSORS 2021 (July 2021) Summer school: Commercializing Biosensors, Busan/Online